EXPLORING INFRASOUND WAVEFIELDS TO CHARACTERIZE VOLCANIC ERUPTIONS

By

Alexandra M. Iezzi, B.A.

A Dissertation Submitted in Partial Fulfillment of the Requirements

for the Degree of

Doctor of Philosophy

in

Geophysics

University of Alaska Fairbanks

August 2020

APPROVED:

Dr. David Fee, Committee Chair
Dr. Carl Tape, Committee Member
Dr. Michael West, Committee Member
Dr. Pavel Izbekov, Committee Member
Dr. Matthew Haney, Committee Member
Dr. Paul McCarthy, Chair
Department of Geosciences
Dr. Kinchel C. Doerner, Dean
College of Natural Science and Mathematics
Dr. Anupma Prakash,
Provost and Executive Vice Chancellor

Abstract

Infrasound has become an increasingly popular way to monitor and characterize volcanic eruptions, especially when combined with multidisciplinary observations. Regardless of how close the infrasound instruments are to the eruption, the effects from propagation must be considered prior to characterizing and quantifying the source. In this dissertation, we focus on modeling the effects of the atmosphere and topography on the recorded infrasound waveforms in order to better interpret the acoustic source and its implications on the volcanic eruption as a whole.

Alaska has 54 historically active volcanoes, one third of which have no local monitoring equipment. Therefore, remote sensing (including that of infrasound arrays) is relied upon for the detection, location, and characterization of volcanic eruptions. At long ranges, the wind and temperature structure of the atmosphere affects infrasound propagation, however, changes in these conditions are variable both in time and space. We apply an atmospheric reconstruction model to characterize the atmosphere and use infrasound propagation modeling techniques for a few recent eruptions in Alaska. We couple these atmospheric propagation results with array processing techniques to provide insight into detection capability and eruption dynamics for both transient and long-duration eruptions in Alaska. Furthermore, we explore the future implementation of this long-range infrasound propagation modeling as an additional monitoring tool for volcano observatories in real time.

The quantification of volcanic emissions, including volume flow rate and erupted mass, is possible through acoustic waveform inversion techniques that account for the effects of propagation over topography. Previous volcanic studies have generally assumed a simple acoustic source (monopole), however, more complex source reconstructions can be estimated using a combination of monopole and dipole sources (multipole). We deployed an acoustic network around Yasur volcano, Vanuatu, which has eruptions every 1-4 minutes, including acoustic sensors along a tethered aerostat, allowing us to better constrain the acoustic source in three

dimensions. We find that the monopole source is a good approximation when topography is accounted for, but that directionality cannot be fully discounted. Inversions for the dipole components produce estimates consistent with observed ballistic directionality, though these inversions are somewhat unstable given the station configuration. Future work to explore acoustic waveform inversion stability, uncertainty, and robustness should be performed in order to better estimate and quantify the explosion source.

Volcanic explosions can produce large, ash-rich plumes that pose great hazard to aviation. We use a single co-located seismic and infrasound sensor pair to characterize 21 explosions at Mount Cleveland, Alaska over a four-year study period. While the seismic explosion signals were similar, the acoustic signals varied between explosions, with some explosions exhibiting a single main compressional phase while other explosions had multiple compressions in a row. A notable observation is that the seismo-acoustic time lag varied between explosions, implying a change in the path between the source and receiver. We explore the influence of atmospheric effects, nonlinear propagation, and source depth within the conduit on this variable seismo-acoustic time lag. While changes in the atmospheric conditions can explain some of the observed variation, substantial residual time lags remain for many explosions. Additionally, nonlinear propagation does not result in a measurable difference for the acoustic onset. Therefore, using methods such as seismic particle motion analysis and cross correlation of waveforms between events, we conclude that varying source depth within the conduit likely plays a key role in the observed variation in the seismo-acoustic time lags at Mount Cleveland.

Table of Contents

List of Figures

List of Tables

Acknowledgments

First and foremost, I would like to thank my advisor and biggest supporter David Fee. Words cannot describe the amount of support (in all senses of the word) you have given me over the past 5 years and how much it meant to me. I am eternally grateful for every meeting, fieldwork experience, phone call, paper edit, and conference attended that all helped shape the researcher I became. While a dissertation is the concrete evidence of the work that came out of my PhD studies, the life lessons, proper research techniques, and collaboration opportunities you taught me are arguably just as important, which I will carry with me throughout my career path.

I would also like to thank my committee members (Carl Tape, Mike West, Matthew Haney, and Pavel Izbekov) for supporting my research and pushing me over the years. Similarly, I would like to thank my coauthors (Hans Schwaiger, Keehoon Kim, Art Jolly, Robin Matoza, and John Lyons) who very well could have been on my committee for the amount of work they put in to supporting my research and making my PhD possible. Additionally, I would like to thank Phil Blom for giving me the opportunity to explore the national security side of infrasound and helping me grow even more as a researcher.

I owe a huge part of my PhD to the Alaska Volcano Observatory (AVO) and everyone that is a part of it and will be forever grateful for the support and kindness from each and every one of you. Chris Waythomas, you took a chance and brought on a physics major from Connecticut who knew nothing about volcanoes but was convinced it was her life's calling, which absolutely led to my future at the University of Alaska Fairbanks (UAF). Aaron Wech, John Lyons, John Power, and Matt Haney (and many others!), whether it was research, career, or personal, you were all there to help guide me and keep me moving forward.

Thank you to Doug Thompson, my undergraduate advisor who guided me as I worked to build my resume and apply to graduate school. You helped get me my internship with

AVO as an undergrad, which directly led to my graduate education decisions.

Last, but certainly not least, I would like to thank my family and friends who supported me and kept me (somewhat) sane throughout the years. Mom and Steve, although you may not fully understand why I decided to pursue a PhD and move to a cabin in the woods, you were always there to support me every step of the way and I couldn't have done any of it without you! Rich, thank you so much for being there for me since literally day one of the journey, for every step of the roller coaster of emotions that is grad school.

This dissertation is comprised of three manuscripts for which I am the first author. I conducted the majority of the research, data analysis, and writing of the manuscripts, with guidance and edits provided by my coauthors. Coauthors for the three manuscripts are David Fee, Hans Schwaiger, Matthew Haney, Keehoon Kim, Arthur Jolly, Robin Matoza, and John Lyons.

Chapter 1

General Introduction

1.1 Infrasound

Infrasound (or low frequency sound waves below 20 Hz) can be recorded from a variety of natural (e.g. volcanoes, earthquakes, microbarom, and bolides/meteors) and anthropogenic (e.g. rockets, industrial activity, and chemical and nuclear explosions) sources. Infrasound propagates as a compressional (or longitudinal) wave that moves at the speed of sound, which in an ideal gas is defined as

$$c = \sqrt{\gamma RT} \tag{1.1}$$

where γ is the specific heat ratio, R is the universal gas constant, and T is the temperature [*Pierce*, 1981]. At a standard temperature of 20°C (68°F) at sea level, the sound speed (c) is 343 m/s. Temperature, and therefore sound speed, fluctuates as a function of time, space, and altitude. In addition to temperature, the speed at which infrasound propagates is greatly influenced by the wind velocities that may increase or decrease the sound speed.

Infrasound recordings are an indication of shallow to subaerial activity and can be used to detect, locate, characterize, and quantify acoustic sources. It is becoming increasingly popular for volcano monitoring because the propagation of infrasound is not dependent on cloud cover like other remote sensing techniques (i.e. satellite imagery). Additionally, it can propagate for hundreds to thousands of kilometers due to low acoustic attenuation at these low frequencies, allowing for arrays of infrasound sensors to be strategically placed in locations where they can be easily maintained.

1.1.1 The Acoustic Source

The infrasonic multipole source mechanism, similar to the moment tensor in seismology, can be represented as the combination of pressure fluctuations from simple sources. A

monopole (or simple) source represents the net change of mass flow rate in a compact source region, generating sound that radiates equally in all directions. This is the type of source that is assumed most often in infrasound studies. *Lighthill* [1978] defines the pressure at time t and distance r resulting from a monopole source as

$$p(t,r) = \frac{\dot{S}(t - r/c)}{4\pi r} \tag{1.2}$$

where $\dot{S}$ is the source strength (rate of change of the mass flow rate) and c is the speed of sound. The dipole source is equivalent to force or momentum changes within the fluid (i.e. no net introduction of fluid) and can be represented by two closely spaced (with respect to the acoustic wavelength) monopoles that are out of phase by 180°. The acoustic dipole results in directivity of the acoustic radiation pattern, where there is zero pressure change orthogonal to the dipole axis and the maximum pressure change exists at the dipole axis [*Johnson et al.*, 2008; *Lighthill*, 1952]. Dipole source mechanisms are less efficient than a monopole source since the two alternating simple sources have a combined radiation pattern that cancels much of the radiated energy [*Kim et al.*, 2012; *Lighthill*, 1952]. Finally, dipole sources can be combined to form higher order source terms (lateral and longitudinal quadrupoles, etc.).

1.1.2 Linear and Nonlinear Propagation

Linear propagation of acoustic waves is often assumed in many infrasound studies. In linear acoustics, it is assumed that i) the speed of propagation is independent of amplitude and frequency, ii) the speed of the atmosphere is assumed to be substantially less than the speed of sound, iii) the atmosphere returns to its initial state after the sound wave passes, and iv) the principle of superposition holds for the interaction of multiple sound waves [*Atchley*, 2005]. If these assumptions are true and propagation of sound is linear, then it can be simple to characterize the acoustic source such as calculating the explosion yield of an anthropogenic source or a mass flow rate for a volcanic explosion.

For very high amplitude acoustic sources, the sound waves produced can travel faster than

the speed of sound (i.e. supersonic) and propagate nonlinearly. In nonlinear propagation, the speed of propagation is dependent on the instantaneous amplitude [*Atchley*, 2005], which violates the first assumption of linear acoustics previously mentioned. Because of this, the waveform distorts as it travels, where the compressional (positive) phase travels faster than the rarefaction (negative) phase, potentially steepening into a shock wave [*Atchley*, 2005; *Reichman et al.*, 2016; *Maher et al.*, 2020]. This shock wave is often described by the Friedlander equation [*Friedlander*, 1946], which defines the pressure of a shock wave ($p(t)$) as

$$p(t) = P_s e^{-\frac{t}{t^*}} \left(1 - \frac{t}{t^*}\right) \tag{1.3}$$

where P_s is the source overpressure and t^* is the relaxation time (time when the rarefaction begins after the compression returns the ambient pressure). The amplitude of these nonlinear waves decay and transition into linear sound waves after some distance, usually by the time an infrasound sensor placed at a safe distance away from the source can record the signal. Therefore, nonlinear propagation remains somewhat elusive in natural settings, though it is understood in theory.

Since nonlinear propagation can affect both the amplitude and frequency content of explosion waveforms that are recorded, the calculation of explosion size/yield becomes more difficult than if propagation were strictly linear. A recent study by *Maher et al.* [2020] performed detailed analysis of local infrasound data from Sakurajima volcano and the potential impact of spectral energy transfer to higher frequencies due to nonlinear propagation. They find that nonlinear propagation impacts locally recorded waveforms on volcanoes far less than the effects of winds and topography. Another study by *de Groot-Hedlin* [2016] finds that nonlinearity has a greater effect on frequency of the recorded waveform as compared to the amplitude as infrasound propagates away from the source. Therefore, the assumption of linear acoustic propagation is likely valid in many studies.

1.2 Global Sources of Infrasound

Infrasound sensors can be deployed as single sensors, as large scale distributed networks, or as arrays. A network consists of a number of sensors that are distributed around or near a source which allows for precise source localization and often increased source characterization capabilities. An array is a group of sensors spaced closer together in a specific configuration that is away from a source and is tuned to detect coherent waves between the sensors at infrasonic frequencies (i.e. long wavelengths).

The Comprehensive Nuclear-Test-Ban Treaty (CTBT) bans nuclear explosion tests globally and was opened for signature in 1996. In an effort to monitor global compliance, the International Monitoring System (IMS) has been installed and consists of seismic, hydroacoustic, infrasound, and radionuclide sensors to detect underground, underwater, subaerial explosions, and nuclear confirmation, respectively. The infrasound component of the IMS is a network of 60 planned infrasound arrays, 51 of which have been installed as of 2019, and whose placement (average spacing of ~2,000 km) is configured around the ability to detect atmospheric explosions with an equivalent yield of 1 kiloton or more worldwide [*Christie and Campus*, 2010]. While the arrays were set up for detecting potential nuclear explosion testing [e.g. *Assink et al.*, 2016, 2018], the IMS is used to study a variety of other sources of infrasound including volcanic eruptions [e.g. *Matoza et al.*, 2017], earthquakes [e.g. *Evers et al.*, 2014; *Shani-Kadmiel et al.*, 2018; *Pilger et al.*, 2019], bolides/meteors [e.g. *Le Pichon et al.*, 2013; *Pilger et al.*, 2015], chemical explosions [e.g. *Fee et al.*, 2013], and the microbarom [e.g. *Le Pichon et al.*, 2006; *Landès et al.*, 2012].

The EarthScope Transportable Array (TA) is a network of 400 seismometers and atmospheric sensors that were temporary installations of two years that rolled across the United States with roughly 70 km spacing beginning in 2007. The TA project began installing infrasound sensors as part of their normal station setup in 2010, corresponding to the times when the Center and Eastern US networks were installed, as well as in Alaska. So far, the infrasound sensors in this network have been used to study volcanic eruptions [*Fee et al.*,

2017a; *Sanderson et al.*, 2020], gravity waves [*de Groot-Hedlin et al.*, 2014], and meteors [*de Groot-Hedlin and Hedlin*, 2014].

Permanent regional networks of infrasound sensors also exist, such as that run by the Alaska Volcano Observatory (AVO). AVO currently operates 28 single stations and six infrasound arrays to help monitor its 54 historically active volcanoes spanning 2500 km.

1.2.1 Anthropogenic

Anthropogenic sources of infrasound include those from chemical tests (both surface and underground), suspected nuclear explosion tests, mining blasts, industrial noise, and wind farms. Geophysical recordings of chemical tests with known source locations and yields such as the Source Physics Experiment [SPE, *Snelson et al.*, 2013] and Sayarim Calibration Tests [*Fee et al.*, 2013] increase the knowledge of the infrasonic source, effects that the atmosphere and topography have on the propagation, and allow for the development of better analysis tools for infrasound monitoring. As a local recording example, *Jones et al.* [2014] use the ground motion from buried chemical explosions recorded by accelerometers to predict the acoustic pressure signals at distances up to 5 km from the source. At long ranges, the IMS infrasound arrays have been used to help determine values such as explosion depth and yields from underground nuclear tests by the DPRK [*Assink et al.*, 2016, 2018]. Additionally, quasi-continuous sound from wind farms, which is characterized by a fundamental frequency with harmonics, has been used to better understand the changing conditions of the lower part of the atmospheric boundary layer [*Marcillo et al.*, 2015].

1.2.2 Volcanoes

Volcanoes can produce a variety of infrasound signals from eruptions, degassing, and mass wasting events. This is discussed in detail in Section 1.5.

1.2.3 Microbarom

The microbarom is a permanent source of infrasound (between 0.1-0.5 Hz, generally with peaks at ∼0.2-0.3 Hz) that is created by the nonlinear interaction between ocean waves with the atmosphere and can be detected over thousands of kilometers. This is similar to its seismic counterpart, the microseism, which is also created by waves in the ocean and large lakes that can be detected on seismometers around the world. Due to its continuous nature, the microbarom is often used to evaluate detection capabilities of infrasound arrays as well as inferring the atmospheric conditions between the source and receiver [*Le Pichon et al.*, 2006; *Landès et al.*, 2012]. A clear seasonal trend in dominant microbarom source locations has been found, switching between the northern and southern hemispheres [*Landès et al.*, 2012].

1.2.4 Earthquakes

Infrasound can be created by intense ground motions due to large earthquakes. Infrasound radiated from the rupture zone itself is termed "epicentral infrasound", while recent studies have shown that infrasound can be also be produced from secondary regions of ground motion such as mountain ranges. The underwater M_W 8.1 earthquake near Macquarie Ridge, was reported to couple from the water into the atmosphere evanescently [*Evers et al.*, 2014]. *Evers et al.* [2014] found that if the hydroacoustic wavelength is much larger than the source depth, energy can be transferred through the water-air interface at shallow water depths near objects such as seamounts and underwater ridges and recorded by an infrasound array. Back projection methods have been used to relate signals observed at an IMS array to both the epicentral infrasound signal as well as secondary infrasound sources [*Shani-Kadmiel et al.*, 2018; *Pilger et al.*, 2019]. Furthermore, *Pilger et al.* [2019] find no clear connection between infrasound recordings and the supershear nature of the magnitude 7.5 Sulawesi earthquake (i.e. the rupture velocity of the earthquake was greater than the propagation speed of the seismic waves). Recently, *Shani-Kadmiel et al.* [2019] presented on the potential to obtain

earthquake shaking intensity and source mechanism using remote infrasound recordings on the IMS, which could provide another means of quickly quantifying the hazards from large earthquakes. They find good agreement between their results and the USGS estimated ShakeMap and the Global CMT moment tensor for the event.

1.2.5 Bolides/Meteors

Meteors are meteoroids that have entered the Earth's atmosphere and burn up, often referred to as fireballs or shooting stars. One of the largest sources of infrasound, at least in modern times of infrasound recordings, is from the Chelyabinsk meteor in 2013. It was recorded by infrasound arrays up to distances of ~85,000 km, some signals of which travelled around the globe twice [*Le Pichon et al.*, 2013]. This meteor was recorded by at least 20 IMS infrasound arrays [*Le Pichon et al.*, 2013; *Pilger et al.*, 2015], as well as the EarthScope TA [*de Groot-Hedlin and Hedlin*, 2014]. *Pilger et al.* [2015] examined the signals from this meteor on the IMS infrasound arrays, finding that a clear preference for detection of the meteor signal was from stations perpendicular to the trajectory as well as a strong dependence on the diurnal variability of background noise at the arrays.

1.3 Infrasound Propagation Over a Variety of Distances

Infrasound can be studied at a variety of distances spanning local recordings less than 15 km, regional from ~15-250 km, and global infrasound recordings over 250 km from the source [*Fee and Matoza*, 2013]. Because of this, infrasound arrays can be strategically placed in regions where it is not feasible to deploy and maintain infrasound sensors. Arrays can be used to increase the signal to noise ratio especially in places of high wind, as well as to calculate values such as back azimuth and trace velocity in order to better determine which direction the signal came from.

The signal recorded by an infrasound sensor is the combination of the source itself as well as the effects of propagation between the source and the receiver (e.g. topography

and atmospheric conditions). Therefore, prior to being able to fully interpret an acoustic source, the propagation must but characterized. At local distances, it has been shown that topography has a first order effect on the recorded waveform at local distances [e.g. *Kim and Lees*, 2011; *Kim et al.*, 2015; *Fee et al.*, 2017b], while the atmosphere is increasingly important as distance from the source increases [e.g. *Drob et al.*, 2003; *Schwaiger et al.*, 2020].

1.3.1 Local

Early studies of infrasound at local distances assumed propagation was simple compared to seismic and was generally assumed to propagate over a halfspace. It has now been established that infrasound propagation, even at local distances, is highly influenced by topography [*Kim and Lees*, 2011, 2014; *Kim et al.*, 2015; *Lacanna and Ripepe*, 2013]. One avenue of research seeks to constrain the affects of topography using finite-difference time-domain (FDTD) algorithms. *Kim and Lees* [2011] found that significant distortion around the crater rim of Karymsky volcano exists that can be modeled using a FDTD algorithm. At Stromboli volcano, *Lacanna and Ripepe* [2013] found an anomalous decay of the source amplitude up to -11 dB larger than expected (using a simple $1/distance$ assumption) for station not within line of sight of the source. They applied a 2-D FDTD modeling scheme to account for the effects of topography. Similarly, *Kim and Lees* [2014] used a 3-D FDTD model to obtain the full 3D Green's functions that accounts for topography (i.e. response of a simple source from source to receiver). While simple FDTD models are appealing due to their ability to run simple simulations on a personal computer, more computationally expensive, higher order FDTD models exist such as ElAc [*Petersson and Sjögreen*, 2018] as well as spectral element methods [e.g. *Brissaud et al.*, 2017; *Martire et al.*, 2018]. On the other end of the spectrum, simple models for 1-D wave propagation inside a volcanic crater was used to understand changing crater properties [e.g. CRes, *Watson et al.*, 2019], such as from a lava lake whose height moved up and down within a conduit, requiring many propagation model runs to

account for these changes.

The atmospheric boundary layer can play a critical role in the propagation of infrasound over just a few kilometers. However, the effects of the atmosphere in the first few kilometers of altitude is poorly constrained using numerical weather predication models and therefore studies have been performed in order to better constrain the lower atmosphere. For example, *Marcillo and Johnson* [2010] used continuous infrasound from Kilauea to invert for the horizontal wind speeds between the source and receiver. *Kim et al.* [2018] perform waveform inversions for a series of explosions to explore the need for atmospheric constraints on local infrasound propagation, finding that atmospheric heterogeneity has non-negligible impacts on infrasound amplitude. Additionally, radiosondes are becoming increasingly popular as a way to perform in situ measurements of the atmosphere at a given time and location (up to ~30 km altitude), though they can be expensive and difficult to deploy in remote locations.

1.3.2 Regional and Global

The structure of the atmosphere plays a critical role in the propagation of infrasound at regional and global distances. As stated by Equation 1.1, the adiabatic sound speed is dependent on the temperature. However, in a realistic atmosphere, winds also play a large role to enhance or diminish the propagation of sound. Thus, long range infrasound studies generally use the effective sound speed, defined as

$$c_{eff} = c + \vec{v} \cdot \vec{u} \tag{1.4}$$

where c is the adiabatic sound speed (Eq. 1.1) and $\vec{v} \cdot \vec{u}$ the vector component of the horizontal wind velocity in a particular direction [*Fee and Matoza*, 2013; *Salomons*, 2001]. These wind and temperature influences on the effective sound speed are highly anisotropic and enhance the propagation of infrasound in the downwind direction or diminish the propagation in the upwind direction. Infrasound is subject to both spreading and absorption losses in energy [*Salomons*, 2001]. Geometric spreading is independent of frequency and occurs as the sound

spherically spreads away from the source, decreasing in amplitude as $1/r$ (r being the radial distance from the source). Cylindrical spreading can also occur in certain situations, in which amplitudes decrease as $1/\sqrt{r}$. Atmospheric absorption is another type of energy loss for infrasound that is dependent on frequency, as well as temperature and humidity of the medium [*Salomons*, 2001]. The relatively low amount of absorption at infrasonic frequencies (as compared to those in the audible range) allows infrasound to propagate over large distances.

When the effective sound speed surpasses the effective sound speed at the source, the acoustic energy refracts down towards Earth's surface. This causes the formation of ducts, or waveguides, where infrasound is preferentially guided. Infrasound propagates to altitudes up to ~120 km with the three main ducts being the troposheric, stratospheric, and thermospheric ducts. The tropospheric duct spans from Earth's surface to 10-20 km in altitude (higher at the Equator and lower near the poles). Acoustic energy ducted in the troposphere arrives at the station the fastest with the highest amplitude. However, these ducts are ephemeral and can fluctuate between existence and nonexistence over short times scales and over long distances. The stratospheric duct spans altitudes up to ~50 km and its existence is dependent on the zonal winds that reverse with the season (East in the winter hemisphere and West in the summer hemisphere). Exceptions to this trend exist and are referred to as sudden stratospheric warming (SSW) events [e.g. *Smets and Evers*, 2014]. The thermospheric duct spans altitudes up to ~120 km. Signals that propagate to these altitudes are generally lower in both amplitude and frequency due to enhanced attenuation. Any energy with steeper takeoff angles leaving the source close to vertical exceeds the thermospheric duct and does not refract back to the surface.

Because winds and temperature vary as a function of time, altitude, and distance, atmospheric values are non-unique and must be modeled for each event. High resolution atmospheric specifications (both temporally and spatially) for the lower atmosphere exist, however, infrasound can be guided up to ~120 km altitude. Atmospheric reconstruction

ground-to-space models such as NRL-G2S [*Drob et al.*, 2003] and AVO-G2S [*Schwaiger et al.*, 2019] seamlessly integrate the atmospheric specifications for the lower atmosphere with empirical models for winds [HWM, *Hedin et al.*, 1996; *Drob et al.*, 2008, 2015] and temperatures [NRLMSISE-00, *Picone et al.*, 2002] for the upper atmosphere. Propagation modeling through the reconstructed atmosphere can then be used to determine the likely paths (ducts) the infrasound energy is likely to take between the source and receiver. Atmospheric propagation modeling includes ray tracing [e.g. GeoAc, *Blom*, 2014], normal modes [*Waxler et al.*, 2017], and the parabolic equation [*Waxler et al.*, 2015]. Conversely, a few studies use ground-truth infrasound observations to better determine these model atmospheric conditions for infrasound propagation in the upper atmosphere [*Le Pichon et al.*, 2005; *Antier et al.*, 2007].

1.4 Detection, Localization, and Quantification

Some of the overall goals for the growing field of infrasound include detection, localization, and quantification of an event. As discussed earlier, these can all be done at a variety of distances from the source as well as using a variety of station configurations. Some of these techniques are discussed briefly.

1.4.1 Detection

For monitoring and characterizing sources of infrasound, the detection of a coherent, real infrasound signal is often the first step. There are a variety of infrasound processing techniques for detecting signals depending on the arrangement and footprint of the infrasound sensors. For infrasound arrays and therefore array processing techniques, the plane wave approximation is often used. Array processing techniques allow for the computation of the trace velocity (propagation speed across the array), backazimuth (direction the signal came from, measured clockwise from North), and many use beamforming techniques to increase the signal to noise ratio (SNR) [*Johnson and Dudgeon*, 1992]. Common infrasound array

processing methods include the Fisher Ratio [*Melton and Bailey*, 1957], Progressive Multi-Channel Correlation Method (PMCC) [*Cansi*, 1995], least squares estimation [*Szuberla and Olson*, 2004], and least trimmed squares (LTS) [*Bishop et al.*, 2020]. Deployments of single sensors or networks can also be used for signal detection with techniques such as short term average/long term average (STA/LTA) and VINEDA [*Bueno et al.*, 2019].

The detection capability of infrasound sensors, whether it's a single sensor, network, or array configuration, is dependent on the background noise which often comes from wind. The aperture of an infrasound array is designed so that the longer wavelength infrasound waves of interest remain coherent between elements while the shorter wavelength wind noise will be incoherent. Infrasound sensors should be deployed in low-wind environments, such as forests, but this is not always feasible. The effects of wind on an infrasound sensor can be mitigated in a variety of ways, ranging from pipe arrays for spatial averaging (e.g. the IMS array) to small ∼1-m diameter wind domes. Even with noise suppression techniques, storms can be overwhelming and mask small amplitude signals.

1.4.2 Localization

Once a coherent, real signal is detected, it is often of interest to localize the event, or determine where the source was. For array processing, the backazimuth is often the first step, though array processing can only give direction, not range. A recent study by *Green and Nippress* [2019] explores the possibility of using signal duration recorded at an array for transient events as a proxy for source-to-receiver distance, as the duration of the signal increases with distance due to increasing separation of the fast and slow arrivals of the wavefield propagating in the atmospheric ducts. Techniques that involve multiple arrays include back projection [*Shani-Kadmiel et al.*, 2018; *Pilger et al.*, 2019], regional distance reverse-time migration [*Sanderson et al.*, 2020], IMS VASC [*Matoza et al.*, 2017], and Bayesian Infrasonic Source Localization (BISL) [*Modrak et al.*, 2010; *Marcillo et al.*, 2013; *Blom et al.*, 2015]. Time reversal methods have also been used for local networks over

shorter distances to locate volcanic events [*Kim and Lees*, 2014; *Fee et al.*, 2019].

1.4.3 Quantification

Quantification of infrasound recordings is a growing area of research, as obtaining yield or mass eruption rates (MER) is of great interest to the community. A few simple ways to quantify infrasound are intensity, energy, and power. The acoustic intensity is defined as the average rate of flow of energy through a unit area normal to the direction of propagation [*Fee and Matoza*, 2013]

$$I = \frac{P^2}{\rho_{atmos} c} \tag{1.5}$$

where P is the excess pressure and ρ_{atmos} is the density of the atmosphere. The acoustic energy ($E_{acoustic}$) is intensity integrated over time and the region of propagation, which for a simple monopole source reduces to [e.g. *Firstov and Kravchenko*, 1996; *Johnson*, 2003; *Vergniolle et al.*, 2004; *Johnson and Aster*, 2005]

$$E_{acoustic} = \frac{2\pi r^2}{\rho_{atmos} c} \int \triangle P(t)^2 dt \tag{1.6}$$

The acoustic power can be calculated by differentiating the acoustic energy with respect to time.

Waveform inversion techniques have become of particular interest to the volcano community starting in seismology [e.g. *Ohminato et al.*, 1998] and more recently infrasound [*Johnson et al.*, 2008; *Kim et al.*, 2012, 2015; *Fee et al.*, 2017b] as they exploit more information in the recorded waveforms to aid in our understanding of the source mechanism. These techniques use local infrasound recordings and have recently began incorporating the effects of topography using methods such as FDTD to obtain 3D Greens functions for the path between source and receiver [e.g. *Kim et al.*, 2015; *Fee et al.*, 2017b; *Diaz-Moreno et al.*, 2019]. Recent studies on volcano infrasound have focused on the calculation of erupted mass assuming a

monopole source using acoustic waveform inversions [e.g. *Kim et al.*, 2015; *Fee et al.*, 2017b], which is an invaluable measure for volcano monitoring and helps inform predictions for ash transport modeling such as Ash3D [*Schwaiger et al.*, 2012]. Acoustic waveform inversions have also been used for understanding the acoustic source of controlled anthropogenic sources using local infrasound sensor deployments [*Kim*, 2017; *Kim et al.*, 2018].

Quantification of infrasonic sources becomes more complex at longer ranges due to the effects of the atmosphere, but is still an active area of research for the CTBTO community goals. Methods for determining yield can be done using empirical period-yield scaling relations [e.g. for a bolide, *Le Pichon et al.*, 2013] and by combining seismic and infrasound methods to determine the trade-off between depth and yield estimates [e.g. DPRK underground nuclear explosions, *Assink et al.*, 2016].

1.5 Volcano Infrasound

Volcanic eruptions can be hazardous to humans and infrastructure, with proximal hazards including ash/gas emissions, ballistics, lava flows, pyroclastic density currents, and lahars, as well as distal hazards such as drifting ash clouds high in the troposphere (and sometimes into the stratosphere). Eruptions are monitored by a variety of techniques including seismic, infrasound, satellite imagery (visible, thermal, gases), web cameras, deformation, and geologic studies. When volcanoes erupt, a large quantity of the acoustic energy is emitted in the infrasound band. The 1883 eruption of Krakatau volcano, Indonesia is often discussed as the beginning of volcano infrasound studies. During this eruption, audible sounds were heard as far as 5000 km from the volcano and acoustic-gravity waves (very long period) circled the globe at least seven times [*Strachey*, 1888].

Seismology has long been used to study a variety of signals at volcanoes from the transport of magma or other fluids to explosion signals. Infrasound complements its seismic counterpart, as it is an indication of shallow to subaerial activity that might be more ambiguous when interpreting seismic signals alone. Because of this, studies often analyze both

seismic and acoustic signals when trying to understand shallow and subaerial volcanic processes. For some sources of infrasound, such as large explosions, infrasound may couple into the ground as a ground-coupled airwave (GCA) [e.g. *Fee et al.*, 2016; *McKee et al.*, 2018]. Infrasound signals have the advantage of being supplemented by direct and remote observations of quantities such as gas, ash, and thermal activity, which is not always achievable for seismic signals that are produced from sources underground. Thus, infrasound is becoming increasingly useful in both understanding volcanic source processes as well as aiding hazard mitigation techniques in near real time.

1.5.1 Eruption Styles

Volcanoes produce a wide spectrum of eruption styles, ranging from effusive to explosive activity. With the range of eruption styles comes a range of hazards and potential impacts on society, which hopefully can be predicted by observatories and information dispersed to the public to mitigate the harm to humans and infrastructure. These different types of activity also create a variety of infrasound signals. Continuous signals that last tens of seconds to months are referred to as tremor and come in a variety of forms, including monotonic, harmonic, gliding, broadband, spasmodic, and banded [*Fee and Matoza*, 2013]. Some eruptions are characterized by transient explosions that consist of a rapid, high-amplitude compression followed by a rarefaction (decompression), with durations lasting on the order of seconds to minutes. Another category of continuous signal is created by sustained volcanic explosions and has been shown to resemble that of jet noise [*Fee and Matoza*, 2013].

Hawaiian-type eruptions are often effusive but can be explosive at times and are often characterized by lava fountaining and fissure eruptions. These eruptions tend to be from low viscosity basaltic magmas. Infrasound from this type of activity is tremor-like, often with broadband spectra [*Fee et al.*, 2011; *Fee and Matoza*, 2013]. Some open vent Hawaiian systems such as from Pu'u 'Ō'ō (Kīlauea) have been shown to exhibit steady and nearly continuous sound induced by flow [*Garcés et al.*, 2003]. However, the infrasonic character

has been shown to vary with activity (between tremor and impulsive events), such as during the collapse and draining of Pu'u 'Ō'ō crater in mid-2007 [*Fee et al.*, 2011]. In this eruption, azimuthal progression in time of infrasound was also used to track the fissure propagation [*Fee et al.*, 2011].

Strombolian and Vulcanian eruptions involve short duration transient explosions. Strombolian eruptions are thought to occur due to the rising of a gas slug in a relatively open system that results in an explosive release of gas. Vulcanian eruptions are often more violent, higher amplitude, and often longer duration explosions caused by the destruction of a solidified lava dome/plug at the top of a conduit, allowing high pressures to build underneath. Both result in impulsive, relatively short duration infrasound signals with the potential for low amplitude jetting after the first initial blast [*Fee and Matoza*, 2013]. Studies of infrasound recordings on volcanoes such as Stromboli [e.g. *Lacanna and Ripepe*, 2013], Yasur [e.g. *Marchetti et al.*, 2013; *Jolly et al.*, 2017], and Erebus [e.g. *Johnson et al.*, 2008] exhibit classic Strombolian explosion behavior that has remained relatively unchanged for years. Infrasonic recordings from explosions at Sakurajima [e.g. *Yokoo et al.*, 2009; *Fee et al.*, 2014; *Kim et al.*, 2015; *Fee et al.*, 2017b] and Santiaguito [e.g. *Sahetapy-Engel et al.*, 2008; *De Angelis et al.*, 2016] volcanoes exhibit Vulcanian behavior.

Some of the largest and most hazardous eruptions are often classified as sub-Plinian-Plinian eruptions, characterized by sustained eruptions that produce large eruption clouds. In some cases of eruptions with large sustained plumes, very low frequency gravity waves can be produced [e.g. *De Angelis et al.*, 2011]. Infrasound signals from these types of eruptions are often high-amplitude, sustained signals that last minutes to hours [*Fee and Matoza*, 2013]. The frequency content of the eruption tremor is broadband and is often observed to be similar to the spectral content of jet noise [*Fee and Matoza*, 2013]. Jet noise has been observed at eruptions from volcanic eruptions [*Matoza et al.*, 2009, 2013] as well as fumarole acoustics [e.g. *McKee et al.*, 2017]. In sustained volcanic eruptions, the lowermost portion of the plume is where the jet noise is sourced, where the column is driven by momentum

as opposed to buoyancy in the upper part of the plume. Quantification of volcanic jet parameters has been shown to be possible and scaled using the Strouhal number [*Fee and Matoza*, 2013; *McKee et al.*, 2017]

$$St = \frac{f_j D_j}{U_j} \tag{1.7}$$

where f_j is the peak frequency of the jet noise, D_j is the diameter of the jet (i.e. vent diameter), and U_j is the jet velocity.

1.5.2 Infrasound From Mass Wasting Events

Mass wasting events on the steep flanks of volcanoes can occur during periods of eruptive activity as well as during periods of volcanic quiescence. Surficial mass wasting events include lahars and outburst floods, edifice collapses, avalanches, rockfalls, and pyroclastic density currents (PDCs) [*Allstadt et al.*, 2018]. These surficial events produce seismic and infrasound signals that may provide key research and real-time monitoring information for these hazardous phenomena. *Allstadt et al.* [2018] provide a nice overview of mass wasting events and their seismic and infrasound signatures.

Lahars pose great hazard to humans and infrastructure due to their ability to travel large distances (tens of kilometers) and can occur both with and without an associated eruption. The most recent catastrophe involving lahars is those from the June 3, 2018 eruption from Fuego volcano, Guatemala that caused roughly 200 deaths as well as large economic losses in the area [*Cando-Jácome and Martínez-Graña*, 2019]. Infrasound (and seismic) signals produced by lahars characteristically appear as cigar-shaped waxing and waning signals, where a low amplitude signal gradually increases in its amplitude and then more slowly decreases [*Zobin et al.*, 2009]. The exact source location of the infrasound within a lahar, or flowage event in general, is not well-known. *Johnson and Palma* [2015] used a three-element infrasound array to study the lahar flow progression at Volcán Villarrica, Chile, detecting an initial flow pulse travelling at an average speed of 38 m/s down the channel. Infrasound

arrays have been deployed over the last few years for lahar monitoring worldwide, including at Fuego [*De Angelis et al.*, 2019], Mount Rainier [*Thelen et al.*, 2019], and Mount Adams [*Sanderson et al.*, 2018].

1.5.3 Eruption Forecasting

Infrasound is often only effective after an event occurs, because its source is created due to a perturbation to the atmosphere. However, a few recent studies have shown that there may be ways to use infrasound for eruption forecasting in certain situations. For example, lava lakes present in some open volcanic systems have been shown to change levels prior to eruptions. *Johnson et al.* [2018] find that the frequency content of the resonant tones within the crater increased due to increases in the lava lake level two days prior to a paroxysmal eruption at Volcán Villarrica, Chile. *Ripepe et al.* [2018] leverage smaller eruptive activity at Etna volcano that occurs prior to a larger eruption to create an infrasound early warning system for that particular eruption style.

1.5.4 Connection to Multidisciplinary Observations

While using infrasound to characterize volcanic events is valuable, the connection of infrasound observations with other observations is becoming increasingly popular, allowing for greater understanding of volcanic processes. For example, AVO used a multidisciplinary approach to help forecast and detect eruptions from the 2016-2017 eruption of Bogoslof volcano, relying on a combination of distal (>54 km) seismic, regional infrasound, lightning, and satellite imagery [*Coombs et al.*, 2018]. Studies on the June 2019 eruptions of Raikoke and Ulawun during a Cooperative Institute for Dynamic Earth Research (CIDER) workshop allowed participants to integrate data from satellites, the IMS infrasound network, and globally detected lightning [*Maher et al.*, 2019] to quickly asses the eruption.

Many studies have compared infrasound-derived gas volumes with independent measurements from visual imagery [e.g. *Johnson and Miller*, 2014; *Witsil and Johnson*, 2018],

thermal imagery [e.g. *De Angelis et al.*, 2016], UV data [e.g. *Dalton et al.*, 2010; *Delle Donne et al.*, 2016], and ground-based [e.g. *Fee et al.*, 2017b] and satellite [e.g. *Albert et al.*, 2015] ash and gas emissions. Of particular interest to operational monitoring of eruptions is the potential link between infrasound and plume height. *Fee et al.* [2017a] found that the relationship between volcanic tremor (both seismic and infrasound) and plume height varied during the waxing and waning portions of the 2016 eruption of Pavlof volcano, Alaska, exhibiting hysteresis due to vent erosion. Other studies such as *Lamb et al.* [2015] use infrasound to obtain a mass ejection velocity at the vent that is then used as an input value for numerical plume rise models.

1.6 Overview of Chapters

This dissertation is written for a PhD in Geophysics at the University of Alaska Fairbanks and is comprised of three main chapters, two of which have already been published and one that is in review at a journal for publication. Topics explored in this dissertation focus on characterizing the propagation effects between the source and receiver in order to better interpret the acoustic explosion source. The infrasound recordings used span local to long range distances with explosion sources both underground and subaerial.

1.6.1 Chapter 2: Application of an Updated Atmospheric Model to Explore Volcano Infrasound Propagation and Detection in Alaska[1]

Chapter 2 examines the long range infrasound recordings and propagation modeling from recent eruptions in Alaska to help distinguish between propagation and source effects to aid in volcano monitoring efforts. The Aleutian Arc in Alaska is home to 54 historically active volcanoes that span 2500 km, where roughly a third of these volcanoes have no local monitoring equipment. Therefore, AVO depends on remote sensing techniques for monitoring

[1]Iezzi, A.M., Schwaiger, H.F., Fee, D., Haney, M.M. (2019). Application of an updated atmospheric model to explore volcano infrasound propagation and detection in Alaska. *Journal of Volcanology and Geothermal Research*, 371, 192-205.

eruptive activity. In this study, a new open-source atmospheric reconstruction model (AVO-G2S) is applied and predictions are compared to long range infrasound recordings of recent eruptions from Cleveland and Pavlof volcanoes with the intent to better understand the signals recorded. The combination of propagation modeling and quantification of infrasound observations such as celerity, traveltime, trace velocity, and backazimuth allow for enhanced characterization and interpretation of the infrasound waveforms recorded at AVO regional infrasound arrays. The results reiterate that infrasound signals recorded at long ranges can be highly influenced by the atmosphere and shows the necessity of understanding propagation conditions in order to better characterize volcanic eruptions recorded by regional infrasound arrays. Results and interpretations in this study also highlight the current limitations of atmospheric reconstruction models due to limitations in the spatial and temporal resolution of the input weather predication models. The methods used in this study are being applied in near-real time to aid volcano monitoring abilities by AVO, such as to better understand a detection (or lack thereof) at any of the six infrasound arrays for current and future volcanic eruptions in Alaska.

1.6.2 Chapter 3: Three-Dimensional Acoustic Multipole Waveform Inversion at Yasur Volcano, Vanuatu[2]

The second study aims to obtain a robust characterization of the infrasonic explosion source mechanism at Yasur Volcano, Vanuatu by sampling the wave field in the third dimension, allowing for estimates of volume flow rate and acoustic directionality. A network of infrasound sensors was deployed around the volcanic crater both on the ground as well as a novel approach of stringing infrasound sensors aboard a tethered aerostat that was walked around the crater over the course of the deployment. In this study, FDTD modeling is used to obtain the 3D Green's functions that account for topography and acoustic wave-

[2]Iezzi, A.M., Fee, D., Kim, K., Jolly, A.D., and Matoza, R.S. (2019). Three-Dimensional Acoustic Multipole Waveform Inversion at Yasur Volcano, Vanuatu *Journal of Geophysical Research: Solid Earth*, 124.

form inversions are performed for the monopole and multipole source mechanisms. This study presents the first acoustic source inversion results that both account for the effects of topography and investigates the contributions of the vertical dipole component of the source mechanism. It is found that inversions for the volume flow rate (which can further be converted to mass flow rate) remain stable regardless of the assumed source mechanism for the inversion. Results reiterate that neglecting effects of topography, especially in complex topographic regions such as volcanoes, during acoustic waveform inversions leads to overestimation of the volume flow rate. While multipole inversions that attempt to compute acoustic source directionality in all three dimensions are unstable, acoustic source directionality is observed that is not due to topography and is found to roughly agree with azimuths of increased ballistics from explosions. This study shows that the wavefield sampled using only instruments on Earth's surface limit the interpretations that can be made, especially in terms of acoustic directionility, though acoustic waveform inversions show promise for better characterizing the acoustic source from explosions of volcanic and anthropogenic origin.

1.6.3 Chapter 4: Seismo-Acoustic Characterization of Mount Cleveland Volcano Explosions[3]

The study carried out in Chapter 4 takes an observationalist approach to investigate peculiar relationships between the seismo-acoustic signals related to explosive activity at Mount Cleveland, Alaska over a recent 4 year period. Mount Cleveland is one of the most active volcanoes in Alaska with 64 explosions over the last nine years and the potential to disrupt air traffic over the North Pacific with occasional volcanic clouds that surpass 25,000 ft. In this study, we provide the first seismo-acoustic characterization of the explosions using recently installed local sensors. The variable arrival time lags from a co-located seismic and acoustic station is used to analyze 21 explosions and make inferences about what is causing this phenomena. A variety of methods are explored to determine the effects of the

[3]Iezzi, A.M., Fee, D., Haney, M.M., and Lyons, J.J. (*in review*) Seismo-Acoustic Characterization of Mount Cleveland Volcano Explosions, *Frontiers in Earth Science*

atmosphere, nonlinear propagation, and a changing explosion source depth and/or conduit velocity on the variable acoustic arrival time in relation to the seismic arrival. Atmospheric effects on the propagation velocity were found to not be able to explain the variability, and therefore something else must be changing in the source-receiver path, in this case likely changes in the explosion source depth within the volcanic conduit. Even with a single co-located seismic and acoustic sensor that clips for some explosions, results and interpretations from this study show that it is still possible to provide meaningful interpretations on the explosion source depth which may help monitoring agencies understand the volcanic system during times of unrest.

1.7 References

Albert, S., D. Fee, P. Firstov, E. Makhmudov, and P. Izbekov (2015), Infrasound from the 2012-2013 Plosky Tolbachik, Kamchatka fissure eruption, *Journal of Volcanology and Geothermal Research*, *307*, 68–78, doi:10.1016/j.jvolgeores.2015.08.019.

Allstadt, K. E., R. S. Matoza, A. B. Lockhart, S. C. Moran, J. Caplan-Auerbach, M. M. Haney, W. A. Thelen, and S. D. Malone (2018), Seismic and acoustic signatures of surficial mass movements at volcanoes, doi:10.1016/j.jvolgeores.2018.09.007.

Antier, K., A. Le Pichon, S. Vergniolle, C. Zielinski, and M. Lardy (2007), Multiyear validation of the NRL-G2S wind fields using infrasound from Yasur, *Journal of Geophysical Research Atmospheres*, *112*(23), 1–6, doi:10.1029/2007JD008462.

Assink, J., G. Averbuch, S. Shani-kadmiel, P. Smets, and L. Evers (2018), A Seismo-Acoustic Analysis of the 2017 North Korean Nuclear Test, *Seismological Research Letters*, *89*(6), 2025–2033, doi:10.1785/0220180137.

Assink, J. D., G. Averbuch, P. S. M. Smets, and L. G. Evers (2016), On the infrasound detected from the 2013 and 2016 DPRK's underground nuclear tests, *Geophysical Research Letters*, *43*(7), 3526–3533, doi:10.1002/2016GL068497.

Atchley, A. A. (2005), Not Your Ordinary Sound Experience: A Nonlinear-Acoustics Primer, *Acoustics Today*, pp. 19–24.

Bishop, J. W., D. Fee, and C. A. L. Szuberla (2020), Improved infrasound array processing with robust estimators, *Geophysical Journal International*, *221*(3), 2058–2074, doi:10.1093/gji/ggaa110.

Blom, P. (2014), GeoAc: Numerical Tools to Model Acoustic Propagation in the Geometric Limit, *Los Alamos National Laboratory*.

Blom, P. S., O. Marcillo, and S. J. Arrowsmith (2015), Improved Bayesian Infrasonic Source Localization for regional infrasound, *Geophysical Journal International*, pp. 1682–1693, doi:10.1093/gji/ggv387.

Brissaud, Q., R. Martin, R. F. Garcial, and D. Komatitsch (2017), Hybrid Galerkin numerical modelling of elastodynamics and compressible Navier-Stokes couplings: Applications to seismo-gravito acoustic waves, *Geophysical Journal International*, *210*(2), 1047–1069, doi:10.1093/gji/ggx185.

Bueno, A., A. Diaz-Moreno, I. Álvarez, A. De la Torre, O. D. Lamb, L. Zuccarello, and S. De Angelis (2019), VINEDA—Volcanic INfrasound Explosions Detector Algorithm, *Frontiers in Earth Science*, *7*(December), 1–8, doi:10.3389/feart.2019.00335.

Cando-Jácome, M., and A. Martínez-Graña (2019), Determination of primary and secondary lahar flow paths of the Fuego Volcano (Guatemala) using morphometric parameters, *Remote Sensing*, *11*(6), doi:10.3390/rs11060727.

Cansi, Y. (1995), An automatic seismic event processing for detection and location: The P.M.C.C. Method, *Geophysical Research Letters*, *22*(9), 1021–1024, doi:10.1029/95GL00468.

Christie, D. R., and P. Campus (2010), The IMS Infrasound Network: Design and Establishment of Infrasound Stations, in *Infrasound Monitoring for Atmospheric Studies*, edited by L. P. A., B. E., and H. A., pp. 29–75, Springer Netherlands, Dordrecht, doi:10.1007/978-1-4020-9508-5{_}2.

Coombs, M. L., A. G. Wech, M. M. Haney, J. J. Lyons, D. J. Schneider, H. F. Schwaiger, K. L. Wallace, D. Fee, J. T. Freymueller, J. R. Schaefer, and G. Tepp (2018), Short-Term Forecasting and Detection of Explosions During the 2016–2017 Eruption of Bogoslof Volcano, Alaska, *Frontiers in Earth Science*, *6*(September), 1–17, doi:10.3389/feart.2018.00122.

Dalton, M. P., G. P. Waite, I. M. Watson, and P. A. Nadeau (2010), Multiparameter quantification of gas release during weak Strombolian eruptions at Pacaya Volcano, Guatemala, *Geophysical Research Letters*, *37*(9), doi:10.1029/2010GL042617.

De Angelis, S., S. R. McNutt, and P. W. Webley (2011), Evidence of atmospheric gravity waves during the 2008 eruption of Okmok volcano from seismic and remote sensing observations, *Geophysical Research Letters*, *38*(10), 1–6, doi:10.1029/2011GL047144.

De Angelis, S., O. D. Lamb, A. Lamur, A. J. Hornby, F. W. von Aulock, G. Chigna, Y. Lavallée, and A. Rietbrock (2016), Characterization of moderate ash-and-gas explosions at Santiaguito volcano, Guatemala, from infrasound waveform inversion and thermal infrared measurements, *Geophysical Research Letters*, *43*(12), 6220–6227, doi:10.1002/2016GL069098.

De Angelis, S., B. Munkli, A. Lamur, and A. Diaz-Moreno (2019), Acoustic infrasound from activity at Volcan de Fuego, Guatemala, during 2018: a baseline for volcano monitoring, *EGU General Assembly 2019*.

de Groot-Hedlin, C. D. (2016), Long-range propagation of nonlinear infrasound waves through an absorbing atmosphere, *The Journal of the Acoustical Society of America*, *139*(4), 1565–1577, doi:10.1121/1.4944759.

de Groot-Hedlin, C. D., and M. A. Hedlin (2014), Infrasound detection of the Chelyabinsk meteor at the USArray, *Earth and Planetary Science Letters*, *402*(C), 337–345, doi:10.1016/j.epsl.2014.01.031.

de Groot-Hedlin, C. D., M. A. Hedlin, and K. T. Walker (2014), Detection of gravity waves across the USArray: A case study, *Earth and Planetary Science Letters*, *402*(C), 346–352, doi:10.1016/j.epsl.2013.06.042.

Delle Donne, D., M. Ripepe, G. Lacanna, G. Tamburello, M. Bitetto, and A. Aiuppa (2016), Gas mass derived by infrasound and UV cameras: Implications for mass flow rate, *Journal of Volcanology and Geothermal Research*, *325*, 169–178, doi:10.1016/j.jvolgeores.2016.06.015.

Diaz-Moreno, A., A. M. Iezzi, O. D. Lamb, D. Fee, K. Kim, L. Zuccarello, and S. De Angelis (2019), Volume Flow Rate Estimation for Small Explosions at Mt. Etna, Italy, From Acoustic Waveform Inversion, *Geophysical Research Letters*, *46*(20), 11,071–11,079, doi:10.1029/2019GL084598.

Drob, D. P., J. M. Picone, and M. Garcés (2003), Global morphology of infrasound propagation, *Journal of Geophysical Research: Atmospheres*, *108*(D21), doi:10.1029/2002JD003307.

Drob, D. P., J. T. Emmert, G. Crowley, J. M. Picone, G. G. Shepherd, W. Skinner, P. Hays, R. J. Niciejewski, M. Larsen, C. Y. She, J. W. Meriwether, G. Hernandez, M. J. Jarvis, D. P. Sipler, C. A. Tepley, M. S. O'Brien, J. R. Bowman, Q. Wu, Y. Murayama, S. Kawamura, I. M. Reid, and R. A. Vincent (2008), An empirical model of the Earth's horizontal wind fields: HWM07, *Journal of Geophysical Research: Space Physics*, *113*(12), doi:10.1029/2008JA013668.

Drob, D. P., J. T. Emmert, J. W. Meriwether, J. J. Makela, E. Doornbos, M. Conde, G. Hernandez, J. Noto, K. A. Zawdie, S. E. McDonald, J. D. Huba, and J. H. Klenzing (2015), An update to the Horizontal Wind Model (HWM): The quiet time thermosphere, *Earth and Space Science*, *2*(7), 301–319, doi:10.1002/2014EA000089.

Evers, L., D. Brown, K. Heaney, J. Assink, P. Smets, and M. Snellen (2014), Evanescent wave coupling in a geophysical system: Airborne acoustic signals from the Mw 8.1 Macquarie Ridge earthquake, *Geophysical Research Letters*, *41*(5), 1644–1650, doi:10.1002/2013GL058801.

Fee, D., and R. S. Matoza (2013), An overview of volcano infrasound: From hawaiian to plinian, local to global, *Journal of Volcanology and Geothermal Research*, *249*, 123–139, doi:10.1016/j.jvolgeores.2012.09.002.

Fee, D., M. Garces, T. Orr, and M. Poland (2011), Infrasound from the 2007 fissure eruptions of Kīlauea Volcano, Hawai'i, *Geophysical Research Letters*, *38*(6), n/a–n/a, doi:10.1029/2010GL046422.

Fee, D., R. Waxler, J. Assink, Y. Gitterman, J. Given, J. Coyne, P. Mialle, M. Garces, D. Drob, D. Kleinert, R. Hofstetter, and P. Grenard (2013), Overview of the 2009 and 2011 Sayarim Infrasound Calibration Experiments, *Journal of Geophysical Research Atmospheres*, *118*(12), 6122–6143, doi:10.1002/jgrd.50398.

Fee, D., A. Yokoo, and J. B. Johnson (2014), Introduction to an open community infrasound dataset from the actively erupting Sakurajima Volcano, Japan, *Seismological Research Letters*, *85*(6), 1151–1162, doi:10.1785/0220140051.

Fee, D., M. Haney, R. Matoza, C. Szuberla, J. Lyons, and C. Waythomas (2016), Seismic envelope-based detection and location of ground-coupled airwaves from volcanoes in Alaska, *Bulletin of the Seismological Society of America*, *106*(3), doi:10.1785/0120150244.

Fee, D., M. M. Haney, R. S. Matoza, A. R. Van Eaton, P. Cervelli, D. J. Schneider, and A. M. Iezzi (2017a), Volcanic tremor and plume height hysteresis from Pavlof Volcano, Alaska, *Science*, *355*(6320), 45–48, doi:10.1126/science.aah6108.

Fee, D., P. Izbekov, K. Kim, A. Yokoo, T. Lopez, F. Prata, R. Kazahaya, H. Nakamichi, and M. Iguchi (2017b), Eruption mass estimation using infrasound waveform inversion and ash and gas measurements: Evaluation at Sakurajima Volcano, Japan, *Earth and Planetary Science Letters*, *480*, 42–52, doi:10.1016/j.epsl.2017.09.043.

Fee, D., L. Toney, R. S. Matoza, R. Sanderson, M. M. Haney, J. Lyons, A. Iezzi, K. Kim, S. De Angelis, A. Diaz-Moreno, and A. Jolly (2019), A framework for improved infrasound back-projection on local and regional scales, *American Geophysical Union, Fall Meeting 2019, abstract #S41E-0577*.

Firstov, P., and N. Kravchenko (1996), Estimation of the amount of explosive gas released in volcanic eruptions using air waves, *Volcanol. Seismol.*, *17*(4-5), 547–560.

Friedlander, F. (1946), The diffraction of sound pulses. I. Diffraction by a semi-infinite plate, *Proceedings of the Royal Society of London A*, *186*, 322–344.

Garcés, M., A. Harris, C. Hetzer, J. Johnson, S. Rowland, E. Marchetti, and P. Okubo (2003), Infrasonic tremor observed at Kīlauea Volcano, Hawai'i, *Geophysical Research Letters*, *30*(20), doi:10.1029/2003GL018038.

Green, D. N., and A. Nippress (2019), Infrasound signal duration: The effects of propagation distance and waveguide structure, *Geophysical Journal International*, *216*(3), 1974–1988, doi:10.1093/gji/ggy530.

Hedin, A. E., E. L. Fleming, A. H. Manson, F. J. Schmidlin, S. K. Avery, R. R. Clark, S. J. Franke, G. J. Fraser, T. Tsuda, F. Vial, and R. A. Vincent (1996), Empirical wind model for the upper, middle and lower atmosphere, *Journal of Atmospheric and Terrestrial Physics*, *58*(13), 1421–1447, doi:10.1016/0021-9169(95)00122-0.

Johnson, D., and D. Dudgeon (1992), *Array Signal Processing: Concepts and Techniques*, Simon & Schuster.

Johnson, J., R. Aster, K. R. Jones, P. Kyle, and B. McIntosh (2008), Acoustic source characterization of impulsive Strombolian eruptions from the Mount Erebus lava lake, *Journal of Volcanology and Geothermal Research*, *177*(3), 673–686, doi:10.1016/j.jvolgeores.2008.06.028.

Johnson, J. B. (2003), Generation and propagation of infrasonic airwaves from volcanic explosions, *Journal of Volcanology and Geothermal Research*, *121*(1-2), 1–14, doi:10.1016/S0377-0273(02)00408-0.

Johnson, J. B., and R. C. Aster (2005), Relative partitioning of acoustic and seismic energy during Strombolian eruptions, *Journal of Volcanology and Geothermal Research*, *148*(3-4), 334–354, doi:10.1016/j.jvolgeores.2005.05.002.

Johnson, J. B., and A. J. C. Miller (2014), Application of the Monopole Source to Quantify Explosive Flux during Vulcanian Explosions at Sakurajima Volcano (Japan), *Seismological Research Letters*, *85*(6), 1163–1176, doi:10.1785/0220140058.

Johnson, J. B., and J. L. Palma (2015), Lahar infrasound associated with Volcán Villarrica's 3 March 2015 eruption, *Geophysical Research Letters*, *42*(15), 6324–6331, doi:10.1002/2015GL065024.

Johnson, J. B., L. M. Watson, J. L. Palma, E. M. Dunham, and J. F. Anderson (2018), Forecasting the Eruption of an Open-Vent Volcano Using Resonant Infrasound Tones, *Geophysical Research Letters*, *45*(5), 2213–2220, doi:10.1002/2017GL076506.

Jolly, A. D., R. S. Matoza, D. Fee, B. M. Kennedy, A. M. Iezzi, R. H. Fitzgerald, A. C. Austin, and R. Johnson (2017), Capturing the Acoustic Radiation Pattern of Strombolian Eruptions using Infrasound Sensors Aboard a Tethered Aerostat, Yasur Volcano, Vanuatu, *Geophysical Research Letters*, *44*(19), 9672–9680, doi:10.1002/2017GL074971.

Jones, K. R., R. W. Whitaker, and S. J. Arrowsmith (2014), Modelling infrasound signal generation from two underground explosions at the Source Physics Experiment using the Rayleigh integral, *Geophysical Journal International*, pp. 777–788, doi:10.1093/gji/ggu433.

Kim, K. (2017), infraFDTD: User Guide: Version 0.6.

Kim, K., and J. M. Lees (2011), Finite-difference time-domain modeling of transient infrasonic wavefields excited by volcanic explosions, *Geophysical Research Letters*, *38*(6), doi:10.1029/2010GL046615.

Kim, K., and J. M. Lees (2014), Local Volcano Infrasound and Source Localization Investigated by 3D Simulation, *Seismological Research Letters*, *85*(6), 1177–1186, doi:10.1785/0220140029.

Kim, K., J. M. Lees, and M. Ruiz (2012), Acoustic multipole source model for volcanic explosions and inversion for source parameters, *Geophysical Journal International*, *191*(3), 1192–1204, doi:10.1111/j.1365-246X.2012.05696.x.

Kim, K., D. Fee, A. Yokoo, and J. M. Lees (2015), Acoustic source inversion to estimate volume flux from volcanic explosions, *Geophysical Research Letters*, *42*(13), 5243–5249, doi:10.1002/2015GL064466.

Kim, K., A. Rodgers, and D. Seastrand (2018), Local Infrasound Variability Related to In Situ Atmospheric Observation, *Geophysical Research Letters*, *45*(7), 2954–2962, doi:10.1002/2018GL077124.

Lacanna, G., and M. Ripepe (2013), Influence of near-source volcano topography on the acoustic wavefield and implication for source modeling, *Journal of Volcanology and Geothermal Research*, *250*, 9–18, doi:10.1016/j.jvolgeores.2012.10.005.

Lamb, O. D., S. De Angelis, and Y. Lavallée (2015), Using infrasound to constrain ash plume rise, *Journal of Applied Volcanology*, *4*(1), doi:10.1186/s13617-015-0038-6.

Landès, M., L. Ceranna, A. Le Pichon, and R. S. Matoza (2012), Localization of microbarom sources using the IMS infrasound network, *Journal of Geophysical Research: Atmospheres*, *117*(6), 1–6, doi:10.1029/2011JD016684.

Le Pichon, A., E. Blanc, and D. Drob (2005), Probing high-altitude winds using infrasound, *Journal of Geophysical Research: Atmospheres*, *110*(20), 1–4, doi:10.1029/2005JD006020.

Le Pichon, A., L. Ceranna, M. Garcés, D. Drob, and C. Millet (2006), On using infrasound from interacting ocean swells for global continuous measurements of winds and temperature in the stratosphere, *Journal of Geophysical Research Atmospheres*, *111*(11), doi:10.1029/2005JD006690.

Le Pichon, A., L. Ceranna, C. Pilger, P. Mialle, D. Brown, P. Herry, and N. Brachet (2013), The 2013 Russian fireball largest ever detected by CTBTO infrasound sensors, *Geophysical Research Letters*, *40*(14), 3732–3737, doi:10.1002/grl.50619.

Lighthill, J. (1978), *Waves in Fluids*, Cambridge University Press.

Lighthill, M. J. (1952), On sounds generated aerodynamically. I. General Theory, *Proceedings of the Royal Society A, Mathematical, Physical and Engineering Science*, *211*(1107), 564–587.

Maher, S., C. M. Smith, K. F. McKee, K. Reath, E. Snee, R. S. Matoza, S. A. Carn, L. G. Mastin, D. E. Damby, D. C. Roman, A. Degterev, A. Rybin, and M. Chibisova (2019), Multi-disciplinary characterization of the June 2019 eruptions of Raikoke (Kuril Islands) and Ulawun (Papua New Guinea) volcanoes using remote techniques, *American Geophysical Union, Fall Meeting 2019, abstract #V23F-0259.*

Maher, S. P., R. S. Matoza, C. D. Groot-Hedlin, K. L. Gee, D. Fee, and A. Yokoo (2020), Investigating Spectral Distortion of Local Volcano Infrasound by Nonlinear Propagation at Sakurajima Volcano, Japan, *Journal of Geophysical Research: Solid Earth*, *125*(3), doi:10.1029/2019JB018284.

Marchetti, E., M. Ripepe, D. Delle Donne, R. Genco, A. Finizola, and E. Garaebiti (2013), Blast waves from violent explosive activity at Yasur Volcano, Vanuatu, *Geophysical Research Letters*, *40*(22), 5838–5843, doi:10.1002/2013GL057900.

Marcillo, O., and J. B. Johnson (2010), Tracking near-surface atmospheric conditions using an infrasound network, *The Journal of the Acoustical Society of America*, *128*(1), EL14–EL19, doi:10.1121/1.3442725.

Marcillo, O., S. Arrowsmith, R. Whitaker, D. Anderson, A. Nippress, D. N. Green, and D. Drob (2013), Using physics-based priors in a Bayesian algorithm to enhance infrasound source location, *Geophysical Journal International*, *196*(1), 375–385, doi:10.1093/gji/ggt353.

Marcillo, O., S. Arrowsmith, P. Blom, and K. Jones (2015), On infrasound generated by wind farms and its propagation in low-altitude tropospheric waveguides, *Journal of Geophysical Research Atmospheres*, *120*, 9855–9868, doi:10.1038/175238c0.

Martire, L., Q. Brissaud, V. H. Lai, R. F. Garcia, R. Martin, S. Krishnamoorthy, A. Komjathy, A. Cadu, J. A. Cutts, J. M. Jackson, D. Mimoun, M. T. Pauken, and A. Sournac (2018), Numerical Simulation of the Atmospheric Signature of Artificial and Natural Seismic Events, *Geophysical Research Letters*, *45*(21), 085–12, doi:10.1029/2018GL080485.

Matoza, R. S., D. Fee, M. A. Garcés, J. M. Seiner, P. A. Ramón, and M. A. Hedlin (2009), Infrasonic jet noise from volcanic eruptions, *Geophysical Research Letters*, *36*(8), doi:10.1029/2008GL036486.

Matoza, R. S., D. Fee, T. B. Neilsen, K. L. Gee, and D. E. Ogden (2013), Aeroacoustics of volcanic jets: Acoustic power estimation and jet velocity dependence, *Journal of Geophysical Research: Solid Earth*, *118*(12), 6269–6284, doi:10.1002/2013JB010303.

Matoza, R. S., D. N. Green, A. Le Pichon, P. M. Shearer, D. Fee, P. Mialle, and L. Ceranna (2017), Automated detection and cataloging of global explosive volcanism using the International Monitoring System infrasound network, *Journal of Geophysical Research: Solid Earth*, *122*(4), 2946–2971, doi:10.1002/2016JB013356.

McKee, K., D. Fee, A. Yokoo, R. S. Matoza, and K. Kim (2017), Analysis of gas jetting and fumarole acoustics at Aso Volcano, Japan, *Journal of Volcanology and Geothermal Research*, *340*, doi:10.1016/j.jvolgeores.2017.03.029.

McKee, K., D. Fee, M. Haney, R. S. Matoza, and J. Lyons (2018), Infrasound Signal Detection and Back Azimuth Estimation Using Ground-Coupled Airwaves on a Seismo-Acoustic Sensor Pair, *Journal of Geophysical Research: Solid Earth*, *123*(8), 6826–6844, doi:10.1029/2017JB015132.

Melton, B., and L. Bailey (1957), Multiple Signal Correlators, *Geophysics*, *22*(3), 523–713, doi:https://doi.org/10.1190/1.1438390.

Modrak, R. T., S. J. Arrowsmith, and D. N. Anderson (2010), A Bayesian framework for infrasound location, *Geophysical Journal International*, *181*(1), 399–405, doi:10.1111/j.1365-246X.2010.04499.x.

Ohminato, T., B. A. Chouet, P. B. Dawson, and S. Kedar (1998), Waveform inversion of very-long-period impulsive signals associated with magmatic injections beneath Kilauea Volcano, Hawaii, *J. Geophys. Res.*, *103*(10), 23,839–23,862, doi:10.1029/98JB01122.

Petersson, N. A., and B. Sjögreen (2018), High Order Accurate Finite Difference Modeling of Seismo-Acoustic Wave Propagation in a Moving Atmosphere and a Heterogeneous Earth Model Coupled Across a Realistic Topography, *Journal of Scientific Computing*, *74*(1), 290–323, doi:10.1007/s10915-017-0434-7.

Picone, J. M., A. E. Hedin, D. P. Drob, and A. C. Aikin (2002), NRLMSISE-00 empirical model of the atmosphere: Statistical comparisons and scientific issues, *Journal of Geophysical Research: Space Physics*, *107*(A12), doi:10.1029/2002JA009430.

Pierce, A. (1981), *Acoustics: An Introduction to its Physical Principles and Applications*, McGraw-Hill, New York.

Pilger, C., L. Ceranna, J. O. Ross, A. L. Pichon, P. Mialle, and M. A. Garcés (2015), CTBT infrasound network performance to detect the 2013 Russian fireball event, *Geophysical Research Letters*, *42*, 2523–2531, doi:10.1002/2015GL063482.

Pilger, C., P. Gaebler, L. Ceranna, A. Le Pichon, J. Vergoz, A. Perttu, D. Tailpied, and B. Taisne (2019), Infrasound and seismoacoustic signatures of the 28 September 2018 Sulawesi super-shear earthquake, *Natural Hazards and Earth System Sciences*, *19*(12), 2811–2825, doi:10.5194/nhess-19-2811-2019.

Reichman, B. O., K. L. Gee, T. B. Neilsen, and K. G. Miller (2016), Quantitative analysis of a frequency-domain nonlinearity indicator, *The Journal of the Acoustical Society of America*, *139*(5), 2505–2513, doi:10.1121/1.4945787.

Ripepe, M., E. Marchetti, D. Delle Donne, R. Genco, L. Innocenti, G. Lacanna, and S. Valade (2018), Infrasonic Early Warning System for Explosive Eruptions, *Journal of Geophysical Research: Solid Earth*, *123*(11), 9570–9585, doi:10.1029/2018JB015561.

Sahetapy-Engel, S. T., A. J. Harris, and E. Marchetti (2008), Thermal, seismic and infrasound observations of persistent explosive activity and conduit dynamics at Santiaguito lava dome, Guatemala, *Journal of Volcanology and Geothermal Research*, *173*(1-2), 1–14, doi:10.1016/j.jvolgeores.2007.11.026.

Salomons, E. (2001), *Computational Atmospheric Acoustics*, 335 pp., Kluwer Academic Publishers, Dordrecht, The Netherlands.

Sanderson, R., R. Matoza, R. Haymon, J. Steidl, and P. Hegarty (2018), Lahar detection using infrasound: Pilot experiment at Mount Adams, WA, *American Geophysical Union, Fall Meeting 2018, abstract #V13D-0118.*

Sanderson, R. W., R. S. Matoza, D. Fee, M. M. Haney, and J. J. Lyons (2020), Remote Detection and Location of Explosive Volcanism in Alaska With the EarthScope Transportable Array, *Journal of Geophysical Research: Solid Earth*, *125*(4), 23, doi: 10.1029/2019JB018347.

Schwaiger, H., A. Iezzi, and D. Fee (2019), AVO-G2S: A modified, open-source Ground-to-Space atmospheric specification for infrasound modeling, *Computers and Geosciences*, *125*, 90–97, doi:10.1016/j.cageo.2018.12.013.

Schwaiger, H. F., R. P. Denlinger, and L. G. Mastin (2012), Ash3d: A finite-volume, conservative numerical model for ash transport and tephra deposition, *Journal of Geophysical Research: Solid Earth*, *117*(4), doi:10.1029/2011JB008968.

Schwaiger, H. F., J. J. Lyons, A. M. Iezzi, D. Fee, and M. M. Haney (2020), Evolving infrasound detections from Bogoslof volcano, Alaska: insights from atmospheric propagation modeling, *Bulletin of Volcanology*, *82*(3), 27, doi:10.1007/s00445-020-1360-3.

Shani-Kadmiel, S., J. D. Assink, P. S. Smets, and L. G. Evers (2018), Seismoacoustic Coupled Signals From Earthquakes in Central Italy: Epicentral and Secondary Sources of Infrasound, *Geophysical Research Letters*, *45*(1), 427–435, doi:10.1002/2017GL076125.

Shani-Kadmiel, S., G. Averbuch, P. S. M. Smets, J. D. Assink, and L. G. Evers (2019), Earthquake shaking intensity and source mechanism passively retrieved from remote infrasonic signals, in *American Geophysical Union, Fall Meeting 2019, abstract #S41E-0573.*

Smets, P. S., and L. G. Evers (2014), The life cycle of a sudden stratospheric warming from infrasonic ambient noise observations, *Journal of Geophysical Research*, *119*(21), 084–12, doi:10.1002/2014JD021905.

Snelson, C., R. Abbot, S. Broome, R. Mellors, H. Patton, A. Sussman, A. Townsend, and W. Walter (2013), Chemical Explosion Experiments to Improve Nuclear Test Monitoring, *Eos*, *94*(27).

Strachey, R. (1888), On the air waves and sounds caused by the eruption of Krakatoa in August, 1883, in *Krakatau 1883*, edited by T. Simkin and R. Friske, pp. 368–374, Smithsonian Instituation Press.

Szuberla, C. A. L., and J. V. Olson (2004), Uncertainties associated with parameter estimation in atmospheric infrasound arrays, *The Journal of the Acoustical Society of America*, *115*(1), 253–258, doi:10.1121/1.1635407.

Thelen, W., K. Allstadt, R. Kramer, C. Lockett, A. Lockhart, B. Pauk, and S. Moran (2019), Current Status of the Mount Rainier (Washington) Lahar Detection System, *American Geophysical Union, Fall Meeting 2019, abstract #V51K-0254.*

Vergniolle, S., M. Boichu, and J. Caplan-Auerbach (2004), Acoustic measurements of the 1999 basaltic eruption of Shishaldin volcano, Alaska 1. Origin of Strombolian activity, *Journal of Volcanology and Geothermal Research*, *137*, 109–134, doi:10.1016/j.jvolgeores.2004.05.003.

Watson, L. M., E. M. Dunham, and J. B. Johnson (2019), Simulation and inversion of harmonic infrasound from open-vent volcanoes using an efficient quasi-1D crater model, *Journal of Volcanology and Geothermal Research*, *380*, 64–79, doi:10.1016/j.jvolgeores.2019.05.007.

Waxler, R., C. Hetzer, D. Velea, J. Assink, P. Blom, and J. Lonzaga (2015), Atmospheric Infrasound Propagation Package Version 1.1 Extension and Finalization NCPA Infrasound Propagation Modeling Package.

Waxler, R., J. Assink, and D. Velea (2017), Modal expansions for infrasound propagation and their implications for ground-to-ground propagation, *The Journal of the Acoustical Society of America*, *141*(2), 1290–1307, doi:10.1121/1.4976067.

Witsil, A. J., and J. B. Johnson (2018), Infrasound explosion and coda signal investigated with joint analysis of video at Mount Erebus, Antarctica, *Journal of Volcanology and Geothermal Research*, *357*, 306–320, doi:10.1016/j.jvolgeores.2018.05.002.

Yokoo, A., T. Tameguri, and M. Iguchi (2009), Swelling of a lava plug associated with a Vulcanian eruption at Sakurajima Volcano, Japan, as revealed by infrasound record: Case study of the eruption on January 2, 2007, *Bulletin of Volcanology*, *71*(6), 619–630, doi:10.1007/s00445-008-0247-5.

Zobin, V., I. Plascencia, G. Reyes, and C. Navarro (2009), The characteristics of seismic signals produced by lahars and pyroclastic flows: Volcán de Colima, México, *Journal of Volcanology and Geothermal Research*, *179*(1-2), 157–167.

Chapter 2

Application of an Updated Atmospheric Model to Explore Volcano Infrasound Propagation and Detection in Alaska[4]

2.1 Abstract

Winds and temperature gradients greatly affect the long-range propagation of infrasound. The spatio-temporal variability of these parameters must therefore be accurately characterized to correctly interpret recorded infrasound at long distances, specifically to differentiate between source and propagation effects. Here we present the first results of an open source reanalysis model, termed Alaska Volcano Observatory Ground-to-Space (AVO-G2S), constructed to accurately characterize the atmosphere and model long-range infrasound propagation from volcanic eruptions in Alaska. We select a number of case studies to examine recent eruptions of Alaskan volcanoes whose ash emissions posed a threat to air traffic, including the two most recent eruptions of Pavlof Volcano and two typical explosions from Cleveland Volcano. Strong tropospheric ducting and low noise at the station during the 21 July 2015 explosion of Cleveland Volcano led to an automated detection of the explosion at an infrasound array 992 km away, whereas low signal-to-noise ratio for the 6 November 2014 Cleveland Volcano explosion helps explain the non-detection in real-time of a predicted strong stratospheric arrival. For the November 2014 Pavlof eruption, discrepancies between local seismic data and a distal infrasound array 460 km away cannot be solely explained by changes in atmospheric conditions, though some features of the complex propagation predictions follow the trends in long-range infrasound signals. The most recent eruption of Pavlof Volcano in March 2016 shows minimal changes in propagation conditions throughout the eruption and therefore indicates that the signals detected at long-range primarily reflect source processes. These results show how detailed examination of the acoustic propagation

[4]Iezzi, A.M., Schwaiger, H.F., Fee, D., and Haney, M.M. (2019). Application of an updated atmospheric model to explore volcano infrasound propagation and detection in Alaska. *Journal of Volcanology and Geothermal Research*, 371, 192-205.

conditions provides insight into detection capability and eruption dynamics. Future work will implement AVO-G2S and high-resolution long-range infrasound propagation modeling in realtime for Alaskan volcanoes of interest.

2.2 Introduction

Alaska's over 50 historically active volcanoes span 2,500 km and their eruptions pose great threats to aviation. On any given day, roughly 70,000 passengers fly over the North Pacific and have the potential to be affected by ash released from Alaskan volcanoes [*Bureau of Transportation Statistics*, 2016]. This makes both prompt observations of explosion onsets, as well as characterization of their eruption style and dynamics, critical for monitoring and eruption response. When volcanoes erupt, the majority of the acoustic energy is emitted in the infrasound band, defined as sound waves below 20 Hz. Infrasound complements its seismic counterpart, as it is an indication of shallow to subaerial activity that might be more ambiguous when interpreting seismic signals alone. It is an especially crucial tool in Alaska because infrasonic energy propagation is not obstructed by frequent cloud cover, which often hinders another key monitoring tool for remote volcanoes–satellite imagery. Additionally, due to relatively weak attenuation in the atmosphere at these low frequencies and strong ducts in the atmosphere, infrasound can propagate hundreds to thousands of kilometers under suitable conditions and be detected by infrasound sensors, either at an array or on single sensors.

Because of their expansive range and remoteness, Alaskan volcanoes are predominantly monitored by local seismic networks supplemented with remote observations including satellite imagery and infrasound sensors. Centralized infrasound arrays have been key in monitoring eruptions in Alaska because they can be strategically placed and more easily maintained than single stations scattered around the numerous volcanoes (Figure 2.1) [*De Angelis et al.*, 2012]. However, infrasound station coverage is still relatively sparse in Alaska. Furthermore, strong wind and temperature gradients in the atmosphere can create multiple ducts and

shadow zones where propagation of infrasound is enhanced and diminished, respectively. As infrasound propagates, it often retains a significant amount of information about the source process, and can be used to detect and characterize eruption style and dynamics [*Fee and Matoza*, 2013, and references therein]. To accurately constrain volcanic source information and understand the long-range propagation, a detailed characterization of the spatial and temporal variability of the atmosphere is vital. This long-range propagation modeling increases our ability to determine if a detected signal (or lack thereof) is a result of source or path effects, which can aid volcano monitoring efforts in near real-time and in retrospective analysis.

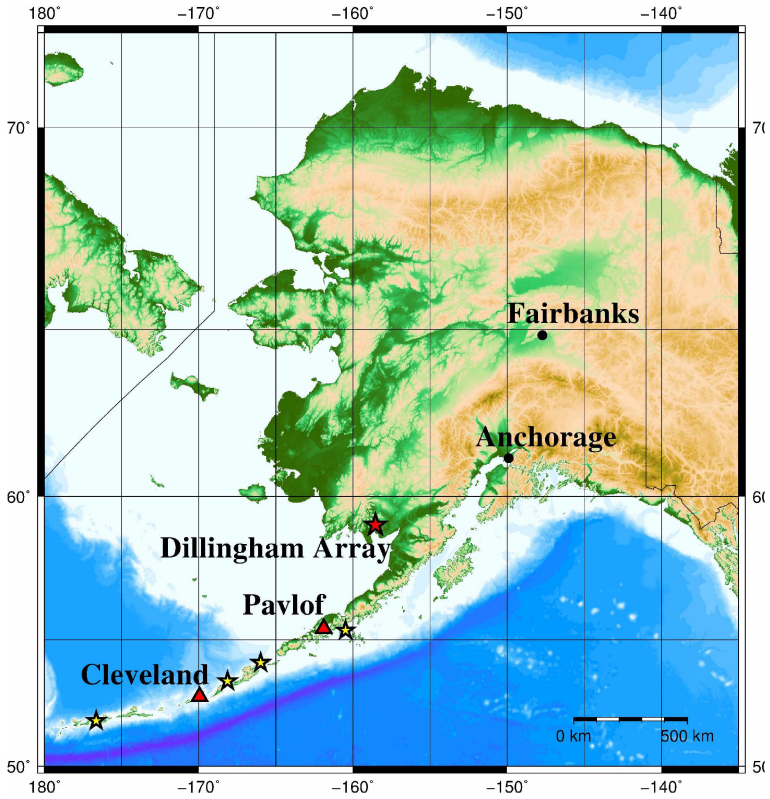

Figure 2.1: Map of Alaska and infrasound arrays and volcanoes discussed in this manuscript. Pavlof and Cleveland volcanoes are shown with red triangles and the Dillingham (DLL) infrasound array as a red star. Other infrasound arrays maintained by AVO are shown by yellow stars. The propagation distance from Cleveland to DLL is ∼990 km and Pavlof to DLL is ∼460 km. (uses ETOPO1, [*Amante and Eakins*, 2009])

2.2.1 *Infrasound Propagation in the Atmosphere*

Infrasound propagates as a compressional wave that moves at the speed of sound, which in an ideal gas is defined as

$$c = \sqrt{\gamma RT} \tag{2.1}$$

where γ is the specific heat ratio, R is the universal gas constant, and T is the temperature [*Pierce*, 1981]. The long-range propagation of infrasound can generally be described using the effective sound speed (approximation explored in depth by *Waxler et al.* [2017]), defined as

$$c_{eff} = c + \vec{v} \cdot \vec{u} \tag{2.2}$$

where c is the adiabatic sound speed (Eq. 2.1) and $\vec{v} \cdot \vec{u}$ is the vector component of the horizontal wind velocity in a particular direction [*Fee and Matoza*, 2013; *Salomons*, 2001]. Wind velocities are generally decomposed into components from west to east (zonal) and from south to north (meridional). These wind influences on the effective sound speed are highly anisotropic and enhance the propagation of infrasound in the downwind direction or diminish the propagation in the upwind direction.

Infrasound, though not attenuated as greatly as higher acoustic frequencies, is still subject to both spreading and absorption losses in energy. Geometric spreading is independent of frequency and occurs as sound spreads away from a source; for a homogeneous atmosphere the amplitude decreases as 1/r (r being the radial distance from the source). Sound absorption is typically frequency dependent, and increases dramatically in the upper atmosphere due to lower air density [*Salomons*, 2001; *Sutherland and Bass*, 2004]. Therefore, infrasound refracting from thermospheric altitudes tends to be lower in amplitude and frequency [*de Groot-Hedlin and Hedlin*, 2014].

Following Snell's Law of refraction, when the effective sound speed surpasses the effective

sound speed at the source, the energy is refracted back down towards the surface. This produces ducts, or waveguides, within the atmosphere in which infrasound is preferentially propagated. Starting at the Earth's surface, temperature generally decreases up to the tropopause (upper limit of the troposphere), increases to the stratopause (upper limit of stratosphere), then decreases in the mesosphere, and increases again in the thermosphere (Figure 2.2). This leads to three main ducts for infrasound propagation: i) tropospheric; ii) stratospheric; and iii) thermospheric. Energy can be split between these ducts, as well as within the ducts, and propagate with different paths (termed "multipathing"); therefore, multiple arrivals at an infrasound array are often observed [*De Groot-Hedlin et al.*, 2009]. The tropospheric duct spans altitudes of 0 to 10–20 km (lower at the poles and higher at the Equator). It is a crucial duct for the detection of infrasonic events at local to regional distances (<250 km), as they tend to contain the highest amplitudes due to the least amount of energy losses from geometric spreading and absorption [*Drob et al.*, 2003]. Additionally, tropospheric ducts are the only arrival possible within stratospheric and thermospheric duct shadow zones at local to regional distances. Tropospheric arrivals appear first at a station as a result of their more direct propagation path. Tropospheric ducts generally only exist when the lower atmospheric winds are towards the receiver and are strongly dependent on the local atmospheric conditions [*Ceranna et al.*, 2009]. Therefore, these ducts can disappear at distances on the order of a few hundred kilometers [*Ceranna et al.*, 2009; *Drob et al.*, 2003; *Le Pichon et al.*, 2006]. However, there are cases when tropospheric arrivals can be detected at distances >1000 km, such as in *Fee et al.* [2013].

The stratospheric duct extends from the surface to an altitude of ~50 km. The main influence on the existence of this duct is seasonal zonal wind patterns in the stratosphere, which blow east in the winter hemisphere and west in the summer hemisphere. Studies such as *Le Pichon et al.* [2006] conclude that the prevailing stratospheric zonal winds have a strong influence on global infrasonic detection capabilities, finding that the number of detections are 2–3 times greater in the direction of these winds. Stratospheric ducts are known to exist

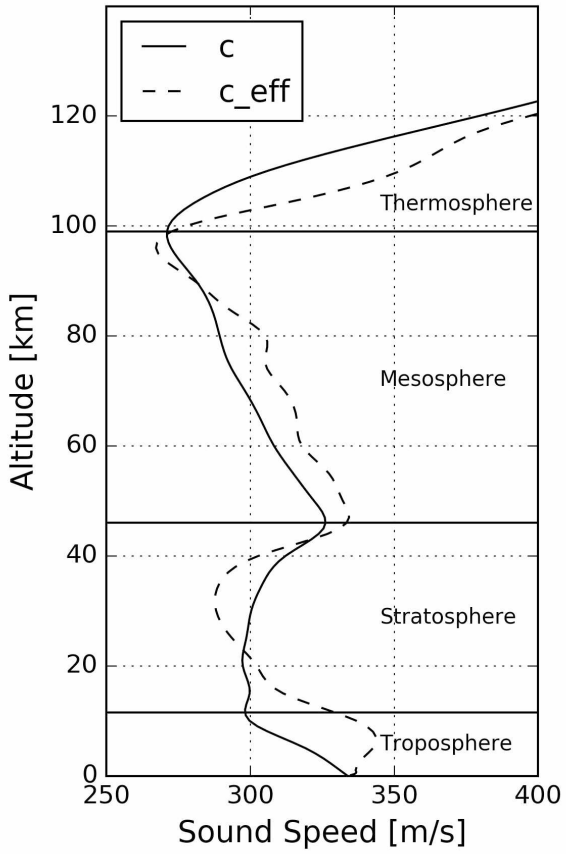

Figure 2.2: Example sound speed profile and major regions in the atmosphere. The effective sound speed profile (c_{eff}) includes the wind component in the direction of propagation while c is the sound speed. The effective sound speed shows the potential propagation ducts from Pavlof Volcano to DLL at 00:00 UTC on 28 March 2016.

for thousands of kilometers [*Ceranna et al.*, 2009; *Le Pichon et al.*, 2006]. While tropospheric ducts tend to diminish at these global distances (<250 km), stratospheric arrivals are often the most energetic arrivals detected [e.g. *Ceranna et al.*, 2009; *Drob et al.*, 2003].

The thermospheric duct consists of the lower thermosphere, spanning the surface to ~120 km, and is susceptible to significant temperature variations associated with space weather (e.g. solar tides). This duct exists at all times due to high temperatures (and therefore high sound speed) in the lower thermosphere [*Le Pichon et al.*, 2002], which is sufficient to refract energy without the addition of wind. However, infrasonic signals guided by the thermosphere are the faintest and often go undetected for small signals due to increased geometric spreading

and attenuation partially caused by lower particle density in the upper atmosphere [*Ceranna et al.*, 2009; *Le Pichon et al.*, 2006; *Sutherland and Bass*, 2004]. Thermospheric arrivals can be significantly distorted due to nonlinear propagation related to decreased density in the thermosphere [*Rogers and Gardner*, 1980].

Finally, acoustic energy with steep takeoff angles, or energy that leaves the source closer to vertical, that is not ducted in the thermosphere will escape to higher altitudes and not refract back down to the surface.

2.2.2 Constraining Atmospheric Variability

In order to properly model infrasound propagation within the atmosphere, variables such as temperature and winds at altitudes from 0 to ~150 km in the atmosphere must be accurately estimated both spatially and temporally. Lower atmospheric conditions (up to mid-stratospheric and lower), can be obtained by a variety of numerical weather prediction models, with some recent products providing values up to midmesopheric levels such as NASA GEOS-5 [*Molod et al.*, 2012] and ECMWF [*Molteni et al.*, 1996]. Above this level, we rely on empirical models such as the Horizontal Wind Model (HWM) [*Drob et al.*, 2008, 2015; *Hedin et al.*, 1996] and the NRLMSISE-00 model [*Picone et al.*, 2002]. Infrasound propagation modeling requires a smooth transition and reconstruction of these data in one, two, or three dimensions, such as has been done in the Naval Research Lab ground-to-space model (G2S) [*Drob et al.*, 2003]. The Alaska Volcano Observatory (AVO) chose to make an in-house model, AVO-G2S [*Schwaiger et al.*, 2019], based upon the G2S work of *Drob et al.* [2003] for the following reasons: i) G2S is not open source; ii) G2S specifications are not readily available for retrospective analysis; and iii) an in-house model enables greater flexibility specific to the variable atmospheric conditions in the region. For example, higher spatial and temporal resolution (up to 2.95 km spatially and hourly) models can be constructed for specific source-receiver scenarios. The reader is referred to *Schwaiger et al.* [2019] for more details on the methods and motivation.

Once the atmosphere is reconstructed, infrasound propagation can be simulated and visualized using a variety of methods including classical ray tracing [*Blom*, 2014], normal modes [*Waxler et al.*, 2017], and parabolic equation [*Waxler et al.*, 2015]. In this manuscript we choose to focus on ray tracing methods because we are mainly interested in determining if the long-range detection of an eruption can be explained by the propagation modeling, as well as assessing the accuracy of infrasonic traveltimes for monitoring purposes. Amplitude and full waveform modeling studies are beyond the scope of this paper.

Ray tracing is a method of calculating the propagation paths of acoustic waves through a varying medium using a high frequency approximation and allows visualization of the likely propagation path of infrasound energy in the atmosphere. Ray tracing treats the propagation of infrasound as rays that refract in a layered atmosphere and reflect off the surface (bounce) back into the atmosphere. Eigenrays are a subset of rays that connect the direct path from source (volcano) to receiver (infrasound array) within a specified tolerance, and have an associated traveltime, celerity (defined as range over traveltime), and arrival inclination.

2.2.3 Propagation Path Indicators

It is important to accurately distinguish between arrival types to obtain a correct traveltime that can be used to back-calculate the signal origin time at the source. An exact origin time facilitates comparison with other geophysical observations [*Fee et al.*, 2010]. A few ways to confirm the propagation predictions include investigating trace velocity (or apparent velocity) and celerity of the long-range signals seen on an infrasound array. Although trace velocity and celerity are usually reliable in helping to determine arrival type, they should be used as indicators only and their interpretations treated with caution [*Ceranna et al.*, 2009].

Trace velocity is the phase velocity across an array of sensors. It generally increases for energy that reaches higher altitudes due to the increased steepness of arrival trajectory [*Ceranna et al.*, 2009; *Dabrowa et al.*, 2011]. According to a study by *Ceranna et al.* [2009], general guidelines for trace velocity are: i) tropospheric arrivals being on the order of the

local sound speed; ii) stratospheric arrivals from the local sound speed to ∼360 m/s; and iii) thermospheric arrivals with trace velocities >350 m/s.

Celerity is defined as the epicentral distance between source and receiver divided by the total traveltime, therefore it will decrease with increasing refraction heights [*Ceranna et al.*, 2009]. Celerity values are typically: i) the speed of sound (330–340m/s) for tropospheric arrivals; ii) 280–320m/s for stratospheric arrivals; and iii) 230–280m/s for thermospheric arrivals [*Brown et al.*, 2002; *Ceranna et al.*, 2009; *Evers and Haak*, 2007; *Fee et al.*, 2013; *Green et al.*, 2011; *Nippress et al.*, 2014].

2.2.4 Volcano Monitoring Uses in Alaska

In this study we focus on Cleveland and Pavlof Volcanoes. Cleveland Volcano is one of the most active volcanoes in Alaska. It has had over 50 explosions since 25 December 2011, the most recent at the time of writing being on 18 December 2017 [*www.avo.alaska.edu*]. The first local instrumentation on the island, consisting of seismometers, an infrasound array, and web camera was deployed in the summer of 2014, allowing for recent detailed studies of the volcano. Due to a longer history of data to compare with, remote sensing (including remote infrasound monitoring) has been heavily relied upon and continues to play a key role in detecting activity at Cleveland Volcano [*De Angelis et al.*, 2012; *Werner et al.*, 2017]. Pavlof Volcano is close enough to the communities of Cold Bay, King Cove, and Nelson Lagoon that local ashfall hazards must be considered in addition to the threat to air traffic. Characteristic eruptions include low-energy lava fountaining, lahars, and emissions of ash, gas, and steam [*Waythomas et al.*, 2014; *www.avo.alaska.edu*]. Pavlof eruptions have been known to affect air travel for days. A recent example of ash impacts in Alaska was from the 2016 eruption of Pavlof Volcano, that sent ash to 8–9 km above sea level and extended over 600 km northeast across interior Alaska, cancelling over 100 flights during the course of a few days [*Fee et al.*, 2017]. Both Cleveland and Pavlof Volcanoes often have little to no precursory activity before eruptions, making them difficult to forecast; therefore, the detection of an explosion

onset is often the first sign of an eruption. Once the first signs of emissions are detected, AVO uses Ash3d [*Schwaiger et al.*, 2012] to model airborne volcanic ash concentration and tephra deposition and help inform the Federal Aviation Administration (FAA) and National Weather Service (NWS) of the volcanic hazard.

In this manuscript we introduce the first uses of the new atmospheric reconstruction model AVO-G2S for volcano monitoring in Alaska, both as a reanalysis method and a future tool for real-time monitoring. We focus on the post-processing and application of the AVO-G2S atmospheric specifications for use on long-range infrasound propagation in Alaska and explore its capability through a differential look at atmospheric conditions and infrasound propagation for: i) two discrete explosions of Cleveland Volcano; and ii) two hours-to-days long continuous eruptions at Pavlof Volcano. The main infrasound array used in this study is located in Dillingham, Alaska (DLL), with local stations at both Cleveland and Pavlof Volcanoes supplementing our analyses with better-constrained source parameters. DLL is 460 km away from Pavlof Volcano and 992 km from Cleveland Volcano (Figure 2.1).

2.3 Methods

2.3.1 Atmospheric Modeling

AVO-G2S is composed of a global grid of lower-atmospheric meteorological values extended to the upper-atmosphere. Reanalysis data are provided every six hours for events that occurred in the last few years, so the atmospheric conditions were reconstructed using AVO-G2S for the time closest to each eruption. All times in this paper are in UTC and ERA-Interim [*Dee et al.*, 2011] files are used for the lower atmosphere. Conditions for Cleveland Volcano are obtained for 6 November 2014 at 06:00 and 21 July 2015 at 18:00. For the two Pavlof examples where the eruption durations were from hours to days, atmospheric models are reconstructed every six hours using AVO-G2S from 12 November 2014 12:00 to 16 November 2014 12:00 and from 27 March 2016 18:00 to 29 March 2016 06:00. The upper-atmospheric nodes are populated with values derived from the empirical model HWM14

[*Drob et al.*, 2015] for wind speeds and NRLMSISE-00 [*Picone et al.*, 2002] for temperatures.

Similar to the methods outlined in *Drob et al.* [2003], each dataset is decomposed into spherical harmonic coefficient files and a smooth representation of the coefficients is generated as a function of height using a B-spline representation. From this set of coefficients, interpolated spherical harmonic coefficients can be retrieved at any altitude, then the values of interest (e.g. meridional and zonal winds, temperature) can be reconstructed. In this study, we recreate the atmosphere up to 180 km with altitude spacing of 0.2 km. Once the coefficients are calculated, atmospheric models are sub-sampled on 3D volumes.

For local infrasound propagation, a 1D stratified atmosphere is usually sufficient, but for longer range propagation such as those in this study, a range-dependent atmosphere is necessary [*Fee and Matoza*, 2013, and references therein]. Infrasound propagation modeling is performed using range-dependent atmospheres, with the exception of the July 2015 Cleveland explosion where outputs from range-independent modeling are also included to supplement the results. Range-dependent models are assembled using a grid of 1D columns from the reconstructed atmosphere with nodes every 1° latitude and ∼2° longitude to make an approximately square grid at 60° latitude.

The main tool used for propagation simulation is the ray tracing software GeoAc [*Blom*, 2014], which is publically available from https://github.com/LANL-Seismoacoustics/GeoAc. Inputs include the volcano and station coordinates, as well as the atmospheric specifications that are output by AVO-G2S in the previous step. We use GeoAc to launch rays from an elevated source, assuming the explosive source is at the volcano's summit (1.73 km for Cleveland and 2.57 km for Pavlof) between 15° and 45° from the horizontal in increments of 0.5°, allowing for up to 30 bounces and a 5° deviation in azimuth for the eigenray search option. Outputs to the post-processing, in addition to the ray tracing visualization, include modeled traveltime, celerity, and arrival inclination for eigenrays.

We define the effective sound speed ratio as the effective sound speed divided by the effective sound speed at the source. Therefore, an altitude where the effective sound speed

ratio is above 1 indicates a region which can act as an upper boundary for a duct, dependent upon the angle of incidence of the upward refracting infrasonic energy.

2.3.2 Data Processing

We compare the predicted propagation paths with the DLL data to help identify long-range infrasound propagation paths for a few example eruptions in Alaska. DLL is a 6-element array spanning 1.2 km; however, only 5 elements were working for most of the events in this study (Cleveland 2014/2015 and Pavlof 2014). Array processing techniques to determine back azimuth, MCCM (mean cross-correlation maxima), and trace velocity were performed via least squares for the slowness of a plane wave crossing the array [*Szuberla and Olson*, 2004]. Array processing techniques for DLL are used as a monitoring tool by AVO to detect eruptions, as well as in reanalysis studies for Alaskan volcanoes [*De Angelis et al.*, 2012; *Fee et al.*, 2017]. DLL data for the Cleveland examples are band-pass filtered between 0.5 and 5 Hz, historical band-pass filter used for monitoring signals from Cleveland to DLL in real-time, while Pavlof examples are filtered between 1 and 5 Hz to be more consistent with the results published by *Fee et al.* [2017]. A standard delay-and-sum beamforming technique is applied to increase the signal-to-noise ratio (SNR). DLL infrasound data are corrected for the propagation time by subtracting the predicted traveltime from the arrival time at DLL.

Observed data and predicted propagation model outputs using AVO-G2S are compared to assess the model's accuracy and effectiveness. We use wind and temperature data from the Dillingham, AK airport weather station PADL [*http://mesonet.agron.iastate.edu/*] to calculate the receiver effective sound speed. This is then compared to the trace velocity calculated by array processing (termed observed trace velocity) to help distinguish between arrival types (Section 2.2.3). If an eigenray is predicted for a particular event, we compare the modeled traveltime from ray tracing with the traveltime observed via differencing the onset time of the explosions from the local station to DLL. Additionally, for the Cleveland examples where the onsets were impulsive and easy to identify, we use calculated celerity to

help support the propagation path predicted by AVO-G2S, as it is a relatively clear indicator used to distinguish between ducts (Section 2.2.3).

Local seismic data are included in the interpretations for both Pavlof eruptions. For the November 2014 eruption, we analyze data from the local seismic station PS4A to compare with the infrasound data at DLL. PS4A is located on the south side of Pavlof Volcano (8 km from the summit) and was operational throughout the entire eruptive episode [*www.avo.alaska.edu*], though there are a few >1 min gaps in the data. For the Pavlof 2016 eruption, local seismic station PS1A was used in a similar fashion as PS4A in 2014 analyses. PS1A stayed on scale for the entirety of the eruption sequence and is located on the southeast side of the volcano (9 km from summit). During the eruptions, both PS4A and PS1A consisted of short-period (1 Hz) seismometers with a sampling frequency of 100 Hz. We calculate the amplitude envelope for both the distal acoustic and local seismic data via Hilbert transform, and apply a convolutional filter with a window length of 10-min to smooth the envelope. We also remove the acoustic traveltime to facilitate direct comparison between the seismic and acoustic data.

2.4 Results

2.4.1 Cleveland Volcano

We explore propagation conditions and data collected at DLL for two typical explosions from Cleveland Volcano occurring on 6 November 2014 and 21 July 2015. Both events were similar in duration, lasting a few tens of seconds with no precursory activity. Using data from the CLCO array (15.4 km from the summit), unfiltered amplitudes are 14 Pa for the 2014 event and 30 Pa for the 2015 event.

2.4.1.1 6 November 2014

On 6 November 2014 an explosion at Cleveland Volcano occurred at 07:42; however, the infrasound alarm at DLL (∼992 km from Cleveland Volcano) did not automatically trigger

an alert, which would have indicated that an amplitude threshold was surpassed and that the back azimuth is consistent with an explosion from Cleveland Volcano. Array processing for this explosion at DLL is shown in Figure 2.3a–d. Figure 2.3a shows the beamformed DLL data and Figure 2.3b shows the calculate MCCM values with a peak of ∼0.75, just above the noise (MCCM of 0.4–0.6). Receiver effective sound speed is 0.332 km/s, which is in agreement with the observed trace velocity of ∼0.331 km/s (Figure 2.3c). True back azimuth from DLL to Cleveland is 230.6°, with the observed back azimuth for this explosion being ∼230° (Figure 2.3d).

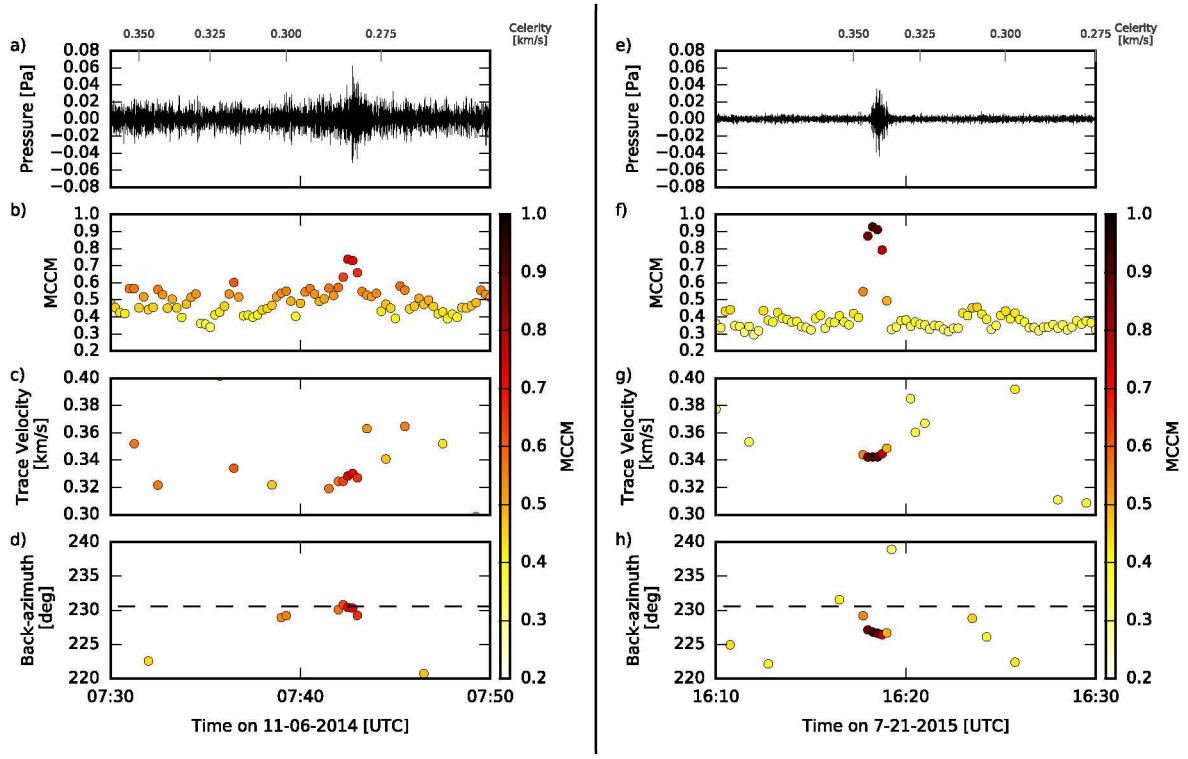

Figure 2.3: DLL array processing results for the Cleveland Volcano explosions. Data are band pass filtered between 0.5-5.0 Hz for explosions on: (a-d): 06 November 2014; (e-h): 21 July 2015. Data are also corrected for traveltime. Panels a) and e) show the beamformed DLL data, panels b) and f) are the mean cross-correlation maxima (MCCM), panels c) and g) are the trace velocity values colored according to MCCM, and panels d) and h) show the back azimuth, also colored according to MCCM value. Celerities are given in km/s on top of a) and e), also shifted by the same traveltime. Dotted line in d) and h) is the back azimuth to Cleveland Volcano.

Figure 2.4a–c shows the atmospheric specifications for this explosion. The specifications

are assembled for 06:00, ∼1.75 h before the explosion, with Figure 2.4a,b profiles above the volcano and 2.4c using range-dependent modeling. Figure 2.4a shows the zonal (red) and meridional winds (blue) along with the wind velocity in the direction of propagation (black); Figure 2.4b shows the sound speed (solid), the effective sound speed (dotted), and a vertical line denoting the effective sound speed at the source; and Figure 2.4c shows the predicted propagation paths from source (on the left) to receiver (towards the right). The black rays are the eigenrays. During this explosion, winds are light (<8 m/s) below 30 km altitude above the volcano (Figure 2.4a), so a tropospheric duct is not predicted for this time and source-receiver configuration. Above 30 km, the wind velocity in the direction of propagation is positive ranging from 0 to 25 m/s, increasing with altitude (Figure 2.4a); therefore a moderately strong (effective sound speed ratio=1.05) stratospheric duct is seen in the ray tracing (Figure 2.4c). The rays predicted would arrive at DLL directly on the fourth bounce, indicating favorable conditions for stratospherically ducted energy towards the receiver. The stratospheric eigenray from this scenario predicts a celerity of 0.290 km/s (modeled traveltime of 3416 s), quite similar to the celerity of 0.284 km/s that was observed (observed traveltime 3491 s). Celerities are indicated on top of Figure 2.3a, also shifted by the same traveltime as the DLL data. Two eigenrays are predicted in the thermospheric duct as well with 1–2 surface bounces.

2.4.1.2 21 July 2015

Another explosion at Cleveland Volcano occurred on 21 July 2015 16:17, yet this explosion was clearly detected at DLL in near real-time. The amplitude at DLL (0.04 Pa) for this event is slightly smaller than the 2014 event (0.06 Pa) (Figure 2.3e) even though at short range the amplitude was twice as high. However, background noise is extremely low for this event (Figure 2.3e) so the signal appears clearly with high SNR. Array processing shown in Figure 2.3f–h indicates higher peak MCCM values than the November 2014 explosion, surpassing 0.9 above lower background MCCM values of 0.3–0.45 (Figure 2.3f). This event exceeded

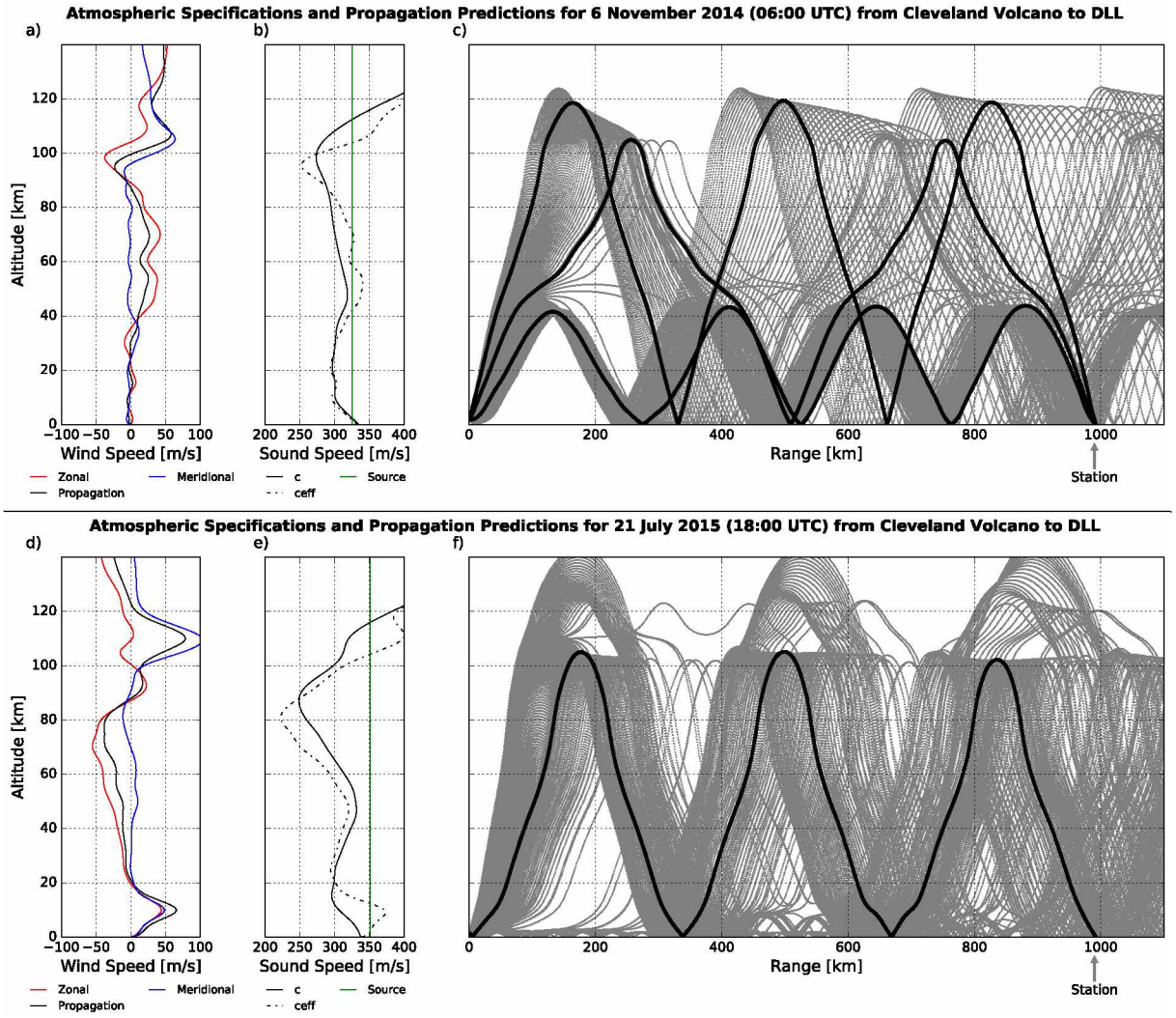

Figure 2.4: AVO-G2S specifications with GeoAc ray tracing results for the propagation of infrasound from Cleveland Volcano to DLL for: (a-c): 06 November 2014 (07:42 UTC) explosion modeled at 06:00 UTC; (d-f): 21 July 2015 (16:17 UTC) explosion modeled at 18:00 UTC. a) shows the zonal (red) and meridional winds (blue) along with the wind velocity in the direction of propagation (black); b) shows the sound speed (solid), the effective sound speed (dotted), and a vertical line denoting the sound speed at the source; and c) shows the predicted propagation paths from source (on the left) to receiver (towards the right). The black rays are the eigenrays.

the detection threshold for the real-time AVO explosion detection alarm, and sent an alert to AVO staff indicating that an explosion occurred from Cleveland Volcano. Receiver effective sound speed is 0.341 km/s, which agrees with the observed array processing trace velocity of 0.342 km/s (Figure 2.3g). The observed back azimuth is 227°, yielding a deviation of ∼4°

from the true back azimuth (Figure 2.3h).

Figure 2.4d–f show atmospheric specifications for 21 July 2015 18:00, ∼1.75 h after the explosion, using the range-dependent atmosphere. Atmospheric conditions above the volcano show strong zonal and meridional winds that reach up to 49 m/s to both the north and east in the troposphere (Figure 2.4d). These wind components resolve to 63 m/s in the direction of the DLL array, contributing to the strong effective sound speed observed in Figure 2.4e, and also a component <30 m/s perpendicular to the direction of propagation. A tropospheric duct can be seen in Figure 2.4f to propagate for up to 850 km before disappearing. This duct comes close to DLL, but is not predicted to make a direct arrival. Therefore, as a proxy, rough estimates for celerity, traveltime, and arrival inclination for a tropospheric arrival at this time were obtained using a range-independent atmosphere, which produces a sustained tropospheric duct between Cleveland and DLL. Observed celerity for this explosion is 0.349 km/s (traveltime of 2839 s) and modeled celerity for the range-independent tropospheric eigenrays with 10–20 bounces is ∼0.350–0.354 km/s (traveltimes between 2796 and 2827 s) with arrival inclinations of 20–22°. Thermospherically ducted energy from the range-dependent modeling yields a direct eigenray with two bounces and a celerity of 0.250 km/s (traveltime of 3959 s). All values from both explosions are summarized in Table 2.1, highlighting the differences between the two events.

2.4.2 Pavlof Volcano

Here we analyze the infrasound signals observed at DLL and the propagation conditions for the November 2014 and March 2016 Pavlof eruptions. For both eruptions, there were no operational local infrasound sensors, therefore AVO relied upon long-range infrasound detected at DLL (460 km away). Due to their long duration (hours to days), propagation modeling interpretations for eruptions at Pavlof Volcano are complex and highlight the ephemeral nature of lower atmospheric ducts.

Table 2.1: Infrasound predictions and observations of the 06 November 2014 and 21 July 2015 explosions of Cleveland Volcano to the DLL array. Tropospheric values for the 21 July 2015 explosion are from a range-independent atmosphere for comparison purposes. Predicted trace velocity is the receiver effective sound speed and does not account for angle of incidence.

Date of Explosion	06 Nov 2014		21 Jul 2015	
	Observed	Predicted	Observed	Predicted
Traveltime [s]	3491	3416 (Stratospheric)	2839	2796 - 2827 (Tropospheric)
		3465 - 3882 (Thermospheric)		3959 (Thermospheric)
Celerity [km/s]	0.284	0.290 (Stratospheric)	0.349	0.350 - 0.354 (Tropospheric)
		0.255 - 0.286 (Thermospheric)		0.250 (Thermospheric)
Arrival Inclination [°]	–	13 (Stratospheric)	–	19-22 (Tropospheric)
		21 - 37 (Thermospheric)		24 (Thermospheric)
Trace Velocity [km/s]	0.331	0.332	0.342	0.341
MCCM	0.75		>0.9	

2.4.2.1 November 2014 Eruption

The onset of the November 2014 Pavlof eruption was detected with strong seismic tremor, as well as a combination of remote sensing and visual observations late UTC time on 12 November 2014 [*www.avo.alaska.edu*]. However, infrasound was not strongly detected at DLL (∼460 km away) until a full 24 h later. Figure 2.5a-f shows the eruption seismo-acoustic signals and infrasound array processing techniques from 12 November 2014 12:00 to 16 November 2014 12:00. The first two panels show beamformed DLL data (Figure 2.5a), as well as data from local seismic station PS4A (Figure 2.5b). Figure 2.5c is the envelope of the infrasound (red) and seismic (black) data, showing the seismic and long-range infrasound amplitudes do not track each other well. While the seismic data show a rather steady increase in amplitude, the longrange infrasound amplitudes appear as pulses and are more

irregular. Figure 2.5d–f show the MCCM, trace velocity, and back azimuth calculations from infrasound array processing, respectively, further indicating that the detection of infrasound at DLL is sporadic and inconsistent throughout the eruption. The receiver effective sound speed at DLL varied slightly throughout the November eruption and on average is 0.34 km/s. Similarly, the observed trace velocity is ∼0.33 km/s and varies by ±0.02 km/s (Figure 2.5e). The observed back azimuth is consistent with propagation from Pavlof to DLL at 208° for periods with high MCCM values (Figure 2.5f), with some scatter during periods of lower MCCM.

The tropospheric and stratospheric ducts vary throughout the eruption. Figure 2.5g summarizes the effective sound speed ratio from 0 to 60 km altitude using a 1D representation of the atmosphere above Pavlof Volcano for the duration of the eruption. Range-dependent atmospheric variability is considered in the next paragraph. Values are centered on the reconstructed times (every six hours) and plotted to ±3 h. A weak tropospheric duct (ceff = 1.02) exists from 0–10 km altitude until 13 November 12:00. After this the principal duct is in the stratosphere where the effective sound speed ratio reaches 1.02. This stratospheric duct fluctuates slightly throughout the eruption, with effective sound speed ratios hovering right around 1, indicating a marginal duct. On 13 November 2014 18:00, weak infrasound from Pavlof is detected at DLL and neither a tropospheric nor stratospheric duct is clearly predicted to exist (Figure 2.5g), though a low number of tropospheric rays are apparent in the range-dependent modeling of Supplementary Video 1. Similarly, we do not detect clear infrasound from 09:00 to 14:00 on 15 November 2014, which also corresponds to a weak or non-existent duct (Figure 2.5g). However, similar atmospheric conditions are predicted for about 12 h prior to this period while infrasound was clearly detected. This highlights that at times of marginal tropospheric and stratospheric ducting it is difficult to identify the correct propagation path using a 1D atmosphere.

The variable range-dependent ducting during the 2014 Pavlof eruption generally coincides with changes in infrasound detections at DLL (Figure 2.5), given the coarse 6h temporal

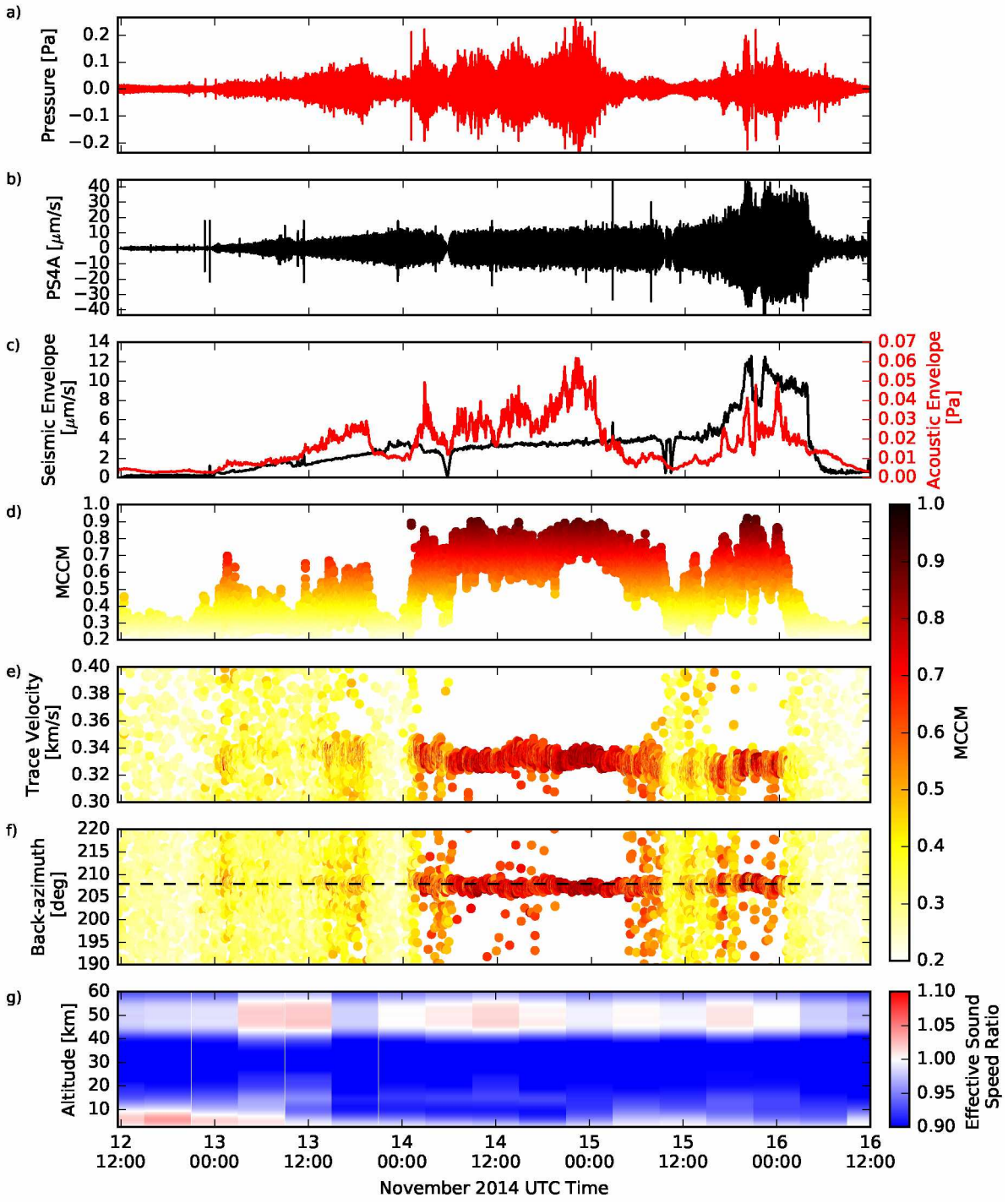

Figure 2.5: DLL infrasound array processing results for data band pass filtered between 1.0-5.0 Hz from 12 November 2014 at 12:00 UTC to 16 November 2014 at 12:00 UTC: a): beamformed DLL data; b): local seismic data; c) acoustic (red) and seismic (black) envelopes; d) mean cross-correlation maxima (MCCM); e) trace velocity colored according to MCCM value; f) back azimuth colored according to MCCM; and g) effective sound speed ratio as a function of height, centered at times of reconstruction and extended by ±3 hours.

resolution for the wind files. At the beginning of the eruption, a tropospheric duct existed for a few hundred kilometers in distance, then transitioned into a stratospheric duct of variable spatial extent, to only a thermospheric duct, and then back to stratospheric duct by the end of the eruption. For a full description of infrasound detection at DLL and the corresponding atmospheric conditions, the reader is referred to Table 2.2 and Supplementary Video 1. Figure 2.6 shows two notable examples of the atmospheric specifications and propagation simulations during the 2014 Pavlof eruption. Figure 2.6a–c roughly corresponds to the start of the eruption based on seismic data (13 November 2014 00:00), and shows a weak tropospheric duct initially guiding acoustic energy for ∼300 km. This duct then disappears, upon which energy is then refracted up into the thermosphere and does not return to the Earth's surface at DLL (Figure 2.6c). Wind speed toward the receiver reaches 29 m/s at an altitude of 10 km (Figure 2.6a), and contributes to the initial tropospheric duct. However, wind velocities change as a function of distance from the volcano and become unfavorable for tropospheric propagation. On 14 November 2014 12:00 when clear infrasound is detected at DLL, a weak stratospheric duct has been established and persists past DLL (Figure 2.6d–f). At this time DLL lies in a predicted shadow zone. The strong meridional tropospheric winds have weakened significantly (Figure 2.6d), making the overall contribution of the wind in the direction of propagation nearly zero below 40 km. The reduction of effective sound speed at the source from the previous day (Figure 2.6b,e), causes the appearance of the weak (effective sound speed ratio just over 1) stratospheric duct. Thermospheric arrivals are predicted for the entirety of the eruption.

Table 2.2: Comparison between seismic, long-range infrasound detections at DLL, and propagation conditions for Pavlof Volcano to DLL (∼460 km) from 12:00 UTC 12 November 2014 to 12:00 UTC 16 November 2014. Column 3 is the average MCCM centered at times of atmospheric reconstruction and extended by ±3 hours

Date (UTC Time)	Seismic	Average MCCM	Infrasound Detection	Range-Dependent Propagation
12 Nov 2014 12:00 UTC	No	0.30	None	Tropospheric duct exists for 300 km

Date (UTC Time)	Seismic	Average MCCM	Infrasound Detection	Range-Dependent Propagation
12 Nov 2014 18:00 UTC	No	0.27	None	Tropospheric duct exists for 300 km, where a stratospheric duct forms between 15-50 km (doesn't reach surface)
13 Nov 2014 00:00 UTC	Yes	0.32	Weak with scatter in back azimuth and trace velocity	Tropospheric duct exists for 250 km
13 Nov 2014 06:00 UTC	Yes	0.32	Very little to none	Tropospheric duct exists for 200 km, where a stratospheric duct forms between 15-50 km (doesn't reach surface)
13 Nov 2014 12:00 UTC	Yes	0.31	Weak	Stratospheric duct for 300 km where a tropospheric duct reforms
13 Nov 2014 18:00 UTC	Yes	0.42	Very little to none	Only thermospheric duct
14 Nov 2014 00:00 UTC	Yes	0.33	Begins around 01:00 UTC	Only thermospheric duct; Stratospheric duct on the verge of forming
14 Nov 2014 06:00 UTC	Yes	0.64	Becomes more clear	Stratospheric duct with DLL in a shadow zone; Only thermospheric after DLL
14 Nov 2014 12:00 UTC	Yes	0.73	Clear (some scatter back azimuth and trace velocity)	Stratospheric duct stronger and no longer converts to only thermospheric duct after DLL
14 Nov 2014 18:00 UTC	Yes	0.72	Very clear	Stratospheric duct with bounces closer to DLL
15 Nov 2014 00:00 UTC	Yes	0.78	Clear	Only thermospheric duct but stratospheric duct is very close to forming
15 Nov 2014 06:00 UTC	Yes	0.64	Clear (some scatter back azimuth and trace velocity)	Stratospheric duct (5-50 km) with DLL in a shadow zone; Only thermospheric after DLL
15 Nov 2014 12:00 UTC	Yes	0.41	Weak	Stratospheric duct (5-50 km) with DLL in a shadow zone; Only thermospheric after 400 km
15 Nov 2014 18:00 UTC	Yes	0.57	Becomes more clear	Stratospheric duct reformed with DLL in the shadow zone
16 Nov 2014 00:00 UTC	Yes	0.56	None	Stratospheric duct (weaker) with DLL in the shadow zone

Date (UTC Time)	Seismic	Average MCCM	Infrasound Detection	Range-Dependent Propagation
16 Nov 2014 06:00 UTC	No	0.26	None	Only thermospheric duct
16 Nov 2014 12:00 UTC	No	0.24	None	Only thermospheric duct; Tropospheric duct close to reforming

2.4.2.2 March 2016 Eruption

In contrast, we detect uninterrupted long-range infrasound for the entire March 2016 eruption of Pavlof Volcano at DLL. The infrasound amplitudes follow similar trends as the local seismic station [*Fee et al.*, 2017], with only minor deviations. Figure 2.7 has a similar layout to Figure 2.5, but the time spans 27 March 2016 20:00 to 29 March 2016 00:00 and uses seismic station PS1A instead of PS4A (Figure 2.7b). Figure 2.7c shows the infrasonic and seismic envelopes where amplitudes overall track each other closely for this eruption. Seismicity and infrasound increase starting around 28 March 2016 00:00 and continue at a peak level until about 17:00 when both datasets begin to decrease to background levels. Observed trace velocities begin around 0.32–0.33 km/s and transition more towards 0.34 km/s partway through the eruption on 28 March 2016 09:30 (Figure 2.7e). The receiver effective sound speed was around 0.338 km/s during this eruption. The observed back azimuth is consistent with propagation from Pavlof Volcano to DLL (208°), beginning the eruption closer to 205°, increasing to 207° on 28 March 2016 at 12:00, and ending the eruption at ∼208° (Figure 2.7f).

Propagation conditions remain relatively consistent throughout the eruption. Figure 2.7g summarizes the peak effective sound speed ratio above the volcano as a function of time. Winds in the troposphere toward DLL remained positive and relatively strong throughout the eruption, especially when compared with the 2014 Pavlof eruption. The tropospheric duct is fairly low altitude (up to 10 km), with peak winds in the direction of propagation from 30 to 40 m/s that decrease steadily with time. A slight increase in strength of the stratospheric

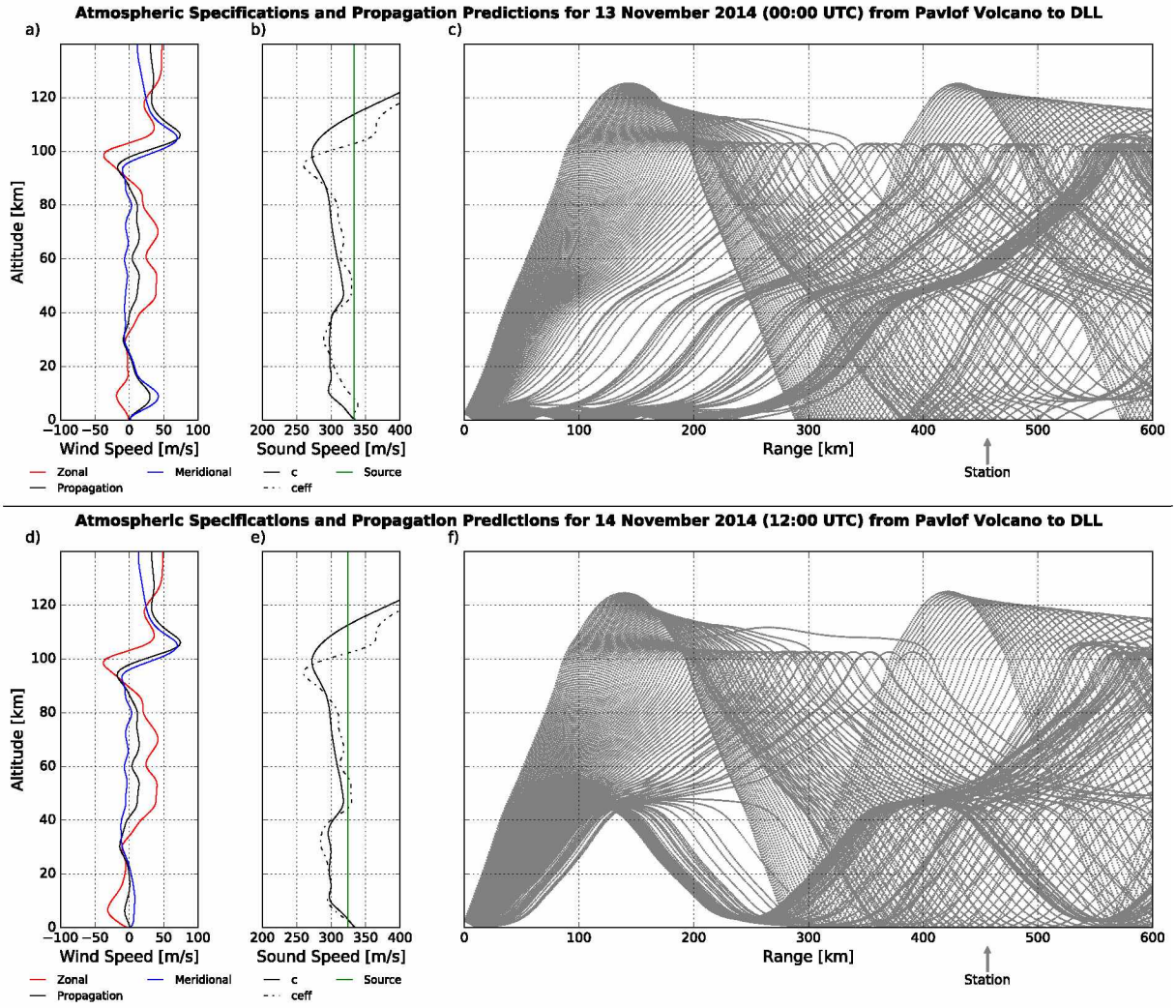

Figure 2.6: AVO-G2S specifications with GeoAc ray tracing results from DLL to Pavlof Volcano for: a-c): 13 November 2014 modeled at 00:00 UTC; d-f): 14 November 2014 modeled at 12:00 UTC. Subplots and colors same as in Figure 2.4.

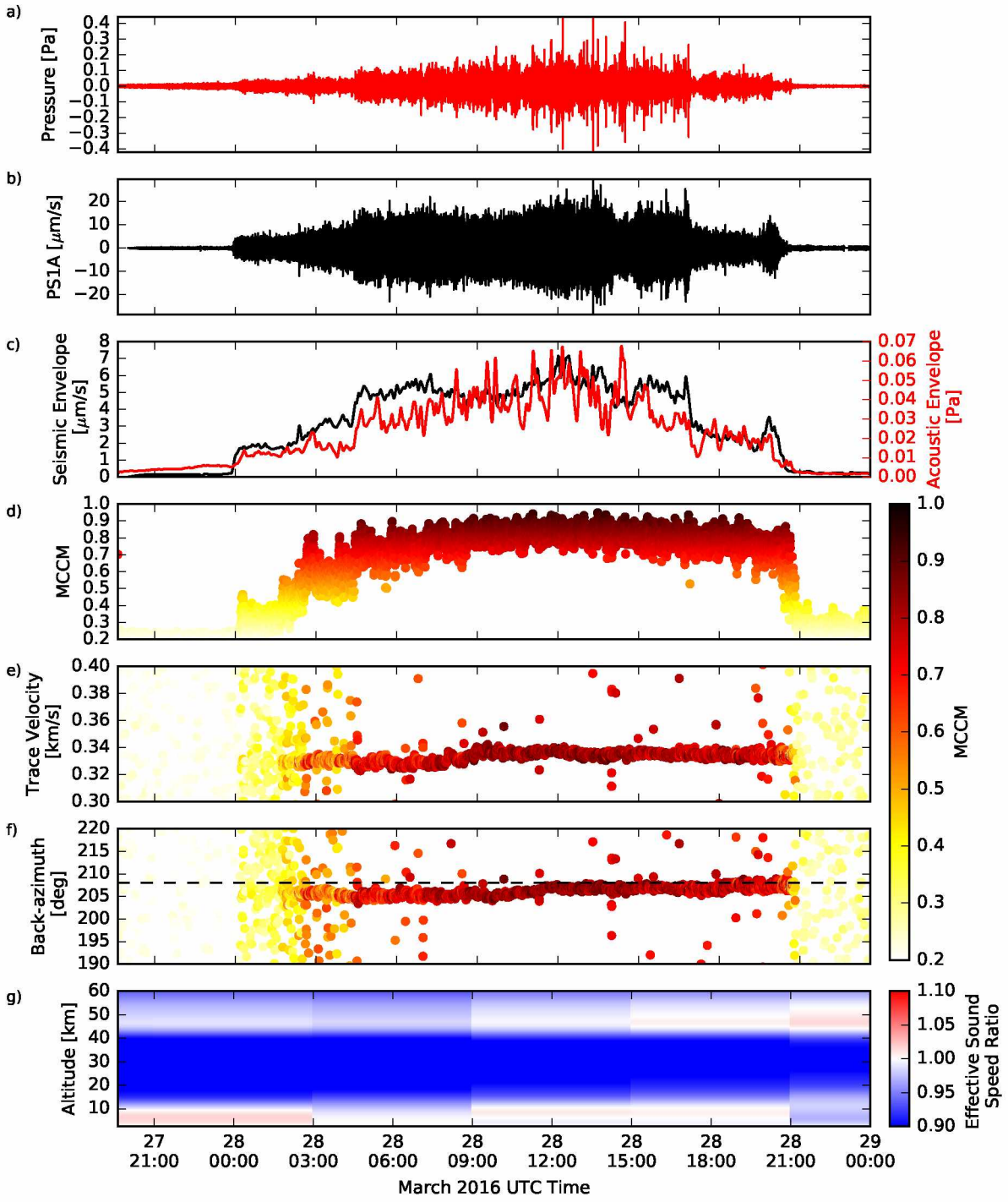

Figure 2.7: DLL array processing results for data band pass filtered between 1.0-5.0 Hz from 27 March 2016 at 20:00 UTC to 29 March 2016 at 00:00 UTC. Subplots same as in Figure 2.5.

duct as a function of time can be seen in Figure 2.7g by 28 March 2016 12:00 (effective sound speed ratio >1 after this time), around the time of the increase in observed back azimuth.A representative ray tracing diagram from Pavlof to DLL during the March 2016 eruption is shown in Figure 2.8. For the most part, marginal tropospheric and stratospheric ducts are predicted for the entire duration of the eruption (with minor fluctuations), as well as the typical thermospheric duct.

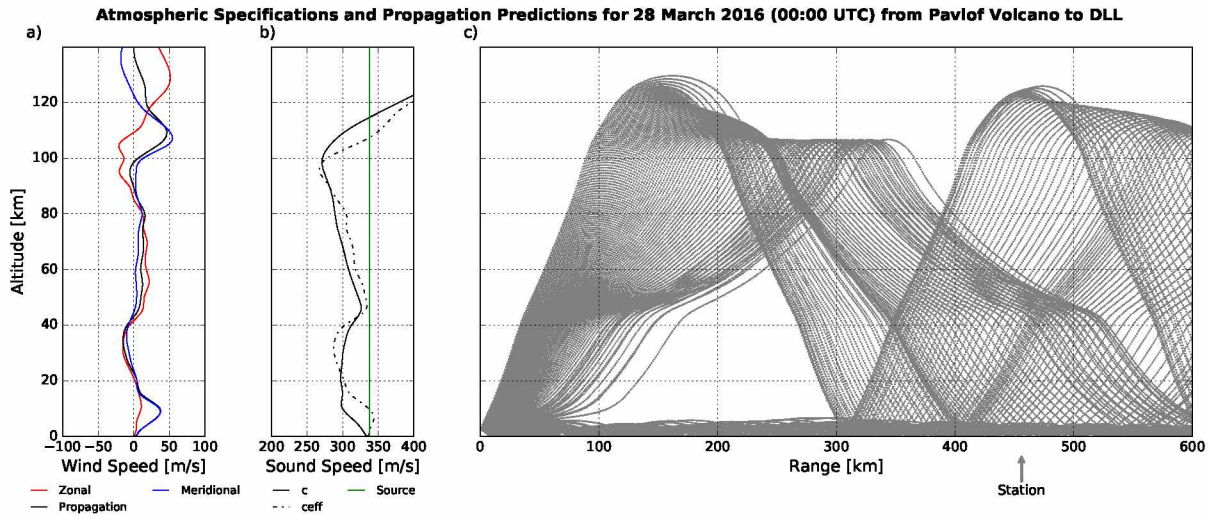

Figure 2.8: AVO-G2S specifications with GeoAc ray tracing results from DLL to Pavlof Volcano for 28 March 2016 modeled at 00:00 UTC. Subplots and colors same as in Figure 2.4.

2.5 Discussion

2.5.1 Cleveland Volcano

Atmospheric propagation modeling for the 6 November 2014 explosion of Cleveland Volcano predicts a strong stratospheric duct to DLL, as well as thermospheric arrivals (Figure 2.4a–c). Tropospheric winds provided by the reanalysis products (and therefore the AVO-G2S model as well) are blowing in the opposite direction of DLL, therefore limiting the chance of detecting tropospheric arrivals. The receiver effective sound speed and observed trace velocity at DLL, 0.332 and 0.331 km/s, respectively, are similar for this explosion,

which would suggest a low arrival angle (troposphere or stratosphere). The observed celerity (0.284 km/s) is on the higher end of those predicted by the thermospheric eigenrays and almost exactly the same as the predicted celerity from the stratosphere at 0.290 km/s (see Table 2.1). These results strongly suggest sound propagation from Cleveland to DLL in a stratospheric duct for this explosion. Because the propagation conditions are conducive for stratospheric ducting but the signal at DLL was relatively weak (Figure 2.3a), we suggest the lack of detection at DLL in real-time was likely related to the low SNR from relatively high background noise, and not because of insufficient propagation conditions.

For the 21 July 2015 explosion at Cleveland Volcano, stratospheric arrivals are unlikely given that the stratospheric winds were blowing in the opposite direction of DLL for this time (Figure 2.4d–f). Tropospheric winds peaked at over 60 m/s in the direction of propagation at the source, creating a strong duct. However, range-dependent atmospheric modeling suggests this tropospheric duct does not exist past 850 km in range, or about 150 km shy of reaching DLL. Tropospheric ducts are dependent on local weather systems and conditions that can change rapidly [*Drob et al.*, 2003] and might not be captured in the temporal resolution of the reanalysis files (6 h), therefore the duct may have persisted at the time of propagation [e.g. *Evers et al.*, 2014]. Additionally, sub-grid size spatial changes in local weather may affect the range-dependent propagation modeling. We also note that while tropospheric ducts can disappear after a few hundred kilometers [*Ceranna et al.*, 2009; *Drob et al.*, 2003; *Le Pichon et al.*, 2006], there are cases in which tropospheric arrivals are detected at ranges >1000 km, as shown in *Fee et al.* [2013] and *De Angelis et al.* [2012] for a similar propagation scenario. The receiver effective sound speed and observed trace velocity were 0.341 km/s and 0.342 km/s, respectively, for the July 2015 Cleveland explosion (see Table 2.1), supporting the conclusion that the arrival at DLL came from either the troposphere or stratosphere. The back azimuth deviation of 4° can be partially explained by a component of the tropospheric winds perpendicular to the direction of propagation, which deflect the signal laterally and make it appear to originate from a slightly different azimuth. This is plausible for the given

scenario due to the positive and strong zonal winds (Figure 2.4d). An accurate calculation of the back azimuth deviation for the troposphere using GeoAc was not possible due to the lack of a range-dependent tropospheric eigenray for this example. Both the predicted and observed celerities are high (see Table 2.1), similar to that of the speed of sound for this explosion, which also suggests a tropospheric arrival. This high celerity (and therefore low traveltime) could not have been from a signal in the thermosphere. A high MCCM value for this explosion means that the shape of the waveform across the array elements at DLL are highly similar, and that background noise was extremely quiet during this event. Due to the high celerity, strong tropospheric winds, unfavorable stratospheric ducting conditions, and low trace velocity, we conclude that the 21 July 2015 explosion at Cleveland Volcano traveled primarily in the troposphere, even though the ray tracing diagram in Figure 2.4f is somewhat inconsistent with this assertion.

2.5.2 Pavlof Volcano

Long-range infrasound propagation conditions between the two most recent eruptive episodes at Pavlof Volcano vary significantly. The predicted propagation conditions from Pavlof to DLL fluctuate throughout the course of the 2014 eruption (Figure 2.5), with plausible paths in a combination of tropospheric, stratospheric, and thermospheric ducts. Meridional tropospheric winds above the volcano were strong during the beginning of the eruption when seismic tremor was occurring, but weakened to near zero when the first clear infrasound detection occurred at DLL (Figure 2.5g). Therefore, winds in the troposphere no longer helped or hindered the guiding of infrasonic energy at these altitudes when infrasound becomes clearly detected. Discrepancies between local seismic and distal infrasound (Figure 2.5a–c)may be related to variability in the volcanic source or temporal changes in the atmosphere that are not captured in our analyses. Atmospheric modeling limitations such as fluctuations between the 6h wind files and inaccuracies in the wind files themselves do not allow us to perfectly predict the propagation paths within the atmosphere, and therefore we

cannot completely differentiate the contributions of possible source and atmospheric variations. Trends begin to appear in the comparison between detections at DLL and propagation conditions as a function of time when keeping these inaccuracies into account (see Table 2.2 and Supplementary Video 1). For example, when infrasound begins to be detected around 14 November 2014 01:00, propagation conditions are changing from only a thermospheric duct at 14 November 2014 00:00 to a stratospheric duct as well at 06:00 (see Table 2.2, Figure 2.5). Similarly, on 15 November 2014 12:00, infrasound detections are weak and propagation conditions show that the stratospheric duct disappears at a range of 400 km, before reaching DLL. Infrasound detections become clearer by 18:00, when the stratospheric duct reformed for the entire distance from Pavlof to DLL (see Table 2.2). Though we cannot confirm that favorable propagation conditions were the primary factor in the changes in detectability a DLL for the duration of the November 2014 Pavlof eruption, we do see some indications of the changes in propagation conditions being reflected in the long-range infrasound detections.

Because the trace velocity was similar to the receiver sound speed (0.32–0.34 km/s as compared with 0.34 km/s), it is possible that the signal could be a combination of tropospherically and stratospherically ducted energy, either occurring simultaneously (multipathing) or changing as a function of distance and time. This eruption occurred near the winter, where seasonal stratospheric arrivals are likely to the east (e.g. towards DLL). Additionally, westerly tropospheric winds blowing towards the east are stronger in this region during the winter due to the increased strength of the tropospheric polar jet stream winds [*Archer and Caldeira*, 2008]. Therefore, the seasonality of both the tropospheric and stratospheric winds were towards the receiver for propagation from Pavlof to DLL for this eruption.

The observations during the March 2016 eruption of Pavlof show a marked difference to those from November 2014, with local seismic and long-range infrasound signal amplitudes having similar temporal trends and we detect infrasound during the entirety of the eruption. Here we show that only very minor changes in the strength of the tropospheric and stratospheric ducts occur throughout the eruption (Figure 2.7g), suggesting that the

propagation conditions did not significantly change. This was discussed briefly in *Fee et al.* [2017], where it was interpreted that long-range infrasound signals at DLL primarily reflected changes in the volcanic tremor source amplitude as opposed to propagation effects. Based on the atmospheric conditions and modeling outlined in this study, infrasound arrivals at DLL were likely a combination of tropospheric and stratospheric ducting throughout the eruption (multipathing). Because the stratospheric duct increases in strength slightly as the tropospheric duct decreases (Figure 2.7g), the increase in trace velocity and back azimuth around 08:00 and 11:00, respectively, could be due to the increasing contribution of the stratospheric duct, which would increase the inclination angle (trace velocity and decrease the back azimuth deviation due to crosswinds in the troposphere.

The observed changes in the back azimuth and trace velocity throughout the eruption (Figs. 2.5, 2.7) may also be affected by the inherent uncertainties for the DLL array processing, local temperature changes affecting trace velocity, temperature and wind variability not captured by the model, and a changing signal to noise ratio through time. We also compute the infrasound array uncertainties following the method of *Szuberla and Olson* [2004]. For the events when only 5 elements were working at DLL (Cleveland 2014/2015 and Pavlof 2014), uncertainty for back azimuth is 1.2° and trace velocity is 0.007 km/s given a 95% confidence interval, while for the Pavlof 2016 eruption when all 6 elements were functioning, the uncertainties decrease to 0.6° in back azimuth and 0.003 km/s for trace velocity. The higher back azimuth uncertainties for the earlier events may help explain some of the array processing results.

2.5.3 Other Influences on Infrasound Propagation

The existence of ducts allows for efficient infrasound propagation though the atmosphere for hundreds to thousands of kilometers. Range- and time-dependent infrasound propagation modeling is needed in order to constrain these ducts and how they might change both spatially and temporally, especially in a location such as Alaska that has significant

atmospheric variability. For example, a range-independent model during the November 2014 eruption of Pavlof Volcano predicts a tropospheric duct in the beginning of the eruption that transitioned into a stratospheric duct because it is only based on the atmospheric conditions directly above the volcano (Figure 2.6 a,b,d,e). However, our range-dependent modeling (Figure 2.6 c,f) show that changing atmospheric conditions along the source-receiver path help explain the discrepancies with the recorded data. The tropospheric duct dissipated on 13 November 2014 (Figure 2.6c) after ∼200 km and likely did not propagate energy all the way to DLL. If a range-dependent global model were not used for that particular eruption, then the interpretation of the signals detected at DLL would differ.

The analyses we have presented solely use coarse resolution reanalysis atmospheric data due to the limited availability of higher resolution data. This restricts our analysis for some of the events with unexplained features, such as the November 2014 eruption of Pavlof Volcano. The unexplained migration of sound energy between the ducts likely caused by spatial and temporal changes in wind during this eruption is a prime example of the need to have the high-resolution aspect of AVO-G2S model, as outlined in *Schwaiger et al.* [2019]. Higher resolution lower atmospheric data such as from the NCEP North American Mesoscale Forecast System were incorporated into AVO-G2S starting in 2017 for forecasting with higher resolution wind files in Cartesian coordinates in the Alaskan region. Unfortunately, many of the high resolution wind files prior to 2017 are not currently available as they were not stored by AVO until the AVO-G2S projected grid model was operational; therefore reanalysis of this eruption using the high resolution data was not possible for this study. For future eruptions in Alaska, higher resolution files can be used and will hopefully allow for a better understanding of the atmospheric conditions and their influence on infrasound propagation. In addition to being higher resolution, the Alaskan-specific model outlined in *Schwaiger et al.* [2019] takes approximately one-third the computation time than the coarser resolution global model, and is therefore preferred as AVO plans to implement real-time forecasting of infrasound propagation.

A radiosonde is located in Cold Bay, Alaska (~60 km from Pavlof Volcano) and is used to validate AVO-G2S atmospheric modeling variables for the troposphere and lower stratosphere every 12 h throughout the course of both Pavlof eruptions. Figs. S1 and S2 of the Supplemental Material show a comparison of zonal and meridional wind speeds as well as the static sound speed profile calculated from the temperature. AVO-G2S and radiosonde sound speed profiles agree well and are within a few m/s of each other, while wind speed profiles differ by <10 m/s for all time periods. Slight differences in winds can be attributed to modeled results being smoothed representations of the true winds as well as profile locations being 60 km apart.

In middle and high latitude regions like Alaska where differences in atmospheric conditions (e.g. surface temperature, tropospheric and stratospheric wind jets) between seasons are great [*Fee and Matoza*, 2013], time of year must be taken into account when interpreting infrasound signals at long-range. Using examples from this paper, we can see that the sound speed (not including winds) at the source was about 325 m/s for the November 2014 Cleveland explosion and about 350 m/s for the July 2015 explosion. This sound speed is easily calculated using AVO-G2S. An accurate prediction of the celerity/traveltime would impact the estimate of the origin time of the event, which can vary on the order of minutes between propagation paths at these distances.

Many of the infrasound signals AVO has observed at DLL are longrange tropospheric arrivals from Alaskan volcanoes to the southwest (Figure 2.1) [*De Angelis et al.*, 2012; *Fee et al.*, 2017]. However, when the lower atmospheric winds are not directed towards DLL, then stratospheric arrivals [*Fee and Matoza*, 2013] and even thermospheric arrivals [*Fee et al.*, 2010] are observed. Because stratospheric winds blow east in the winter hemisphere and west in the summer hemisphere, and given the current configuration of volcanoes and infrasound arrays in Alaska (Figure 2.1), AVO is more likely to detect explosions from the stratosphere in the winter than in the summer. This is becoming less of an issue with the recent installations of infrasound arrays near Cleveland Volcano (CLCO) and Adak (ADKI)

towards the western end of the Aleutian arc. AVO and its collaborators now maintain arrays at DLL, Sand Point, Akutan, Okmok, CLCO and Adak (Figure 2.1), as well as an increasing number of single sensors across Alaskan volcanoes, which will expand and strengthen AVO's year-round infrasound monitoring capabilities. The EarthScope Transportable Array has now also been deployed across Alaska, with 210 co-located seismic and acoustic sensors on the Alaska mainland and peninsula. *Fee et al.* [2017] found clear infrasound signals from the 2016 Pavlof eruption on four Transportable Array stations.

The AVO-G2S model uses state-of-the-art atmospheric specifications, yet portions of the atmosphere are still poorly constrained. Wind and temperature data are fairly reliable up to around 55–60 km; however, the higher altitude winds are empirical, based on a statistical representation of over 50 years of measurements, and are therefore not as well constrained [*Drob et al.*, 2008, 2015; *Hedin et al.*, 1996; *Lalande and Waxler*, 2016; *Picone et al.*, 2002]. This can lead to large discrepancies between predicted and observed infrasound propagation. Current research is being conducted to better constrain the conditions of the atmosphere that can be used in the field of infrasound [e.g. *Drob et al.*, 2015]. Small scale variability from gravity waves and other phenomena are not yet included in the atmospheric modeling, which may produce scattering of acoustic energy into the predicted "shadow zones" predicted by ray theory [*De Angelis et al.*, 2012; *de Groot-Hedlin et al.*, 2008; *De Groot-Hedlin et al.*, 2009; *Le Pichon et al.*, 2010]. An example of this scatter can be seen for some portions of the November 2014 Pavlof eruption where DLL was predicted to be in a shadow zone. However, sound energy still reached the station through diffraction and/or limitations in the atmospheric specifications and ray tracing technique [*Fee and Matoza*, 2013; *Fee et al.*, 2010; *Matoza et al.*, 2011]. Some recent studies such as *Drob et al.* [2013] and *Lalande and Waxler* [2016] have incorporated these small-scale perturbations in order to help explain why signals are frequently detected in classically predicted shadow zones. Physically reasonable representations of gravity wave perturbations can be added stochastically to the atmospheric conditions and used in propagation modeling [*Drob et al.*, 2013]. Some of the discrepancies

and unexplained phenomena we observe may be related to propagation perturbations from gravity waves or other variability.

2.6 Conclusions and Future Work

The AVO-G2S atmospheric specifications will help guide interpretation of infrasound signals observed from volcanoes and other sources at regional to global ranges. This capability will be valuable for volcano monitoring in Alaska, both in retrospective and real-time analyses. In this study, we focus on a few case studies examining remote infrasound data by exploring AVO-G2S guided propagation modeling and its relationship with infrasound observations, such as celerity, traveltime, and trace velocity. It important to consider the limitations of atmospheric reconstruction models like AVO-G2S, which are restricted by the spatial and temporal resolution of the input weather prediction models. Similarly, limitations exist in the propagation modeling such as ray tracing, which may not capture every detail in the atmosphere that affects propagation (e.g. gravity waves). Our findings reiterate that variable atmospheric conditions play a vital role in the propagation of infrasound, and constraining these conditions using modeling techniques similar to those outlined in this study is important for long-range infrasound signal interpretations. We note that even with state-of-the-art atmospheric specifications careful analysis and interpretation of long-range propagation modeling must be used.

Using a combination of array processing, celerity, and propagation modeling in Alaska can help differentiate between propagation paths and refine interpretations of infrasound detections at long-range. We show that the combination of strong tropospheric ducting and extremely low noise at DLL likely contributed to the triggering of the AVO infrasound alarm for the 21 July 2015 Cleveland Volcano explosion. In comparison, the 6 November 2014 Cleveland explosion occurred during a time of strong stratospheric ducting but higher noise levels which prevented a clear detection at DLL. Infrasound propagation during the November 2014 Pavlof eruption was complex, with the propagation paths changing drasti-

cally over the days of the eruption. The changing atmosphere likely played a role in the differences in long-range infrasound observations. Propagation modeling as presented in this study begins to explain temporal changes in long-range infrasound detection for this eruption with stronger signals seen during times when lower atmospheric ducts (tropospheric and stratospheric) form and persist to the range of DLL (see Table 2.2). However, changes in the infrasonic source may have also contributed to the signal observed at DLL. For the Pavlof 2016 eruption, changes in propagation conditions were minimal, with a slight increase in the strength of the stratospheric duct through time. This shows that changes in the DLL infrasound signals were largely representative of the changes in the volcanic tremor source amplitude. Our analysis supports the necessity for a range-dependent, post-processing model to constrain long-distance infrasound propagation to stations like DLL due to rapidly changing atmospheric conditions in Alaska.We also show that for some eruptions, such as Pavlof 2014 and Cleveland 2015, even higher spatial and temporal resolution files might be necessary to constrain the propagation conditions better. These higher resolution North American Mesoscale (NAM) files (up to 2.95 km spatially and hourly) are incorporated into the AVO-G2S model starting in 2017 [*Schwaiger et al.*, 2019].

An increased number of infrasound arrays allows increased opportunities to monitor each volcano from different azimuths, increasing the likelihood that even smaller activity will be detected throughout the entire year. AVO-G2S helps explain why signals are preferentially detected at some arrays and not others, determine if a signal represents more of the source or propagation effects, and allows determination of the most accurately available modeled traveltime and therefore origin time of the event at the volcano. With the use of the open source AVO-G2S program, this can all be done in near-real-time. AVO has used the AVO-G2S on a test-basis for the March 2016 eruption of Pavlof Volcano, as well as the 2016–2017 eruption of Bogoslof Volcano. Future work will include implementing AVO-G2S in real-time to automatically recreate atmospheric conditions and post-process propagation conditions for all volcanoes that show elevated activity. This will provide a quick estimate of the likely

propagation paths to each of AVO's arrays, as well as EarthScope Transportable Array single infrasound stations.

Supplementary data to this article can be found online at `https://doi.org/10.1016/j.jvolgeores.2018.03.009`.

2.7 Acknowledgments

Funding for this study has been provided by the National Science Foundation Grant 1331084 and the Alaska Volcano Observatory. The authors would like to thank David Green, Daniel Bowman, and John Lyons for helpful reviews and comments of this manuscript. We also thank Curt A. L. Szuberla for the array processing code that was modified by the authors, Peter Cervelli for air traffic computations, and Philip Blom for use and discussions on the GeoAc ray tracing code. NCEP Reanalysis data were provided by the NOAA/OAR/ESRL PSD, Boulder, Colorado, USA, from their Web site at `http://www.esrl.noaa.gov/psd/` and ERA-Interim Reanalysis data provided through NCAR/UCAR Research Data Archive at `https://rda/ucar.edu/datasets/ds627.0/`. Observations of volcanic activity were made by AVO and are detailed on its website (`www.avo.alaska.edu`). Any use of trade, firm, or product names is for descriptive purposes only and does not imply endorsement by the U.S. Government.

2.8 References

Amante, C., and B. Eakins (2009), ETOPO1 1 Arc-Minute Global Relief Model: Procedures, Data Sources and Analysis.

Archer, C. L., and K. Caldeira (2008), Historical trends in the jet streams, *Geophysical Research Letters*, *35*(8), doi:10.1029/2008GL033614.

Blom, P. (2014), GeoAc: Numerical Tools to Model Acoustic Propagation in the Geometric Limit, *Los Alamos National Laboratory*.

Brown, D. J., C. N. Katz, R. Le Bras, M. P. Flanagan, J. Wang, and A. K. Gault (2002), Infrasonic signal detection and source location at the prototype International Data Centre, *Pure and Applied Geophysics*, *159*(5), 1081–1125, doi:10.1007/s00024-002-8674-2.

Bureau of Transportation Statistics (2016), Table t-100 segment (all carriers), *Tech. rep.*

Ceranna, L., A. Le Pichon, D. N. Green, and P. Mialle (2009), The Buncefield explosion: a benchmark for infrasound analysis across Central Europe, *Geophysical Journal International*, *177*(2), 491–508, doi:10.1111/j.1365-246X.2008.03998.x.

Dabrowa, A. L., D. N. Green, A. C. Rust, and J. C. Phillips (2011), A global study of volcanic infrasound characteristics and the potential for long-range monitoring, *Earth and Planetary Science Letters*, *310*(3-4), 369–379, doi:10.1016/j.epsl.2011.08.027.

De Angelis, S., D. Fee, M. Haney, and D. Schneider (2012), Detecting hidden volcanic explosions from Mt. Cleveland Volcano, Alaska with infrasound and ground-coupled airwaves, *Geophysical Research Letters*, *39*(21), doi:10.1029/2012GL053635.

de Groot-Hedlin, C. D., and M. A. Hedlin (2014), Infrasound detection of the Chelyabinsk meteor at the USArray, *Earth and Planetary Science Letters*, *402*(C), 337–345, doi:10.1016/j.epsl.2014.01.031.

de Groot-Hedlin, C. D., M. A. H. Hedlin, K. T. Walker, D. P. Drob, and M. A. Zumberge (2008), Evaluation of infrasound signals from the shuttle Atlantis using a large seismic network, *The Journal of the Acoustical Society of America*, *124*(3), 1442–1451, doi:10.1121/1.2956475.

De Groot-Hedlin, C. D., M. A. Hedlin, and D. P. Drob (2009), Atmospheric variability and infrasound monitoring, in *Infrasound Monitoring for Atmospheric Studies*, pp. 475–507, doi:10.1007/978-1-4020-9508-5{_}15.

Dee, D. P., S. M. Uppala, A. J. Simmons, P. Berrisford, P. Poli, S. Kobayashi, U. Andrae, M. A. Balmaseda, G. Balsamo, P. Bauer, P. Bechtold, A. C. Beljaars, L. van de Berg, J. Bidlot, N. Bormann, C. Delsol, R. Dragani, M. Fuentes, A. J. Geer, L. Haimberger, S. B. Healy, H. Hersbach, E. V. Hólm, L. Isaksen, P. Kållberg, M. Köhler, M. Matricardi, A. P. Mcnally, B. M. Monge-Sanz, J. J. Morcrette, B. K. Park, C. Peubey, P. de Rosnay, C. Tavolato, J. N. Thépaut, and F. Vitart (2011), The ERA-Interim reanalysis: Configuration and performance of the data assimilation system, *Quarterly Journal of the Royal Meteorological Society*, *137*(656), 553–597, doi:10.1002/qj.828.

Drob, D. P., J. M. Picone, and M. Garcés (2003), Global morphology of infrasound propagation, *Journal of Geophysical Research: Atmospheres*, *108*(D21), doi:10.1029/2002JD003307.

Drob, D. P., J. T. Emmert, G. Crowley, J. M. Picone, G. G. Shepherd, W. Skinner, P. Hays, R. J. Niciejewski, M. Larsen, C. Y. She, J. W. Meriwether, G. Hernandez, M. J. Jarvis, D. P. Sipler, C. A. Tepley, M. S. O'Brien, J. R. Bowman, Q. Wu, Y. Murayama, S. Kawamura, I. M. Reid, and R. A. Vincent (2008), An empirical model of the Earth's horizontal wind fields: HWM07, *Journal of Geophysical Research: Space Physics*, *113*(12), doi:10.1029/2008JA013668.

Drob, D. P., D. Broutman, M. A. Hedlin, N. W. Winslow, and R. G. Gibson (2013), A method for specifying atmospheric gravity wavefields for long-range infrasound propagation calculations, *Journal of Geophysical Research Atmospheres*, *118*(10), 3933–3943, doi:10.1029/2012JD018077.

Drob, D. P., J. T. Emmert, J. W. Meriwether, J. J. Makela, E. Doornbos, M. Conde, G. Hernandez, J. Noto, K. A. Zawdie, S. E. McDonald, J. D. Huba, and J. H. Klenzing (2015), An update to the Horizontal Wind Model (HWM): The quiet time thermosphere, *Earth and Space Science*, *2*(7), 301–319, doi:10.1002/2014EA000089.

Evers, L., D. Brown, K. Heaney, J. Assink, P. Smets, and M. Snellen (2014), Evanescent wave coupling in a geophysical system: Airborne acoustic signals from the Mw 8.1 Macquarie Ridge earthquake, *Geophysical Research Letters*, *41*(5), 1644–1650, doi:10.1002/2013GL058801.

Evers, L. G., and H. W. Haak (2007), Infrasonic forerunners: Exceptionally fast acoustic phases, *Geophysical Research Letters*, *34*(10), doi:10.1029/2007GL029353.

Fee, D., and R. S. Matoza (2013), An overview of volcano infrasound: From hawaiian to plinian, local to global, *Journal of Volcanology and Geothermal Research*, *249*, 123–139, doi:10.1016/j.jvolgeores.2012.09.002.

Fee, D., A. Steffke, and M. Garces (2010), Characterization of the 2008 Kasatochi and Okmok eruptions using remote infrasound arrays, *Journal of Geophysical Research Atmospheres*, *115*(18), doi:10.1029/2009JD013621.

Fee, D., R. Waxler, J. Assink, Y. Gitterman, J. Given, J. Coyne, P. Mialle, M. Garces, D. Drob, D. Kleinert, R. Hofstetter, and P. Grenard (2013), Overview of the 2009 and 2011 Sayarim Infrasound Calibration Experiments, *Journal of Geophysical Research Atmospheres*, *118*(12), 6122–6143, doi:10.1002/jgrd.50398.

Fee, D., M. M. Haney, R. S. Matoza, A. R. Van Eaton, P. Cervelli, D. J. Schneider, and A. M. Iezzi (2017), Volcanic tremor and plume height hysteresis from Pavlof Volcano, Alaska, *Science*, *355*(6320), 45–48, doi:10.1126/science.aah6108.

Green, D. N., J. Vergoz, R. Gibson, A. Le Pichon, and L. Ceranna (2011), Infrasound radiated by the Gerdec and Chelopechene explosions: Propagation along unexpected paths, *Geophysical Journal International*, *185*(2), 890–910, doi:10.1111/j.1365-246X.2011.04975.x.

Hedin, A. E., E. L. Fleming, A. H. Manson, F. J. Schmidlin, S. K. Avery, R. R. Clark, S. J. Franke, G. J. Fraser, T. Tsuda, F. Vial, and R. A. Vincent (1996), Empirical wind model for the upper, middle and lower atmosphere, *Journal of Atmospheric and Terrestrial Physics*, *58*(13), 1421–1447, doi:10.1016/0021-9169(95)00122-0.

http://mesonet.agron.iastate.edu/ (), Iowa Environmental Mesonet (IEM).

Lalande, J. M., and R. Waxler (2016), The interaction between infrasonic waves and gravity wave perturbations: Application to observations using UTTR rocket motor fuel elimination events, *Journal of Geophysical Research*, *121*(10), 5585–5600, doi:10.1002/2015JD024527.

Le Pichon, A., M. Garcés, E. Blanc, M. Barthélémy, and D. P. Drob (2002), Acoustic propagation and atmosphere characteristics derived from infrasonic waves generated by the Concorde, *The Journal of the Acoustical Society of America*, *111*(1), 629–641, doi:10.1121/1.1404434.

Le Pichon, A., L. Ceranna, M. Garcés, D. Drob, and C. Millet (2006), On using infrasound from interacting ocean swells for global continuous measurements of winds and temperature in the stratosphere, *Journal of Geophysical Research Atmospheres*, *111*(11), doi:10.1029/2005JD006690.

Le Pichon, A., E. Blanc, and A. Hauchecorne (2010), *Infrasound Monitoring for Atmospheric Studies*, Springer.

Matoza, R. S., A. Le Pichon, J. Vergoz, P. Herry, J. M. Lalande, H. i. Lee, I. Y. Che, and A. Rybin (2011), Infrasonic observations of the June 2009 Sarychev Peak eruption, Kuril Islands: Implications for infrasonic monitoring of remote explosive volcanism, *Journal of Volcanology and Geothermal Research*, *200*(1-2), 35–48, doi:10.1016/j.jvolgeores.2010.11.022.

Molod, A., L. Takacs, M. Suarez, J. Bacmeister, I.-S. Song, and A. Eichmann (2012), *NASA / TM – 2012-104606 / Vol 28 Technical Report Series on Global Modeling and Data Assimilation , Volume 28 The GEOS-5 Atmospheric General Circulation Model : Mean Climate and Development from MERRA to Fortuna April 2012*, vol. 28.

Molteni, F., R. Buizza, T. N. Palmer, and T. Petroliagis (1996), The ECMWF ensemble system: Methodology and validation, *Q. J. Roy. Meteor. Soc.*, *122*, 73–119.

Nippress, A., D. N. Green, O. E. Marcillo, and S. J. Arrowsmith (2014), Generating regional infrasound celerity-range models using ground-truth information and the implications for event location, *Geophysical Journal International*, *197*(2), 1154–1165, doi:10.1093/gji/ggu049.

Picone, J. M., A. E. Hedin, D. P. Drob, and A. C. Aikin (2002), NRLMSISE-00 empirical model of the atmosphere: Statistical comparisons and scientific issues, *Journal of Geophysical Research: Space Physics*, *107*(A12), doi:10.1029/2002JA009430.

Pierce, A. (1981), *Acoustics: An Introduction to its Physical Principles and Applications*, McGraw-Hill, New York.

Rogers, P., and J. Gardner (1980), Propagation of sonic booms in the thermosphere, *Journal of the Acoustical Society of America*, *67*(1), 78–91.

Salomons, E. (2001), *Computational Atmospheric Acoustics*, 335 pp., Kluwer Academic Publishers, Dordrecht, The Netherlands.

Schwaiger, H., A. Iezzi, and D. Fee (2019), AVO-G2S: A modified, open-source Ground-to-Space atmospheric specification for infrasound modeling, *Computers and Geosciences*, *125*, 90–97, doi:10.1016/j.cageo.2018.12.013.

Schwaiger, H. F., R. P. Denlinger, and L. G. Mastin (2012), Ash3d: A finite-volume, conservative numerical model for ash transport and tephra deposition, *Journal of Geophysical Research: Solid Earth*, *117*(4), doi:10.1029/2011JB008968.

Sutherland, L. C., and H. E. Bass (2004), Atmospheric absorption in the atmosphere up to 160 km, *The Journal of the Acoustical Society of America*, *115*(3), 1012–1032, doi:10.1121/1.1631937.

Szuberla, C. A. L., and J. V. Olson (2004), Uncertainties associated with parameter estimation in atmospheric infrasound arrays, *The Journal of the Acoustical Society of America*, *115*(1), 253–258, doi:10.1121/1.1635407.

Waxler, R., C. Hetzer, D. Velea, J. Assink, P. Blom, and J. Lonzaga (2015), Atmospheric Infrasound Propagation Package Version 1.1 Extension and Finalization NCPA Infrasound Propagation Modeling Package.

Waxler, R., J. Assink, and D. Velea (2017), Modal expansions for infrasound propagation and their implications for ground-to-ground propagation, *The Journal of the Acoustical Society of America*, *141*(2), 1290–1307, doi:10.1121/1.4976067.

Waythomas, C. F., M. M. Haney, D. Fee, D. J. Schneider, and A. Wech (2014), The 2013 eruption of Pavlof Volcano, Alaska: a spatter eruption at an ice- and snow-clad volcano, *Bulletin of Volcanology*, *76*(10), doi:10.1007/s00445-014-0862-2.

Werner, C., C. Kern, D. Coppola, J. J. Lyons, P. J. Kelly, K. L. Wallace, D. J. Schneider, and R. L. Wessels (2017), Magmatic degassing, lava dome extrusion, and explosions from Mount Cleveland volcano, Alaska, 2011–2015: Insight into the continuous nature of volcanic activity over multi-year timescales, *Journal of Volcanology and Geothermal Research*, *337*, 98–110, doi:10.1016/j.jvolgeores.2017.03.001.

www.avo.alaska.edu (), Alaska Volcano Observatory.

Chapter 3

Three-Dimensional Acoustic Multipole Waveform Inversion at Yasur Volcano, Vanuatu[5]

3.1 Abstract

Acoustic waveform inversions can provide estimates of volume flow rate and erupted mass, enhancing the ability to estimate volcanic emissions. Previous studies have generally assumed a simple acoustic source (monopole); however, more complex and accurate source reconstructions are possible with a combination of equivalent sources (multipole). We deployed a high-density acoustic network around Yasur volcano, Vanuatu, including acoustic sensors on a tethered aerostat that was moved every ∼15-60 minutes. Using this unique dataset we invert for the acoustic multipole source mechanism using a grid-search approach for 80 events to examine volume flow rates and dipole strengths. Our method utilizes Finite-Difference Time-Domain modeling to obtain the full 3-D Green's functions that account for topography. Inversion results are compared using a monopole-only, multipole (monopole and dipole), simulations that do not include topography, and those that use a subset of sensors. We find that the monopole source is a good approximation when topography is considered. However, initial compression amplitude is not fully captured by a monopole source so source directionality cannot be ruled out. The monopole solution is stable regardless of whether a monopole-only or multipole inversion is performed. Inversions for the dipole components produce estimates consistent with observed source directionality, though these inversions are somewhat unstable given station configurations of typical deployments. Our results suggest infrasound waveform inversion shows promise for realistic quantitative source estimates, but additional work is necessary to fully explore inversion stability, uncertainty, and robustness.

[5]Iezzi, A.M., Fee, D., Kim, K., Jolly, A.D., and Matoza, R.S. (2019). Three-Dimensional Acoustic Multipole Waveform Inversion at Yasur Volcano, Vanuatu *Journal of Geophysical Research: Solid Earth*, 124.

3.2 Introduction

Volcanic eruptions emit a considerable amount of acoustic energy in the infrasonic band (acoustic signals < 20 Hz) with minimal absorption that can be recorded from local (<15 km) to global (>250 km) distances and used to detect, locate, and quantify volcanic emissions in real-time [e.g. *Fee and Matoza*, 2013; *Matoza et al.*, 2019]. Acoustic waveform inversions can provide estimates of volume flow rate and mass eruption rate (MER), which are invaluable parameters for volcano monitoring and ash transport models [*Fee et al.*, 2017; *Kim et al.*, 2015]. Similar methods can be applied to anthropogenic sources to estimate explosion yield [*Kim and Rodgers*, 2016].

Acoustic signals from volcanic explosions comprise the source as well as propagation effects the wave encounters along the path from the source to receiver (e.g. topography, atmospheric conditions). Proper modeling of these propagation effects allows the unknown acoustic source parameters of the explosion to be recovered from the recorded waveforms [e.g. *Kim et al.*, 2015]. While some studies have shown that atmospheric conditions can be retrieved from acoustic waveforms [e.g. *Johnson et al.*, 2012; *Ortiz et al.*, 2018], they are often assumed to have negligible impact on the acoustic waveforms at local distances of less than a few kilometers [e.g. *Fee et al.*, 2017; *Johnson and Miller*, 2014; *Kim et al.*, 2015]. However, numerous studies [e.g. *Fee et al.*, 2017; *Kim and Lees*, 2014; *Kim et al.*, 2015; *Lacanna and Ripepe*, 2013; *Matoza et al.*, 2009] have established that the local topography of a volcanic edifice can affect the recorded waveforms and therefore the calculation of mass flow rate via waveform source inversion. Therefore, it is important to account for topography in acoustic source inversions for locations with intricate topographic features (i.e. most volcanoes).

Previous volcanic studies have generally assumed a simple volumetric acoustic source (monopole), however more complex and accurate source reconstructions can be estimated using a combination of pressure fluctuations from volume changes and shifts in momentum of a fluid (multipole) [*Johnson et al.*, 2008; *Kim et al.*, 2012]. The actual acoustic source is likely dependent on the type of volcanic activity, where blast-type explosions may be best

represented by a simple volumetric source [*Fee and Matoza*, 2013; *Fee et al.*, 2017; *Johnson*, 2003; *Kim et al.*, 2015; *Matoza et al.*, 2014; *Woulff and McGetchin*, 1976], while sustained eruptions likely have a more complicated mechanism similar to jet noise [*Matoza et al.*, 2009, 2013].

Our study aims to determine if acoustic directionality is resolvable and explore the stability of both monopole and multipole source inversions of discrete explosions of Yasur volcano by sampling the wavefield in both the horizontal and vertical directions. Our deployment consists of a traditional deployment of infrasound sensors on the ground surface, as well as a sensor onboard a tethered aerostat that was fixed at various locations around the volcanic crater, capturing explosions from a variety of azimuths and inclinations [*Jolly et al.*, 2017]. We use Finite-Difference Time-Domain (FDTD) modeling to obtain the full 3-D Green's functions for each propagation path from source to receiver. This method, following *Kim and Lees* [2014], takes into account realistic topography based on a high-resolution digital elevation model created using structure-from-motion techniques. We then invert for the minimum error solution source location and acoustic source mechanism using a grid-search approach [*Kim et al.*, 2015]. We perform this inversion for 80 events from the two vents of Yasur to examine the source characteristics of the vents, including an infrasound-derived volume flow rate as a function of time and acoustic radiation directionality after the influences of topography are removed.

3.3 Background

3.3.1 Acoustic Multipole Sources

A well-constrained acoustic source inversion requires extensive station coverage in order to fully sample the wavefield [*Kim et al.*, 2012]. If the acoustic source region is compact (small compared to the wavelength of interest), the source can be represented as a sum of equivalent point sources [*Kim et al.*, 2012; *Matoza et al.*, 2013]. An acoustic multipole source mechanism is a combination of pressure fluctuations from monopole, dipole, and quadrupole

sources [*Lighthill*, 1952]. A monopole (or simple) source represents the net change of mass flow rate in a compact source region. *Lighthill* [1978] defines the pressure at time t and distance r resulting from a monopole source as

$$p(t,r) = \frac{\dot{S}(t - r/c)}{4\pi r} \tag{3.1}$$

where $\dot{S}$ is the source strength (rate of change of the mass flow rate) and c is the speed of sound. The monopole generates sound that radiates equally in all directions (Figure 3.1a). The dipole source is equivalent to force or momentum changes within the fluid (i.e. no net introduction of fluid) and can be represented by two closely spaced (with respect to the acoustic wavelength) monopoles that are out of phase by 180° (Figure 3.1b). The acoustic dipole results in directivity of the acoustic radiation pattern, where there is zero pressure change orthogonal to the dipole axis and the maximum pressure change exists at the dipole axis [*Johnson et al.*, 2008; *Lighthill*, 1952]. Dipole source mechanisms are less efficient than a monopole source since the two alternating simple sources have a combined radiation pattern that cancels much of the radiated energy [*Kim et al.*, 2012; *Lighthill*, 1952]. Dipole sources can be combined to form higher order source terms (lateral and longitudinal quadrupoles, etc.). In this study, we focus on the monopole and dipole components and refer to their combination as a multipole.

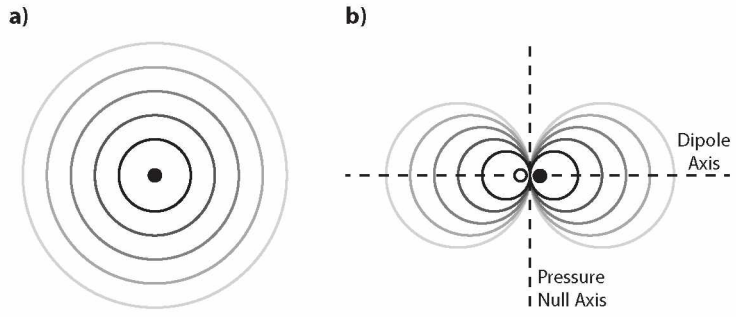

Figure 3.1: Radiation pattern of an acoustic a) monopole and b) dipole. Black and white circles represent positive and negative monopole sources, respectively.

Volcanoes erupt in a variety of styles including lava fountaining and effusive activity

(Hawaiian), discrete blasts (Strombolian and Vulcanian), and high-energy sustained ash emissions (Subplinian-Plinian). While impulsive, blast-type volcanic explosions such as those common to Yasur volcano have been shown to be well approximated by a monopole source [e.g. *Fee and Matoza*, 2013; *Fee et al.*, 2017; *Johnson*, 2003; *Kim et al.*, 2015; *Witsil and Johnson*, 2018; *Woulff and McGetchin*, 1976], higher order acoustic terms might also be present and provide valuable information about the eruption [*De Angelis et al.*, 2016; *Johnson et al.*, 2008].

Multipole radiation can be expressed as a combination of a monopole, horizontal dipole, and vertical dipole [*Johnson et al.*, 2008; *Kim et al.*, 2012]. The vertical dipole has previously been neglected for many studies of volcanic eruptions due to infrasound sensors only being placed on the Earth's surface [*Matoza et al.*, 2013]. *Johnson et al.* [2008] solved for a sub-vertical dipole orientation where sensors located on the crater rim were above the crater floor. Studies such as *McKee et al.* [2017] and *Rowell et al.* [2014] have taken advantage of surrounding topography for network deployments at Aso and Karymsky volcanoes, respectively, in order to improve vertical coverage of infrasound sensors; however, not all volcanoes have the advantage of nearby high relief topography. This study, for the first time, incorporates the vertical dipole component using acoustic data collected on a tethered aerostat, which has great flexibility for sensor location and may sample closer to a hypothetical vertical dipole axis.

3.3.2 Acoustic Source Inversion

Waveform inversion techniques allow the construction of quantitative source models for a wide range of volcanic processes and hence have become popular for the studies of both seismic [e.g. *Chouet et al.*, 2005; *Ohminato et al.*, 1998] and acoustic [e.g. *Johnson et al.*, 2008; *Kim et al.*, 2012, 2015] data. Previous infrasound studies have assumed monopole [e.g. *Fee et al.*, 2017; *Johnson and Miller*, 2014; *Kim and Lees*, 2011; *Kim et al.*, 2015], dipole [e.g. *Caplan-Auerbach et al.*, 2010; *Lamb et al.*, 2015], and multipole [e.g. *De Angelis et al.*,

2016; *Johnson et al.*, 2008; *Kim et al.*, 2012] source mechanisms. Additionally, many studies have compared infrasound-derived gas volumes with UV camera data [e.g. *Dalton et al.*, 2010; *Delle Donne et al.*, 2016], visual camera [e.g. *Johnson and Miller*, 2014; *Witsil and Johnson*, 2018], thermal imagery [e.g. *De Angelis et al.*, 2016], and ground-based [e.g. *Fee et al.*, 2017] and satellite [e.g. *Albert et al.*, 2015] ash and gas emission estimates. These multidisciplinary studies have allowed for greater insight into the acoustic source mechanism by using independent measures to compare with the infrasound results. However, these comparisons are complicated by the fact that all methods have their own inherent assumptions and associated errors.

A few studies have inverted for the combined monopole and dipole source mechanism, though none have incorporated the effects of topography and numerical Green's functions. *Johnson et al.* [2008] inverted for the volume flux of a volcanic explosion using the monopole-only, dipole-only, and multipole source mechanisms for lava lake explosions at Mt. Erebus, Antarctica. They found that the initial tearing of the bubble membrane likely radiated as a dipole source that transitions into a predominantly monopole source as the bubble membrane is fully compromised. *Kim et al.* [2012] performed multipole (monopole and dipole) source inversions for explosions at Tungurahua volcano, Ecuador and concluded that the observed strong directivity of infrasound radiation can be explained by an "effective dipole" largely resulting from volcanic crater topography preferentially directing the sound radiation.

At local distances, topography can alter the recorded acoustic waveforms. Therefore, constraining the effects of topography has proven important for acoustic source inversions [*Kim and Lees*, 2014; *Kim et al.*, 2015]. The FDTD code used in this study to constrain topographic influences was first published in *Kim and Lees* [2011], where diffraction of acoustic waves on the vent rim edge was observed both in recorded and synthetically-produced waveforms at Karymsky volcano, Russia. *Lacanna and Ripepe* [2013] used a FDTD method in 2-D cartesian coordinates to constrain the influence of topography on the acoustic wavefield assuming a simple monopole source. *Kim and Lees* [2014] incorporated a digital elevation

model for the FDTD forward model to calculate the full 3-D Green's functions, finding that including effects of topography can improve reverse time modeling techniques for source localization. *Kim et al.* [2015] then used the updated FDTD forward model methods from *Kim and Lees* [2014] and source inversion work by *Kim et al.* [2012] to invert for the monopole source-time function, finding that a monopole source was sufficient to accurately model explosions at Sakurajima volcano, Japan. *Kim et al.* [2012] and *Lacanna and Ripepe* [2013] showed that neglecting topography for acoustic waveform inversions can lead to large source estimation errors and should therefore be accounted for. More recently, the methods laid out in *Kim et al.* [2015] were extended to determine total erupted mass and then compared with independent estimates derived from ash collection systems and gas measurements by *Fee et al.* [2017], finding good agreement between the two methods.

While previous work has focused on quantifying the volume and mass flow rates for volcanic eruptions, a multipole acoustic waveform inversion that includes both the vertical dipole component and accounts for 3-D topography simultaneously has not been performed. Here we build upon these previous studies by using the inversion method of *Kim et al.* [2015] and including the multipole source. By accounting for topography to create the synthetic waveforms, we can examine how much of the observed directive radiation pattern [*Jolly et al.*, 2017] is due to topography or source directivity (i.e. a dipole source mechanism), a problem evident in *Kim et al.* [2012] that has remained undetermined.

3.3.3 Yasur volcano, Vanuatu

Yasur volcano (360 m above sea level) is a basaltic to basaltic-andesitic scoria cone located on the island of Tanna, Vanuatu. Activity is characterized by continuous gas emissions punctuated by frequent Strombolian to Vulcanian explosive activity for at least the past 300 years [*Simkin et al.*, 1981]. Eruption rates at Yasur are high, with up to several explosions per minute [*Battaglia et al.*, 2016a; *Meier et al.*, 2016]. Passive degassing composition differs from that of gases released by explosions, suggesting explosions are driven by deep volatile

exsolution [*Métrich et al.*, 2011], which is typical for volcanoes with Strombolian activity. The 400-m wide summit crater is divided into two sub-craters, North (Vent C) and South (Vents A and B) (Figure 3.2). Yasur's multiple vents are thought to come from a single homogeneous magma supply based on seismic [*Kremers et al.*, 2013] and petrologic [*Kremers et al.*, 2012] evidence. Yasur is a prolific and reliable source of infrasound which is regularly detected as far as 600 km and used to validate and update wind models [*Assink et al.*, 2014; *Le Pichon et al.*, 2005]. A number of recent studies have focused on seismic and infrasound signals at Yasur volcano and their relation to other multidisciplinary datasets including UV, thermal imagery, and Doppler radar [e.g. *Battaglia et al.*, 2016b,a; *Jolly et al.*, 2017; *Kremers et al.*, 2013; *Marchetti et al.*, 2013; *Meier et al.*, 2016].

3.4 Methods

3.4.1 Data Collection

The field campaign at Yasur occurred in July to August 2016 and was a joint effort between the University of Alaska Fairbanks (UAF), University of California Santa Barbara (UCSB), GNS New Zealand, University of Canterbury in New Zealand, and the Vanuatu Meteorology and Geohazards Department. We focus on data from six ground-based Chaparral Physics Model 60 UHP infrasound sensors, five located around the crater rim (YIF1-5) and one $\sim$1 km from the vent (YIB2.1) (Figure 3.2). An infraBSU-type sensor was deployed on the aerostat. This sensor uses a MEMS transducer with an operation similar to that described in *Marcillo et al.* [2012]. Because the aerostat sensor was in a different location for every explosion, we name them as separate stations (and therefore events) as YBAL.3(vent)(event number). Chaparral Physics Model 60 UHP infrasound sensors have a flat response between 33 s to Nyquist and pressure range of $\pm$1000 Pa, and were sampled at 400 Hz. The BSU-type sensor with flat response from 30 s to Nyquist on the aerostat were sampled at 200 Hz. Infrasound data were digitized using the Omnirecs DATA-CUBE digitizers.

The aerostat operated from July 29th to August 1st, 2016 during the daytime hours

and was moved every 15-60 minutes to a new stationary tether position. By the end of the experiment, the aerostat occupied 38 loiter positions that spanned ~200° in azimuth and 50° in takeoff angle (defined as the angle viewed from the eruption crater with vertical equal to 90°) [*Jolly et al.*, 2017]. The five crater stations spanned an azimuth of 207°. Unfortunately, a sixth crater station (YIF6.1) located to the northwest side only had data for July 28th to July 29th, leaving an azimuthal gap in acoustic wavefield coverage for nearly the entire experiment when the tethered aerostat sensor was deployed. Therefore, we do not use YIF6.1 in our study as we favor data collected aboard the tethered aerostat. In addition to the acoustic equipment, the campaign included 8 broadband seismometers, an unmanned aerial vehicle (UAV) supplemented by survey-grade GPS, high-definition video, multi-angle GoPro video, forward looking infrared camera (FLIR), and Fourier transform infrared spectroscopy (FTIR). However, we focus only on infrasound data in this study. *Jolly et al.* [2017] describe the details on the aerostat deployment and observations.

3.4.2 Digital Elevation Model (DEM) Creation

At local distances, previous studies have indicated that topography can largely affect acoustic waveforms [e.g. *Kim and Lees*, 2011, 2014; *Kim et al.*, 2015]. Therefore we can investigate source dynamics once topography is considered in the modeling using an accurate digital elevation model (DEM). However, obtaining a high-resolution DEM at active volcanoes is challenging. DEMs derived using visible band sensors are generally the most cost effective and feasible options for a remote island (Tanna, Vanuatu) and a highly active volcano (Yasur, explosions every 1-4 minutes), but the images we acquired for Yasur were obscured by both meteorological and volcanic clouds in the vent region. Additionally, the crater morphology can change over short periods of time due to the frequent explosions, thus requiring a DEM acquired near the time of the experiment. To account for this we combined DEMs created by i) an unmanned aerial vehicle (UAV) using structure-from-motion techniques within the crater (resolution 1.5 m); ii) Worldview02 satellite stereo pairs collected

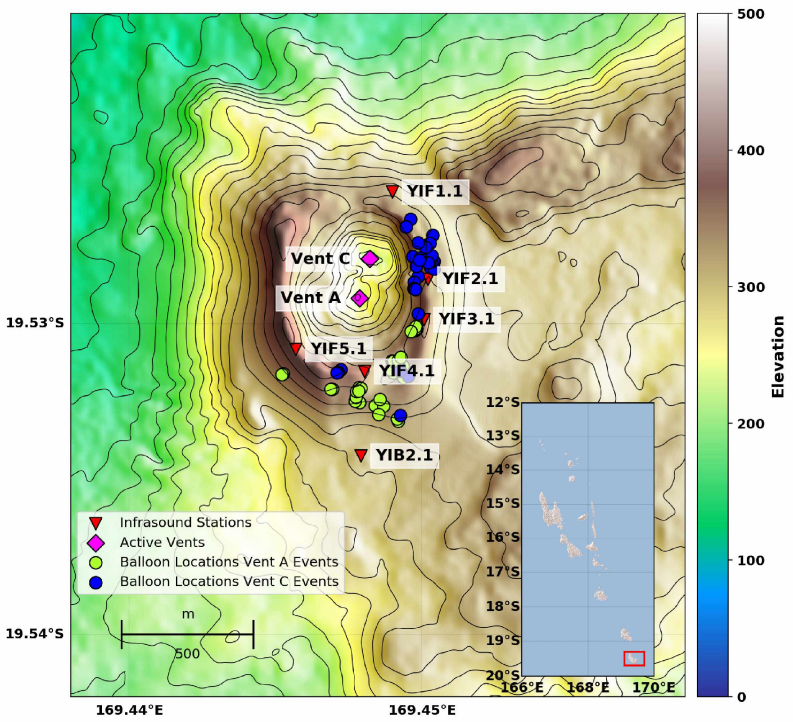

Figure 3.2: Yasur location map and sensor deployment. The volcanic edifice is represented by the digital elevation model using 20-meter contour intervals. Red inverted triangles represent infrasound stations used in this study, pink diamonds represent active vents (Vent C is north and Vent A is south), and green and blue circles show the aerostat locations in the x-y plane for the Vent A and Vent C explosions used in this study, respectively. Inset shows the location of Yasur volcano in the Vanuatu archipelago.

on 26 September 2012 around the volcanic edifice (resolution 2 m); and iii) ASTER Global (resolution 29 m) further out from the crater and within the holes of the Worldview-derived DEM where clouds (both volcanic and meteorological) existed. These three DEMs were stitched together and smoothed in order to create a composite DEM. In the crater area where infrasound is most affected by topography, resolution was ∼2 m. For computational reasons, the entire combined DEM was evenly resampled using 2 m grid spacing.

3.4.3 Inverse Model for the Acoustic Multipole Source Mechanism

The inversion method here follows that first proposed by *Kim et al.* [2015], which minimizes the misfit between the data and synthetic waveforms for a grid of trial source nodes over an assumed source region. We simulate the full 3-D numerical Green's functions (i.e. re-

sponse from a simple source to receiver) for a monopole and horizontal and vertical dipole using Finite-Difference Time-Domain (FDTD) modeling by solving a set of first-order, velocity-pressure coupled differential equations [*Kim and Lees*, 2011; *Ostashev et al.*, 2005]. The FDTD modeling follows *Kim and Lees* [2014] which incorporates the use of a DEM to account for realistic topography and uses a graphics processing unit (GPU)-based approach in a compute unified device architecture (CUDA) environment, with compilation of the codes done using nvcc (NVIDIA compiler for CUDA-enabled codes). A simple source (Blackman Harris window function) with a cutoff frequency of 10 Hz is propagated over the aforementioned DEM (section 3.2). Earth's surface is treated as a rigid boundary, though in reality some energy is likely absorbed [*Kim et al.*, 2012]. The Perfectly Matched Layers (PML) technique is employed at the other model boundaries to create an absorbing boundary and remove reflections. The model grid is 2.2 x 2.4 x 0.5 km with spacing of 2 m. This corresponds to 22 grid nodes per shortest wavelength in our filtered data (0.1-8 Hz), which is greater than the recommended minimum of 10 grid nodes [*Wang*, 1996]. We use a grid-search over 15x15 points with nodes spaced 15 m apart for the likely source location and pin these points to the DEM surface. Green's functions are computed for a duration of 6 s with a time step 0.001 s, which is long enough for the source to propagate well past all stations in the deployment. Sound speed and air density are assumed to be homogeneous at 346.4 m/s and 1.18 kg/m^3, respectively, based on a representative temperature value collected during the field campaign. Our method ignores wind and nonlinear behavior, which we examine further in the discussion section.

Acoustic pressure $p(\mathbf{x_r}, t)$ at distance $\mathbf{x_r}$ and time t can be represented by a monopole (mass flow rate) and the x, y, and z components of a dipole force given by *Pierce* [1989]

$$p(\mathbf{x_r}, t) = G(\mathbf{x_r}, t; \mathbf{x_s}) * \frac{\partial S(t)}{\partial t} + \frac{\partial G(\mathbf{x}, t; \mathbf{x_s})}{\partial x_s} * F_x(t) + \frac{\partial G(\mathbf{x}, t; \mathbf{x_s})}{\partial y_s} * F_y(t) + \frac{\partial G(\mathbf{x}, t; \mathbf{x_s})}{\partial z_s} * F_z(t) \tag{3.2}$$

where $G(\mathbf{x_r}, t; \mathbf{x_s})$ is the Green's function for a monopole, and $\mathbf{x_r}$ and $\mathbf{x_s}$ are the receiver and

source position, respectively. Here, $S(t)$ is the mass flow rate at the source, and $F_x(t)$, $F_y(t)$, and $F_z(t)$ are the time histories of forces in x, y, and z directions, respectively. $\partial/\partial x_s$, $\partial/\partial y_s$, and $\partial/\partial z_s$ denote partial derivatives with respect to the source coordinate. The reader is referred to *Morse and Ingard* [1986] and *Kim et al.* [2012] for details on the monopole and dipole source mechanisms.

According to Equation 3.2, the Green's functions for an arbitrary dipole, F_x, F_y, and F_z, can be defined by the spatial derivative of the monopole Green's function.

$$D_x \equiv \frac{\partial G(\mathbf{x_r}, t; \mathbf{x_s})}{\partial x_s} \tag{3.3}$$

$$D_y \equiv \frac{\partial G(\mathbf{x_r}, t; \mathbf{x_s})}{\partial y_s} \tag{3.4}$$

$$D_z \equiv \frac{\partial G(\mathbf{x_r}, t; \mathbf{x_s})}{\partial z_s} \tag{3.5}$$

For the grid search method, the Green's functions G, D_x, D_y, and D_z can be determined by 3-D numerical simulation for every possible source location, which is computationally very expensive. Here, we use the reciprocal property of the Green's function [*Morse and Ingard*, 1986] to reduce the number of simulations. The reciprocity theorem leads to

$$G(\mathbf{x}, t; \mathbf{x_s}) = G(\mathbf{x_s}, t; \mathbf{x}) \tag{3.6}$$

$$\frac{\partial G(\mathbf{x}, t; \mathbf{x_s})}{\partial x_s} = \frac{\partial G(\mathbf{x_s}, t; \mathbf{x})}{\partial x_s} \tag{3.7}$$

Therefore, instead of running 225 numerical simulations for the monopole Green's functions at the 15x15 source grid, we can obtain the same Green's functions by only 7 simulations with a source at each receiver position. In addition, the dipole Green's functions can be calculated by spatial differentiation of the monopole Green's functions without additional simulations. The spatial derivatives of the Green's function can be further converted to temporal derivatives of particle motions by the first-order equation of motion [*Morse and*

Ingard, 1986] that leads to

$$\frac{\partial p(\mathbf{x},t)}{\partial x} = -\rho(\mathbf{x})\frac{\partial v_x(\mathbf{x},t)}{\partial t} \tag{3.8}$$

where $\rho(\mathbf{x})$ is the density, and $v_x(\mathbf{x_s},t;\mathbf{x})$ is the x component of acoustic particle velocity. By substituting Equation 3.8 in Equation 3.6, the dipole Green's function can be rewritten as

$$D_x = \frac{\partial G(\mathbf{x_s},t;\mathbf{x})}{\partial x_s} = -\rho(\mathbf{x_s})\frac{\partial v_x(\mathbf{x_s},t;\mathbf{x})}{\partial t} \tag{3.9}$$

and substituted back into Equation 3.2 and similarly for the other two components (y and z). Because the output of numerical simulation is a time series, temporal differentiation is often more straightforward than spatial differentiation which requires additional time series at adjacent grid points. The model simulations output a pressure time history response to the Blackman Harris window function source recorded at the station, which we refer to as the 3D Green's functions, similar to previous studies [e.g. *Fee et al.*, 2017; *Kim et al.*, 2015].

We perform a linearized waveform inversion using the observed acoustic data and Green's functions calculated in the previous steps to solve for the source location and multipole (monopole and dipole simultaneously) source-time function using a grid-search approach. Building on the methods of *Kim et al.* [2015] we use a simple rearranged version of Equation 3.2

$$\begin{bmatrix} G & D_x & D_y & D_z \end{bmatrix} \begin{bmatrix} \dot{S} \\ F_x \\ F_y \\ F_z \end{bmatrix} = \mathbf{Gm} = \mathbf{d} \tag{3.10}$$

where $\mathbf{m}$ is the solution vector of the mass flow rate and forces, $\mathbf{G}$ is the matrix representing the monopole and dipole Green's functions calculated from the FDTD forward model, and $\mathbf{d}$ is the observed acoustic pressures. Data are band-pass filtered between 0.1 and 8 Hz using a zero-phase filter and a window length of 5.5 s after the explosion onset. We zero each trace prior to the explosion onset and allow for slight discrepancies in arrival time at

the stations (e.g. unaccounted for winds, temperature, station/vent location) by allowing a cross-correlation time-shift between Green's functions and observations of up to 0.04 seconds (a similar study by *Fee et al.* [2017] used 0.5 s).

The source location is determined by calculating the waveform misfit (residual) for the inversion using each grid point as the source location by solving the following equation using a LSQR iterative solver for linear equations.

$$R = \frac{(\mathbf{d} - \mathbf{Gm})^T(\mathbf{d} - \mathbf{Gm})}{\mathbf{d}^T\mathbf{d}} \tag{3.11}$$

The grid point with the minimum residual is chosen as the preferred source location on the surface of the DEM. We perform the grid-search inversion for the monopole-only source and use the grid point with the minimum residual as the source location for the multipole inversions. The inversion produces the expected synthetic acoustic waveform in Pascals (Pa) at each station as well as the associated solution vector, or mass flow rate $S(t)$ in kg/s, at the source. This mass flow rate is simply converted to a volume flow rate of displaced air [e.g. *Fee et al.*, 2017; *Johnson et al.*, 2008] using

$$V(t) = \frac{1}{\rho_{air}} * S(t) \tag{3.12}$$

where $\rho_{air} = 1.18 kg/m^3$. Finally, we apply a simple linear trend correction to the final volume flow rate, detailed in the following section (section 3.4.4).

3.4.4 Signal Conditioning

For volcanic explosions, the recorded infrasound waveform's integrated compression (positive pressure) is not necessarily equivalent to that of the rarefaction (negative pressure). Therefore, while infrasound traces may taper to zero after an explosion has ceased, the integrated pressure (flow rate) may not go to zero after the explosion signal has ended. Consequently, the twice integrated pressure (cumulative flow rate) does not plateau, as it should

under a linear assumption as mass is assumed to no longer be ejected from the vent. *Johnson and Miller* [2014] propose a signal correction technique, Finite Window Zero Pressure Zero Flux (FWZPZF), to mitigate the offset by performing a linear detrend on each station's waveform prior to performing the inversion. The detrend point for each station occurs where the integrated flow rate returns to zero. This method is effective at removing the flow rate offset, but the detrend for each station is applied to waveforms prior to the inversion that contains both source and path effects. It is not viable for our multi-station, grid-search inversion incorporating numerical Green's functions and could lead to potential errors. *Kim et al.* [2015] removes the linear trend from the flow rate after the inversion, but does not explore how this compares to the results following *Johnson and Miller* [2014] exactly. *Fee et al.* [2017] apply a linear detrend and demean to six stations using a different start and endpoint for each station following *Johnson and Miller* [2014]. However, this simple detrend does not appear to bring the flow rate back to zero for all of the 49 explosions examined [see Figure 3 in *Fee et al.*, 2017]. *Anderson et al.* [2018] use a slightly different method for detrending where the optimal drift minimizes the L2 norm of the estimated flow rate:

$$q_t = H_{ij}(p_j - mt_j) \tag{3.13}$$

where q_t is the mass flow rate, H_{ij} is the ordinary-least squares generalized inverse of the Green's functions, p_j is the recorded pressure, m is the slope of the instrument drift, and t_j is time.

Here we propose a linear detrend on the post-inversion flow rate that yields similar results to the FWZPZF method and does not rely on detrending the raw waveforms. We choose the first substantial increase in flow rate to be the start point for the linear detrend, and the last value in the flow rate to be the end point of the detrend. We compare linear detrending both pre- and post-acoustic source inversion for an example explosion at Yasur in Figure 3.3. The linear trend correction both pre- and post-inversion yields similar cumulative flow rates that

level off after the explosion has ceased (as compared with the uncorrected inversion result). This figure also illustrates the necessity of detrending acoustic inversion results in general.

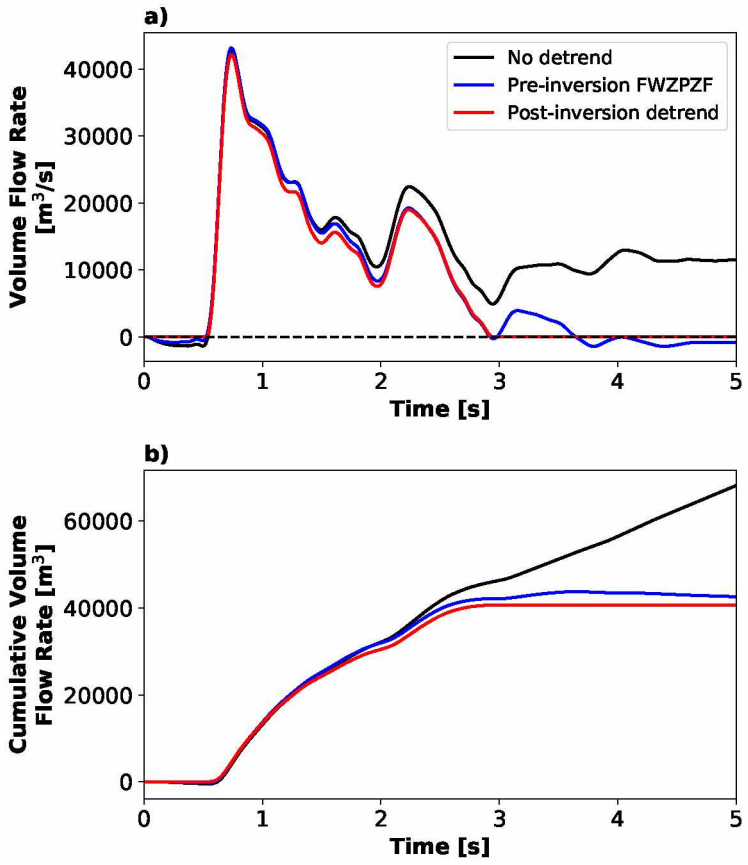

Figure 3.3: Comparison of linear detrending pre- and post-inversion for an example Vent C explosion. a) Shows the volume flow rate and b) shows the cumulative volume, both as a function of time. The output of our inversion model without modification is shown in black, the inversion using the FWZPZF method of *Johnson and Miller* [2014] is shown in blue, and our proposed post-inversion linear correction is shown in red.

3.4.5 Event Selection

We select a limited number of explosions for inversion due to the high level of activity during the campaign and the computational cost of running the FDTD forward model for each of the aerostat sensor locations. Because the aerostat station location was different for each explosion, the Green's functions had to be uniquely calculated for each explosion. Out of the entire infrasound dataset, we only searched for explosions during times when the

aerostat station was tethered (and therefore the sensor location was well-constrained). To select events we apply a simple recursive STA/LTA (length of short term average window = 0.005 s, length of long term average window = 0.15 s) on the aerostat sensor data using a trigger threshold of 8, yielding a total of 201 events. Events are distinguished between the north and south crater based on the arrival times at the crater stations, which was later confirmed in the grid-search inversion discussed in Section 3.3. We then select 40 events for each vent and ensure a wide distribution of aerostat locations (Figure 3.2). We examine each event to confirm that the waveforms taper to zero and only one event is present during the 6 s time window. We see the same transition from predominantly Vent C (North crater) to Vent A (South crater) eruptions on August 1st mentioned in *Jolly et al.* [2017].

3.4.6 Evaluation of the Dipole Component

To help evaluate the significance of each dipole component (x, y, and z) to the source inversion, we calculate the Akaike Information Criterion (AIC). AIC evaluates the significance of free parameters in an inversion while imposing a penalty for increasing the number of model parameters to discourage over-fitting the data. We follow the formula used in *Ohminato et al.* [1998]

$$AIC = N * log(S) + 2r \tag{3.14}$$

where N is the number of data points, S is the squared error for the whole waveform, and r represents the number of free parameters. AIC is a relative calculation in which the lowest AIC should be the ideal number of model parameters. We note that while adding the force components to a moment tensor inversion in seismology (i.e. going from 6 to 9 free parameters) is an increase in number of parameters by 50%, our multipole acoustic inversion increases the number of free parameters from 1 (monopole only) to 4 (monopole and three dipole components), which is an increase in number of parameters in the inversion by 400%.

To further evaluate the dipole component and determine whether or not the inferred dipole vector has a dominant direction, we draw similarities with particle motion in seismol-

ogy. We use rectilinearity [*Montabetti and Kanasewich*, 1970], defined as

$$F_r = 1 - \frac{\lambda_2}{\lambda_1} \tag{3.15}$$

where λ_1 is the principal eigenvalue (i.e. a measure of the long axis) and λ_2 is the second eigenvalue (i.e. a measure of the short axis). This equation yields results between 0 and 1, where $F_r = 1$ represents purely rectilinear motion. We set a threshold based on visual inspection of $F_r \geq 0.65$ to distinguish between events that have a dominant dipole direction from those that do not. The eigenvalues are calculated from the dipole time series from 0.5 to 1.5 seconds, which corresponds to the highest amplitude oscillations of the dipole component for the explosions, and therefore the most likely time period of a dipole source mechanism, if it exists. The dominant direction is found by fitting a line in 3-D to the dipole solution using singular value decomposition (SVD), allowing for an azimuth and inclination to be determined using the first principal component. Explosions with directivity will likely have rectilinear acoustic dipole components.

Additionally, we examine the stability of the inversions by varying the number of iterations the LSQR iterative solver completes before returning a solution $\mathbf{m}$. We present these results as a convergence curve of the solution norm versus squared error (residual), in which the number of iterations that gives the solution closest to the corner of the convergence curve (i.e. location of maximum curvature) is the ideal number of iterations [e.g. *Aster et al.*, 2013]. We examine solutions for a select number of iterations to determine the dependence of the solution on the number of iterations performed, and therefore an estimate of stability of the inversion.

3.5 Results

3.5.1 Monopole Inversion

Waveforms for 80 explosions of Yasur volcano (40 per active vent) are inverted for the monopole acoustic source time function over a 15 x 15 grid of possible source locations. Results for example event YBAL.3A8 are shown in Figure 3.4. The 225 possible grid-search source locations are colored by the squared error of the waveform fit, or residual, in Figure 3.4a where lower residuals correspond to a better fit to the data than source locations with higher residuals. The slight smearing of low residuals in the northwest-southeast directions is likely due to the lack of station coverage in those azimuths (station YIF6.1 that did not collect data during the aerostat campaign was located to the northwest), which decreased location constraint in that direction. The inversion source location (minimum residual, red star) is consistent with the assumed Vent A location at the DEM minimum in that sub-crater (black star). The inferred source time function as the volume flow rate as a function of time is shown in Figure 3.4b, with a peak volume flow rate of 5.2 x 10^4 m^3/s and duration of ~2.5 s. The cumulative volume flow rate (i.e. integrated form of Figure 3.4b) is shown in Figure 3.4c, yielding a cumulative erupted volume of 4.4 x 10^4 m^3. In our model, the volume flow rate corresponds to the gas injection into the atmosphere. The waveform fit for the inversion is shown in Figure 3.4d, where the data are red and synthetics are black. The residual for this monopole-only inversion for the full waveform over 5.5 s is 0.14, which indicates a good fit to the data but other source terms might still be present that cannot be fit by an isotropic source. The relative arrival time of the initial compression between 1–2 seconds matches well for all stations; however, the amplitude of the initial compression of the synthetic waveforms differs from the data for some stations (e.g. YIF1.1, YIF4.1, and YIF5.1).

Inversion results for all 80 events show similarities and differences between the two active vents. Overall, the grid-search method locates the events within ~30 m of the lowest point of the crater, or assumed vent location (Figure 3.4a, black star). This confirms that events

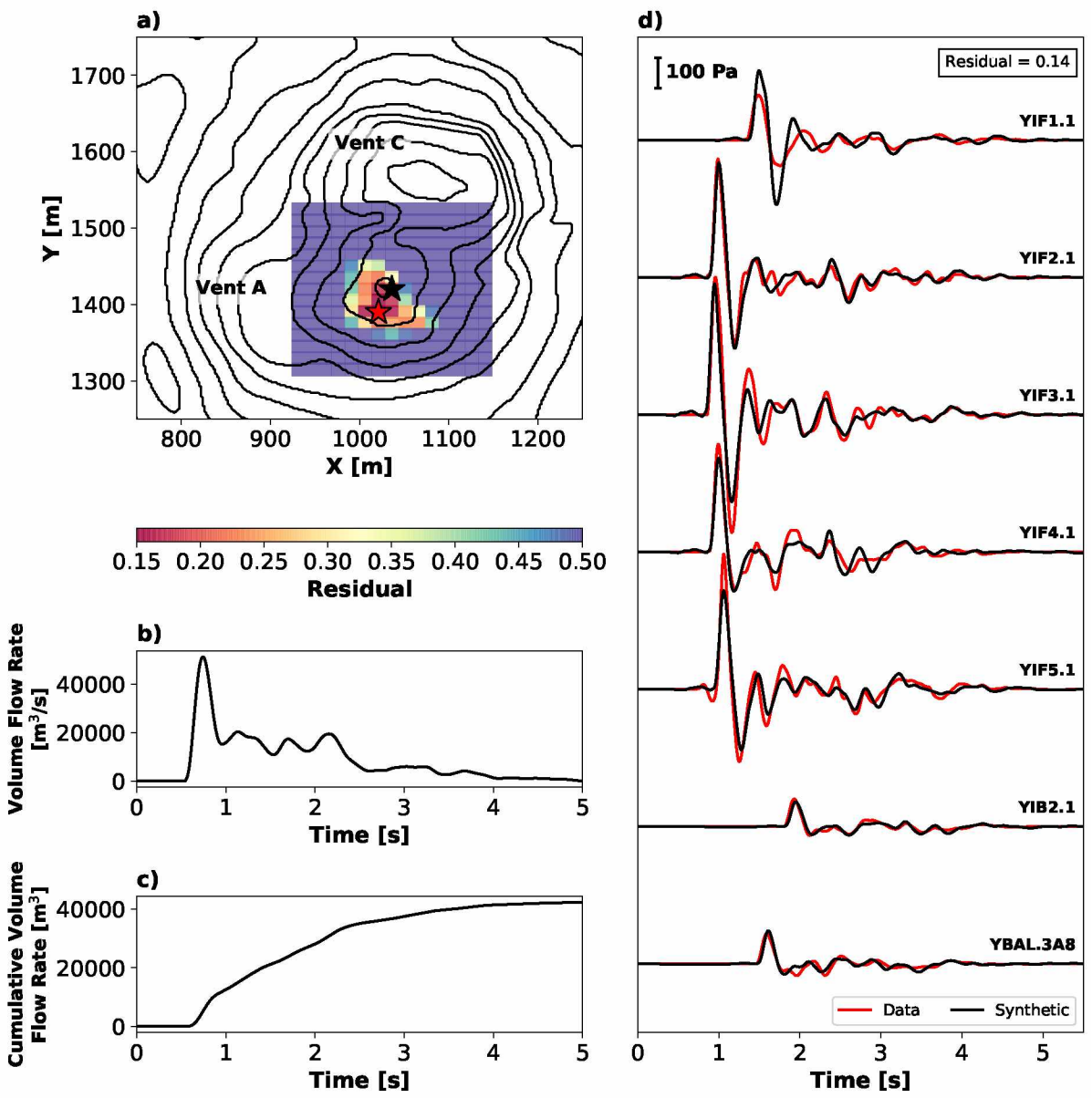

Figure 3.4: Monopole-only inversion results for example event YBAL.3A8. a) Residual map of the grid-search for the best source location, yielding a minimum residual (red star) within 34 meters of the low point of the DEM in the Vent A crater (black star). Grid cells are spaced 15 meters apart in a 15 x 15 grid around the crater. Inferred b) volume flow rate, and c) cumulative erupted volume. d) Data (red) and synthetic (black) waveforms for each station with an overall residual of 0.14.

are from the correct active crater. We leave high resolution source location studies to other methods such as reverse time migration [e.g. *Kim and Lees*, 2014] as source location is not the main focus of this study. The normalized volume flow rates using the monopole inversion

for explosions 1–40 for vents A and C are shown in Figure 3.5a,b, respectively. Vent A explosion volume flow rates generally have an abrupt onset that decreases rapidly during the first few tenths of a second, where Vent C explosion volume flow rates decrease more smoothly as a function of time. While explosion amplitudes cover a wide range for the 80 events investigated, volume flow rates have similar shape within each vent category, with a main onset that tapers back to zero after roughly 2.5–3 seconds. The average peak volume flow rate for 40 Vent A explosions is 3.7 x 10^4 m^3/s and average cumulative erupted volume is 4.0 x 10^4 m^3. Vent C explosion volume flow rates are smaller than Vent A, with an average peak volume flow rate of 9.1 x 10^3 m^3/s and average cumulative erupted volume is 1.4 x 10^4 m^3. The results are summarized in Table 3.1. Peak volume flow rate and cumulative volume for vents A and C are plotted in Figure 3.6a, indicating that events with higher peak volume flow rates tend to have higher cumulative volumes. Peak volume flow rates generally correlate with cumulative volumes. Peak volume flow rate does not appear to correlate with inversion residual in Figure 3.6b, suggesting that waveform fit is not dependent on the size of an eruption.

We next investigate the stability of the monopole inversions by changing the number of iterations performed in the LSQR iterative solver, ranging from 10 to 100000 iterations. The monopole-only volume flow rate solutions are nearly identical and not dependent on the number of iterations used in the iterative solver, as shown in Figure S1. Our stability test indicates that the solution converges fast and that small changes in fit to the data do not impact the volume flow rate solution.

3.5.2 Multipole Inversion

We perform a multipole (monopole and dipole in x, y, and z) acoustic waveform inversion for the the same example event as the previous section (YBAL.3A8), finding that the multipole inversion provides a better fit to the data. The source location is set to the minimum-residual location determined by the monopole grid-search to facilitate comparison

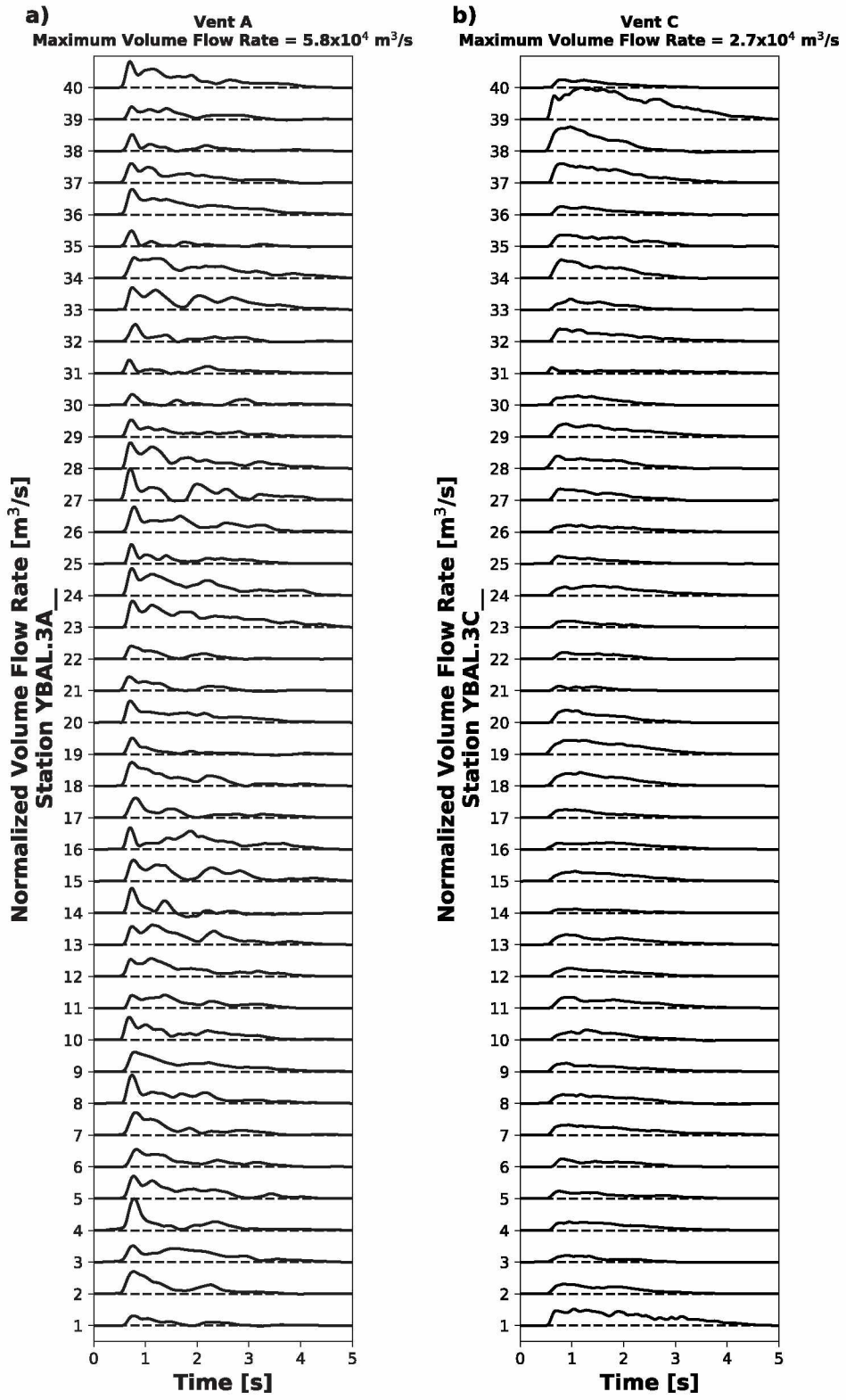

Figure 3.5: Volume flow rates ordered chronologically for selected events from a) Vent A and b) Vent C. Amplitudes are normalized to the peak of the largest event for each vent.

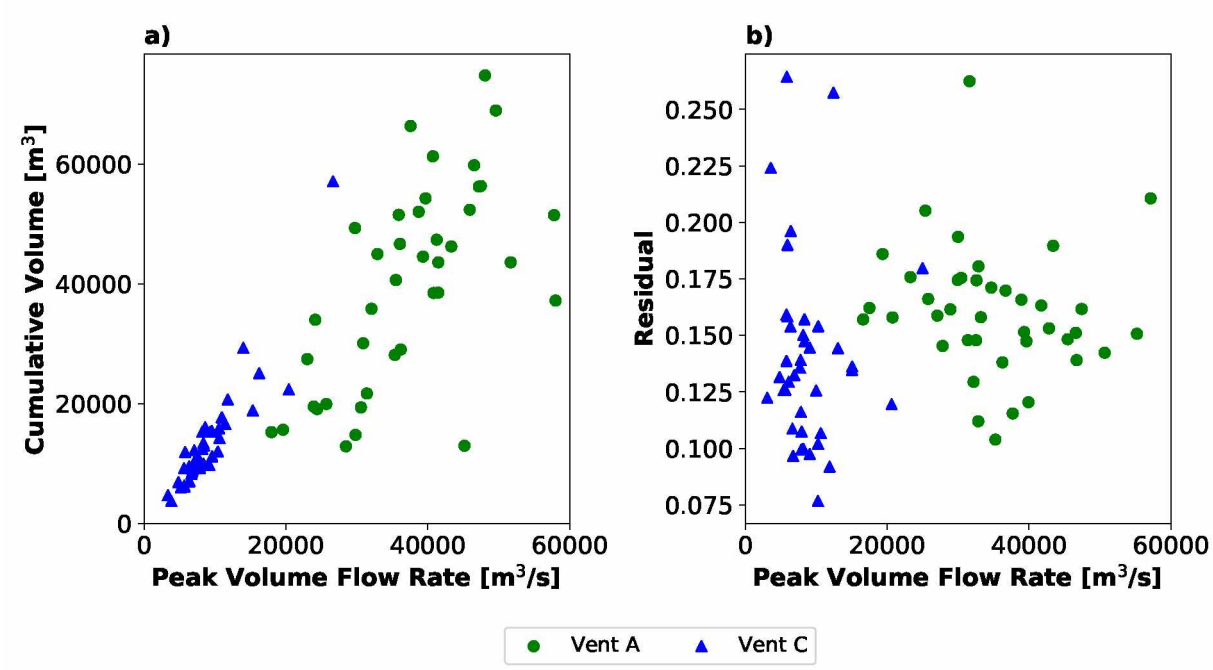

Figure 3.6: Comparison of monopole source inversion results for selected events. a) Cumulative volume versus peak volume flow rate. b) Residual versus peak volume flow rate. Vent A results are shown as green circles and Vent C results as blue triangles.

with the monopole inversion (Figure 3.4). While not shown, a grid-search for the multipole mechanism results in a less distinct minimum source location than the monopole inversion due to the increased number of model parameters. The multipole-derived volume flow rate as a function of time is shown in Figure 3.7a, with a peak volume flow rate of 5.1 x 10^4 m^3/s and duration of ~2.5 s, producing a cumulative volume of 4.0 x 10^4 m^3. The shape of the volume flow rate solution (solid line) is very similar to that of the monopole-only inversion (dotted line), with the peak and cumulative volume values being slightly smaller by 2.0% and 9.3%, respectively. This is a common trend for many events, as will be discussed below. The differentiated volume flow rate, which allows for the monopole and dipole sources to be more easily compared in the the same physical dimension (acceleration), is shown by Figure 3.7b. The dipole forces in the x, y and z directions are shown in Figure 3.7c-e, yielding a peak dipole strength (sum of the squares of the forces in x, y, and z) of 6.4 x 10^7 N. The fact that the monopole and dipole source components are in phase suggests that the same physical source responsible for both, or that the inversion wants to partition the same

Table 3.1: Inversion volume flow rate summary for the 80 events used in this study for vents A and C.

		Vent A		Vent C	
		No Topography	Topography	No Topography	Topography
Monopole-Only Peak Volume Flow Rate [10^4 m^3/s]	Range	1.9 – 6.1	1.8 – 5.8	0.37 – 3.6	0.33 – 2.7
	Average	4.1	3.7	1.1	0.91
Multipole Peak Volume Flow Rate [10^4 m^3/s]	Range	2.1 – 6.5	1.7 – 5.7	0.36 – 3.3	0.31 – 2.5
	Average	4.3	3.5	1.1	0.88
Monopole-Only Cumulative Volume [10^4 m^3]	Range	1.2 – 7.8	1.3 – 7.5	0.30 – 5.9	0.38 – 5.7
	Average	4.0	4.0	1.3	1.4
Multipole Cumulative Volume [10^4 m^3]	Range	1.3 – 7.2	1.0 – 7.2	0.24 – 4.9	0.33 – 5.1
	Average	3.7	3.5	1.1	1.3
Monopole-Only Residual	Range	0.18 – 0.75	0.10 – 0.26	0.27 – 0.69	0.08 – 0.26
	Average	0.37	0.16	0.47	0.14
Multipole Residual	Range	0.12 – 0.30	0.03 – 0.11	0.090 – 0.17	0.021 – 0.11
	Average	0.18	0.065	0.13	0.050

source-time function between monopole and dipole components. This can be interpreted as an explosion mechanism that is not perfectly omnidirectional (monopole), but has some directivity (dipole) structure to it. The vertical dipole that is larger than the horizontal dipoles may indicate a directional explosion in which the displaced fluid by jetting solid objects and gas/fluid phase is accelerated mainly in the vertical direction [*Chouet et al.*, 1974; *Gerst et al.*, 2008; *Johnson et al.*, 2008]. The waveform fit for the multipole inversion for all stations is shown in Figure 3.7f. The residual has decreased to 0.03 for the multipole inversion from 0.14 for the monopole-only inversion and the amplitude of the synthetics for

the first compression match the data well with the addition of the dipole components. These dipole components can be better visualized spatially in Figure 3.8. The inferred dipole for event YBAL.3A8 is predominantly positive in the vertical dimension and to the northeast, with an inclination of 67° from horizontal and azimuth of 19° clockwise from north. This event had a rectilinearity of 0.93, which is one of the highest rectilinearities and may indicate a strong dipole component for this explosion.

The volume flow rate solutions for the multipole inversions for all 80 events investigated in this study are similar in both magnitude and shape to that of the monopole-only inversion (Table 3.1). The peak volume flow rate and cumulative volume generally decrease slightly when the dipole components are added to the inversion. For Vent A, including the dipole components in the inversion causes an average decrease of 6.0% for peak volume flow rate and 11% in cumulative volume. For Vent C, the additional components, on average, decrease the peak volume flow rate by 2.7% and cumulative volume by 5.8%.

Vents A and C have distinct dipole characteristics both in amplitude and direction. Peak dipole strengths range between 6.8–75 x 10^6 N with an average of 3.3 x 10^7 N for Vent A and 2.4–25 x 10^6 N with an average of 6.1 x 10^6 N for Vent C. Explosions with higher peak volume flow rates tend to have higher peak dipole strengths (see Figure 3.9a, where peak dipole strength is plotted with volume flow rate). This is in agreement with the results of Figure 6b of *Kim et al.* [2012], where it is shown that events at Tungurahua volcano with higher volume flux have higher dipole strengths. We note that Figure 3.9a also indicates that the dipole strength is substantially greater for Vent A than for Vent C events. A 3-D view of the dipole component of the multipole inversion for the first 12 events for each vent is shown in Figure 3.10. Explosions from Vent A not only have higher dipole strengths, but also have a more defined dominant dipole direction than those from Vent C, meaning that the dipole more closely resembled a line in three dimensions (Figure 3.10). We further quantify the dipole direction using rectilinearity, where events that were considered to have a dominant dipole direction had rectilinearities greater than 0.65. Rectilinearities for Vent

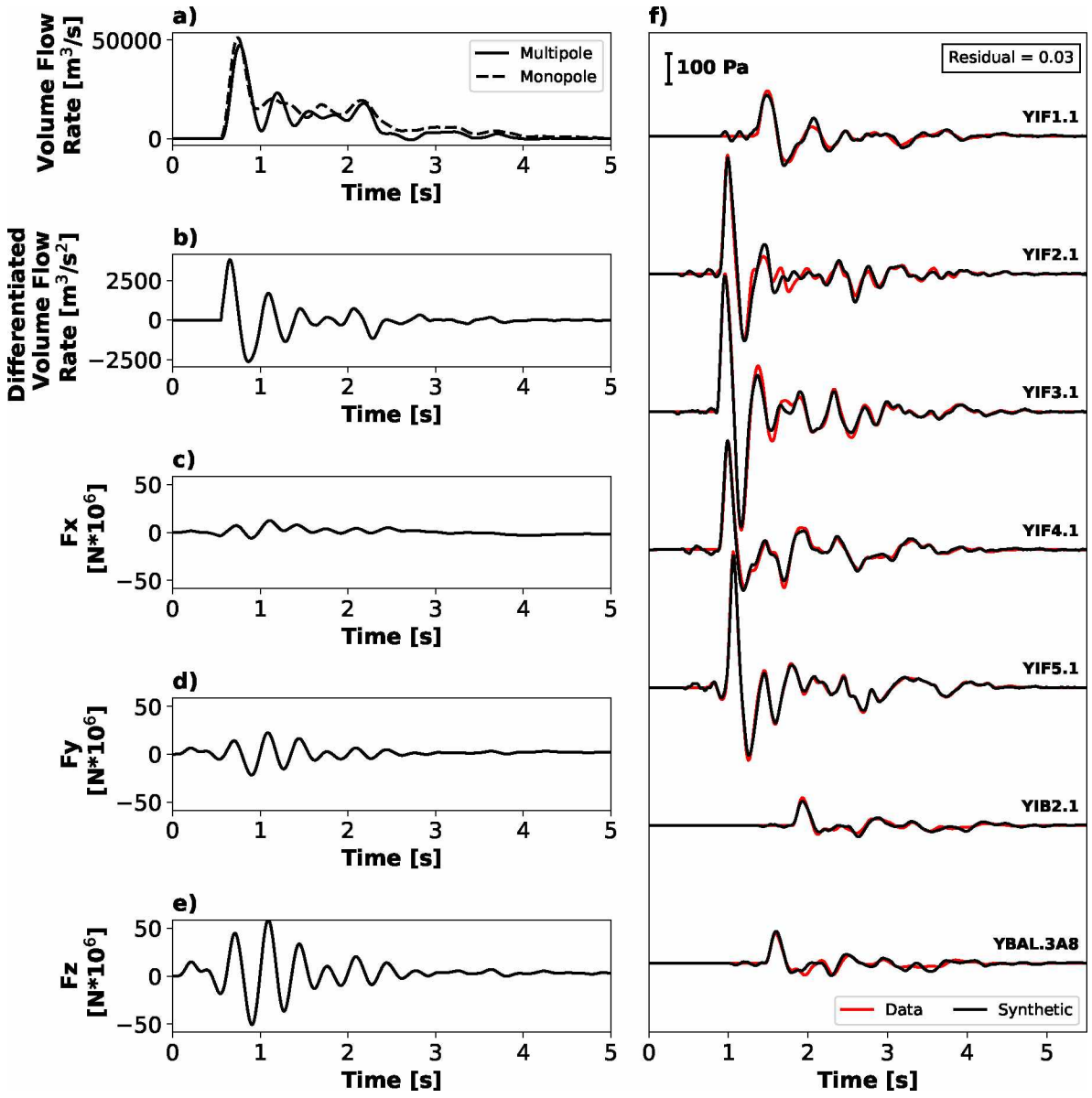

Figure 3.7: Inversion results for the multipole (monopole and three force components) for event YBAL.3A8. a) Volume flow rate for the monopole component of the multipole inversion (solid line) and monopole-only inversion (dotted line). b) Differentiated volume flow rate (acceleration). Force in c) x-, d) y-, and e) z-directions. f) Data (red) and synthetic (black) waveforms for each station. A residual of 0.03 is calculated using the full waveforms over the duration of 5.5 s.

A ranged from 0.11–0.93, with an average of 0.71, while rectilinearities for Vent C ranged from 0.09–0.75 with an average of 0.47. Using a rectilinearity threshold of 0.65, 29 of 40 Vent A events and 6 of 40 Vent C events have dominant dipole directions. The rectilinearity

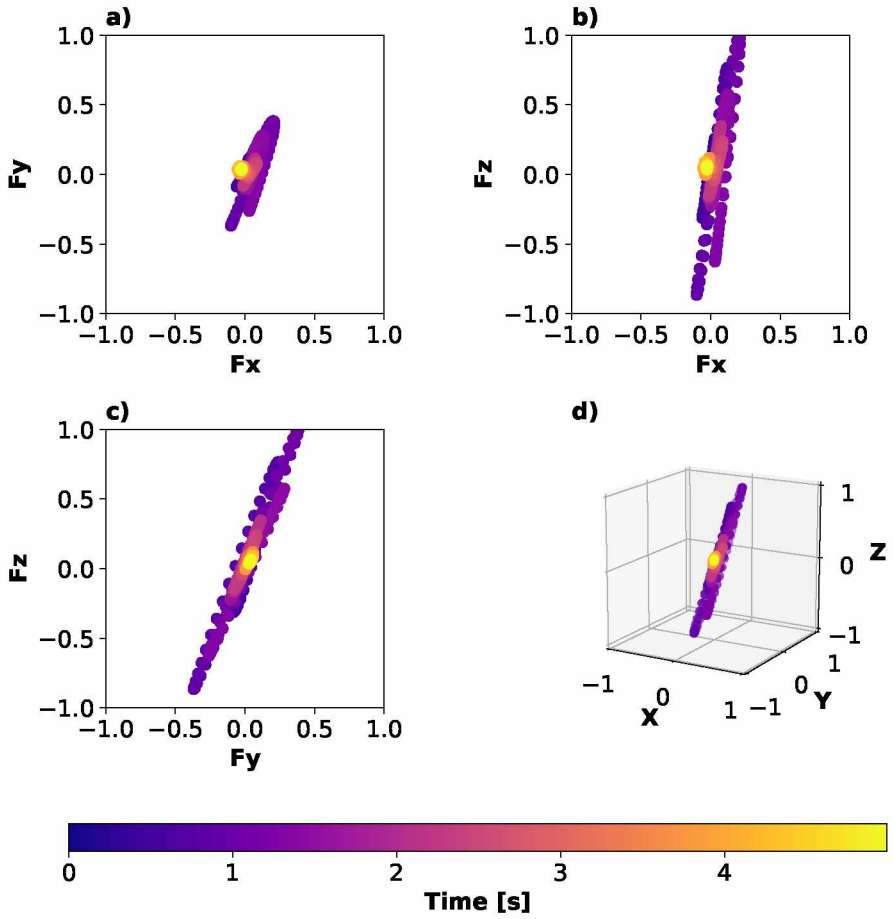

Figure 3.8: Dipole direction results for the multipole inversion (monopole and three force components) for example event YBAL.3A8 in the three principal planes. a) View of dipole in the X-Y plane. b) View of dipole in the X-Z plane. c) View of dipole in the Y-Z plane. d) View of dipole in 3D from a viewing azimuth of 300° and an elevation of 15°. Note, the coordinate system used is +x (East), +y (North), and +z (up). Plots are normalized to the maximum dipole component value for the explosion and colored by time.

is plotted as a function of peak dipole strength for Vents A and C (Figure 3.9b). Vent A explosions with high peak dipole strengths tend to have high rectilinearity as well. For low peak dipole strength for Vent A and most explosions from Vent C the trend is not very clear. This suggests that events with higher dipole strengths tend to have more-defined dominant dipole directionality. It is unclear whether smaller events have less distinct directionality, or if it is just due to lower signal to noise ratio.

To further evaluate the significance of each dipole component (x, y, and z) to the source inversion, we calculate the Akaike Information Criterion (AIC). AIC decreases as free pa-

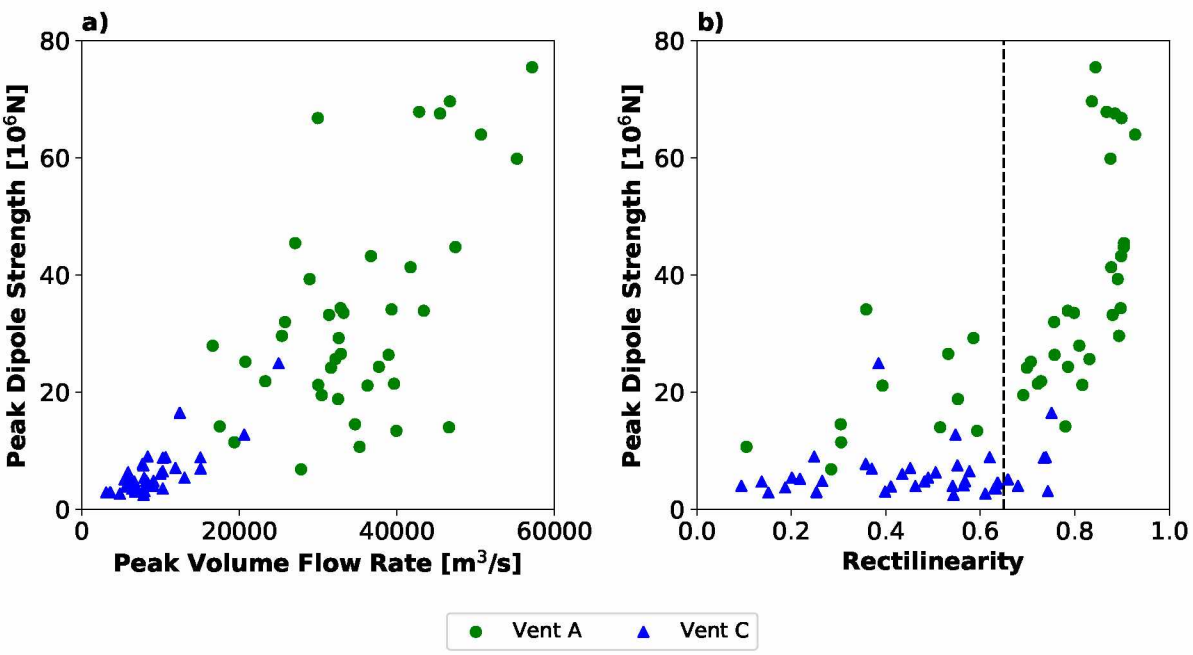

Figure 3.9: Comparison of monopole source inversion results for all events. a) Peak dipole strength versus peak volume flow rate. b) Peak dipole strength versus rectilinearity. Vertical dotted line in b) denotes the $F_r \geq 0.65$ cutoff for events considered to have a dominant dipole directions.

rameters are added to the inversion (Table 3.2). This calculation suggests that all three dipole components lowers the AIC score and may be the best solution according to the AIC calculation.

Table 3.2: AIC calculation using the residual for the entire waveform for example event YBAL.3A8.

	Squared Error	AIC
Monopole	0.14	-6520
Monopole + Fx	0.12	-6098
Monopole + Fx + Fy	0.07	-7067
Monopole + Fx + Fy + Fz	0.03	-9466

AIC calculations for the majority of our multipole inversions shows that the addition of dipole components in the source inversions lowers the AIC score. For Vent A, 26 of 40 events had AIC values for all 4 components less than that of the monopole only inversion, while 17

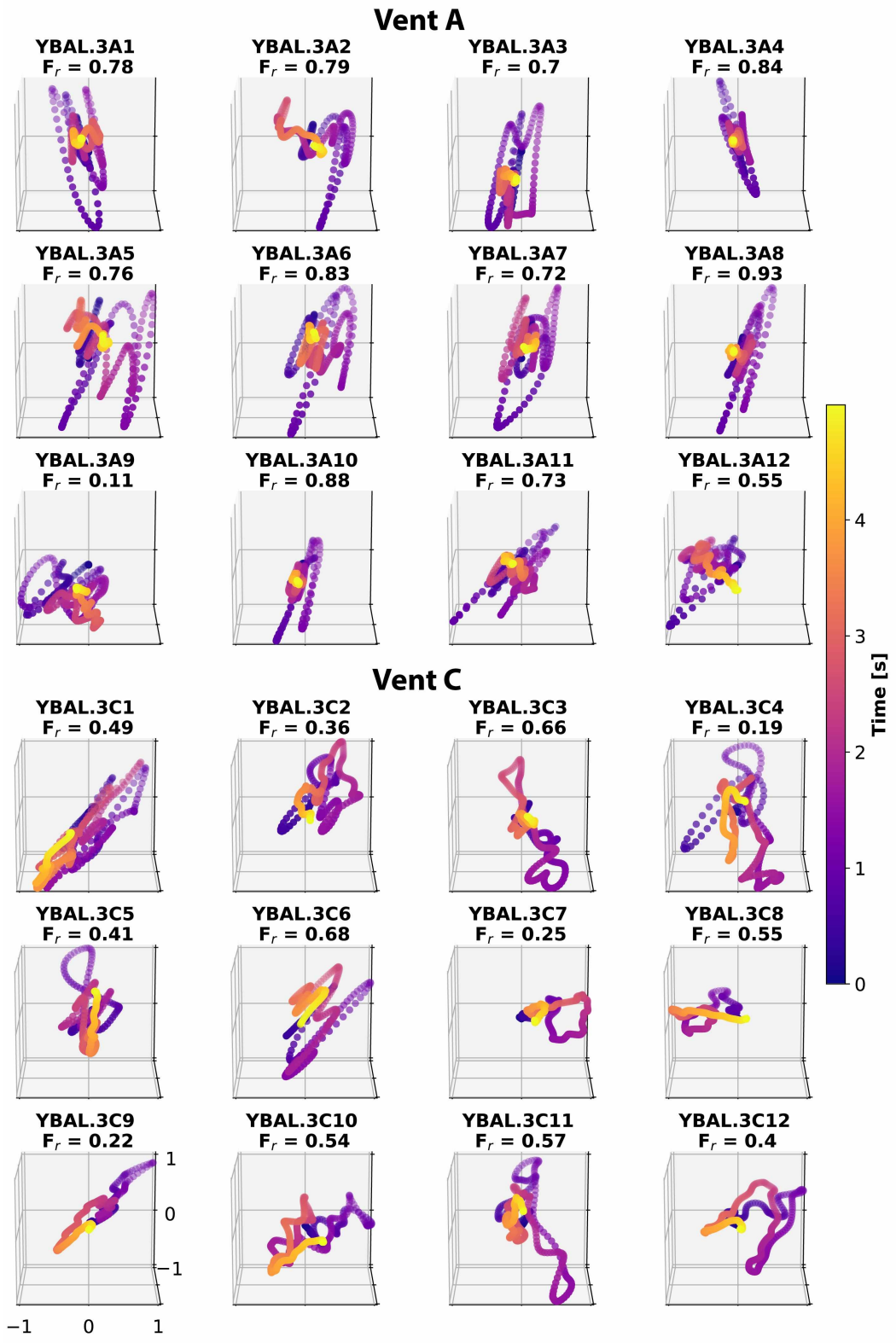

Figure 3.10: Visualization of the dipole component of the multipole inversion for the first 12 events investigated for both vents. The x, y, and z components of the dipole solution are normalized for each event to emphasize dipole solution shape, with axes labeled on the bottom left plot. Rectilinearity for each event is given by F_r.

of 40 events had the inversion with all 4 components as the minimum AIC overall (i.e. out of the monopole, monopole + Fx, monopole + Fx + Fy, and monopole + Fx + Fy + Fz). For Vent C, 39 of 40 events had AIC values for all 4 components less than the monopole only inversion, while 21 of 40 events had the inversion with all 4 components as the minimum AIC overall. These AIC calculations show that the addition of dipole components in the source inversion lowers the AIC score and likely not only fitting the noise. However, AIC is only one metric for evaluating inversions with increasing number of free parameters.

We also investigate the stability of the multipole inversion by varying the number of iterations in the LSQR iterative solver. A convergence curve of the norm of the solution (||x||) and squared error (residual) with respect to number of iterations for example event YBAL.3A8 with the source location fixed is shown by Figure 3.11a. This curve illustrates that there are multiple local maximum curvature points as the number of iterations is increased (as opposed to the more traditional "L-shape"), creating a step-like pattern with jumps in solution norm corresponding to very small changes in residual. The volume flow rate, Fx, Fy, and Fz solution vectors are shown by Figure 3.11b-e, respectively, for 100, 1000, and 10000 iterations. We find that the volume flow rate solution remains stable, even with an extreme case of 10000 iterations (Figure 3.11b). This indicates that the volume flow values for monopole source are reliable, regardless of whether the dipole components are included in the source inversion or not. However, the dipole component solutions show large solution variations between iterations with small improvement in the data fitting (Figure 3.11c-e).

3.5.3 Directionality

We explore the acoustic radiation pattern using simple waveform amplitude observations, specifically the difference in amplitude for the initial compression between the synthetic waveforms from the monopole inversion and the data (e.g. Figure 3.4d, stations YIF1.1, YIF4.1, and YIF5.1). Differences in amplitude between the data and model for the monopole inversion may be related to a dipole component or noise. We calculate this amplitude deviation

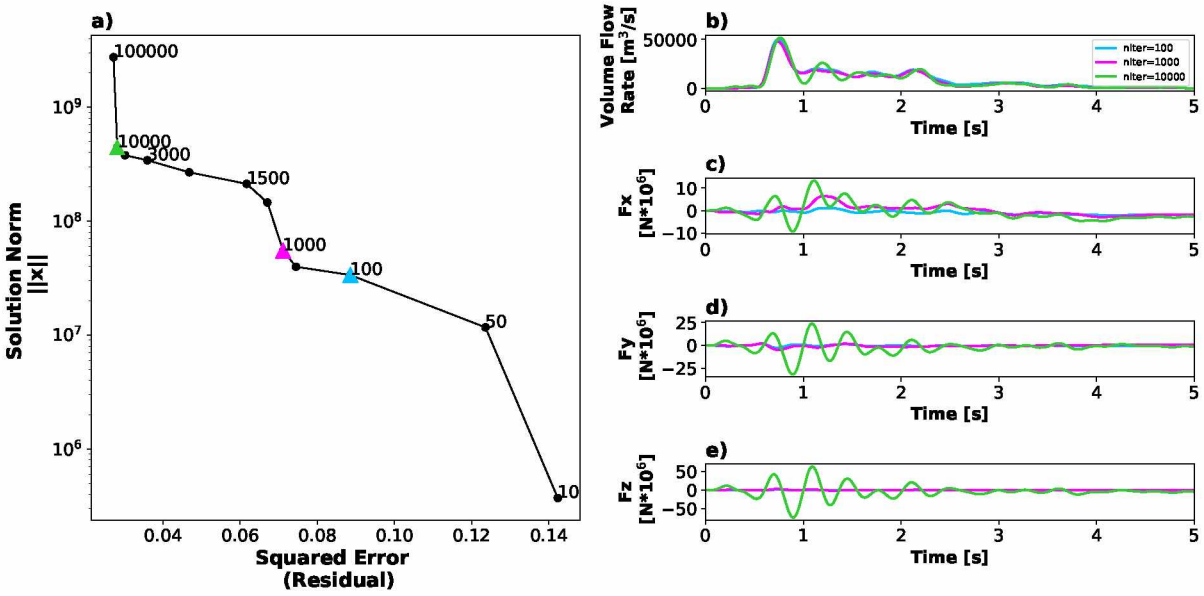

Figure 3.11: Multipole inversion stability test. a) Convergence curve of the norm of the solution (||x||) and squared error (residual) with respect to number of iterations allowed by the least squares iterative solver for example event YBAL.3A8. b-e) show the volume flow rate, Fx, Fy, and Fz solution vectors, respectively, for 100 (blue), 1000 (pink), and 10000 (green) iterations. Blue, pink and green triangles in a) correspond to volume flow rate vectors plotted in b-e).

(A_{dev}), or fractional misfit between the peak data compression amplitude ($A_d(t_{max,d})$) and corresponding synthetic value ($A_m(t_{max,d})$) divided by the peak data amplitude, for each station as follows

$$A_{dev} = \frac{A_d(t_{max,d}) - A_m(t_{max,d})}{A_d(t_{max,d})} \tag{3.16}$$

These percent differences are plotted as a function of azimuth from the vent for vents A (Figure 3.12a) and C (Figure 3.12b), where red corresponds to data amplitude being larger than the synthetics (i.e. synthetic under-predicts data amplitude) and blue denotes synthetic amplitude being larger than data amplitude (i.e. synthetic over-predicts data amplitude). This analysis shows that the monopole source mechanism under-predicts amplitudes to the east and south (e.g. YIF2-5) but over-predicts the amplitude to the north (e.g. YIF1.1), even after the effects of topography are accounted for in the synthetic waveforms.

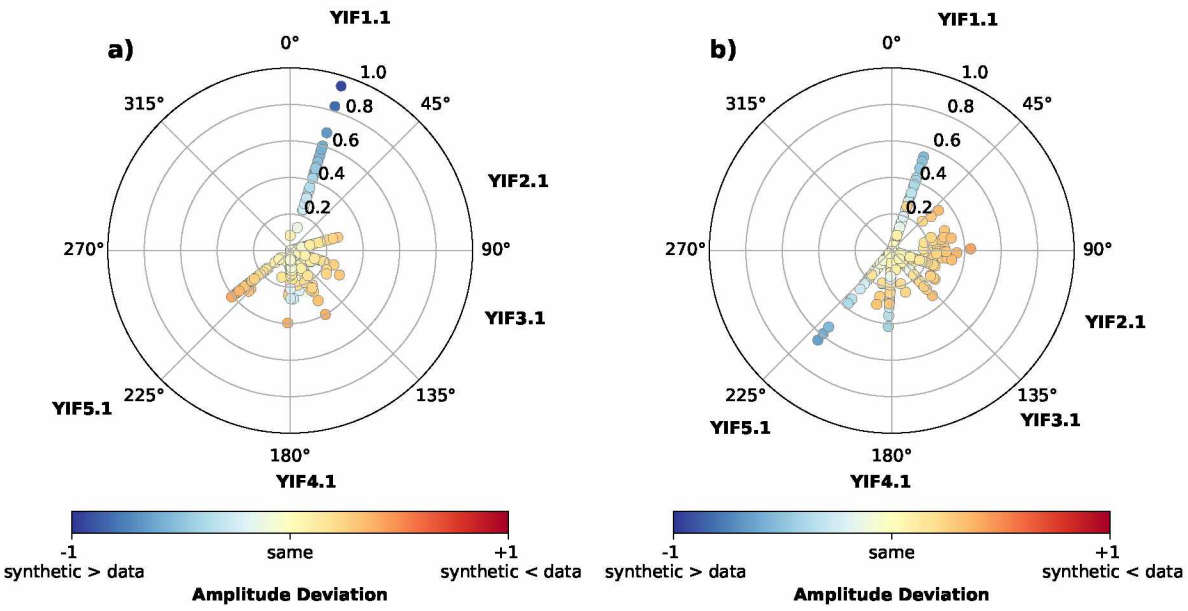

Figure 3.12: Difference in amplitude of the peak initial compression between modeled waveforms from a monopole-only inversion and the data for explosions from a) Vent A and b) Vent C. Positive differences signify that data amplitudes are higher than the model (red), while negative differences correspond to model amplitudes greater than the data (blue). Points near the center mean that the amplitudes match well, with zero being a perfect match.

3.5.4 Topographic Impact on Waveform Inversions

We re-run our source inversions using 1-D Green's functions obtained by simulating across a flat horizontal plane to assess the significance of topography on the Green's functions and inversion. This is the acoustic equivalent of a 1-D vs. 3-D seismic ground motion simulation [e.g. *Rodgers et al.*, 2018] to quantify path effects. The peak volume flow rate for example event YBAL.3A8 for a 1-D simulation is 5.7 x 10^4 m^3/s, as compared to 5.2 x 10^4 m^3/s for the 3-D simulation with topography. For this example, this results in a 8.7% decrease in peak volume flow rate when topography is included. We find that the peak volumetric flow rate for the 80 events examined in this study is overestimated by 10% for Vent A events and 16% for Vent C events. Additionally, waveform fit is worse when topography is not accommodated. The residuals for the 80 events explored in this study are, on average, 53% and 69% higher for vents A and C, respectively, for simulations propagated across a horizontal plane than when topography is considered. We summarize the values both with and without accounting for topography for peak volume flow rate, cumulative volume, and residual in Table 3.1.

A stability test and convergence curve is constructed for inversions propagated across a 1-D horizontal plane (Figure 3.13a). The inversion results for the volume flow rate remains stable and is not dependent on the number of iterations (Figure 3.13b). Figure 3.13c,d show similar solutions for the Fx and Fy components of the dipole that do not vary largely with number of iterations compared to the multipole inversion results across topography (Figure 3.11c,d). However, the vertical dipole (Fz) remains dependent on the number of iterations as shown in Figure 3.13e, making results unreliable with the given station coverage (only a single sensor on the tethered aerostat). These results indicate that the multipole inversion is more stable with the Green's functions across a plane for the Fx and Fy components than when topography is accounted for, but the vertical dipole remains unstable. This increased stability may be due to those Green's functions being simpler than the Green's functions across topography, or possibly due to an effective dipole component induced by topography being better modeled by a single dipole approximation.

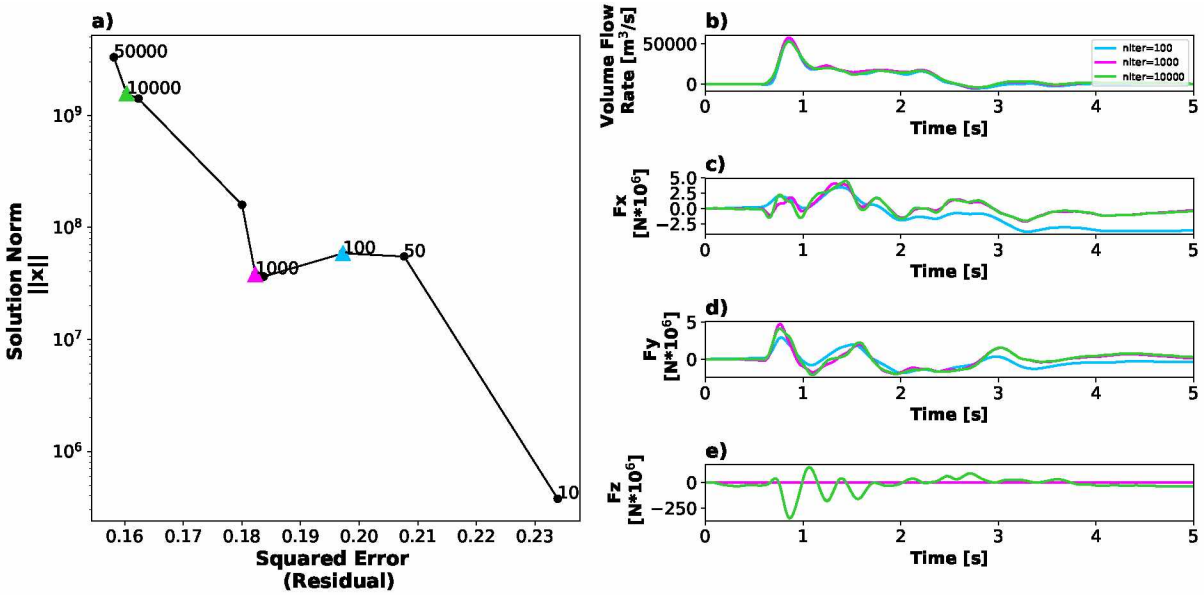

Figure 3.13: Multipole inversion stability test over a 1-D plane. a) L-curve of the norm of the solution (||x||) and norm of the residual (||r||) with respect to number of iterations for example event YBAL.3A8. b-e) show the volume flow rate, Fx, Fy, and Fz solution vectors, respectively, for 100 (blue), 1000 (pink), and 10000 (green) iterations. Blue, pink and green triangles in a) correspond to volume flow rate vectors plotted in b-e). The Fz component is highly sensitive to the iteration number.

3.5.5 Contribution of the Aerostat Station to the Inversion

An enhanced characterization of the dipole component and acoustic directionality is afforded by including a sensor in the vertical dimension (in our case, aboard a tethered aerostat) that is not seen when only using stations placed on the Earth's surface (see *Jolly et al.* [2017], their Figure 1 for diagram of the tethered aerostat). Figure 3.14 shows the dipole component solution when the aerostat sensor is included for source inversion (top row, a-d) and when the aerostat sensor is not included (bottom row, e-h) for event YBAL.3A8. All components in Figure 3.14 are normalized to the global maximum across both inversions to facilitate visual comparison. Including the aerostat sensor yields a clear dominant dipole direction (Figure 3.14a-d), while only using the ground stations yields a much smaller dipole amplitude and less clear dominant dipole direction (Figure 3.14e-h). Peak volume flow rate with and without the aerostat sensor is 5.1 x 10^4 m^3/s and 4.4 x 10^4 m^3/s, cumulative volume is 4.0 x 10^4 m^3 and 3.6 x 10^4 m^3, and peak dipole strength is 6.4 x 10^7 N and 1.8 x 10^7 N, respectively. These are all large differences, highlighting the potential importance of vertical sensors. We note that the aggregate residual decreases when the aerostat sensor is included in the multipole inversion, in this case from 0.14 to 0.03. Some individual events have a residual increase when the aerostat sensor is included in the inversion.

Similarly, we perform a "jackknifing resampling" test for the entire network to assess bias in the inversion. We systematically remove each one of the 7 sensors from the multipole inversion and compare results including peak volume flow rate, peak dipole strength, rectilinearity, and residual (Table 3.3). Rectilinearity and peak dipole strength remain high (>0.90 and >4.7 x 10^7 N, respectively) when YIB2.1, YIF3.1, or YIF2.1 are removed from the inversion. This indicates that the inversion is least sensitive to these stations, which happen to be in the middle of the azimuthal distribution of the stations deployed (Figure 3.2). Rectilinearity and peak dipole strength decrease greatly when YBAL.3, YIF5.1, or YIF1.1 are removed from the inversion, which are the three stations that stretch the azimuthal and vertical coverage of the deployment. We note that YIF1.1 - YIF5.1 were located on the crater

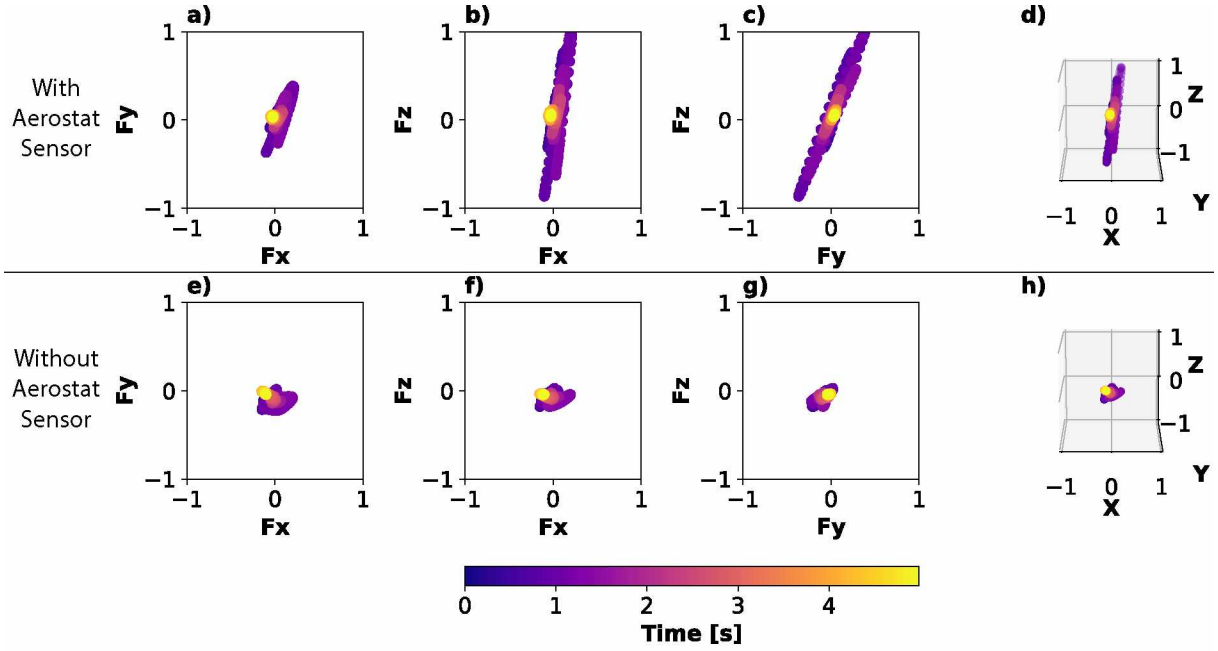

Figure 3.14: Comparison of dipole inversion results including the aerostat sensor in the inversion results (top row, a-d) and without (bottom row, e-h) for event YBAL.3A8. All components are normalized to the maximum of all components across both inversions. Dipole magnitude and directions are all more pronounced when the aerostat sensor is included.

rim and therefore had similar vertical coverage, while YBAL.3 (aerostat) expand the vertical coverage of the network. A similar analysis for station configuration impact on source parameters is performed by *Kim et al.* [2012], where it was found that multipole inversions that do not account for topography are only stable if at least three stations spanning 180° around the infrasound source are used.

3.6 Discussion

The multipole acoustic source inversion can provide valuable information on a volcanic explosion source, yet the dipole components may be unstable even with good azimuthal ground station coverage and a station on a tethered aerostat. The acoustic monopole inversion is stable, converges fast, and solutions of volume flow rate are reliable given the network distribution of this Yasur volcano campaign (Figure S1). The monopole results are presented in the form of volume flow rate, which can easily be converted to mass flow rate

Table 3.3: Results of a jackknife resampling test for the multipole inversion of example event YBAL.3A8. Inversions were systematically performed using only 6 stations, each time with one station excluded from the inversion. The inversion result for all 7 stations is included as the first row for reference.

Excluded Station	Peak Volume Flow Rate [10^4 m^3/s]	Peak Dipole Strength [10^7 N]	Rectilinearity	Residual	Largest Azimuthal Gap [°]
None	**5.1**	**6.4**	**0.93**	**0.03**	**145**
YBAL.3	4.4	1.8	0.32	0.14	145
YIB2.1	5.1	6.3	0.93	0.16	145
YIF5.1	4.0	2.0	0.17	0.14	205
YIF4.1	4.4	1.7	0.51	0.14	145
YIF3.1	5.0	4.7	0.90	0.14	145
YIF2.1	5.0	6.7	0.95	0.16	145
YIF1.1	2.9	4.1	0.61	0.30	203

[see *Fee et al.*, 2017]. Our grid-search method indicates the minimum residual solution for most events is located within 30 m of the lowest point of the crater (i.e. our inferred vent location), demonstrating that events can easily be distinguished between the active vents at Yasur. Explosions from vents A and C show different characteristics from one another, but the shape and duration of explosion volume flow rates are similar to other explosions from the same vent. We find that Vent A explosions are larger and have volume flow rate peaks that decrease more rapidly than those from Vent C.

Although the dipole components may be unstable and/or nonexistent, we contend there is still utility in analyzing the dipole solutions and their importance to the overall acoustic source. By taking the optimal solution in the bend of the convergence curve, we make inferences on the source using the most reliable solution (albeit non-unique). The inclusion of the dipole components in the inversion yields results that indicate a dipole component may exist for explosions at Yasur, even after topography is accounted for. We use rectilinearity as a measure of evaluating the dipole component, where events with higher rectilinearity were determined to have a dominant dipole direction. We find that 29 of 40 events from Vent

A and only 6 of 40 events from Vent C had a dominant dipole direction according to this classification. Explosions from Vent A tend not only to have stronger directionality and a higher dipole strength, but also have a more linear motion as one would expect from a dipole source mechanism than explosions from Vent C. Furthermore, we show that inversions for the monopole solution (and hence volume flow rate) remain stable regardless of whether the inversion includes a monopole or a multipole (monopole and dipole) source mechanism. The shape and amplitudes of the volume flow rate for the monopole and multipole inversions are relatively similar (Figure 3.7a), despite dipole components being allowed to vary freely in the multipole inversion. The peak volume flow rate and cumulative volume generally decreased slightly when the dipole components were added to the inversion because part of acoustic pressure is attributed to the presence of a dipole, which does not generate the net change of mass in the source region.

Using an infrasound sensor elevated from the Earth's surface yields an unprecedented view of the acoustic wavefield from volcanic explosions, an idea proposed by *Matoza et al.* [2013]. We use a tethered aerostat to achieve the vertical sensor coverage, but some studies such as *McKee et al.* [2017] and *Rowell et al.* [2014] have used nearby topography for an improvement in vertical station coverage for a network around a volcano. Including the aerostat sensor in the inversions yielded a measurable increase in dipole strength that would have otherwise been unobservable, and shows the importance of both the vertical sensor coverage and multipole inversion. For many explosions examined here, the peak dipole strength nearly doubled when the aerostat sensor was included in the source inversion. Inversions only using ground sensors often showed no realistic dipole component. There is a distinct dominant dipole when the aerostat sensor is used and a more random dipole shape when the aerostat sensor is excluded (see Figure 3.14). Therefore, 2-D source estimates of volcanic, and potentially anthropogenic, explosions may have underestimated (or at least poorly constrained) directionality. We caution that this study only uses one infrasound sensor hanging from a tethered aerostat as a proof-of-concept. Because of this, we performed a brief investigation

to ensure that the calculated dominant dipole direction (azimuth and inclination) was not directly linked to the azimuth and inclination of the aerostat sensor as it moved to various loiter positions. While we do not see a strong correlation, future work should include more infrasound sensors in the vertical direction at varying azimuths and inclinations simultaneously to further sample the acoustic wavefield and constrain acoustic source directionality. For a dipole source, there are directions in which radiated acoustic energy density are greatest and some where radiated dipole energy cannot be detected (analogous to the nodal plane in a seismic moment tensor). Therefore, dense station coverage at a variety of azimuths and inclinations will be necessary for future studies that perform acoustic waveform inversions with the intent to solve for a dipole solution, if it exists.

3.6.1 Reliability of the Dipole Component

Many acoustic source inversion studies have assumed that their inversions are stable due to good waveform fit, station coverage, etc. [e.g. *Fee et al.*, 2017; *Johnson et al.*, 2008; *Johnson and Miller*, 2014; *Kim et al.*, 2015]. However, our results and analysis suggest that the monopole solution is valid using numerical Green's function, but the dipole component(s) may still be unstable and non-unique. Including the dipole components causes decrease in residual by ~0.10; however, the dipole components are highly-dependent on number of iterations for our scenario (e.g. Figure 3.11) and station configuration (Table 3.3). This indicates that a small amount of noise in the data may change the dipole solution completely. Our results indicate that the multipole inversion as currently formulated may be ill-posed because the data we collected is not sufficient to fully constrain the source. Therefore, while our methods find a solution to the multipole inversion, we cannot uniquely determine that it is the true solution. Consequently, careful attention should be used for interpretations of our dipole results as they are non-unique. We caution that the commonly used (in volcano seismology) metric AIC which tests the significance of the number of free parameters can provide misleading results. Of the 80 events we explored, 65 have smaller "goodness of fit"

AIC numbers for all 4 components than that of the monopole-only inversion. This reiterates that the model that provides the best fit (i.e. lowest residual) is not always the true solution [e.g. *Aster et al.*, 2013; *Bean et al.*, 2008; *O'Brien et al.*, 2010]. We stress that this is likely the case for many volcano deployments, as we use 6 ground stations with good azimuthal coverage as well as a sensor on a tethered aerostat, and still cannot reliably resolve the dipole component, if it exists. Stability analysis and sensitivity tests should be performed for future studies before the dipole component results can be considered reliable.

3.6.2 Eruption Directionality

In a volcanic environment, it is important to make a distinction between dipole radiation resulting from the source mechanism itself (e.g. the interaction of fluid with the vent walls and solid particles [*Caplan-Auerbach et al.*, 2010; *Woulff and McGetchin*, 1976]), and that of an "effective dipole" where the environment directs acoustic radiation preferentially (e.g. diffraction and reflection of sound induced by topography, a sub-vertical conduit, or wind) [*Kim et al.*, 2012]. While we cannot reliably solve for the dipole components using an acoustic source inversion, we can make first order observations about the unresolved amplitude differences from the monopole inversion that account for topography influences on the acoustic radiation pattern. *Jolly et al.* [2017] investigated explosions from Yasur during the same field experiment using both infrasound and video data to explore explosion directivity and found a high amplitude infrasound anomaly at azimuths of ∼60°–130° for explosions from the Vent C and ∼80°–120° for explosions from Vent A (i.e. acoustic amplitudes are higher at the aerostat station than at the crater rim). They also find an increase in explosion amplitude for higher takeoff angles and that this amplitude anomaly exists for discrete explosions, as well as low-level (tremor-like) activity. However, they do not account for topography in their interpretations, so acoustic directivity seen in *Jolly et al.* [2017] could be due to path effects from topographic scattering by the crater walls [e.g. *Kim et al.*, 2012] or from source directivity. The analysis of video data for ballistic trajectories that have

consistent directionality to the east by *Jolly et al.* [2017] should remain true regardless of whether topography is considered for acoustic analysis. Our results are consistent with these findings, where the monopole source causes an under-prediction of initial compression amplitudes towards the east and south but an over-prediction the amplitude at YIF1.1 to the north for both vents (Figure 3.12). This shows that even though a reliable source inversion for the dipole or directionality cannot be performed, we see that explosions have directivity, and a monopole source cannot fully explain the data. Furthermore, this study indicates that multiple stations with excellent azimuthal coverage should be used, even for monopole source inversions, in order to obtain a more reliable estimate of the volume flow rate and other source parameters. Comparing our results directly to *Jolly et al.* [2017] is difficult as different events were used for the analysis of ballistic trajectories and those in this study. However, the existence of ballistic trajectory directionality supports our interpretation in our directionality results generally towards the east and south as ballistic trajectories may be less affected by topography than infrasound (like the amplitude ratio calculations of *Jolly et al.* [2017] can be) and are likely indicative of source directionality. A recent study by *Fitzgerald et al.*, (currently in review), also using data at Yasur volcano from a few months around our deployment, found higher spatial densities of mapped ballistics to the south-southeast and toward the east, further indicating preferential eruption directionality at Yasur.

Our method aims to understand the acoustic radiation pattern of volcanic explosions and determine the relative influence of crater topography versus source mechanism on the observed directionality. While this method does not solve for the source physics causing that radiation, we briefly mention some potential mechanisms. An explosion represented as a monopole is relatively easy to envision, whether it is a Strombolian gas bubble burst or any explosion that radiates infrasound equally in all directions. The physical representation of the volcanic dipole, however, is not as well understood. *Johnson et al.* [2008] attribute the dipole source of Strombolian explosions at Mt. Erebus to be the result of the random location of initial bubble membrane failure that lead to fluid advection. *Jolly et al.* [2016]

explain infrasound source directivity from a mud heave as the result of a gas slug moving through a viscous mud/sulfur lake, though we note that station coverage was limited and topography effects were not accounted for in their study. If the vent opening is vertical, one would expect the vertical flow of material through the conduit to be modeled as a vertical dipole [*Kim et al.*, 2012]; however, a sub-vertically oriented conduit could cause a horizontal dipole component. Similarly, one might expect dipole radiation from a lateral blast, such as for the onset of the 1980 Mount St. Helens eruption [*Lipman and Mullineaux*, 1981]. The ability to constrain a reliable dipole could yield information on ballistic directivity, as well as a more accurate calculation of volume flow rate via acoustic source inversion methods. While the dipole component at Yasur, if it exists, is likely small, larger eruptions could exhibit a larger dipole component, which may affect the calculation of volume flow rate to a greater extent.

3.6.3 Assumptions and Potential Sources of Error

Results highlighted in this study may have important implications for the volcano hazards community interested in calculating eruption mass via infrasound and source directivity, but there are still some notable assumptions and potential sources of error. In our inversion, we assume that once the effects of topography are incorporated into the calculation of 3-D Green's functions, the rest of the complexity in the waveform must be due to the source mechanism. In doing so, we assume a 1-D homogeneous atmosphere, i.e. no winds or density changes. The farthest station we use in this study is roughly 1 km from the active vents, with most stations being within 0.5 km. At these short distances, winds would have to be very strong in order to have a measurable effect on the acoustic waveforms [*Johnson and Ripepe*, 2011; *Kim et al.*, 2015; *Kim and Lees*, 2014]. *Jolly et al.* [2017] note that winds were light (<10 m/s) and in the opposite direction (toward the west-northwest) of the observed directionality here.

We only account for linear sound propagation in our inversions. If nonlinear propagation

was present [e.g. *Marchetti et al.*, 2013], eruptive volumes would be underestimates of their true values [*Anderson et al.*, 2018; *Fee et al.*, 2017]. Therefore, our results should be considered a minimum estimate where true volumes (and therefore masses) could be higher. Our inversion procedure yields low residuals even for high amplitude events (>400 Pa at a distances less than 1 km from the vent). For each of the 80 events, we performed a grid-search for the source location, yielding good agreement with the inferred vent location, meaning that waves likely did not surpass the speed of sound and propagate nonlinearly along most of the path [*Fee et al.*, 2017]. We assume that if a nonlinear component existed, it did not appear to last for a considerable amount of time and, therefore, nonlinear effects were likely weak [e.g. *Fee et al.*, 2017].

Residuals for other recent monopole inversions such as *Kim et al.* [2015] and *Fee et al.* [2017] are smaller (generally <0.15, see *Fee et al.* [2017], Figure 4) than the ones calculated in this study (ranging from 0.08 to 0.26 for the monopole). We suggest this is because i) Yasur may have a stronger dipole component; ii) we have 7 stations (compared to 5 and 6 of previous studies), including one on a tethered aerostat; and iii) we are fitting higher frequencies than the other inversion studies (we filter between 0.1 - 8 Hz, while *Kim et al.* [2015] and *Fee et al.* [2017] use 0.001–2 Hz and 0.05–3 Hz, respectively). This also raises potential concern in assuming only a monopole source in the inversion as the true source mechanism may have higher order terms.

Due to the difficulty in obtaining a very accurate, high-resolution (<2 m) DEM in the visual band, we were forced to stitch together multiple DEMs from different methods (see Section 3.2). Using other methods, such as LiDAR, that are not affected by residual steam and gas would be preferable. We also note that topography can change between explosions over short time scales due to the frequent and explosive nature of Yasur, therefore the DEM should be created near the time of the field experiment. Another limitation of our inversion related to the DEM is that we assume a rigid topography. In reality near-surface layers have lower impedance.

Another potential source of error is the vertical location of the aerostat sensor. While the horizontal location (latitude and longitude) were recorded by the DATA-CUBE digitizer that was hanging from the tethered aerostat with the acoustic sensor, the vertical location was not recorded. Tests in similar atmospheric conditions were performed (outlined in *Jolly et al.* [2017]) and indicate that vertical errors are on the order of 15 m while lateral errors are around 10 m. Given a reasonable speed of sound of 346 m/s, this yields arrival time errors on the order of 0.043 s vertically and 0.029 s horizontally. Our inversion uses a cross correlation component which allows for timing errors up to 0.04s, as well as an individual grid-search for each individual event to help mitigate the effect of aerostat and vent migration location errors on the inversion. We refer to *Jolly et al.* [2017] for a full description of how the vertical locations were calculated. Similarly, the main vents migrated as much as 20 m laterally over short time scales during this deployment [*Jolly et al.*, 2017] as documented by daily UAV flyovers. These changes were also mitigated by this cross correlation component. Additionally, while our method accounts for potential vent migration between events by performing a grid search for the monopole-only inversion, we assume that the source is fixed during an explosion. Visual imagery suggests that the vents did not have measurable spatial variations within the explosions, however, there could be some spatial variation of the acoustic source over the course of a few seconds.

The events used in this study were discrete, short duration, Strombolian-type explosions. Due to the large number of explosions (thousands over the field campaign) and computational time for the FDTD calculation of the Green's functions, we limited our study to 80 explosions with high signal-to-noise ratio and whose waveforms taper back to zero within a six second window. We also did not include time periods when measurable acoustic energy was emanating from both vents simultaneously. Future work should begin to expand acoustic source inversions to include more complex and sustained volcanic activity, including more energetic and hazardous eruptions. Additionally, this work would benefit greatly from a denser set of observations spatially and temporally. Our study also presents some of the first

inversion results using infrasound sensors aboard a tethered aerostat, showing promise for their use in future experiments. Future work should include more infrasound sensors in the vertical direction at varying azimuths and inclinations simultaneously to further constrain acoustic source directionality.

3.7 Conclusions

Two goals in volcano infrasound research we address in this study are (1) to invert acoustic data to infer erupted mass or mass eruption rate from an explosion and (2) to characterize the explosion directional radiation pattern. Here we assess the ability of typical network deployments and a new acoustic multipole inversion scheme that accounts for 3-D topography along with an acoustic sensor aboard a tethered aerostat to provide stable volcanic source constraints. We compare results for inversions that use a monopole-only source, multipole (monopole and dipole) source, propagation across a horizontal plane, and with varying station deployment geometries. We find that the monopole source mechanism is a good approximation for explosions at Yasur volcano as it is stable, reliable, and leads to relatively small waveform residuals when topography is included using numerical Green's functions. The predominantly monopole explosions of Yasur Volcano are in agreement with previous studies of acoustic inversions that account for topography [e.g. *Fee et al.*, 2017; *Kim et al.*, 2015]. We introduce a simple linear trend correction method applied post-inversion to detrend the volume flow rate solution. We find that vents A and C have distinct dipole characteristics, where both volume flow rate and dipole strength are substantially greater for Vent A than for Vent C events. Additionally, the peak dipole strength nearly doubled when the aerostat sensor was included in the source inversion, compared to a very small dipole component when only ground sensors where used. Therefore, 2-D deployments and subsequent source estimates of volcanic explosions may have underestimated and poorly constrained directionality. Our results indicate that inversions for the multipole source mechanism with all three dipole components (Fx, Fy, Fz) are unstable, even with an enhanced network that

included an acoustic sensor on a tethered aerostat. We show that a non-unique multipole solution can be determined and metrics such as rectilinearity can be used to quantify them. We stress that improved waveform fits due to including the dipole components as free parameters in subsequent calculations of AIC do not necessarily imply improved source inversion results. Stability of future acoustic inversions should be explored [e.g. *Bean et al.*, 2008] before dipole components can be considered reliable and interpreted in their entirety. Even though a fully stable, unique source inversion for the dipole is not available here, we find that explosions exhibit directionality and that a monopole source, after topography is accounted for, cannot explain the data fully. First compression amplitude comparisons between data and synthetics show that amplitudes are under-predicted towards the east of the volcano and may therefore not be fully modeled by an isotropic source. This is consistent with ballistic directionality towards the east and likely represents explosion source directionality. The implications for understanding eruption source dynamics and associated hazards, such as the direction in which ballistics are likely to fall, are explored in a paper by [*Fitzgerald et al.*, currently in review]. Furthermore, we reiterate that neglecting effects of topography especially in complex topographic regions such as volcanoes during acoustic waveform inversions leads to overestimation of the volume flow rate [e.g. *Kim et al.*, 2015]. These factors should be considered in future acoustic source studies, particularly if used for volcano monitoring purposes to infer erupted mass of explosions. The effect of limited acoustic wavefield sampling should also be explored further using synthetic tests other real examples, both for volcanic and anthropogenic sources.

3.8 Acknowledgments

Data collection was made possible by the field crew and support from Vanuatu Meteorology and Geohazards Department (Esline Garaebiti, Sandrine Cevuard, Janvion Cevuard, Athanase Worwor, and Julius Mala). Additionally, we thank Richard Johnson, Bruce Christenson, Ben Kennedy, Geoff Gilgour, Nick Key, Rebecca Fitzgerald, Adrian Tessier, Allison

Austin, and Di Christenson for the hard work and help in the field, as well as Chris Gomez, Emma Marcucci, and Richard Buzard for assistance with the DEM creation. The authors would like to thank Jeffrey Johnson and an anonymous reviewer for helpful reviews and comments of this manuscript. This study benefited from useful discussion with Michael West, Carl Tape, Silvio DeAngelis, and Alejandro Diaz-Moreno. This work was supported by NSF Grants EAR-1331084 (AMI and DF),EAR-1620576 (RSM), and EAR-1847736 (RSM), the Alaska Volcano Observatory (AMI and DF), and New Zealand Strategic Science Investment funding (ADJ). Data is available through the IRIS DMC with temporary network code 3E (`https://doi.org/10.7914/SN/3E\_2016`).

3.9 References

Albert, S., D. Fee, P. Firstov, E. Makhmudov, and P. Izbekov (2015), Infrasound from the 2012-2013 Plosky Tolbachik, Kamchatka fissure eruption, *Journal of Volcanology and Geothermal Research*, *307*, 68–78, doi:10.1016/j.jvolgeores.2015.08.019.

Anderson, J. F., J. Johnson, M. Ruiz, H. Ortiz, and B. D. Brand (2018), Diverse eruptive activity revealed by acoustic and electromagnetic observations in the 14 July 2013 intense vulcanian eruption of Tungurahua (Ecuador), *Geophysical Research Letters*, pp. 1–10, doi: 10.1002/2017GL076419.

Assink, J., A. Le Pichon, E. Blanc, M. Kallel, and L. Khemiri (2014), Evaluation of wind and temperature profiles from ECMWF analysis on two hemispheres using volcanic infrasound, *Journal of Geophysical Research*, *119*(14), 8659–8683, doi:10.1002/2014JD021632.

Aster, R. C., B. Borchers, and C. H. Thurber (2013), *Parameter Estimation and Inverse Problems*, 2 ed., 1–360 pp., Elsevier.

Battaglia, J., J. P. Métaxian, and E. Garaebiti (2016a), Short term precursors of Strombolian explosions at Yasur volcano (Vanuatu), *Geophysical Research Letters*, *43*(5), 1960–1965, doi:10.1002/2016GL067823.

Battaglia, J., J. P. Métaxian, and E. Garaebiti (2016b), Families of similar events and modes of oscillation of the conduit at Yasur volcano (Vanuatu), *Journal of Volcanology and Geothermal Research*, *322*, 196–211, doi:10.1016/j.jvolgeores.2015.11.003.

Bean, C., I. Lokmer, and G. O'Brien (2008), Influence of near-surface volcanic structure on long-period seismic signals and on moment tensor inversions: Simulated examples from Mount Etna, *Journal of Geophysical Research: Solid Earth*, *113*(B8), doi:10.1029/2007JB005468.

Caplan-Auerbach, J., A. Bellesiles, and J. K. Fernandes (2010), Estimates of eruption velocity and plume height from infrasonic recordings of the 2006 eruption of Augustine Volcano, Alaska, *Journal of Volcanology and Geothermal Research*, *189*(1-2), 12–18, doi: 10.1016/j.jvolgeores.2009.10.002.

Chouet, B., N. Hamisevicz, and T. R. McGetchin (1974), Photoballistics of volcanic jet activity at Stromboli, Italy, *Journal of Geophysical Research*, *79*(32), 4961–4976, doi: 10.1029/jb079i032p04961.

Chouet, B., P. Dawson, and A. Arciniega-Ceballos (2005), Source mechanism of Vulcanian degassing at Popocatépetl Volcano, Mexico, determined from waveform inversions of very long period signals, *Journal of Geophysical Research: Solid Earth*, *110*(7), 1–20, doi: 10.1029/2004JB003524.

Dalton, M. P., G. P. Waite, I. M. Watson, and P. A. Nadeau (2010), Multiparameter quantification of gas release during weak Strombolian eruptions at Pacaya Volcano, Guatemala, *Geophysical Research Letters*, *37*(9), doi:10.1029/2010GL042617.

De Angelis, S., O. D. Lamb, A. Lamur, A. J. Hornby, F. W. von Aulock, G. Chigna, Y. Lavallée, and A. Rietbrock (2016), Characterization of moderate ash-and-gas explosions at Santiaguito volcano, Guatemala, from infrasound waveform inversion and thermal infrared measurements, *Geophysical Research Letters*, *43*(12), 6220–6227, doi: 10.1002/2016GL069098.

Delle Donne, D., M. Ripepe, G. Lacanna, G. Tamburello, M. Bitetto, and A. Aiuppa (2016), Gas mass derived by infrasound and UV cameras: Implications for mass flow rate, *Journal of Volcanology and Geothermal Research*, *325*, 169–178, doi:10.1016/j.jvolgeores.2016.06.015.

Fee, D., and R. S. Matoza (2013), An overview of volcano infrasound: From hawaiian to plinian, local to global, *Journal of Volcanology and Geothermal Research*, *249*, 123–139, doi:10.1016/j.jvolgeores.2012.09.002.

Fee, D., P. Izbekov, K. Kim, A. Yokoo, T. Lopez, F. Prata, R. Kazahaya, H. Nakamichi, and M. Iguchi (2017), Eruption mass estimation using infrasound waveform inversion and ash and gas measurements: Evaluation at Sakurajima Volcano, Japan, *Earth and Planetary Science Letters*, *480*, 42–52, doi:10.1016/j.epsl.2017.09.043.

Fitzgerald, R., B. Kennedy, C. Gomes, T. Wilson, B. Simons, G. Leonard, A. Jolly, R. Matoza, and E. Garabiti (), Ballistic deposition from a frequently erupting volcano: Yasur Volcano, Vanuatu, *Volcanica (in review)*.

Gerst, A., M. Hort, P. R. Kyle, and M. Vöge (2008), 4D velocity of Strombolian eruptions and man-made explosions derived from multiple Doppler radar instruments, *Journal of Volcanology and Geothermal Research*, *177*(3), 648–660, doi:10.1016/j.jvolgeores.2008.05.022.

Johnson, J., R. Aster, K. R. Jones, P. Kyle, and B. McIntosh (2008), Acoustic source characterization of impulsive Strombolian eruptions from the Mount Erebus lava lake, *Journal of Volcanology and Geothermal Research*, *177*(3), 673–686, doi:10.1016/j.jvolgeores.2008.06.028.

Johnson, J. B. (2003), Generation and propagation of infrasonic airwaves from volcanic explosions, *Journal of Volcanology and Geothermal Research*, *121*(1-2), 1–14, doi:10.1016/S0377-0273(02)00408-0.

Johnson, J. B., and A. J. C. Miller (2014), Application of the Monopole Source to Quantify Explosive Flux during Vulcanian Explosions at Sakurajima Volcano (Japan), *Seismological Research Letters*, *85*(6), 1163–1176, doi:10.1785/0220140058.

Johnson, J. B., and M. Ripepe (2011), Volcano infrasound: A review, *Journal of Volcanology and Geothermal Research*, *206*(3-4), 61–69, doi:10.1016/j.jvolgeores.2011.06.006.

Johnson, J. B., J. Anderson, O. Marcillo, and S. Arrowsmith (2012), Probing local wind and temperature structure using infrasound from Volcan Villarrica (Chile), *Journal of Geophysical Research Atmospheres*, *117*(17), 1–16, doi:10.1029/2012JD017694.

Jolly, A., B. Kennedy, M. Edwards, P. Jousset, and B. Scheu (2016), Infrasound tremor from bubble burst eruptions in the viscous shallow crater lake of White Island, New Zealand, and its implications for interpreting volcanic source processes, *Journal of Volcanology and Geothermal Research*, *327*, 585–603, doi:10.1016/j.jvolgeores.2016.08.010.

Jolly, A. D., R. S. Matoza, D. Fee, B. M. Kennedy, A. M. Iezzi, R. H. Fitzgerald, A. C. Austin, and R. Johnson (2017), Capturing the Acoustic Radiation Pattern of Strombolian Eruptions using Infrasound Sensors Aboard a Tethered Aerostat, Yasur Volcano, Vanuatu, *Geophysical Research Letters*, *44*(19), 9672–9680, doi:10.1002/2017GL074971.

Kim, K., and J. M. Lees (2011), Finite-difference time-domain modeling of transient infrasonic wavefields excited by volcanic explosions, *Geophysical Research Letters*, *38*(6), doi:10.1029/2010GL046615.

Kim, K., and J. M. Lees (2014), Local Volcano Infrasound and Source Localization Investigated by 3D Simulation, *Seismological Research Letters*, *85*(6), 1177–1186, doi:10.1785/0220140029.

Kim, K., and A. Rodgers (2016), Waveform inversion of acoustic waves for explosion yield estimation, *Geophysical Research Letters*, *43*(13), 6883–6890, doi:10.1002/2016GL069624.

Kim, K., J. M. Lees, and M. Ruiz (2012), Acoustic multipole source model for volcanic explosions and inversion for source parameters, *Geophysical Journal International*, *191*(3), 1192–1204, doi:10.1111/j.1365-246X.2012.05696.x.

Kim, K., D. Fee, A. Yokoo, and J. M. Lees (2015), Acoustic source inversion to estimate volume flux from volcanic explosions, *Geophysical Research Letters*, *42*(13), 5243–5249, doi:10.1002/2015GL064466.

Kremers, S., Y. Lavallée, J. Hanson, K. U. Hess, M. O. Chevrel, J. Wassermann, and D. B. Dingwell (2012), Shallow magma-mingling-driven Strombolian eruptions at Mt. Yasur volcano, Vanuatu, *Geophysical Research Letters*, *39*(21), doi:10.1029/2012GL053312.

Kremers, S., J. Wassermann, K. Meier, C. Pelties, M. van Driel, J. Vasseur, and M. Hort (2013), Inverting the source mechanism of Strombolian explosions at Mt. Yasur, Vanuatu, using a multi-parameter dataset, *Journal of Volcanology and Geothermal Research*, *262*, 104–122, doi:10.1016/j.jvolgeores.2013.06.007.

Lacanna, G., and M. Ripepe (2013), Influence of near-source volcano topography on the acoustic wavefield and implication for source modeling, *Journal of Volcanology and Geothermal Research*, *250*, 9–18, doi:10.1016/j.jvolgeores.2012.10.005.

Lamb, O. D., S. De Angelis, and Y. Lavallée (2015), Using infrasound to constrain ash plume rise, *Journal of Applied Volcanology*, *4*(1), doi:10.1186/s13617-015-0038-6.

Le Pichon, A., E. Blanc, D. Drob, S. Lambotte, J. X. Dessa, M. Lardy, P. Bani, and S. Vergniolle (2005), Infrasound monitoring of volcanoes to probe high-altitude winds, *Journal of Geophysical Research Atmospheres*, *110*(13), 1–12, doi:10.1029/2004JD005587.

Lighthill, J. (1978), *Waves in Fluids*, Cambridge University Press.

Lighthill, M. J. (1952), On sounds generated aerodynamically. I. General Theory, *Proceedings of the Royal Society A, Mathematical, Physical and Engineering Science*, *211*(1107), 564–587.

Lipman, P. W., and D. R. Mullineaux (Eds.) (1981), *The 1980 Eruption of Mount St. Helens, Washington*, Geological Survey Professional Paper 1250.

Marchetti, E., M. Ripepe, D. Delle Donne, R. Genco, A. Finizola, and E. Garaebiti (2013), Blast waves from violent explosive activity at Yasur Volcano, Vanuatu, *Geophysical Research Letters*, *40*(22), 5838–5843, doi:10.1002/2013GL057900.

Marcillo, O., J. B. Johnson, and D. Hart (2012), Implementation, characterization, and evaluation of an inexpensive low-power low-noise infrasound sensor based on a micromachined differential pressure transducer and a mechanical filter, *Journal of Atmospheric and Oceanic Technology*, *29*(9), 1275–1284, doi:10.1175/JTECH-D-11-00101.1.

Matoza, R., D. Fee, D. Green, and P. Mialle (2019), Volcano Infrasound and the International Monitoring System, in *Infrasound Monitoring for Atmospheric Studies*, edited by A. L. Pichon, E. Blanc, and A. Hauchecorne, chap. 33, pp. 1023–1077, Springer, doi:10.1007/978-3-319-75140-5{_}33.

Matoza, R. S., D. Fee, M. A. Garcés, J. M. Seiner, P. A. Ramón, and M. A. Hedlin (2009), Infrasonic jet noise from volcanic eruptions, *Geophysical Research Letters*, *36*(8), doi:10.1029/2008GL036486.

Matoza, R. S., D. Fee, T. B. Neilsen, K. L. Gee, and D. E. Ogden (2013), Aeroacoustics of volcanic jets: Acoustic power estimation and jet velocity dependence, *Journal of Geophysical Research: Solid Earth*, *118*(12), 6269–6284, doi:10.1002/2013JB010303.

Matoza, R. S., D. Fee, and T. M. Lopez (2014), Acoustic Characterization of Explosion Complexity at Sakurajima, Karymsky, and Tungurahua Volcanoes, *Seismological Research Letters*, *85*(6), 1187–1199, doi:10.1785/0220140110.

McKee, K., D. Fee, A. Yokoo, R. S. Matoza, and K. Kim (2017), Analysis of gas jetting and fumarole acoustics at Aso Volcano, Japan, *Journal of Volcanology and Geothermal Research*, *340*, doi:10.1016/j.jvolgeores.2017.03.029.

Meier, K., M. Hort, J. Wassermann, and E. Garaebiti (2016), Strombolian surface activity regimes at Yasur volcano, Vanuatu, as observed by Doppler radar, infrared camera and infrasound, *Journal of Volcanology and Geothermal Research*, *322*, 184–195, doi:10.1016/j.jvolgeores.2015.07.038.

Métrich, N., P. Allard, A. Aiuppa, P. Bani, A. Bertagnini, H. Shinohara, F. Parello, A. Di Muro, E. Garaebiti, O. Belhadj, and D. Massare (2011), Magma and volatile supply to post-collapse volcanism and block resurgence in Siwi caldera (Tanna Island, Vanuatu arc), *Journal of Petrology*, *52*(6), 1077–1105, doi:10.1093/petrology/egr019.

Montabetti, J. F., and E. R. Kanasewich (1970), Enhancement of teleseismic body wave phases with a polarisation analysis, *Geophys. J. R. Astron. Soc.*, *21*(July), 119–129.

Morse, P. M., and K. U. Ingard (1986), *Theoretical Acoustics*, 1–927 pp., Princeton University Press, Princeton, NJ.

O'Brien, G. S., I. Lokmer, and C. J. Bean (2010), Statistical selection of the "best" seismic source mechanisms from inversions of synthetic volcanic long-period events, *Journal of Geophysical Research: Solid Earth*, *115*(9), 1–13, doi:10.1029/2009JB006958.

Ohminato, T., B. A. Chouet, P. B. Dawson, and S. Kedar (1998), Waveform inversion of very-long-period impulsive signals associated with magmatic injections beneath Kilauea Volcano, Hawaii, *J. Geophys. Res.*, *103*(10), 23,839–23,862, doi:10.1029/98JB01122.

Ortiz, H. D., J. B. Johnson, P. G. Ramón, and M. C. Ruiz (2018), Using infrasound waves to monitor tropospheric weather and crater morphology changes at Volcán Tungurahua, Ecuador, *Journal of Volcanology and Geothermal Research*, *349*, 205–216, doi:10.1016/j.jvolgeores.2017.11.001.

Ostashev, V. E., D. K. Wilson, L. Liu, D. F. Aldridge, N. P. Symons, and D. Marlin (2005), Equations for finite-difference, time-domain simulation of sound propagation in moving inhomogeneous media and numerical implementation, *The Journal of the Acoustical Society of America*, *117*(503), doi:10.1121/1.1841531.

Pierce, A. D. (1989), *Acoustics: An Introduction to Its Physical Properties and Applications*, 1–678 pp., Acoustical Society of America, Melville, NY.

Rodgers, A. J., A. Pitarka, N. A. Petersson, B. Sjögreen, and D. B. McCallen (2018), Broadband (0–4 Hz) Ground Motions for a Magnitude 7.0 Hayward Fault Earthquake With Three-Dimensional Structure and Topography, *Geophysical Research Letters*, *45*(2), 739–747, doi:10.1002/2017GL076505.

Rowell, C. R., D. Fee, C. A. Szuberla, K. Arnoult, R. S. Matoza, P. P. Firstov, K. Kim, and E. Makhmudov (2014), Three-dimensional volcano-acoustic source localization at Karymsky Volcano, Kamchatka, Russia, *Journal of Volcanology and Geothermal Research*, *283*, 101–115, doi:10.1016/j.jvolgeores.2014.06.015.

Simkin, T., L. Siebert, L. McClelland, D. Bridge, C. Newhall, and J. H. Latter (1981), *Volcanoes of the world: A regional directory, gazetteer, and chronology of volcanism during the last 10,000 years.*, US Hutchinson Ross Publishing.

Wang, S. (1996), Finite-difference time-domain approach to underwater acoustic scattering problems, *Journal of the Acoustical Society of America*, *99*(4), 1924–1931, doi:10.1121/1.415375.

Witsil, A. J., and J. B. Johnson (2018), Infrasound explosion and coda signal investigated with joint analysis of video at Mount Erebus, Antarctica, *Journal of Volcanology and Geothermal Research*, *357*, 306–320, doi:10.1016/j.jvolgeores.2018.05.002.

Woulff, G., and T. R. McGetchin (1976), Acoustic noise from volcanos - theory and experiment, *Geophysical Journal of the Royal Astronomical Society*, *45*(3), 601–616, doi:10.1111/j.1365-246X.1976.tb06913.

Chapter 4

Seismo-Acoustic Characterization of Mount Cleveland Volcano Explosions[6]

4.1 Abstract

Transient explosions can produce large, ash-rich volcanic plumes that pose great hazard to aviation, yet often have few precursory geophysical signals. Mount Cleveland is one of the most active volcanoes in the Aleutian Arc with at least 64 explosions since December 2011. We characterize the seismo-acoustic signals from explosions at Mount Cleveland over a period of four years using local instrumentation. While the seismic explosion signals were similar, the acoustic signals varied between explosions, with some explosions exhibiting a single main compressional phase while other explosions had multiple compressions in a row. The time lag between seismic and acoustic arrivals varies considerably (up to 2.20 s) at a single station ∼3 km from the vent. We apply a variety of methods to explore the potential contributions to this variable time lag from atmospheric conditions, nonlinear propagation, and source depth within the conduit. This variable time lag has been observed elsewhere, but no clear explanation exists. Our results indicate that while changes in atmospheric conditions can explain some of the variation in acoustic arrival time relative to the seismic, substantial residual time lag variations often still exist. Additionally, nonlinear propagation modeling results do not yield a change in the onset time of the acoustic arrival with source amplitudes comparable (and larger) to Cleveland explosions. We find that seismic cross-correlation between events and particle motion analysis suggests that a varying explosion source depth within the conduit likely plays a dominant role in the observed variations in seismo-acoustic time lag. Explosion source depths appear to range from very shallow depths down to ∼1.5-2 km beneath the summit. Understanding the seismo-acoustic time lag and the subsequent indication of a variable explosion source depth may help inform explosion source modeling for Mount Cleveland, which is relatively not well-understood. We show that even

[6]Iezzi, A.M., Fee, D., Haney, M.M., and Lyons, J.J. (*in review*) Seismo-Acoustic Characterization of Mount Cleveland Volcano Explosions, *Frontiers in Earth Science*

with a single co-located seismic and acoustic sensor that clips sometimes, it is possible to provide meaningful interpretations on the explosion source depth which may help monitoring agencies understand the volcanic system during future times of unrest.

4.2 Introduction

Coupled seismic and acoustic analyses can be used to help understand shallow to subaerial explosion sources, including buried chemical explosions [e.g. *Arrowsmith et al.*, 2010; *Jones et al.*, 2014; *Blom et al.*, in review] and volcanic eruptions [e.g. *Johnson and Aster*, 2005; *Petersen and McNutt*, 2007; *Wech et al.*, 2018]. While some volcanoes are heavily instrumented and monitored, many eruptions occur in remote regions where minimal local monitoring equipment exists. Therefore, the ability to characterize a volcanic system with limited equipment [e.g. a single seismo-acoustic pair of sensors, *McKee et al.*, 2018] is valuable to the volcano monitoring community.

Vulcanian eruptions tend to be violent in nature due to the formation of a rigid dome or plug at the top of the conduit allowing for a buildup of pressure beneath. The explosive fragmention of this dome or plug results in ash-rich volcanic plumes that are hazardous to aviation and pyroclastic fallout that can impact local communities or observers. Infrasound recordings of Vulcanian eruptions are typically characterized by short duration, high-amplitude signals with the potential for jetting or sustained tremor to occur for several minutes after the initial blast [*Fee and Matoza*, 2013]. Sakurajima volcano is often viewed as a classic example of a Vulcanian system and its seismic and infrasonic explosion signals have been well studied over many years [e.g. *Tameguri et al.*, 2002; *Yokoo et al.*, 2009; *Fee et al.*, 2014; *Kim et al.*, 2015; *Fee et al.*, 2017]. *Tameguri et al.* [2002] describe the "bottom-up" explosion source model of Sakurajima as beginning with an isotropic expansion at a few kilometers depth, whose pressure waves propagate up the conduit, inducing an expansion of the lava cap or plug (viewed as a small increase in pressure on the infrasound sensor) followed by the main acoustic explosion signal. In contrast, a "top-down" model is sometimes

considered, where the explosion initiates near the surface due to the pressurized build-up and failure of the plug or lava dome. This model also causes a very long period earthquake (VLP) at depth [*Lyons and Waite*, 2011]. The seismo-acoustic signals at Mount Cleveland, Alaska, appear Vulcanian in nature [*De Angelis et al.*, 2012], yet due to its remote setting, the volcanic system is not well-understood.

Mount Cleveland is one of the most active volcanoes in the Aleutian Arc, with recent activity characterized by nearly continuous degassing and elevated surface temperatures, punctuated by short-lived ash-rich explosions that destroy small domes [*De Angelis et al.*, 2012; *Dixon et al.*, 2017; *Werner et al.*, 2017; *www.avo.alaska.edu*]. Prompt and accurate characterization of explosions is essential due to the ash hazard to aviation. Satellite observations of cloud heights resulting from these explosions can be limited because of meteorological clouds as well as latency issues, so geophysical instrumentation is often used for explosion characterization. The first local instrumentation, two stations, was installed at Mount Cleveland in the summer of 2014, so permanent local monitoring data are limited. Temporary, non-telemetered deployments help better understand the volcanic system, such as the one from 2015-2016 [*Werner et al.*, 2020; *Haney et al.*, in prep; *Power et al.*, in prep]. Remote infrasound recordings supplement the local instrumentation for monitoring [e.g. *De Angelis et al.*, 2012; *Iezzi et al.*, 2019a]. While the Alaska Volcano Observatory (AVO) makes observations of Mount Cleveland at the time of each explosion, detailed characterization of the seismo-acoustics signals from Cleveland has not been performed. Here we use local seismo-acoustic instrumentation to better understand and characterize the explosions and volcanic system, and take a holistic look at trends in the data from numerous explosions.

A notable feature of the seismo-acoustic observations from Mount Cleveland explosions over a four-year time period is that the difference between the acoustic arrival time in relation to the seismic arrival at station CLES (referred to as the "seismo-acoustic time lag") is found to vary by up to 2.20 s. If the path and propagation conditions between the explosion source and the receiver are the same, the relative timing between the seismic and

acoustic arrivals are expected to also be the same. However, a variable time delay between seismic and acoustic arrivals is observed at many volcanoes similar to Cleveland, implying that the path between the explosion source and the receiver may also change. This relative timing between the seismic and acoustic arrivals at a co-located seismo-acoustic station has been used to help constrain the explosion source location within the conduit of Vulcanian systems, although full explanations are still elusive. *Yamada et al.* [2016] found that the arrival time differences between the seismic and acoustic waveforms vary between 0.5 to 2.1 s at a distance of 5.1 km from the vent of Lokon-Empung volcano, Indonesia. They propose that the cause of the discrepancies does not appear to solely be the atmosphere based on a simple calculation of sound speed given realistic temperature and wind conditions (T = 293 K, winds +/- 5 m/s), and therefore may be due to source depth changes within the conduit. *Ruiz et al.* [2006] noted varying time lags of ∼9.3-12.6 s (3.516 km from vent) at Tungurahua volcano, Ecuador, which they contend supports a model where explosions occur at different depths within the shallow portion of the conduit (<200 m depth). *Ruiz et al.* [2006] presented a model consisting of a spatially fixed point source with a variable velocity of the pressure wave in the conduit, but deemed it less likely than the spatially varying source depth. *Sahetapy-Engel et al.* [2008] use the thermo-acoustic delay times to calculate explosion source depths between 100 and 600 m below the vent at Santiaguito volcano, Guatemala. More recently, *Wallace et al.* [2020] observe single station seismo-acoustic time lags between ∼6 to 17 s (2.1 km from the vent) at Santiaguito over a four-year study, and conclude that the larger time differences suggest a potentially deeper fragmentation source, which is consistent with their petrologic analyses. However, *Wallace et al.* [2020] do not explore the variability further to calculate corresponding depths of the seismo-acoustic time lag and assumed fragmentation depth. While these studies explore a few of the factors that may affect the seismo-acoustic time delay, none combine the three effects we assume most plausible: changes in the atmosphere, nonlinear propagation, and a variable source depth within the conduit.

In this manuscript, we perform the first local seismic and acoustic analyses and characterization of explosions at Mount Cleveland between 2014 and 2018. We identify three main factors that may affect the seismo-acoustic time lag, and explore their relative contributions: atmospheric conditions, nonlinear propagation, and source depth within the conduit. We apply a variety of methods on acoustic, seismic, and coupled seismo-acoustic observations aimed at extracting as much information as possible about the remote Mount Cleveland using a single co-located seismo-acoustic station. We then combine the methods to interpret their meaning for the volcanic system and how it may be evolving through time.

4.3 Mount Cleveland

Mount Cleveland is a remote stratovolcano located in the central Aleutians on Chuginadak Island that is roughly 8.5 km in diameter near its base and 1.73 km in elevation above sea level [*Miller et al.*, 1998]. As of June 2020, Cleveland has exploded 64 times since December 25, 2011, making it one of the most frequently active volcanoes in Alaska and the U.S. Recent activity is characterized by nearly continuous degassing and elevated surface temperatures, as well as short-lived ash-rich explosions that destroy small domes [*Dixon et al.*, 2017; *Werner et al.*, 2017; *www.avo.alaska.edu*]. The closest inhabited community is the village of Nikolski, located 75 km to the east of the volcano on Umnak Island. Due to its remote location, the main hazards from Mount Cleveland explosions are to aviation and scientists visiting the island, with at least ten explosions since 2014 resulting in detectable ash plumes to an altitude surpassing 15,000 ft [*www.avo.alaska.edu*]. Explosions occur with little to no known precursory activity suggesting explosion sources to be shallow and/or aseismic.

Previous studies on Mount Cleveland include those using satellite observations [*Simpson et al.*, 2002; *Dean et al.*, 2004; *Gu et al.*, 2005; *Worden et al.*, 2014; *Wang et al.*, 2015; *Werner et al.*, 2017], sparse summit gas flights [*Werner et al.*, 2017, 2020], temporary seismic deployments [*Janiszewski et al.*, 2020; *Power et al.*, in prep; *Haney et al.*, in prep], and

long range infrasound recordings [*De Angelis et al.*, 2012; *Iezzi et al.*, 2019a]. *Janiszewski et al.* [2020] used receiver functions to find a low seismic velocity zone below Cleveland with a minimum vertical extent of 10-17.5 km below sea level that is <5 km in diameter. This suggests a vertically extensive magma storage region with a lack of sharp horizontal boundaries at the top and bottom of this region [*Janiszewski et al.*, 2020]. *Janiszewski et al.* [2020] note that their results are consistent with a well-developed open volcanic conduit system, which may help explain the general lack of precursory and general seismicity at Cleveland. A recent study by *Werner et al.* [2020] uses a combination of volcanic gas emission rates and melt inclusion compositions from 2016 and find evidence that magma may be residing and degassing in a vertically extensive conduit region ranging in depth between 0.5 and 3.0 km below the summit. *Power et al.* [in prep] focused on characterizing the general seismicity at Mount Cleveland and located hypocenters of volcano-tectonic earthquakes using a temporary seismic deployment in 2015-2016. *Haney et al.* [in prep] perform moment tensor inversions on the three explosions that occurred during the same 2015-2016 deployment, finding a volumetric source in the VLP band (0.25-0.5 Hz) located 400-640 m above sea level (depths of ∼1090-1330 m beneath the summit). *Werner et al.* [2017] utilized gas emissions, thermal output, and lava extrusion rates to inform their interpretations on the Cleveland volcanic system. They suggest that the lack of precursory geophysical signals are due to small magma volumes, slow ascent rates, and low magma viscosity. *Werner et al.* [2017] also note that the persistently high thermal output of Mount Cleveland, even in inter-eruptive periods, is indicative of hot magma high in the conduit and suggest that convection causes the continued presence of shallow magma in the upper conduit. Previous studies such as *De Angelis et al.* [2012] and *Iezzi et al.* [2019a] have analyzed infrasound signals from Cleveland explosions. However, these studies were based on long-range signals where source observations are complicated by propagation in the atmosphere.

4.3.1 Monitoring Data

Prior to the installation of the local instruments at Mount Clevelend, the closest seismic station was ∼75 km away (Nikolski) and infrasound monitoring was predominantly done using the Dillingham infrasound array [992 km away, *De Angelis et al.*, 2012; *Iezzi et al.*, 2019a] as well as ground-coupled airwaves (GCAs) on nearby seismic networks [*De Angelis et al.*, 2012; *Fee et al.*, 2016]. Cleveland is also monitored by AVO using satellite imagery, both in the visible and infrared bands, but the region is regularly cloudy which often obscures smaller explosion plumes below the cloud deck. Temporary seismic deployments, such as a year-long deployment from 2015-2016 [*Janiszewski et al.*, 2020; *Haney et al.*, in prep; *Power et al.*, in prep], have also been used to gain information about Mount Cleveland, though they were not telemetered in real time.

The first permanent local instrumentation was installed in the summer of 2014, allowing for more detailed studies of the volcano than previously possible. This instrumentation currently consists of two stations, each with multiple geophysical instruments. Station CLES (52.8235°N, 169.8951°W) is located 3.5 km east of the summit (Figure 4.1) and consists of a Trillium Compact (120 s period) broadband seismometer sampled at 50 Hz as well as an infrasound sensor. Beginning in August 2014, the infrasound sensor was a VDP-5 sampled at 50 Hz which was replaced in July 2016 by a Chaparral 60UHP sensor sampled at 100 Hz. Station CLCO, located on Concord Point 15.6 km east-southeast of the summit, has a broadband and short period seismometer, web camera, and a 5-element infrasound array (Figure 4.1). In this study we focus on explosion signals recorded by the closest station (CLES) with co-located seismic and infrasound sensors. We do not use station CLCO for most of the analyses due to the increased influence of path effects over the longer distance, lower signal-to-noise ratio (SNR), and the station being roughly in line with station CLES and the summit, thereby not increasing azimuthal coverage around the explosion source. Additionally, part of the purpose of this study is to determine how much information about the explosion mechanism can be extracted from a single co-located seismic and infrasound

sensor pair, which can sometimes be the only local instrumentation at remote volcanoes.

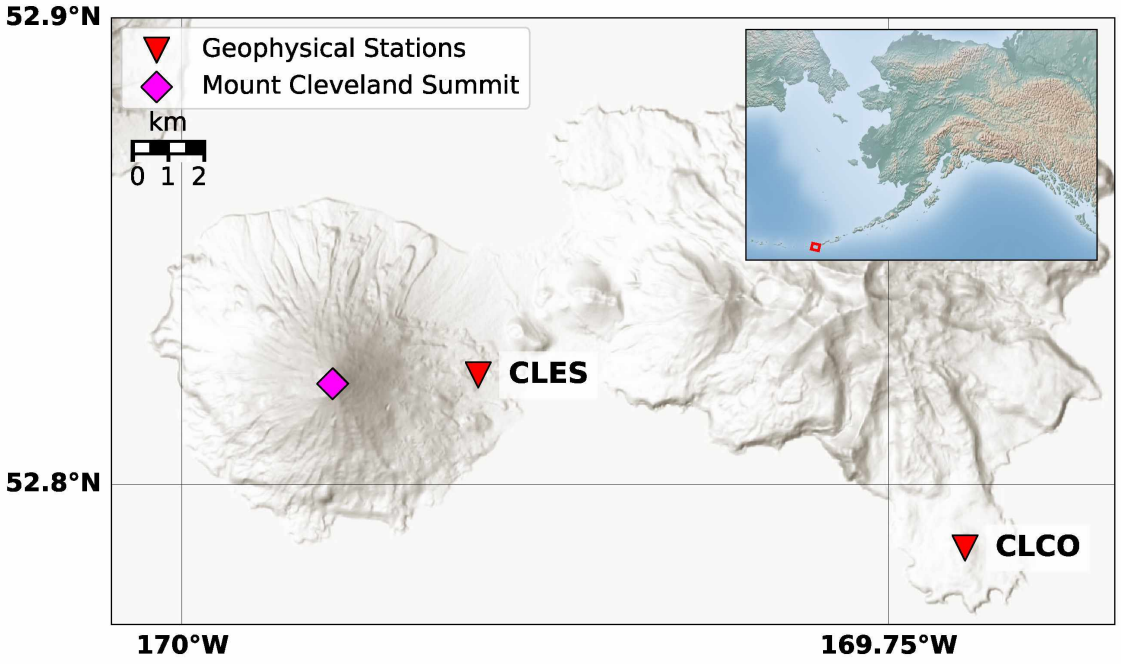

Figure 4.1: Map of Mount Cleveland and the surrounding area. The summit is denoted by a pink diamond, while the two geophysical stations CLES (3.5 km from summit) and CLCO (15.4 km from summit) are denoted by inverted red triangles. Inset map shows location of Mount Cleveland (red square) in relation to the state of Alaska.

4.4 Explosion Characterization

AVO began consistently numbering Mount Cleveland explosions on December 25, 2011 with monitoring capabilities consisting of remote infrasound arrays, GCAs on regional seismic networks, and satellite imagery [*De Angelis et al.*, 2012]. From 2011 onward, most of the activity at Cleveland consisted of cycles of dome building and subsequent dome destruction via explosive eruptions. This study focuses on 21 explosions between November 2014 and May 2018 which corresponds to Explosions 37 through 58 of the current AVO catalog. The explosion numbers considered here are limited by the installation in the summer of 2014 and a long term data outage that began in September 2018. Detailed information on the explosions used in this study are found in Table 4.1. The seismic and infrasound traces at station

CLES for these explosions are shown in Figure 4.2A and 4.2B, respectively. Explosions are, in general, short-duration Vulcanian blasts, sometimes with infrasonic tremor occurring for several minutes after the initial explosion signal. The characteristics of the seismic signal produced by explosions consists of a low amplitude compressional first motion on the vertical component (Figure 4.2A) and positive first motion on the radial component (outward). The peak velocity for the first 9 seconds of the explosion signal on the vertical component ranges between 109 and 376 μm/s (Table 4.1). For most explosions, the higher frequency GCA shows up on the seismometer after >9.5 seconds from the initial arrival, also showing the same variable seismo-acoustic time lag observed on the infrasound sensor. Unlike the repetitive nature of the seismic signals, the characteristics of the infrasound signal varies substantially between explosions. Peak pressures at 3.5 km distance range between 21 and 260+ Pa (Table 4.1) and were short-duration. Note that 260 Pa represented the maximum pressure range of the infrasound sensor for much of the time period, thus numerous signals are "clipped". Some explosions exhibit a single main compressional phase (e.g. Explosions 43-49, Figure 4.2B), while other explosions have multiple compressions in a row (e.g. Explosion 42, Figure 4.2B). A few explosions have a preceding low amplitude infrasound phase <0.5 s prior to the main explosion onset (e.g. Explosion 40, Figure 4.2B).

The state of dome emplacement in Vulcanian systems affects the pressurization in the shallow conduit system and thus influences the explosion process. The repose time (number of days since previous explosion), as calculated from explosion dates provided by AVO [*www.avo.alaska.edu*], varied between 2 and 257 days over the 4-year study period but generally decreased with time (Figure 4.3B). In some instances, for example between Explosions 45-49 and 55-58, the repose time remained relatively similar at less than 54 and 22 days, respectively. AVO reported that at least 9 of the 21 explosions resulted in eruption plumes visible in satellite imagery greater than 15,000 ft in altitude [*www.avo.alaska.edu*], reinforcing the desire and importance to characterize Mount Cleveland explosions. When possible, AVO records observations of the lava dome in Cleveland's crater using satellite imagery. There

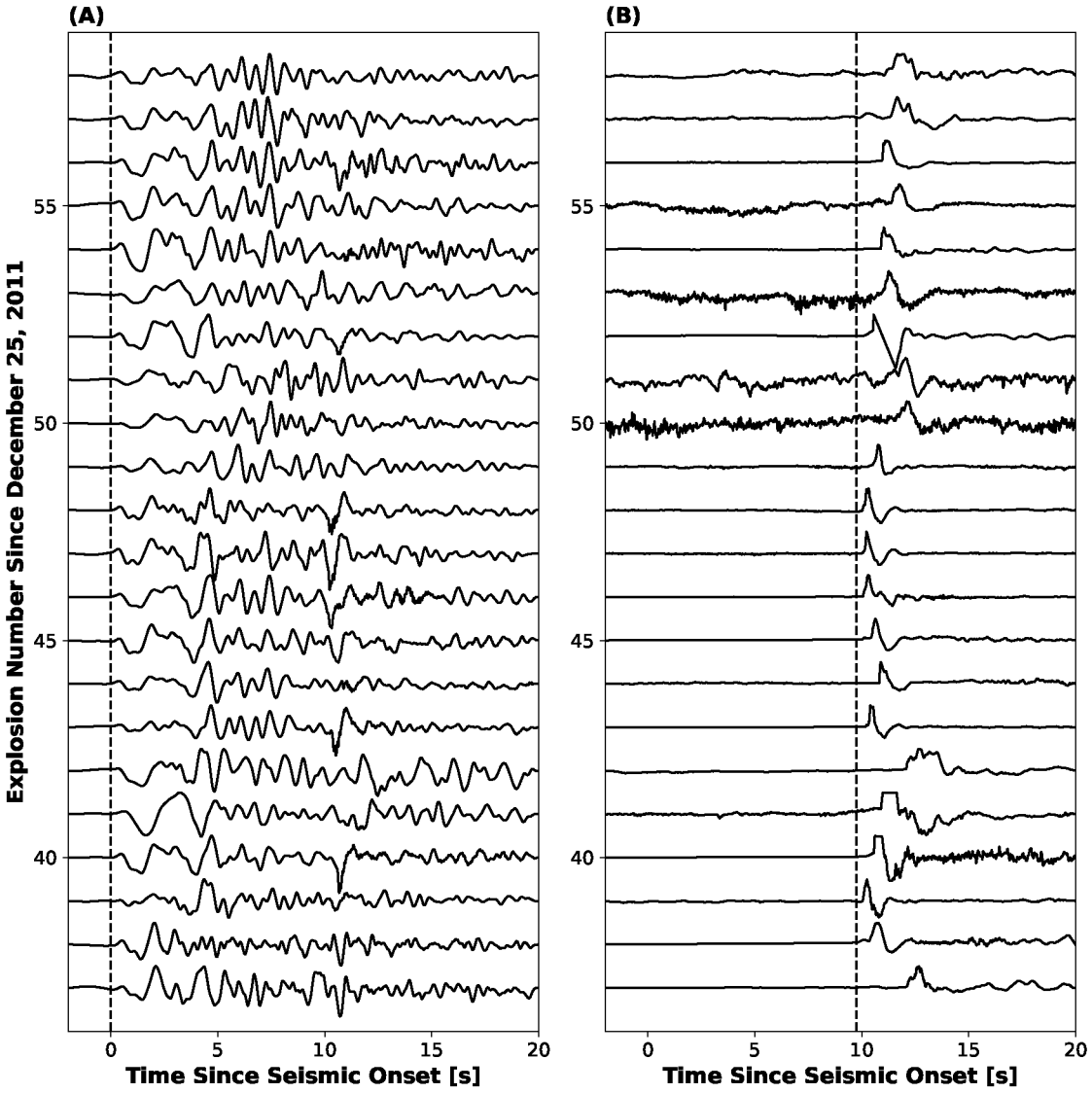

Figure 4.2: Normalized, unfiltered **(A)** seismic and **(B)** infrasound waveforms for station CLES for explosions used in this study (Explosions 37-58). Waveforms are aligned where time zero corresponds to the onset of the explosion signal on the seismometer. The higher frequency ground-coupled airwave can be seen in **(A)** for most explosions arriving after ~9.75 seconds. Vertical line in **(B)** represents the earliest acoustic arrival of 9.75 s.

appears to be no clear relationship between whether there is no visible dome at the bottom of the crater, dome growth, or a static dome (i.e. dome that has stopped growing) prior to an explosion (Figure 4.3A). Explosions 37-58 (November 2014 to May 2018) are also plotted in Figure 4.3A, showing the varying repose time over the course of the study period. Of the 16 explosions we have decent satellite observations before and after the explosion, 8 explosions

destroyed an existing dome, 2 explosions left at least part of the dome intact, and 4 explosions occurred with no confirmed dome prior to the explosion. Dome observations, including whether there was no dome, a growing dome, or a static dome prior to explosion, as well as the dome area (and therefore height calculation) used in the propagation calculations, are subject to the availability of clear satellite imagery.

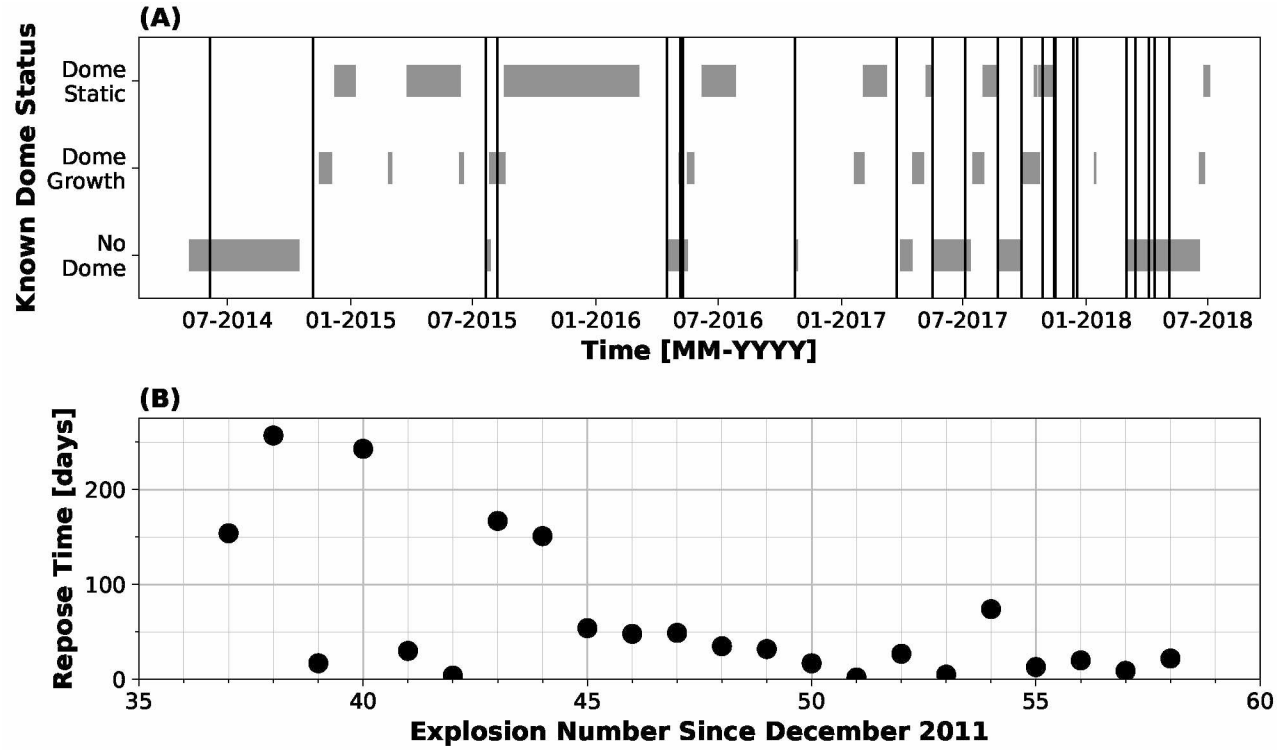

Figure 4.3: Dome emplacement and explosion relationship from mid-2014 to mid-2018. **(A)** Dome status confirmed by satellite imagery. Categories consist of (i) "no dome": when there was no visible dome within the crater, (ii) "dome growth": when a dome was actively growing in size, and (iii) "dome static": when there was a dome that had ceased growing. Vertical lines denote explosions, which vary in repose time over the course of the study period. **(B)** Repose time [in days] prior to each explosion as a function of explosion number.

We note two important caveats for CLES data analysis. The first is that amplitude- and frequency-based analysis can only be used for some of the explosions due to clipping of the CLES infrasound sensor for larger explosions (5 explosions, see Figure 4.2B). Additionally, a GCA appears on CLES seismic data for most explosions (see Figure 4.2A), so some analyses are limited to the first ∼9 seconds of the explosion signal recorded by the seismometer.

Station CLCO is farther away where propagation effects are likely to be more substantial. Therefore, arrival time-based analysis of Cleveland acoustic signals at station CLES is the most complete and reliable parameter, more so than amplitude- or frequency-based calculations at either station.

4.5 Seismo-Acoustic Time Lag Investigation

The observed variable seismo-acoustic time lag (tt_{obs}) can be defined as the time difference between the explosion onset and the arrival of the pressure wave that is recorded on the infrasound sensor (tt_{infra}) and the explosion onset and the arrival time at the seismic station (tt_{seis})

$$tt_{obs} = tt_{infra} - tt_{seis} \tag{4.1}$$

The acoustic arrival time in relation to the seismic arrival of the explosion signal at station CLES is found to vary up to 2.20 s for the 21 explosions investigated, as shown by Figure 4.2B where traces are aligned to the seismic arrival. The seismic and acoustic arrival times are picked on unfiltered vertical seismic and infrasound data, respectively, first using a short term average long term average algorithm (STA/LTA, STA length = 0.01 s, LTA length = 0.3 s) then values are manually refined. These seismo-acoustic time lags vary as a function of explosion number (Figure 4.4A) and span a range of 9.75 to 11.95 s at a distance of 3.5 km from the vent. The distribution of seismo-acoustic time lags for the 21 explosions investigated is skewed towards lower time lags, with a mean time lag of 10.56 s and median of 10.25 s (Figure 4.4B).

A breakdown of the seismo-acoustic propagation paths is shown by Figure 4.5. The seismic wave travels directly from the explosion source (Figure 4.5, Location 1) to station CLES (Figure 4.5, Location 4). This distance is dependent on the explosion source depth. However, because the seismic velocity is an order of magnitude greater than the acoustic velocity, the exact distance does not have a major effect on the seismic travel time (tt_{seis}). We also assume that the seismic velocity is constant and does not change between explosions

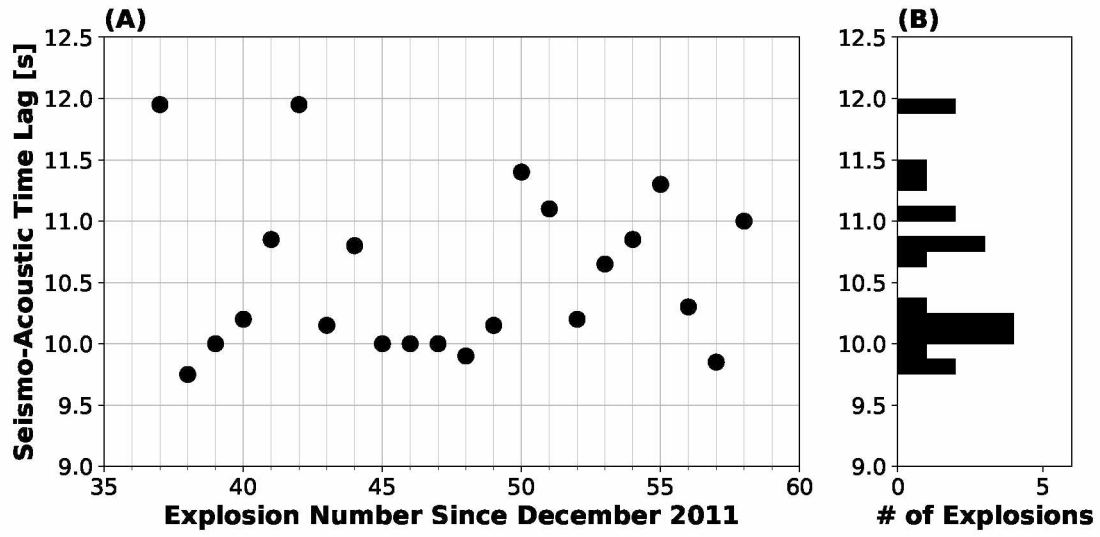

Figure 4.4: Seismo-acoustic time lag for Mount Cleveland explosions **(A)** as a function of explosion number and **(B)** as a histogram of the time lag distribution. Histogram bins are 0.125 s in width.

or along the path. The calculation of tt_{seis} is shown by the following equation.

$$tt_{seis} = \frac{d_{seis}}{v_{seis}} \tag{4.2}$$

Using values of $v_{seis} = 2500$ m/s and $d_{seis} = 3800$ m (assuming an explosion source near the summit), the seismic travel-time between the explosion and receiver (tt_{seis}) is 1.52 s. The wave recorded on the infrasound sensor has a more complex propagation path. It propagates from the explosion source in the conduit (Figure 4.5, Location 1) to the bottom of the crater (Figure 4.5, Location 2) at acoustic velocity within the conduit ($v_{conduit}$) over a distance equivalent to the source depth (d_{source}). Then, the wave propagates from the bottom of the crater (Figure 4.5, Location 2) to the top of the crater (Figure 4.5, Location 3) then to station CLES (Figure 4.5, Location 4) at the effective sound speed (c_{eff}) (Section 4.5.1).

The travel time of the pressure wave that is recorded on the infrasound sensor (tt_{infra}), and therefore variable observed acoustic time lag (tt_{obs}), is most likely affected by the atmosphere (tt_{atm}, Section 4.5.1), potential nonlinear propagation ($tt_{nonlinear}$, Section 4.5.2), and

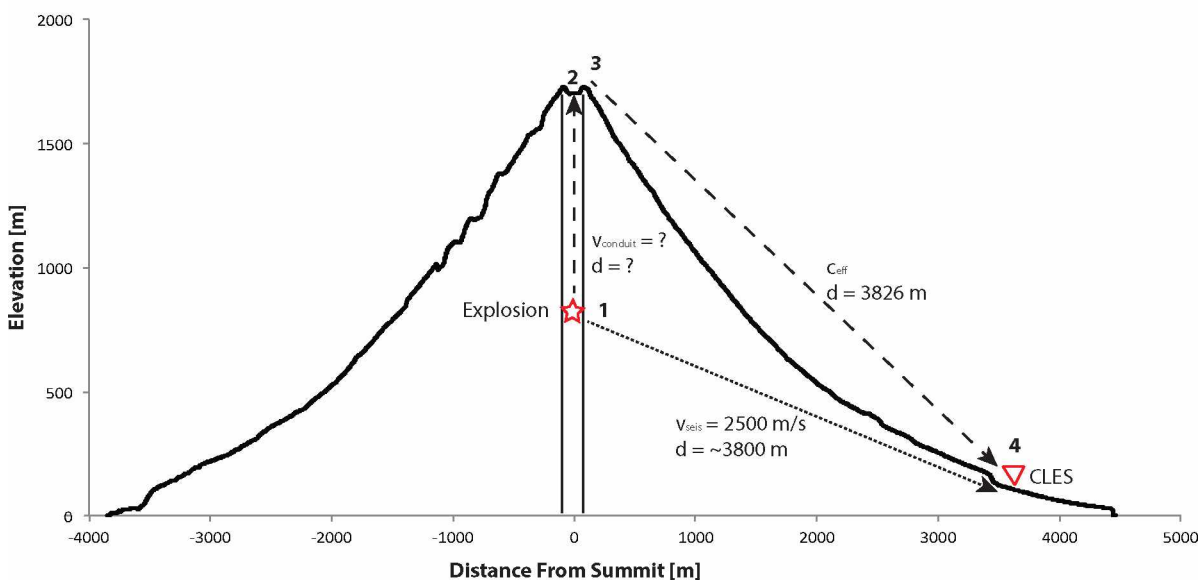

Figure 4.5: Breakdown of propagation segments for the seismic and infrasound paths. Location 1 is the explosion, Location 2 is the bottom of the crater (dome surface), Location 3 is the summit, and Location 4 is station CLES. The signal recorded by the infrasound sensor (dashed line) propagates from Location 1 through Locations 2, 3, and 4, while the initial signal recorded by the seismometer (dotted line) travels directly from Location 1 to Location 4. Elevation profile from the Polar Geospatial Center ArcticDEM [*Porter et al.*, 2018].

source depth within the conduit (d_{source}) coupled with potentially varying conduit material velocities ($tt_{conduit}$, Section 4.5.3). We summarize the various contributions on the arrival time recorded by the infrasound sensor (tt_{infra}) as follows, and discuss them in subsequent sections:

$$tt_{infra} = tt_{atm} - \Delta tt_{nonlinear} + tt_{conduit} \tag{4.3}$$

4.5.1 Atmospheric Effects

Variations in wind and temperature affect the propagation velocity of infrasound. These effects have been the source of multiple recent studies of volcanic explosions in Alaska [e.g. *De Angelis et al.*, 2012; *Iezzi et al.*, 2019a; *Schwaiger et al.*, 2019, 2020]. Infrasound propagates in the atmosphere at the speed of sound, defined as

$$c = \sqrt{\gamma RT} \tag{4.4}$$

where γ is the specific heat ratio, R is the universal gas constant, and T is the temperature [*Pierce*, 1981]. In a realistic moving atmosphere, this adiabatic sound speed (EQ 4.4) is modified by the vector component of the horizontal wind velocity in a particular direction ($\vec{u} \cdot \vec{v}$) and is termed the effective sound speed (c_{eff}), defined as [*Fee and Matoza*, 2013; *Salomons*, 2001]

$$c_{eff} = c + \vec{u} \cdot \vec{v} \tag{4.5}$$

For Cleveland explosions registered at station CLES, the shortest observed time lag is 9.75 s (requiring a c_{eff} of 0.392 km/s) while the longest time lag is 11.95 s (requiring a c_{eff} of 0.320 km/s). This spread in effective sound speeds is unlikely, even considering the range of extreme wind and temperatures at Cleveland, as it would require winds of approximately 70 m/s. This would create very high noise levels at the site. We apply two different methods for inferring the contribution of the atmosphere on acoustic arrival time at CLES (i.e. estimating a unique c_{eff} for each explosion).

The first method to better understand the possibility of the atmosphere causing the variable observed seismo-acoustic time lags uses an atmospheric reconstruction model, AVO-G2S [*Schwaiger et al.*, 2019], as no local weather stations or in-situ atmospheric data are available. The atmospheric conditions at Mount Cleveland are reconstructed at the closest 6-hour increment for each explosion. Within AVO-G2S we use the National Centers for Environmental Prediction (NCEP) Reanalysis data [*Kistler et al.*, 2001] for the lower atmosphere with resolution of 2.5 degrees spatially and 6 hours temporally. Once the atmosphere is reconstructed, a 1D stratified atmospheric profile at the location of Mount Cleveland (52.822°N, 169.945°W) is extracted from the reconstruction. The scalar value for effective sound speed (c_{eff}) above the vent (z = 1.8 km) in the direction of CLES (86.6° from N) is used to calculate the predicted acoustic travel time from the summit to CLES based on atmospheric

conditions at the time of each explosion:

$$tt_{atm} = \frac{d}{c_{eff}} \tag{4.6}$$

where $d = 3.826$ km (the hypotenuse distance from the summit to station CLES) plus the hypotenuse distance from the top of the dome to the crater rim (Figure 4.5, Locations 2 to 3). This distance is calculated by converting the dome area observed in satellite imagery by AVO to a dome height above the crater floor, using the ArcticDEM digital elevation model [*Porter et al.*, 2018] for crater shape. We note that the presence or absence of a dome only changed the infrasonic path length by ∼40 m at most (depending on the size of the dome), which at a reasonable acoustic speed corresponds to 0.12 s.

The second method leverages the use of the explosion signal arrival time at one of the elements from the infrasound array (CLCO, element 1) that is at a similar azimuth from the vent as station CLES. The azimuths from the Cleveland summit to stations CLES and CLCO are 86.6° and 109.5°, respectively, so the azimuthal difference between the two stations is 22.9°. The infrasound arrival time of the explosion at station CLCO is picked and the two acoustic arrival times are subtracted. Using the distance between the stations (12.33 km) and the difference in arrival times, the effective sound speed based on station arrival times is calculated using Equation 4.6.

Our results indicate that AVO-G2S-derived c_{eff} values are systematically lower than c_{eff} values found using the acoustic arrival time difference between CLES and CLCO by 0-25 m/s (Figure 4.6A). The observed travel time is calculated as the time lag between the seismic and infrasound arrivals at CLES, plus seismic travel time from the conduit to CLES (tt_{seis}, Equation 4.2). Both the observed and predicted (tt_{atm}) travel time as a function of explosion number are shown in Figure 4.6B. It is clearly seen that that the relatively large variation in observed acoustic travel times is not well predicted by either the atmospheric conditions of global reanalysis files (model-based) or calculations between CLES and CLCO

arrivals (data-based). For the rest of our analyses, we choose the second method for effective sound speed (c_{eff}) calculation. If the seismo-acoustic time lags were solely due to changes in the atmosphere, we would expect a very strong correlation with the effective sound speed. However, there is only a weak negative relationship between the two values (Figure 4.6C). From these analyses, we conclude that while changing atmospheric conditions may partially contribute to the variable seismo-acoustic time lag observed at Cleveland, there is a lack of evidence that it is the main cause for the observed variations.

4.5.2 Nonlinear Propagation

A second factor that may contribute to a change in acoustic propagation time is nonlinear propagation, which is often neglected in local infrasound studies but mentioned as a potential source of error and uncertainty [e.g. *Fee et al.*, 2017; *Iezzi et al.*, 2019b]. However, the potential impact of nonlinear propagation on the arrival time ($tt_{nonlinear}$) should be quantified, as nonlinear waves with supersonic sound speeds have been observed for volcanic explosions [e.g. *Yokoo and Ishihara*, 2007; *Marchetti et al.*, 2013].

For very high amplitude acoustic sources such as some Vulcanian explosions, the sound waves produced may travel faster than the speed of sound (i.e. supersonic) and propagate nonlinearly. In nonlinear propagation, the waveform distorts as it travels, where the compressional phase travels faster than the rarefaction, potentially steepening into a shock wave [*Atchley*, 2005; *Reichman et al.*, 2016; *Maher et al.*, 2020]. This shock wave is often described by the Friedlander equation [*Friedlander*, 1946], which defines the pressure of a shock wave ($p(t)$) as

$$p(t) = P_s e^{-\frac{t}{t^*}} \left(1 - \frac{t}{t^*}\right) \tag{4.7}$$

where P_s is the source overpressure and t^* is the relaxation time (time when the rarefaction begins after the compression returns the ambient pressure). This equation for a theoretical blast wave using t^*=0.75 is shown as Figure 4.7A, along with Explosion 44 from Cleveland. A recent study by *Maher et al.* [2020] performed detailed analysis of local infrasound data from

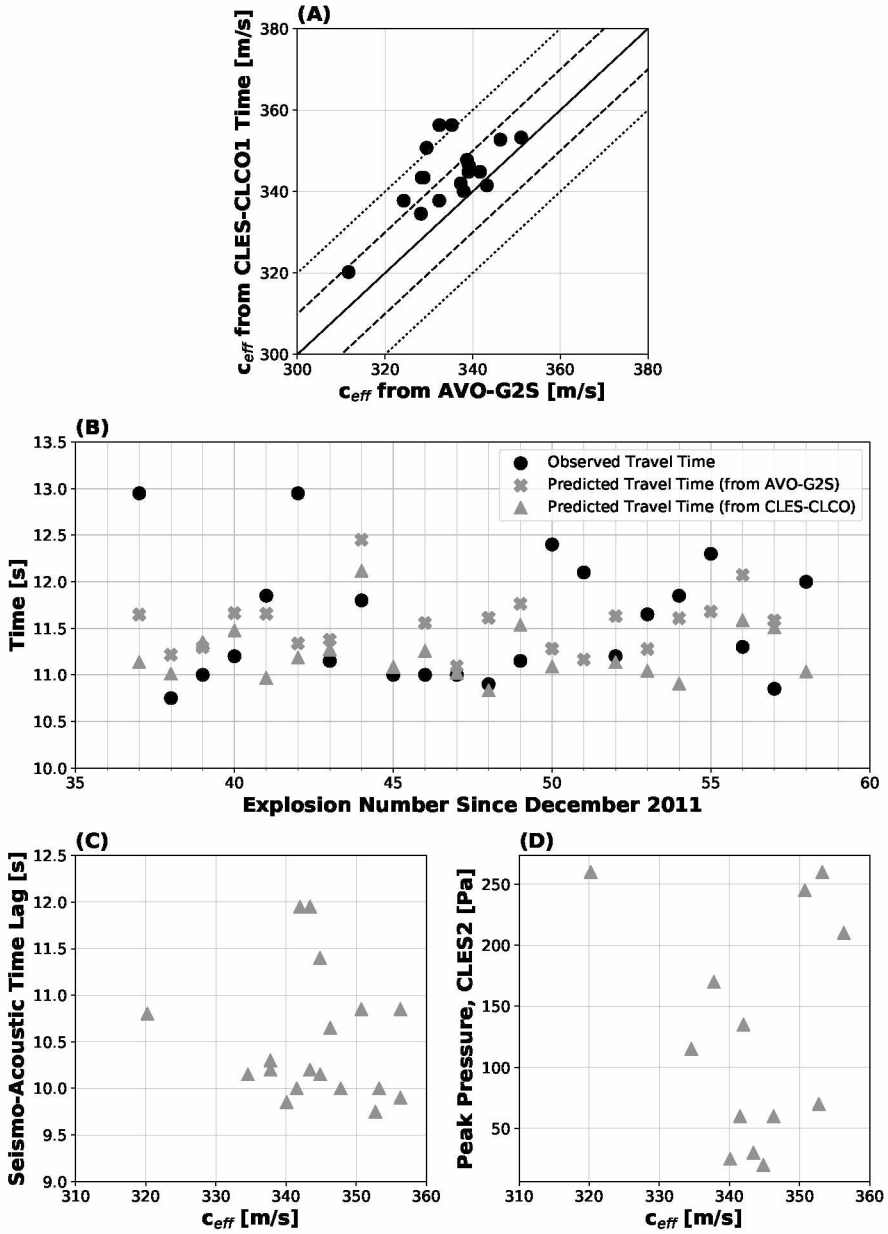

Figure 4.6: Predicted acoustic travel time based on atmospheric effects. **(A)** Derived c_{eff} from the two methods, using AVO-G2S and the acoustic arrival time difference between stations CLES and CLCO1. The solid line is 1:1 (values are exactly the same), with dotted lines being successively offset by 10 m/s. **(B)** Observed (tt_{obs}, black dots) acoustic travel time, predicted (tt_{atm}) acoustic travel time from the summit to station CLES using AVO-G2S (gray crosses), and predicted (tt_{atm}) acoustic travel time from the acoustic arrival time difference between stations CLES and CLCO1 (gray triangles). **(C)** Seismo-acoustic travel time vs effective sound speed (c_{eff}) for each explosion, showing a weak negative relationship. **(D)** Peak pressure at station CLES vs effective sound speed (c_{eff}) for each explosion that did not clip the infrasound sensor. No correlation indicates that the larger amplitude explosions did not happen to occur during times of higher effective sound speeds.

Sakurajima volcano and the potential impact of spectral energy transfer to higher frequencies due to nonlinear propagation. They find that the effects of nonlinear propagation have a second-order impact on source quantification [*Maher et al.*, 2020], whereas the effects of wind and topography may be more influential on the recorded waveform. *de Groot-Hedlin* [2016] find that nonlinearity has a greater effect on the frequency of the waveform as compared to the amplitude as infrasound propagates away from the source. To our knowledge, there has not been a thorough study on the impact on arrival time due to nonlinear propagation for volcanic explosions.

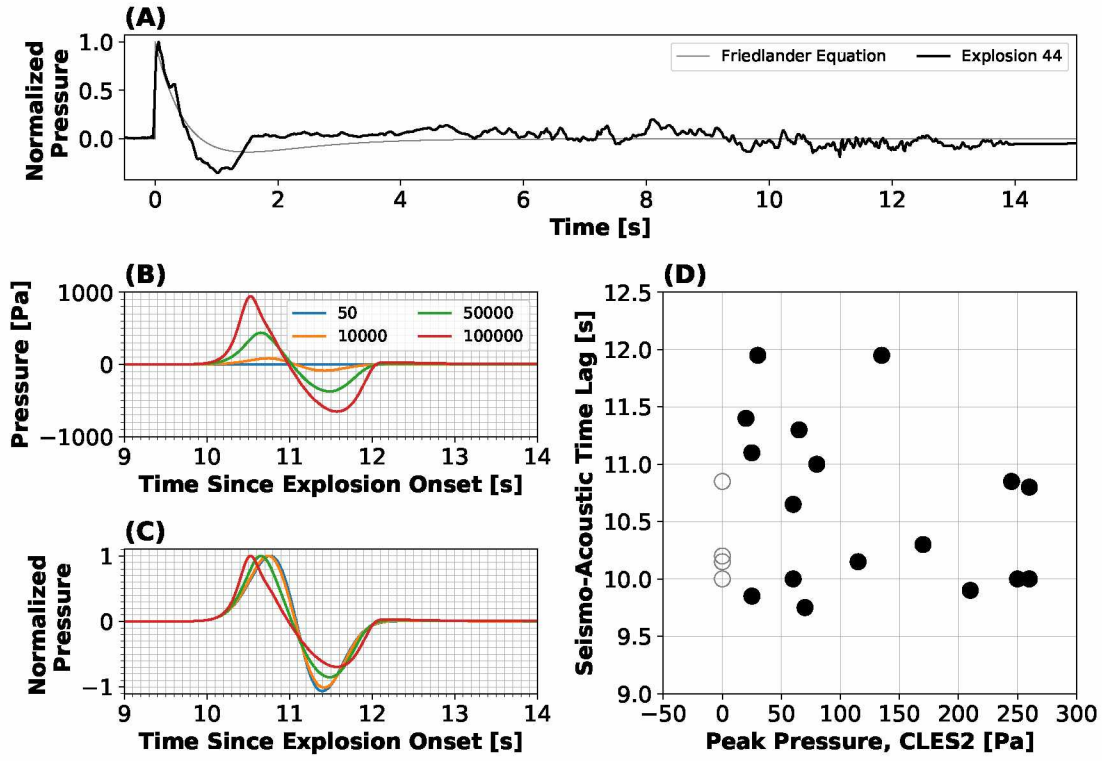

Figure 4.7: Potential contributions on the seismo-acoustic time lag from nonlinear propagation. **(A)** Friedlander Equation for a blast wave (gray) with normalized Explosion 44 waveform (black). **(B)** FDTDWave simulation results over a flat plane for source pressures between 50 Pa and 100 kPa at a range of 3.8 km from the source. **(C)** Normalized FDTDWave simulation results from the previous subplot. **(D)** Seismo-acoustic time lag vs peak pressure at CLES for explosions that did not clip the infrasound sensor. Open circles represent the time lag for explosions that clipped the infrasound sensor, plotted at a peak pressure of zero.

We note that peak pressures at CLES do not appear to strongly correlate with seismo-acoustic time lags (Figure 4.7D), indicating nonlinear propagation (if present) has minimal effect on the seismic-acoustic time lag for Cleveland explosions. This is consistent with the findings of *Maher et al.* [2020], where nonlinear propagation was found to be a secondary effect on the observed waveform. However, it does appear that the highest peak pressures and those that clipped the infrasound sensor (Figure 4.7D, open circles) had lower seismo-acoustic time lags. Additionally, we investigate the connection between higher amplitude explosions and the atmospheric conditions. The lack of correlation between the peak pressure at station CLES (for events that did not clip the sensor) and the effective sound speed (Figure 4.6D), indicates that the larger amplitude explosions did not occur during times of higher effective sounds speeds.

We use a 2D finite-difference time-domain (FDTD) code, FDTDWave [*de Groot-Hedlin*, 2016], to model the potential impact of nonlinear propagation on the acoustic arrival time. Our simulations involve propagating a source with a maximum frequency of 2.0 Hz over a flat plane to a range of 20 km with synthetic receivers spaced every 100 m. We set the transition from nonlinear to linear propagation at 1% ambient pressure, though we note that testing was performed varying this parameter between 0.5-5% with no change in our results. We input source pressures ranging from 50 Pa to 100 kPa and note that current modeling capabilities using this code are limited to a linear, Gaussian input source.

Nonlinear propagation modeling results for a synthetic receiver at 3.8 km from the source (slant distance from the Cleveland summit to station CLES) show the expected distortion due to increasingly nonlinear propagation (Figure 4.7B,C). As the source pressure increases, the compression travels faster while the rarefaction travels relatively slower, similar to results in *Maher et al.* [2020]. Therefore, the arrival time of the peak compression decreases with higher source pressure (Figure 4.7C). However, even using extreme values of source peak overpressures (red line in Figure 4.7C, approximately 1000 Pa at the range of CLES), we are not able to form a full shock front or detect a noticeable change in arrival time of the

explosion onset.

4.5.3 Source Depth Within the Conduit

The effects of the atmosphere and nonlinear propagation can be reasonably approximated using available data and modeling. Therefore, in previous sections we constrained these values first and assume all residual time discrepancies are due to a variable explosion source depth (d_{source}) within the conduit and/or conduit velocity ($v_{conduit}$). Explosion source depth and conduit conditions are less well-understood than other aforementioned factors affecting the seismo-acoustic time lag.

The travel time of a pressure wave in the conduit from the explosion depth to the bottom of the crater can be estimated by:

$$tt_{conduit} = \frac{d_{source}}{v_{conduit}} \tag{4.8}$$

Due to the poorly understood conditions within the conduit and limited seismo-acoustic data, we investigate the potential variable explosion source depth using four techniques: volcano acoustic seismic ratio (VASR), arrival times differences between low and high frequency components of seismic data, seismic cross-correlation between explosions, and seismic particle motion analysis. We are not able to estimate the actual source depth due to the limited data.

4.5.3.1 Volcano Acoustic Seismic Ratio (VASR)

Volcanic explosion energy couples into both the ground as seismic energy and atmosphere as acoustic energy. We follow the methods of *Johnson and Aster* [2005] to calculate the relative partitioning of the energy that is recorded as seismic and acoustic waves, termed Volcano Acoustic Seismic Ratio (VASR). Lower VASR may suggest a deeper explosion source within the conduit; however, caution should be exercised in this interpretation as there are many other factors that can affect the energy partitioning. Note, this can only be used for

explosions that did not clip the infrasound sensor.

Seismic energy ($E_{seismic}$) for an isotropic source located at the top of a homogeneous halfspace can be calculated using [*Boatwright*, 1980; *Johnson and Aster*, 2005]

$$E_{seismic} = 2\pi r^2 \rho_{earth} v_{seis} \frac{1}{A} \int S^2 U(t)^2 dt \tag{4.9}$$

where r is the distance between source and receiver, S is the seismic site response, A is the attenuation, ρ_{earth} is the volcano density, and U^2 is the squared particle velocity. Similarly, the acoustic energy ($E_{acoustic}$) radiated can be calculated by integrating over a hemispherical surface, assuming a monopole source and homogeneous atmosphere [e.g. *Firstov and Kravchenko*, 1996; *Johnson*, 2003; *Vergniolle et al.*, 2004; *Johnson and Aster*, 2005]

$$E_{acoustic} = \frac{2\pi r^2}{\rho_{atmos} c_{atmos}} \int \triangle P(t)^2 dt \tag{4.10}$$

where ρ_{atmos} is the air density, c_{atmos} is the speed of sound, and $\triangle P$ is the excess pressure.

We follow suggestions of *Johnson and Aster* [2005] and use a bandpass filter between 0.5–12 Hz for both acoustic and seismic traces, $\rho_{atmos} = 1.2$ kg/m^3, $c_{atmos} = 340$ m/s, $\rho_{earth} = 2000$ kg/m^3, and $v_{seis} = 2500$ m/s. Note since we do not have good estimates of the seismic attenuation or site response, the values we calculate are only relative to other Cleveland explosions (termed "relative VASR", VASR$_{rel}$) since we set S and A equal to one (i.e. the seismic portion is not true "energy") and should therefore not be compared with values from other studies. A similar method was used in *Fee et al.* [2020]. Energies are calculated over the first 9 seconds of the explosion signal onset (infrasound calculation is delayed by the seismo-acoustic time lag) since GCAs appear for most explosions on the seismic data after this time.

VASR$_{rel}$ is variable for the explosions investigated here (Figure 4.8A), with Explosions 45-47 having the highest VASR$_{rel}$ and the rest of the explosions being lower. While there is no trend observed between low values of VASR$_{rel}$ and the seismo-acoustic time lag (Fig.

4.8b), the three explosions with the highest VASR_{rel} values (Explosions 45-47) have low seismo-acoustic time lags and none of the explosions with higher seismo-acoustic time lags exhibited high values of VASR_{rel}.

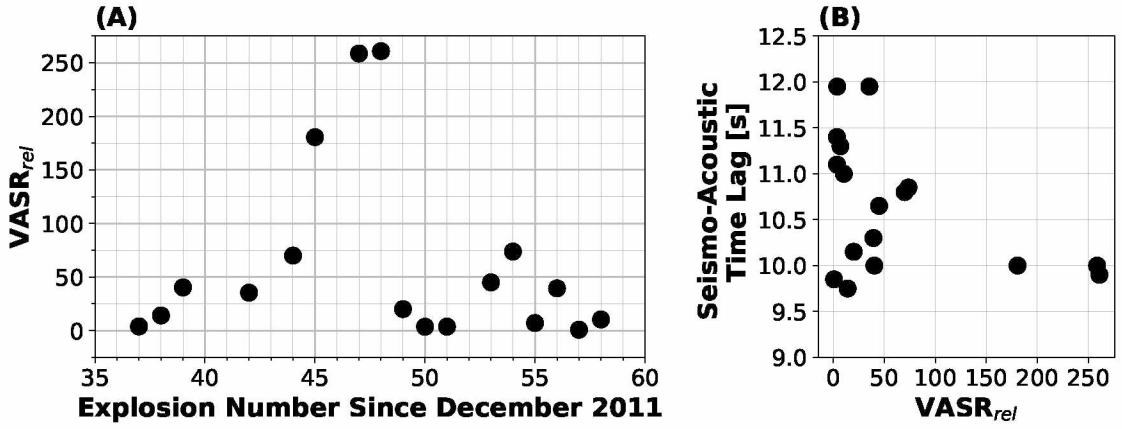

Figure 4.8: Relative VASR (VASR_{rel}) for explosions that did not clip the infrasound sensor **(A)** as a function of explosion number and **(B)** compared to the seismo-acoustic time lag.

4.5.3.2 Arrival Time of Various Seismic Frequency Components

If a bottom-up explosion model is valid at Cleveland, we might expect to see multiple arrivals at the seismometer, the first corresponding to the initiation of the explosion at depth and a second arrival when the dome/plug is exploded at the surface. The frequency content between these arrivals may differ due to the different source processes and be detectable. To examine this possibility the vertical component of CLES seismic data are bandpass filtered in the "low" frequency band (0.25 - 0.5 Hz, which are the lowest frequencies with explosion signals and the frequency band of seismic source inversions by *Haney et al.* [in prep]) and a "high" frequency band (3 - 25 Hz) for example Explosion 45 in Figure 4.9. The frequency at the onset starts with energy <5 Hz, and gradually increases to < 7 Hz over the course of a few seconds (Figure 4.9A). The low and high frequency bands of the seismic explosion signal are shown in the time domain in Figure 4.9B, where the onset time appears similar, and the ground-coupled airwave is clearly visible as the high frequency arrival after ∼10 seconds.

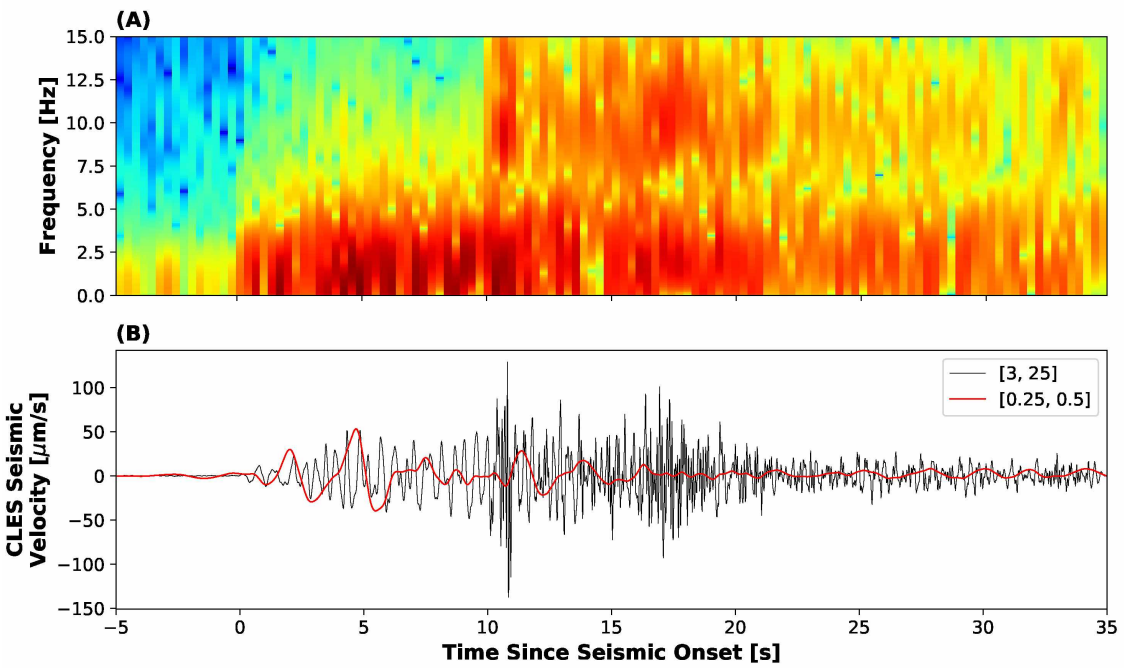

Figure 4.9: Frequency content breakdown for example Explosion 45. **(A)** Spectrogram of the explosion signal between 0-15 Hz. **(B)** Seismic waveform of the explosion signal in the time domain for multiple frequency bands. The ground-coupled airwave is visible as the high frequency arrival ∼10 seconds after the explosion onset.

For most explosions, the low and high energy frequency band arrival times occur at or near the same time. The spectrograms show a gradual addition of higher frequency content (Figure 4.9A), but lack a distinct, quantifiable secondary seismic onset. We find that some explosions, such as Explosion 41, have a measurably different start time for the low frequency seismic energy that precedes the high frequency component, but this is a minority among the explosions in the study. Additionally, there are no examples of the opposite occurring, where the high frequency onset measurably precedes the lower frequency energy. Because of the lack of a clear secondary seismic arrival, we do not include this frequency analysis in our exploration of potential changing explosion source depth.

4.5.3.3 Seismic Cross-Correlation

Correlation between seismic waveforms can be used to help determine precise seismic source locations and identify similar source properties from the recorded waveforms. The premise is that seismicity that occurs in the same location may have very similar waveforms due to the seismicity experiencing the same propagation effects over the same path between the source and receiver [*Green and Neuberg*, 2006; *Varley et al.*, 2010; *Waldhauser and Ellsworth*, 2000]. Using each explosion as a template, we cross-correlate the vertical trace with the rest of the explosions. The seismic data are trimmed to an 10.5 s window surrounding each explosion, starting 1.5 seconds prior to the explosion onset and ending 9 s after to avoid the GCAs. The data are bandpass filtered between 0.1 - 1.0 Hz.

The correlation of the seismic waveforms between explosions is variable. An example of the similarity between the highly correlated Explosions 45 and 46 (correlation value of 0.91) in this frequency band is shown by Figure 4.10A. Cross-correlation results for all explosions are shown in Figure 4.10B, where the clear diagonal line represents each event correlated with itself (cross-correlation value of 1). There is a section of higher correlation values in the center of Figure 4.10B (Explosions 43-48), which not only occur sequentially in time, but also have a fairly stable time lag around 10.0 seconds (Figure 4.4). We discuss this further in Section 4.6.1. Explosion 45 appears to have high correlation values with the other explosions (Figure 4.10B) as well as a time lag close to the median (Figure 4.4A). The cross-correlation values between Explosion 45 and all other explosions are compared with the seismo-acoustic time lag of each explosion (Figure 4.10C). The relationship has a "V" shape, where the cross-correlation value increases slightly/remains constant from the lowest time lag, reaches a maximum correlation value at the time lag associated with Explosion 45 (time lag = 10.00 s, cross-correlation value = 1), then the cross-correlation value decreases again as the time lag continues to increase. This indicates that explosion waveforms become more similar as they approach the time lag of Explosion 45. This pattern occurs, to some extent, for most of

the explosions with time lags around 10 seconds. Therefore, explosions with similar seismic waveforms, as measured by the cross-correlation value between them, may occur at similar depths within the conduit, assuming that the seismo-acoustic time lag is related to the source depth.

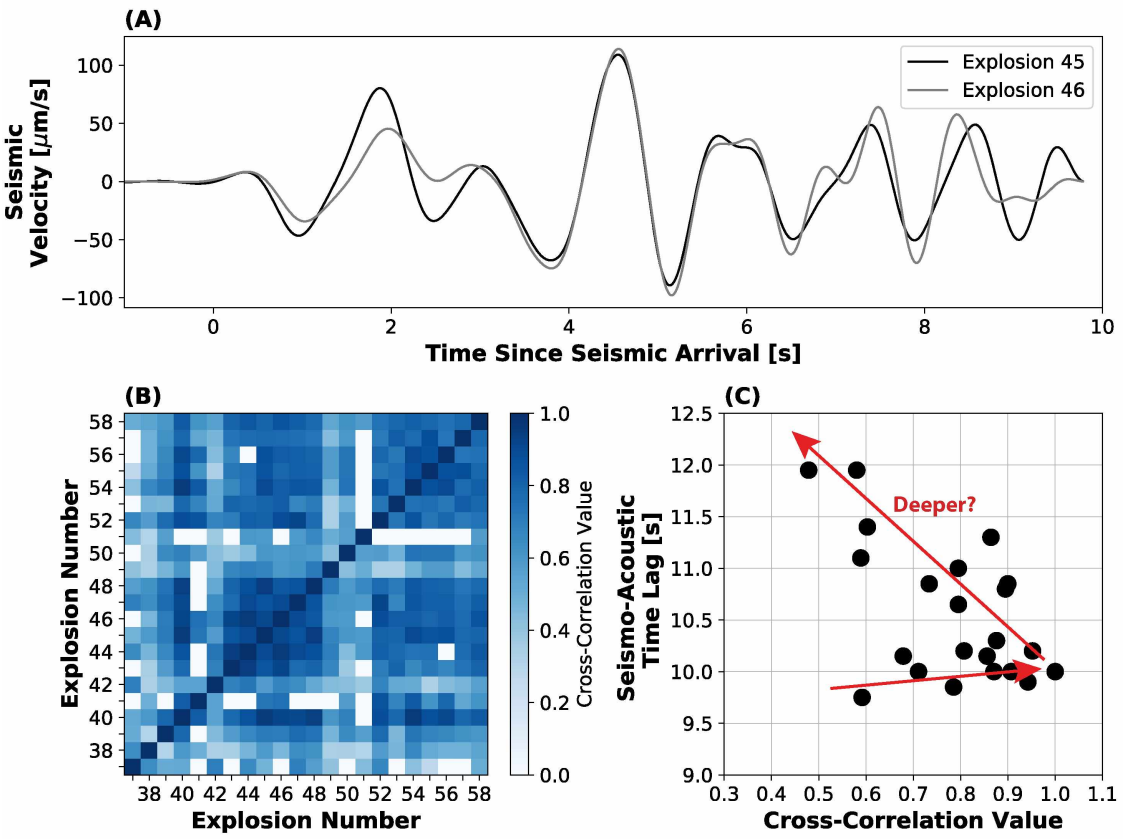

Figure 4.10: Seismic cross-correlation analysis in the 0.1 - 1.0 Hz frequency band. **(A)** Waveforms for Explosions 45 and 46 with a cross-correlation value of 0.91. **(B)** Seismic cross-correlation values for all explosions. **(C)** Seismo-acoustic time lag vs cross-correlation value for example Explosion 45 compared to other explosions. As the time lag increases, the cross-correlation value increases to a maximum and then decreases again (red arrows).

4.5.3.4 Seismic Particle Motion

Analysing the particle motion of the three-component seismic data may help understand the explosion source depth within the conduit [e.g. *Rowe et al.*, 1998], or at least the source depth relative to other explosions at Mount Cleveland. Here we examine the particle motion

and dip angle for each explosion to get an estimate of the depth. Seismic data at station CLES are integrated from velocity to displacement. Then they are bandpass filtered between 0.25 - 0.5 Hz and rotated from North (N) and East (E) components to Radial (R) and Transverse (T) components with respect to the vent location (Figure 4.11A,B). Particle motion analysis is performed for the first 6 seconds of the seismic explosion signals, which generally shows stable particle motion.

The dip angle (θ) is defined as the angle below the horizontal of the least squares fit to the first 6 seconds of the R and Z components of the displacement (Fig. 4.11c). Dip angles range from 21.8 - 48.3 degrees and are distributed fairly uniformly across this range. Most explosions with larger dip angles from horizontal tend to correspond to larger seismo-acoustic time lags (Figure 4.11D). Three explosions are excluded from this analysis (Explosions 39, 49, and 51) for not having rectilinear motion in the first 6 seconds of the explosion, and therefore no clear dip angle. We caution that near-surface effects [e.g. *Neuberg and Pointer*, 2000] may affect the absolute dip angle so a direct conversion to depth is not taken here. However, these near surface effects are assumed to be constant over time and minimal in this low frequency band, therefore the relative changes in dip angle between explosions indicate a changing source depth. The three events with dip angles greater than 40° are Explosions 41, 42, and 50, all of which have large differences (>1 s) between the observed and predicted arrival time based on atmospheric conditions (Figure 4.6B). This suggests relatively deeper sources for explosions with larger time lags than those with shorter time lags. Thus, the pressure wave travels a longer distance prior to reaching CLES, therefore having a larger time delay compared with the seismic arrival.

4.6 Discussion

4.6.1 General Characterization of Explosions

The activity of Mount Cleveland has fluctuated through time and remains one of AVO's most historically active volcanoes. The time period analyzed in this study (2014 to 2018)

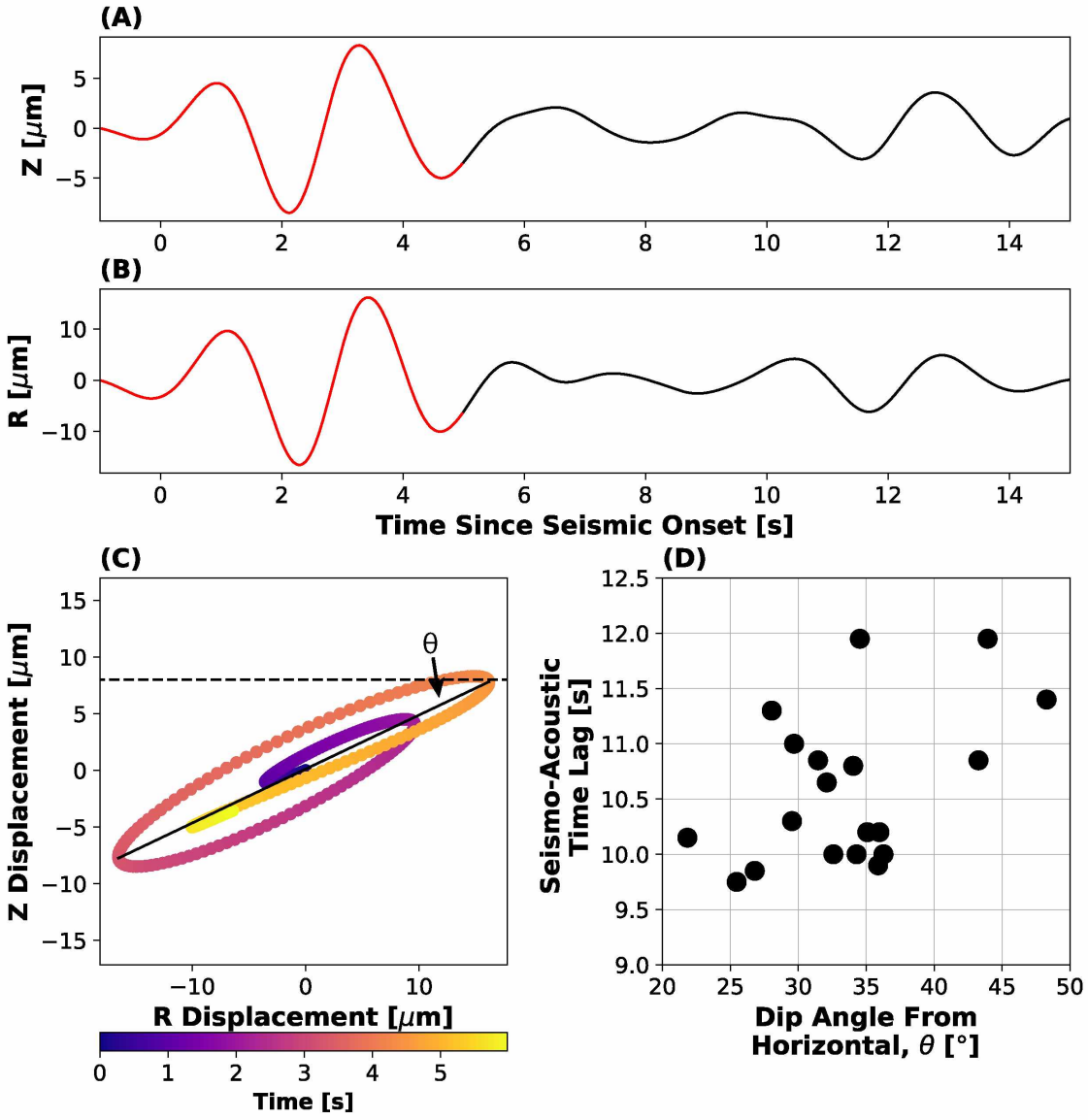

Figure 4.11: Particle motion analysis for example Explosion 38 in the 0.25-0.5 Hz frequency band. **(A)** Vertical seismic displacement. **(B)** Radial seismic displacement. **(C)** Particle motion for the first 6 seconds of the explosion (red section in panels **(A)** and **(B)**, colored as a function of time. The solid black line is the least-squares fit, allowing for the computation of dip angle from horizontal (θ) **(D)** Time lag vs. dip angle from horizontal (θ), generally showing a positive correlation between time lag and dip angle (R-squared value of 0.22).

contains the transient dome building and destruction styles that Cleveland has been known to produce. In 2001, Cleveland exhibited higher eruptive activity with large volcanic plumes [*Dean*, 2002; *Simpson et al.*, 2002; *Dean et al.*, 2004; *Gu et al.*, 2005]. After this time,

the volcano was relatively quiet until December 2011, when activity was again heightened and AVO began recording their current explosion catalog. While most of the activity from 2011 to the time of writing was Vulcanian in nature, two explosions in 2013 book-ended a continuous eruption lasting 44 hours that was recorded by the infrasound array and as GCAs on the seismic network at Okmok volcano [*Power et al.*, 2020]. Additionally, we note that the repose time prior to the most recent explosion at the time of writing (June 2, 2020), was 510 days, the longest repose time in 9 years so it appears the volcano may have entered a new eruptive phase. Explosion dynamics may still be similar though.

Repose time prior to explosions within the study period varied between 2 and 257 days and appeared to occur irrespective of whether a lava dome extruded and was visible on the crater floor (Figure 4.3A). This is a bit surprising, as we expected the existence and size of a dome to have an impact on the amount of pressure that can be built up in the shallow conduit system prior to the explosion. Therefore, we assume that the observation of "no dome" visible on the crater floor in satellite imagery still means that some form of hardened plug occurs at the top of the conduit that causes pressure to build within the conduit and create the next Vulcanian explosion. We note that permanent gas instrumentation may help better understand this relationship between the dome and subsequent build up of pressure, due to the nearly continuous degassing from fractures within the dome surface.

Unlike the repetitive nature of the seismic explosion signals, the characteristics of the infrasound signal varied substantially between explosions. Peak pressures at 3.5 km distance from the summit ranged between 20 and 260+ Pa and were short-duration Vulcanian explosions, sometimes with tremor occurring for several minutes after the initial blast. The waveforms of some explosions were similar to a typical blast wave (e.g. Explosion 44, Figure 4.7A) where the onset is very sharp, and potentially propagated faster than the expected speed of sound. Some explosions have a preceding low amplitude infrasound phase <0.5 s prior to the main explosion onset that may be attributed to a minor increase in pressure due to the swelling or "uncorking" of the lava plug within the crater (e.g. Explosion 40,

Figure 4.2B). This has been seen at other similar volcanoes such as Lokon-Empung [*Yamada et al.*, 2016], Sakurajima [*Yokoo et al.*, 2009], and Suwanosejima [*Yokoo and Iguchi*, 2010]. Some explosions exhibit a single main compressional phase (e.g. Explosions 43-49, Figure 4.2B) while other explosions have multiple compressions in a row, which may correspond to a "slow" or complex destruction of the dome (e.g. Explosion 42, Figure 4.2B). These explosions with multiple compressions have been seen at Sakurajima volcano [e.g. *Fee et al.*, 2014] as well. These observations suggest the surficial component of the explosions, including dome destruction, is complex and variable at Mount Cleveland. We note that some of these features may be obscured in the signals that clipped the infrasound sensor. AVO has since installed an infrasound sensor with a higher dynamic range that should not clip at station CLES for future explosions of Mount Cleveland.

A notable period of activity is the similarity of the cluster of Explosions 45-48 (May 2017 to September 2017, see Figure 4.12). These events had repose intervals between 35 and 54 days (Figure 4.3A), similar seismo-acoustic time lags of ~10.00 s (Figure 4.4A), similar seismic cross-correlation values (Figure 4.10B), and dip angles tightly clustered between 32.5° and 36.3° (Figure 4.11D). Given the plethora of similarities, we conclude that Cleveland was in a relatively stable and regular state of activity during this time period.

4.6.2 Implications for Source Depth within the Conduit

Our results indicate that the explosion depth varied notably between different events and is likely responsible for the variable seismo-acoustic time lag. While an absolute calculation of explosion depth for all 21 explosions in this study does not appear feasible due to our limited data, some trends exist that allow for inferences on relative explosion source depths. Results from the seismo-acoustic time lag investigation are summarized in Table 4.1 and Figure 4.12, where Figure 4.12 shows the repose time, seismo-acoustic time lag, VASR_{rel}, cross-correlation with Explosion 45, and dip angle from horizontal, each normalized between 0 and 1. It is also clear, from analyses of the atmospheric effect on travel time using two

independent methods, that the atmosphere is not the sole cause of the observed variable seismo-acoustic time lags (Figure 4.6B). Additionally, nonlinear propagation modeling did not yield a change in the onset time of the acoustic arrival at 3.8 km range and source amplitudes comparable (and larger) to those of Cleveland explosions, just a change in the arrival time of the peak pressure. Therefore, we conclude that something else must play a critical role in the variable seismo-acoustic time lags observed, which we argue is a change in explosion source depth within the conduit.

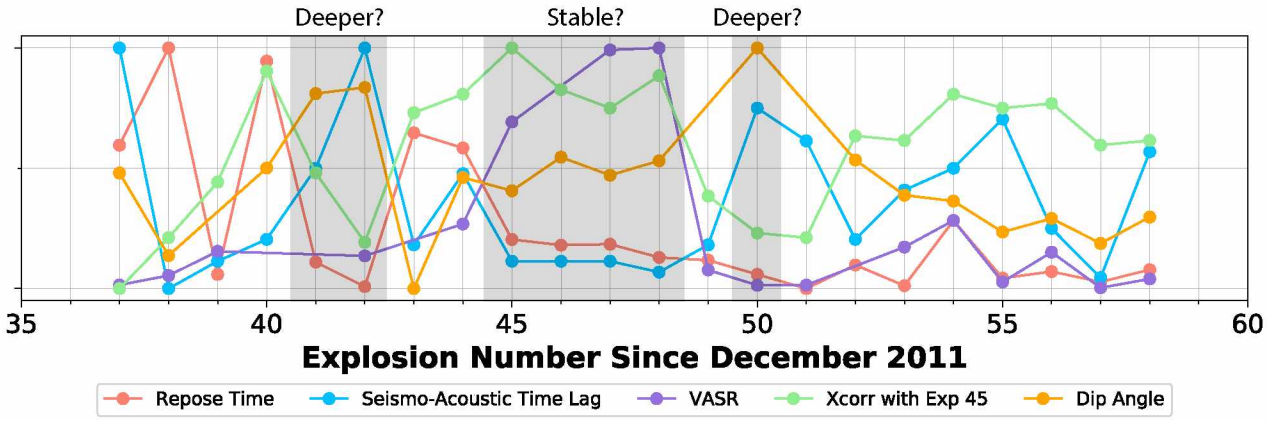

Figure 4.12: Summary figure of trends as a function of explosion number. The five parameters plotted have each been normalized between 0 and 1 and consist of repose time [days], seismo-acoustic time lag [s], VASR_{rel}, cross-correlation value with Explosion 45, and dip angle from horizontal (θ) [°]. The period of apparent stability in the volcanic system (Explosions 45-48) and explosions that are believed to be initiated deeper within the conduit (Explosions 41, 42, and 50) are highlighted with gray shading.

Explosions with shorter seismo-acoustic time lags (<∼10.2 s) may have shallower source depths within the conduit. This is evidenced by small residuals between observed and predicted travel times based on atmospheric effects (<0.5 s) (Figure 4.6B), higher VASR_{rel} in some cases (Explosions 45, 47, and 48, Figure 4.8B), higher seismic-cross correlation values in general (Figure 4.10B) and in relation to Explosion 45 (Figure 4.10C), and lower dip angles based on seismic particle motion (Figure 4.11D). These results are also summarized in Table 4.1 and Figure 4.12. The low residuals between observed and predicted travel times based on atmospheric effects means that the atmospheric predictions for the entire acoustic

propagation path (Locations 1 through 4, Figure 4.5) are well predicted by the path length within the atmosphere (Locations 2 through 4, Figure 4.5). Therefore, the distance between Locations 1 and 2 in Figure 4.5 (i.e. explosion source depth) may be small. Explosions 45, 47, and 48 have high VASR_{rel} values, which indicates that a higher fraction of the explosion energy coupled into the atmosphere as compared with other explosions, also suggesting a shallow source or change in coupling from the conduit to the conduit wall. The seismic signatures of these events have high correlation, suggesting they may occur in a similar location and thus have the same propagation path to the seismic sensor. Finally, the dip angles of the seismic particle motion analysis for these events are smaller than explosions with larger time lags (e.g. Explosions 41, 42, and 50, dip angles >40°), suggesting a shallower source. While the dip angles seem to point to a source lower than station CLES for all explosions (e.g. Figure 4.11C), the travel time residuals are low (i.e. the observed time lag seems to be explained well by the predicted acoustic travel time based on the effective sound speed) and may therefore have a short path within the conduit. This is likely related to the surface displacement for P-waves incident at a sloped free surface [e.g. *Ben-Menahem and Singh*, 2012, their Figure 3.3], which causes the observed motion to be upward and outward even though the explosion source may be shallower than station CLES. The combination of these observations suggests these events have a shallower source than other explosions at Mount Cleveland.

Explosions with larger seismo-acoustic time lags are likely associated with deeper explosions. This is evidenced by the higher travel time residuals between observed values and those predicted using the effective sound speed (Figure 4.6B), low cross-correlation values with respect to Explosion 45 (Figure 4.10C), and larger dip angles from particle motion analysis (>40°, Figure 4.11D) (Table 4.1, Figure 4.12). The three events with dip angles greater than 40° are Explosions 41, 42, and 50, all of which have large differences between the observed and predicted arrival time based on atmospheric conditions (>0.88 s, Figure 4.6B). We use these three likely deeper explosions to perform calculations on maximum source

depths for explosions at Mount Cleveland where the residual travel times (after accounting for atmospheric effects) are 0.88, 1.77, and 1.31 seconds, respectively. *Tameguri et al.* [2002] find a reasonable conduit propagation velocity for Sakurajima to be in the range of 1400 - 1900 m/s and *Yamada et al.* [2016] estimate the velocity of the pressure wave to be >1000 m/s at Lokon-Empung. If we use a lower conduit velocity of $v_{conduit}$ = 1000 m/s, explosion depths would be 880, 1770, and 1310 m, respectively. If we choose a higher conduit velocity of $v_{conduit}$ = 1500 m/s, explosion depths would be 1320, 2655, and 1965 m, respectively. *Haney et al.* [in prep] find volumetric source locations using moment tensor inversions in the VLP band from 0.25-0.5 Hz for the first 2 seconds of the waveform of 400-640 m above sea level (depths of ∼1090-1330 m beneath the summit), which appear to be in the range of our results and favor the lower $v_{conduit}$. We note that moment tensor inversions from similar explosions at Tungurahua volcano, Ecuador, point to a source region 1.5 km below the summit [*Kim et al.*, 2014], also relatively consistent with these deeper explosions at Mount Cleveland. Additionally, the range of potential source depths we calculate are consistent with the proposed vertically extensive region of magma degassing between 0.5 and 3.0 km beneath the summit at Mount Cleveland in 2016 [*Werner et al.*, 2020].

While changing the depth of the seismic explosion source would affect the time the pressure wave propagates up the conduit, the conduit propagation velocity may also vary due to changing composition and density of the conduit material between explosions. This has been hypothesized in previous studies of analog volcanoes, including Tungarahua [*Ruiz et al.*, 2006] and Santiaguito [*Sahetapy-Engel et al.*, 2008]. While this may occur to some extent at Mount Cleveland, we believe that a changing source depth is more likely for Mount Cleveland due to the positive relationship between increasing seismo-acoustic time lag with increasing dip angle from seismic particle motion analysis (Figure 4.11D).

Explosion 37 has a similarly large residual between the observed and predicted arrival time based on atmospheric conditions (1.81 s) but lacks the large dip angle observed for other explosions with large residuals (Explosions 41, 42, and 50, explained above). Upon

closer inspection of the infrasound waveform, a small compression is noted ~1.8 s prior to the main onset. This feature is likely not noise, as it shows up at the infrasound array CLCO. Therefore, we conclude that the small compression may be an arrival from movement of the dome surface, and that the dome did not completely rupture until ~1.8 s later, causing a larger delay in the main acoustic onset.

4.6.3 Other Potential Impacts on Seismo-Acoustic Time Lag

Uncertainties can be introduced when picking the seismic and infrasound onset times. The seismic onsets are low-amplitude compressions which are consistent with studies of similar volcanoes such as Sakurajima [*Tameguri et al.*, 2002], Tungurahua [*Ruiz et al.*, 2006], and Lokon-Empung [*Yamada et al.*, 2016]. We chose to pick seismic arrivals on unfiltered waveforms to obtain the first sign of signal onset, as filtering in certain bands may obscure the subtle onset. The infrasound arrival is generally signified by a rapid increase in pressure. However, some explosions have a slow compressional onset (<0.5 seconds) prior to the rapid onset, which may introduce a small (few tenths of a second) error. Both of these potential onset time errors do not change the fact that large variations (up to 2.20 seconds) in seismo-acoustic time lag exist between explosions at Mount Cleveland.

Two methods were used to determine the impact of the atmosphere on the propagation velocity of the infrasound signal, both of which have pros and cons. The first method used an atmospheric reconstruction model, AVO-G2S [*Schwaiger et al.*, 2019]. Using models such as this to obtain atmospheric information is known to not fully capture the exact atmospheric conditions at the time and location of the event [e.g. *Iezzi et al.*, 2019a; *Schwaiger et al.*, 2020]. For example, these models have been found to be inadequate for the local atmospheric and boundary layer properties for propagation distances similar to that explored in this study [e.g. *Kim et al.*, 2018]. Therefore, atmospheric conditions may not capture smaller-scale changes such as variations within the 6 hour increments, transient wind gusts, or flow around topography (i.e. a volcanic edifice). These inaccuracies and simplifications (both spatially

and temporally) can be due to using coarse resolution input windfiles (NCEP reanalysis files, 2.5 degrees and 6 hours, respectively), as well as smoothing and interpolation during the reconstruction process in order to obtain a 1D atmospheric profile above the volcano. This may explain why the AVO-G2S derived effective sound speed values were systematically lower than those from our second method by 0-25 m/s (Figure 4.6A). The second method used to obtain effective sound speeds took advantage of the infrasound array CLCO, located 12.33 km further and 22.9° south of the CLES-summit azimuth. While 22.9° is a relatively low azimuthal deviation, if winds were strong the effective sound speed comparison would have error. However, we use this value because it is likely a more accurate representation of the atmospheric conditions at the time of each explosion.

To further investigate the potential effect of wind noise that may remain unresolved by both methods for determining the impact of the atmosphere on the propagation velocity, we look at the low frequency (0.02-0.3 Hz) component of infrasound for each explosion, as the spectral amplitude in this frequency band can sometimes be used as a proxy for wind noise [e.g. *Fee and Garces*, 2007]. We include the infrasound power spectral density (PSD) for the 60 minutes prior to each explosion in Supplemental Figure S1, and note that the magnitude of the noise levels in this frequency band varies between explosions and does not show a clear correlation with time lag. However, it is not possible to fully interpret wind-related travel time effects on the time lag analysis because the noise conditions captured by the PSD do not account for directionality of the wind. For future studies that may be interested in obtaining explosion source depth from the seismo-acoustic time lag, we suggest adding an in-situ measurement of wind speed and direction along with the co-located seismic and infrasound sensors, such as an anemometer, in order to more thoroughly capture the influence of the atmosphere.

The nonlinear FDTD modeling results in this study did not produce a measurable difference in the onset time of the explosion signal, nor the formation of a shock front. We note that our interpretations are limited by current modeling capabilities only using a linear

source. Some of the waveforms at CLES show similarities to shock waves, which we believe would impact the acoustic arrival time observed at CLES due to the shock front overtaking the gradual onset observed for many of the Cleveland explosions. We surmise that future simulations performed that include a nonlinear source may produce a more realistic acoustic travel time. While the simulations performed here did not reproduce nonlinear impacts to the explosion arrival times, we believe there still may be a small contribution due to the highest peak pressures and those that clipped (Figure 4.7D, open circles) having lower seismo-acoustic time lags. This could be a coincidence, but should be explored further. Building upon a study on Bromo volcano, Indonesia, by *Gottschämmer and Surono* [2000], *Kim et al.* [2014] corrected their infrasound onset times for explosions at Tungurahua volcano, Ecuador, using a constant shock velocity of 560 m/s within 2 km of the source, then 340 m/s beyond 2 km. However, we do not feel confident enough to include this type of sound speed assumption in our study, especially when we only have data from a single station. Due to the uncertainties from a variety of features of potential nonlinear propagation, we chose to not include the potential contribution to our calculations on explosion source depth.

Observing nonlinear propagation near the source is difficult because infrasound sensors are generally placed far enough away from the source in order to decrease hazard to the field team and equipment. Therefore, interpretations often integrate multidisciplinary observations of pressure waves in order to better understand near source pressure dynamics. The propagation of pressure waves or "flashing arcs" has been observed and studied using image luminance techniques [e.g. *Genco et al.*, 2014] and thermal imagery [e.g. *Marchetti et al.*, 2013] then connected to the acoustic propagation velocity of volcanic explosions. [*Genco et al.*, 2014] find that explosions at Stromboli volcano propagate at the expected speed of sound, not faster. *Marchetti et al.* [2013] find that acoustic waves from explosions at Yasur volcano propagate supersonically, along with the observation of blast wave shapes in the infrasound traces. Recall that in nonlinear propagation every point on the waveform trav-

els with a different speed (compression faster than rarefaction), which begs the question of exactly which part of the acoustic waveform this supersonic propagation speed corresponds to, the initial onset (which we are exploring in this study) or the peak compression (which has been shown to arrive faster in both this study and in others)? This remains unclear and should be investigated more thoroughly in the future.

4.7 Conclusions

Multi-year studies of volcanic activity provide observations of trends, and deviations from those trends, that prove useful for volcano monitoring that may not be apparent for studies using temporary deployment data that may only catch a few explosions [e.g. *Lamb et al.*, 2019; *Wallace et al.*, 2020]. Here we examined the activity at Mount Cleveland from 2014 to 2018 and put it in context of recent work focused on shorter-term, dense observations. We find that Mount Cleveland generally followed a pattern of dome building and subsequent Vulcanian explosions, but parameters including repose time, explosion amplitude, and explosion characteristics varied substantially over the 4 years. In general, seismo-acoustic data from these explosions consisted of typical Vulcanian eruption signals. The seismic arrival for all explosions is a low-amplitude, compressional onset with a GCA often visible on the trace. The acoustic signal generally consists of a high-amplitude compressional onset, followed by a long duration coda. Some acoustic signals resemble high-amplitude, sharp-onset shock waves, while others have a complicated onset indicating the slower, multi-stage destruction of the lava dome. Notably, a variable seismo-acoustic time lag of up to 2.20 s is observed on co-located seismo-acoustic sensors at a station 3.5 km from the summit. Similarly variable seismo-acoustic time lags have been observed at analog volcanoes such as Santiaguito and Tungurahua, though their precise cause is not well understood. We attribute the variable seismo-acoustic time lags to be a combination of varying atmospheric conditions (e.g. winds and temperature), nonlinear propagation, conduit velocity variations, and varying source depth within the conduit. Atmospheric effects were examined using two

independent measurements, neither of which could solely explain the variation observed. Nonlinear propagation impacts were determined to be minimal in relation to the onset time of the infrasound arrival, though they were difficult to quantify and model completely. We find that results from seismic cross-correlation and particle motion analysis suggest that a varying explosion source depth within the conduit may play a role in the observed variations in seismo-acoustic time lag. These results suggest explosion source depths ranging from near the surface down to ~1.5-2 km beneath the summit. We stress that no one method provides a complete depiction of the observed variance for all explosions, but a combination of methods is required to help understand the observations.

This study was performed primarily using a single co-located seismic and acoustic station at a remote volcano. We suggest that similar analyses may be performed at other volcanoes worldwide that have sparse monitoring networks. Even with a single co-located seismic and acoustic sensor that clips sometimes, we show that it is possible to provide meaningful interpretations on the explosion source depth which may help understand the volcanic system during times of unrest. In future years, we anticipate more geophysical and geochemical instrumentation to be installed at Mount Cleveland, which will increase our understanding of the volcanic system, build upon the results of this study, and increase the ability for AVO to monitor and forecast future eruptions of the volcano. Additionally, while this study focuses on volcanic explosions, the goal of finding depth from coupled seismic and acoustic observations is not unique to volcanic studies and can be applied to other disciplines such as the study of buried chemical explosions.

4.8 Acknowledgments

The authors thank Sean Maher and Catherine de Groot-Hedlin for helpful discussion on nonlinear propagation and the use of the FDTDWave code. We are also grateful to Pavel Izbekov, Carl Tape, and Michael West for discussions on the analyses as well as David Green for discussion on the use of seismic cross-correlation. We would also like to

thank Taryn Lopez, Cheryl Searcy, Cheryl Cameron, and Rick Wessels for their help with gathering dome observations and discussions on Mount Cleveland. Observations of volcanic activity were made by AVO and are detailed on its website (www.avo.alaska.edu). Any use of trade, firm, or product names is for descriptive purposes only and does not imply endorsement by the U.S. Government. Supplemental document includes 2 figures. (`frontiers_SupplementaryMaterial.tex`)

Table 4.1: Mount Cleveland seismo-acoustic time lag investigation results. Explosion number in AVO catalog, date of explosion, arrival time of seismic onset [UTC], seismo-acoustic time lag [s], unfiltered peak infrasound pressure at CLES [Pa], unfiltered peak velocity (vertical) at CLES [$\mu m/s$], repose time since previous explosion [days], travel time residual between observed acoustic travel time and the travel time predicted by atmospheric effective sound speed [s], relative VASR (VASR$_{rel}$), cross-correlation value in relation to example Explosion 45, and dip angle from horizontal [°].

Explosion Number	**Date**	**Seismic Onset [UTC]**	**Time Lag [s]**	**Peak Pressure [Pa]**	**Peak Velocity [$\mu m/s$]**	**Repose Time [days]**	**Travel Time Residual [s]**	**VASR$_{rel}$**	**X-Corr with Exp 45**	**Dip Angle [°]**
37	06-Nov-2014	07:42:49.70	11.95	30	162	154	1.81	3.9	0.48	34.5
38	21-Jul-2015	16:17:41.55	9.75	74	200	257	-0.26	14.1	0.59	25.5
39	07-Aug-2015	06:02:57.90	10.00	61	109	17	-0.35	40.3	0.71	-
40	16-Apr-2016	18:58:05.50	10.20	>260	273	243	-0.28	-	0.95	35.1
41	06-May-2016	02:43:33.60	10.85	>260	354	30	0.88	-	0.73	43.3
42	10-May-2016	15:31:38.90	11.95	140	257	4	1.77	35.4	0.58	43.9
43	24-Oct-2016	21:10:24.55	10.15	>260	161	167	-0.12	-	0.86	21.8
44	24-Mar-2017	16:15:23.90	10.80	260	245	151	-0.32	70.0	0.90	34.0
45	17-May-2017	03:17:38.80	10.00	250	186	54	-0.09	180.6	1.0	32.6
46	04-Jul-2017	11:18:48.15	10.00	>260	243	48	-0.26	-	0.91	36.3
47	22-Aug-2017	18:43:44.10	10.00	260	165	49	-0.02	258.7	0.87	34.3
48	26-Sep-2017	01:47:06.35	9.90	200	145	35	0.07	260.9	0.94	35.9
49	28-Oct-2017	18:45:01.55	10.15	110	187	32	-0.39	20.1	0.68	-
50	14-Nov-2017	12:15:24.75	11.40	22	146	17	1.31	3.6	0.60	48.3
51	16-Nov-2017	22:44:06.45	11.10	21	298	2	0.94	3.7	0.59	-
52	13-Dec-2017	13:20:40.90	10.20	>260	372	27	0.06	-	0.81	36.0
53	18-Dec-2017	03:17:46.80	10.65	56	131	5	0.61	45.0	0.80	32.1
54	02-Mar-2018	14:57:01.00	10.85	235	235	74	0.95	73.8	0.90	31.5
55	15-Mar-2018	06:18:55.20	11.30	78	201	13	0.62	7.1	0.87	28.0
56	04-Apr-2018	11:55:21.80	10.30	170	284	20	-0.29	39.4	0.88	29.5
57	13-Apr-2018	15:59:18.50	9.85	24	300	9	-0.66	0.8	0.79	26.8
58	05-May-2018	05:48:45.30	11.00	89	376	22	0.96	10.4	0.80	29.7

4.9 References

Arrowsmith, S. J., J. B. Johnson, D. P. Drob, and M. A. H. Hedlin (2010), The Seismoacoustic Wavefield: A New Paradigm In Studying Geophysical Phenomena, *Reviews of Geophysics*, *48*(4), RG4003, doi:10.1029/2010RG000335.

Atchley, A. A. (2005), Not Your Ordinary Sound Experience: A Nonlinear-Acoustics Primer, *Acoustics Today*, pp. 19–24.

Ben-Menahem, A., and S. J. Singh (2012), *Seismic waves and sources*, Springer Science & Business Media.

Blom, P. S., A. M. Iezzi, and G. Euler (in review), Seismoacoustic analysis of underground explosions using the Rayleigh integral, *Geophysical Journal International*.

Boatwright, J. (1980), A spectral theory for circular seismic sources; simple estimates of source dimension, dynamic stress drop, and radiated seismic energy, *Bulletin of the Seismological Society of America*, *70*(1), 1–27.

De Angelis, S., D. Fee, M. Haney, and D. Schneider (2012), Detecting hidden volcanic explosions from Mt. Cleveland Volcano, Alaska with infrasound and ground-coupled airwaves, *Geophysical Research Letters*, *39*(21), doi:10.1029/2012GL053635.

de Groot-Hedlin, C. D. (2016), Long-range propagation of nonlinear infrasound waves through an absorbing atmosphere, *The Journal of the Acoustical Society of America*, *139*(4), 1565–1577, doi:10.1121/1.4944759.

Dean, K. G. (2002), Satellite Imagery Proves Essential for Monitoring Erupting Aleutian Volcano, *Eos*, *83*(22), 19–21.

Dean, K. G., J. Dehn, K. R. Papp, S. Smith, P. Izbekov, R. Peterson, C. Kearney, and A. Steffke (2004), Integrated satellite observations of the 2001 eruption of Mt. Cleveland, Alaska, *Journal of Volcanology and Geothermal Research*, *135*(1-2), 51–73, doi:10.1016/j.jvolgeores.2003.12.013.

Dixon, J., C. Cameron, A. Iezzi, and K. Wallace (2017), 2015 Volcanic activity in Alaska-Summary of events and response of the Alaska Volcano Observatory, *U.S. Geological Survey Scientific Investigations Report 2017-5104*, doi:https://doi.org/10.3133/sir20175104.

Fee, D., and M. Garces (2007), Infrasonic tremor in the diffraction zone, *Geophysical Research Letters*, *34*(16), doi:10.1029/2007GL030616.

Fee, D., and R. S. Matoza (2013), An overview of volcano infrasound: From hawaiian to plinian, local to global, *Journal of Volcanology and Geothermal Research*, *249*, 123–139, doi:10.1016/j.jvolgeores.2012.09.002.

Fee, D., A. Yokoo, and J. B. Johnson (2014), Introduction to an open community infrasound dataset from the actively erupting Sakurajima Volcano, Japan, *Seismological Research Letters*, *85*(6), 1151–1162, doi:10.1785/0220140051.

Fee, D., M. Haney, R. Matoza, C. Szuberla, J. Lyons, and C. Waythomas (2016), Seismic envelope-based detection and location of ground-coupled airwaves from volcanoes in Alaska, *Bulletin of the Seismological Society of America*, *106*(3), doi:10.1785/0120150244.

Fee, D., P. Izbekov, K. Kim, A. Yokoo, T. Lopez, F. Prata, R. Kazahaya, H. Nakamichi, and M. Iguchi (2017), Eruption mass estimation using infrasound waveform inversion and ash and gas measurements: Evaluation at Sakurajima Volcano, Japan, *Earth and Planetary Science Letters*, *480*, 42–52, doi:10.1016/j.epsl.2017.09.043.

Fee, D., J. Lyons, M. Haney, A. Wech, C. Waythomas, A. K. Diefenbach, T. Lopez, A. Van Eaton, and D. Schneider (2020), Seismo-acoustic evidence for vent drying during shallow submarine eruptions at Bogoslof volcano, Alaska, *Bulletin of Volcanology*, *82*(1), 1–14, doi:10.1007/s00445-019-1326-5.

Firstov, P., and N. Kravchenko (1996), Estimation of the amount of explosive gas released in volcanic eruptions using air waves, *Volcanol. Seismol.*, *17*(4-5), 547–560.

Friedlander, F. (1946), The diffraction of sound pulses. I. Diffraction by a semi-infinite plate, *Proceedings of the Royal Society of London A*, *186*, 322–344.

Genco, R., M. Ripepe, E. Marchetti, C. Bonadonna, and S. Biass (2014), Acoustic wavefield and Mach wave radiation of flashing arcs in strombolian explosion measured by image luminance, *Geophysical Research Letters*, *41*(20), 7135–7142, doi:10.1002/2014GL061597.

Gottschämmer, E., and I. Surono (2000), Locating tremor and shock sources recorded at Bromo Volcano, *Journal of Volcanology and Geothermal Research*, *101*(1-2), 199–209, doi:10.1016/S0377-0273(00)00171-2.

Green, D. N., and J. Neuberg (2006), Waveform classification of volcanic low-frequency earthquake swarms and its implication at Soufrière Hills Volcano, Montserrat, *Journal of Volcanology and Geothermal Research*, *153*(1-2), 51–63, doi:10.1016/j.jvolgeores.2005.08.003.

Gu, Y., W. I. Rose, D. J. Schneider, G. J. S. Bluth, and I. M. Watson (2005), Advantageous GOES IR results for ash mapping at high latitudes : Cleveland eruptions 2001, *32*, 1–5, doi:10.1029/2004GL021651.

Haney, M., J. Lyons, J. Power, and D. Roman (in prep), Moment Tensors of Small Vulcanian Explosions at Mount Cleveland, Alaska, *Journal of Volcanology and Geothermal Research*.

Iezzi, A. M., H. F. Schwaiger, D. Fee, and M. M. Haney (2019a), Application of an updated atmospheric model to explore volcano infrasound propagation and detection in Alaska, *Journal of Volcanology and Geothermal Research*, *371*, 192–205, doi:10.1016/j.jvolgeores.2018.03.009.

Iezzi, A. M., D. Fee, K. Kim, A. D. Jolly, and R. S. Matoza (2019b), Three-Dimensional Acoustic Multipole Waveform Inversion at Yasur Volcano, Vanuatu, *Journal of Geophysical Research: Solid Earth*, *124*(8), 8679–8703, doi:10.1029/2018JB017073.

Janiszewski, H. A., L. S. Wagner, and D. C. Roman (2020), Aseismic mid-crustal magma reservoir at Cleveland Volcano imaged through novel receiver function analyses, *Scientific Reports*, *10*(1780), 1–9, doi:10.1038/s41598-020-58589-0.

Johnson, J. B. (2003), Generation and propagation of infrasonic airwaves from volcanic explosions, *Journal of Volcanology and Geothermal Research*, *121*(1-2), 1–14, doi:10.1016/S0377-0273(02)00408-0.

Johnson, J. B., and R. C. Aster (2005), Relative partitioning of acoustic and seismic energy during Strombolian eruptions, *Journal of Volcanology and Geothermal Research*, *148*(3-4), 334–354, doi:10.1016/j.jvolgeores.2005.05.002.

Jones, K. R., R. W. Whitaker, and S. J. Arrowsmith (2014), Modelling infrasound signal generation from two underground explosions at the Source Physics Experiment using the Rayleigh integral, *Geophysical Journal International*, pp. 777–788, doi:10.1093/gji/ggu433.

Kim, K., J. M. Lees, and M. C. Ruiz (2014), Source mechanism of Vulcanian eruption at Tungurahua Volcano, Ecuador, derived fromseismic moment tensor inversions, *Journal of Geophysical Research: Solid Earth*, *119*(2), 1145–1164, doi:10.1002/2013JB010590.

Kim, K., D. Fee, A. Yokoo, and J. M. Lees (2015), Acoustic source inversion to estimate volume flux from volcanic explosions, *Geophysical Research Letters*, *42*(13), 5243–5249, doi:10.1002/2015GL064466.

Kim, K., A. Rodgers, and D. Seastrand (2018), Local Infrasound Variability Related to In Situ Atmospheric Observation, *Geophysical Research Letters*, *45*(7), 2954–2962, doi:10.1002/2018GL077124.

Kistler, R., E. Kalnay, W. Collins, S. Saha, G. White, J. Woollen, M. Chelliah, W. Ebisuzaki, M. Kanamitsu, V. Kousky, H. Van Den Dool, R. Jenne, and M. Fiorino (2001), The NCEP-NCAR 50-year reanalysis: Monthly means CD-ROM and documentation, *Bulletin of the American Meteorological Society*, *82*(2), 247–267, doi:10.1175/1520-0477(2001)082⟨0247:TNNYRM⟩2.3.CO;2.

Lamb, O. D., A. Lamur, A. Díaz-Moreno, S. De Angelis, A. J. Hornby, F. W. von Aulock, J. E. Kendrick, P. A. Wallace, E. Gottschämmer, A. Rietbrock, I. Alvarez, G. Chigna, and Y. Lavallée (2019), Disruption of long-term effusive-explosive activity at Santiaguito, Guatemala, *Frontiers in Earth Science*, *6*(February), 1–14, doi:10.3389/feart.2018.00253.

Lyons, J. J., and G. P. Waite (2011), Dynamics of explosive volcanism at Fuego volcano imaged with very long period seismicity, *Journal of Geophysical Research: Solid Earth*, *116*(9), 1–18, doi:10.1029/2011JB008521.

Maher, S. P., R. S. Matoza, C. D. Groot-Hedlin, K. L. Gee, D. Fee, and A. Yokoo (2020), Investigating Spectral Distortion of Local Volcano Infrasound by Nonlinear Propagation at Sakurajima Volcano, Japan, *Journal of Geophysical Research: Solid Earth*, *125*(3), doi:10.1029/2019JB018284.

Marchetti, E., M. Ripepe, D. Delle Donne, R. Genco, A. Finizola, and E. Garaebiti (2013), Blast waves from violent explosive activity at Yasur Volcano, Vanuatu, *Geophysical Research Letters*, *40*(22), 5838–5843, doi:10.1002/2013GL057900.

McKee, K., D. Fee, M. Haney, R. S. Matoza, and J. Lyons (2018), Infrasound Signal Detection and Back Azimuth Estimation Using Ground-Coupled Airwaves on a Seismo-Acoustic Sensor Pair, *Journal of Geophysical Research: Solid Earth*, *123*(8), 6826–6844, doi:10.1029/2017JB015132.

Miller, T., R. McGimsey, D. Richter, J. Riehle, C. Nye, M. Yount, and J. Dumoulin (1998), Catalog of Historically Active Volcanoes in Alaska, *U.S. Geological Survey Open File Report*, (98-582).

Neuberg, J., and T. Pointer (2000), Effects of volcano topography on seismic broad-band waveforms, *Geophysical Journal International*, *143*(1), 239–248, doi:10.1046/j.1365-246X.2000.00251.x.

Petersen, T., and S. R. McNutt (2007), Seismo-acoustic signals associated with degassing explosions recorded at Shishaldin Volcano, Alaska, 2003-2004, *Bulletin of Volcanology*, *69*(5), 527–536, doi:10.1007/s00445-006-0088-z.

Pierce, A. (1981), *Acoustics: An Introduction to its Physical Principles and Applications*, McGraw-Hill, New York.

Porter, C., P. Morin, I. Howat, M.-J. Noh, B. Bates, K. Peterman, S. Keesey, M. Schlenk, J. Gardiner, K. Tomko, M. Willis, C. Kelleher, M. Cloutier, E. Husby, S. Foga, H. Nakamura, M. Platson, J. Wethington, Michael, C. Williamson, G. Bauer, J. Enos, G. Arnold, W. Kramer, P. Becker, A. Doshi, C. D'Souza, P. Cummens, F. Laurier, and M. Bojesen (2018), ArcticDEM, doi:10.7910/DVN/OHHUKH.

Power, J., D. Roman, J. Lyons, M. Haney, C. Werner, D. Rasmussen, and T. Plank (in prep), A seismic investigation of Mount Cleveland volcano and pre-historic volcanic vents on Chuginadak Island, Alaska and implications for forecasting eruptions at open-vent volcanoes.

Power, J. A., M. M. Haney, S. M. Botnick, J. P. Dixon, D. Fee, A. M. Kaufman, D. M. Ketner, J. J. Lyons, T. Parker, J. F. Paskievitch, C. W. Read, C. Searcy, S. D. Stihler, G. Tepp, and A. G. Wech (2020), Goals and Development of the Alaska Volcano Observatory Seismic Network and Application to Forecasting and Detecting Volcanic Eruptions, *Seismological Research Letters*, doi:10.1785/0220190216.

Reichman, B. O., K. L. Gee, T. B. Neilsen, and K. G. Miller (2016), Quantitative analysis of a frequency-domain nonlinearity indicator, *The Journal of the Acoustical Society of America*, *139*(5), 2505–2513, doi:10.1121/1.4945787.

Rowe, C. A., R. C. Aster, P. R. Kyle, J. W. Schlue, and R. R. Dibble (1998), Broadband recording of Strombolian explosions and associated very-long-period seismic signals on Mount Erebus volcano, Ross Island, Antarctica, *Geophysical Research Letters*, *25*(13), 2297–2300, doi:10.1029/98GL01622.

Ruiz, M. C., J. M. Lees, J. B. Johnson, M. Hall, C. Box, and C. Hill (2006), Source constraints of Tungurahua volcano explosion events, *Bulletin of Volcanology*, *68*(December 2004), 480–490, doi:10.1007/s00445-005-0023-8.

Sahetapy-Engel, S. T., A. J. Harris, and E. Marchetti (2008), Thermal, seismic and infrasound observations of persistent explosive activity and conduit dynamics at Santiaguito lava dome, Guatemala, *Journal of Volcanology and Geothermal Research*, *173*(1-2), 1–14, doi:10.1016/j.jvolgeores.2007.11.026.

Salomons, E. (2001), *Computational Atmospheric Acoustics*, 335 pp., Kluwer Academic Publishers, Dordrecht, The Netherlands.

Schwaiger, H., A. Iezzi, and D. Fee (2019), AVO-G2S: A modified, open-source Ground-to-Space atmospheric specification for infrasound modeling, *Computers and Geosciences*, *125*, 90–97, doi:10.1016/j.cageo.2018.12.013.

Schwaiger, H. F., J. J. Lyons, A. M. Iezzi, D. Fee, and M. M. Haney (2020), Evolving infrasound detections from Bogoslof volcano, Alaska: insights from atmospheric propagation modeling, *Bulletin of Volcanology*, *82*(3), 27, doi:10.1007/s00445-020-1360-3.

Simpson, J., G. Hufford, D. Pieri, R. Servranckx, J. Berg, and C. Bauer (2002), The February 2001 Eruption of Mount Cleveland, Alaska: Case Study of an Aviation Hazard, *American Meteorological Society*, *17*.

Tameguri, T., M. Iguchi, and K. Ishihara (2002), Mechanism of explosive eruptions from moment tensor analyses of explosion earthquakes at Sakurajima volcano, Japan, *Bulletin of the Volcanological Society of Japan*, *47*(4), 197–215.

Varley, N., R. Arámbula-Mendoza, G. Reyes-Dávila, R. Sanderson, and J. Stevenson (2010), Generation of vulcanian activity and long-period seismicity at volcán de colima, Mexico, *Journal of Volcanology and Geothermal Research*, *198*(1-2), 45–56, doi:10.1016/j.jvolgeores.2010.08.009.

Vergniolle, S., M. Boichu, and J. Caplan-Auerbach (2004), Acoustic measurements of the 1999 basaltic eruption of Shishaldin volcano, Alaska 1. Origin of Strombolian activity, *Journal of Volcanology and Geothermal Research*, *137*, 109–134, doi:10.1016/j.jvolgeores.2004.05.003.

Waldhauser, F., and W. L. Ellsworth (2000), A Double-difference Earthquake location algorithm: Method and application to the Northern Hayward Fault, California, *Bulletin of the Seismological Society of America*, *90*(6), 1353–1368, doi:10.1785/0120000006.

Wallace, P. A., O. D. Lamb, S. D. Angelis, J. E. Kendrick, J. Hornby, A. Díaz-moreno, P. J. González, F. W. V. Aulock, A. Lamur, J. E. P. Utley, A. Rietbrock, G. Chigna, and Y. Lavallée (2020), Integrated constraints on explosive eruption intensification at Santiaguito dome complex , Guatemala, *Earth and Planetary Science Letters*, *536*, 116,139, doi:10.1016/j.epsl.2020.116139.

Wang, T., M. P. Poland, and Z. Lu (2015), Dome growth at Mount Cleveland, Aleutian Arc, quantified by time series TerraSAR-X imagery, *Geophysical Research Letters*, *42*(24), 614–10, doi:10.1002/2015GL066784.

Wech, A., G. Tepp, J. Lyons, and M. Haney (2018), Using Earthquakes, T Waves, and Infrasound to Investigate the Eruption of Bogoslof Volcano, Alaska, *Geophysical Research Letters*, *45*(14), 6918–6925, doi:10.1029/2018GL078457.

Werner, C., C. Kern, D. Coppola, J. J. Lyons, P. J. Kelly, K. L. Wallace, D. J. Schneider, and R. L. Wessels (2017), Magmatic degassing, lava dome extrusion, and explosions from Mount Cleveland volcano, Alaska, 2011–2015: Insight into the continuous nature of volcanic activity over multi-year timescales, *Journal of Volcanology and Geothermal Research*, *337*, 98–110, doi:10.1016/j.jvolgeores.2017.03.001.

Werner, C., D. J. Rasmussen, T. Plank, P. J. Kelly, C. Kern, T. Lopez, J. Gliss, J. A. Power, D. C. Roman, P. Izbekov, and J. Lyons (2020), Linking Subsurface to Surface using Gas Emission and Melt Inclusion data at Mount Cleveland volcano, Alaska, *Geochemistry, Geophysics, Geosystems*, doi:10.1029/2019GC008882.

Worden, A., J. Dehn, and P. Webley (2014), Frequency based satellite monitoring of small scale explosive activity at remote North Pacific volcanoes, *Journal of Volcanology and Geothermal Research*, *286*, 1–14, doi:10.1016/j.jvolgeores.2014.08.019.

www.avo.alaska.edu (), Alaska Volcano Observatory.

Yamada, T., H. Aoyama, T. Nishimura, H. Yakiwara, H. Nakamichi, J. Oikawa, M. Iguchi, M. Hendrasto, and Y. Suparman (2016), Initial phases of explosion earthquakes accompanying Vulcanian eruptions at Lokon-Empung volcano , Indonesia, *Journal of Volcanology and Geothermal Research*, *327*, 310–321, doi:10.1016/j.jvolgeores.2016.08.011.

Yokoo, A., and M. Iguchi (2010), Using infrasound waves from eruption video to explain ground deformation preceding the eruption of Suwanosejima volcano, Japan, *Journal of Volcanology and Geothermal Research*, *196*(3-4), 287–294, doi:10.1016/j.jvolgeores.2010.08.008.

Yokoo, A., and K. Ishihara (2007), Analysis of pressure waves observed in Sakurajima eruption movies, *Earth, Planets and Space*, *59*(3), 177–181, doi:10.1186/BF03352691.

Yokoo, A., T. Tameguri, and M. Iguchi (2009), Swelling of a lava plug associated with a Vulcanian eruption at Sakurajima Volcano, Japan, as revealed by infrasound record: Case study of the eruption on January 2, 2007, *Bulletin of Volcanology*, *71*(6), 619–630, doi:10.1007/s00445-008-0247-5.

Chapter 5

General Conclusions

Characterization of the propagation path infrasound experiences between the source and a receiver is vital in order to better understand the volcanic source itself. The three main chapters in this dissertation explored the topics of long range infrasound propagation modeling, local characterization of infrasound propagation over topography and the resulting directional acoustic source, and the combined seismic and acoustic analyses of explosion signals. Through the research in this dissertation, we have improved the understanding of the propagation of infrasound at a variety of ranges and made advancements in understanding the acoustic source from volcanic eruptions.

It has been well established that spatio-temporal variability in the wind and temperature structure of the atmosphere can highly influence the long range propagation of infrasound. Chapter 2 outlines these effects from the atmosphere and describes the application of a new, open-source atmospheric reconstruction model to recent events in Alaska with the intention of understanding the contributions of the variable propagation path on the observed infrasound signal. It is shown that a combination of array processing, celerity, and propagation modeling in Alaska can help differentiate between propagation paths and refine interpretations of infrasound detections at long range. One aspect of understanding the propagation paths provides a better estimate of the acoustic travel time, allowing for a better integration with multidisciplinary data at the source through time. While propagation modeling capabilities vastly improve the interpretations of infrasound signals at long ranges, we note that even using state-of-the-art atmospheric specification files care must still be used in their interpretation. Finally, the methods used in this study for retrospective analysis of recent volcanic eruptions show promise for implementation in real time as a forecasting tool.

Understanding the acoustic directional radiation pattern of explosions can help determine ballistic and gas trajectories, and therefore increase the safety of tourists, scientists, and

locals visiting an active volcano. Chapter 3 focuses on acoustic waveform inversions of explosions at Yasur volcano, exploring potential existence of acoustic source directionality, even after the effects of topography are accounted for. While typical infrasound deployments consist of infrasound sensors placed on Earth's surface, this study incorporates the use of an infrasound sensor on a tethered aerostat, allowing for a better characterization of the acoustic wavefield in three dimensions. Results from this study indicate that the volume flow rate solution based on infrasound measurements remains stable, regardless of the source mechanism assumed. In other words, even with limited sensors that normally are deployed on volcanoes, an assumption of a simple source that radiates equally in all directions can produce potentially accurate time histories of the volumetric flow rate, which can further be converted to a mass flow rate. While directionality is observed and consisted with ballistic trajectories, additional work is necessary to fully explore the stability, uncertainty, and robustness of acoustic source inversions with directional components included.

Coupled seismic and acoustic analyses can help provide information about volcanic explosions from their initiation in the subsurface as recorded by the seismometer to the path the pressure wave experiences prior to arriving at the infrasound sensor. Chapter 4 provides the first seismo-acoustic characterization for 21 explosions at the remote and active Mount Cleveland using a single local co-located seismic and infrasound sensor. Over the four year study period, the relative timing between the seismic and acoustic arrivals was observed to vary by up to 2.20 s at a station 3.5 km from the summit. The results indicate that changes in atmospheric conditions can explain some of the variation in acoustic arrival time relative to the seismic, but not all of it. We find that seismic cross-correlation between events and particle motion analysis suggests that a varying explosion source depth within the conduit likely plays a role in the observed variations in seismo-acoustic time lag. The study highlights the importance of longer-term, multi-year analysis in order to better characterize the volcanic system as well as observe trends and deviations from those trends that prove useful for future volcano monitoring.

5.1 Future Work

The studies included in this dissertation have spurred the desire for future work, centered on furthering research of the topics discussed as well as a focus on application of techniques used to the operational monitoring of volcanoes.

5.1.1 AVO-G2S Propagation Modeling in Real Time

Infrasound arrays are placed strategically along the Aleutian arc in areas that are easy for AVO to maintain to detect and locate eruptions from any of the 54 historically active volcanoes. The methods outlined in *Schwaiger et al.* [2019] and *Iezzi et al.* [2019a] have been directly applied to multiple other studies by AVO scientists, including the long range detection of infrasonic tremor from the Pavlof 2016 eruption [*Fee et al.*, 2017a], as well as infrasound detections of volcanic thunder [*Haney et al.*, 2018, 2020] and eruption signals [*Lyons et al.*, 2020; *Schwaiger et al.*, 2020] from the 2016-17 eruption of Bogoslof volcano. Additionally, unpublished work includes working with Hans Schwaiger and others to set up propagation modeling in near real time for AVO, where the atmosphere is reconstructed every 6 hours and propagation modeling is performed using each volcano with suspected heightened volcanic activity as a source. The application of propagation modeling to AVO's normal monitoring routine allows for an accurate measure of travel time and anticipate where acoustic energy is likely to be detected for each of AVO's six regional infrasound arrays.

5.1.2 Acoustic Source Inversions in Real Time

Prompt and accurate estimations of erupted mass using infrasound sensors would be beneficial for volcano monitoring in real time. Accurate measurements of the mass flow rate using acoustic source inversions of local infrasound waveforms have been shown to have good agreement with independent measurements of erupted mass [e.g. *Fee et al.*, 2017b]. Additionally, stable volume flow rate solutions have been shown to be possible, regardless of the assumed source mechanism [e.g. *Iezzi et al.*, 2019b], once the effects of topography are

accounted for. Therefore, the implementation of the methods outlined in Chapter 3 in near real time can be useful and likely robust for the volcano monitoring of AVO. We contend that the 3D Green's functions that account for the effects of topography can be computed in advance, and the assumption that the topography doesn't change significantly between explosions can be valid in many cases. AVO has a variety of alarms running continuously, so explosion onset time can be extracted from the messages output from the alarms when an event is detected. The onset time can then be used to obtain the explosion waveforms and the acoustic source inversions can be run relatively quickly, assuming a simple (monopole) source. The volume flow rate solution from the inversions can be converted to a mass flow rate assuming a mixture density of the plume [e.g. *Fee et al.*, 2017b] and results can finally be sent to AVO personnel. These methods should be rather easy to implement for volcanoes in Alaska with infrasound networks and that have the potential for transient volcanic explosions such as Cleveland, Pavlof, Korovin, and Shishaldin.

5.1.3 Infrasound Radiation in Three Dimensions

While we made strides to measure the vertical acoustic wavefields in *Iezzi et al.* [2019b] and *Jolly et al.* [2017] using an infrasound aboard a tethered aerostat, we were still unable to provide a unique solution for the dipole source mechanism. I will be continuing this work as an NSF Postdoctoral Fellow at the University of California Santa Barbara by using a novel approach of collecting infrasound data with sensors aboard multiple unmanned aerial vehicles (UAVs) in addition to traditional sensor deployments on the ground. The UAV-mounted infrasound sensors will record data from unique angles, allowing for acoustic source inversion methods that account for the effects of topography to constrain the directional radiation pattern of explosions in a way not previously possible. The infrasound observations will be validated with ballistic trajectories determined from multiple cameras deployed around the crater rim, which we assume to be similar to the directionality of ash, gas, and steam emissions that may present harm to those near the volcano. Configuring UAV-mounted

infrasound sensors in a vertical line above one of the crater rim stations will, for the first time, allow us to investigate the precise vertical location of the infrasonic source. Finally, we will create a prototype and test a UAV infrasound sensor deployment where the sensor is flown to an inaccessible area, dropped off, and retrieved by the UAV. This technique can be applied for future monitoring during times of eruption crises.

5.2 References

Fee, D., M. M. Haney, R. S. Matoza, A. R. Van Eaton, P. Cervelli, D. J. Schneider, and A. M. Iezzi (2017a), Volcanic tremor and plume height hysteresis from Pavlof Volcano, Alaska, *Science*, *355*(6320), 45–48, doi:10.1126/science.aah6108.

Fee, D., P. Izbekov, K. Kim, A. Yokoo, T. Lopez, F. Prata, R. Kazahaya, H. Nakamichi, and M. Iguchi (2017b), Eruption mass estimation using infrasound waveform inversion and ash and gas measurements: Evaluation at Sakurajima Volcano, Japan, *Earth and Planetary Science Letters*, *480*, 42–52, doi:10.1016/j.epsl.2017.09.043.

Haney, M., A. Van Eaton, J. Lyons, R. Kramer, D. Fee, and A. Iezzi (2018), Volcanic Thunder From Explosive Eruptions at Bogoslof Volcano, Alaska, *Geophysical Research Letters*, *45*(8), doi:10.1002/2017GL076911.

Haney, M. M., A. R. Van Eaton, J. J. Lyons, R. L. Kramer, D. Fee, A. M. Iezzi, R. P. Dziak, J. Anderson, J. B. Johnson, J. L. Lapierre, and M. Stock (2020), Characteristics of thunder and electromagnetic pulses from volcanic lightning at Bogoslof volcano, Alaska, *Bulletin of Volcanology*, *82*(2), doi:10.1007/s00445-019-1349-y.

Iezzi, A. M., H. F. Schwaiger, D. Fee, and M. M. Haney (2019a), Application of an updated atmospheric model to explore volcano infrasound propagation and detection in Alaska, *Journal of Volcanology and Geothermal Research*, *371*, 192–205, doi:10.1016/j.jvolgeores.2018.03.009.

Iezzi, A. M., D. Fee, K. Kim, A. D. Jolly, and R. S. Matoza (2019b), Three-Dimensional Acoustic Multipole Waveform Inversion at Yasur Volcano, Vanuatu, *Journal of Geophysical Research: Solid Earth*, *124*(8), 8679–8703, doi:10.1029/2018JB017073.

Jolly, A. D., R. S. Matoza, D. Fee, B. M. Kennedy, A. M. Iezzi, R. H. Fitzgerald, A. C. Austin, and R. Johnson (2017), Capturing the Acoustic Radiation Pattern of Strombolian Eruptions using Infrasound Sensors Aboard a Tethered Aerostat, Yasur Volcano, Vanuatu, *Geophysical Research Letters*, *44*(19), 9672–9680, doi:10.1002/2017GL074971.

Lyons, J. J., A. M. Iezzi, D. Fee, H. F. Schwaiger, A. G. Wech, and M. M. Haney (2020), Infrasound generated by the 2016–2017 shallow submarine eruption of Bogoslof volcano, Alaska, *Bulletin of Volcanology*, *82*(2), doi:10.1007/s00445-019-1355-0.

Schwaiger, H., A. Iezzi, and D. Fee (2019), AVO-G2S: A modified, open-source Ground-to-Space atmospheric specification for infrasound modeling, *Computers and Geosciences*, *125*, 90–97, doi:10.1016/j.cageo.2018.12.013.

Schwaiger, H. F., J. J. Lyons, A. M. Iezzi, D. Fee, and M. M. Haney (2020), Evolving infrasound detections from Bogoslof volcano, Alaska: insights from atmospheric propagation modeling, *Bulletin of Volcanology*, *82*(3), 27, doi:10.1007/s00445-020-1360-3.